Solid form analysis with special consideration of perfusion calorimetry

Inaugural-Dissertation

zur Erlangung des Doktorgrades
der Mathematisch-Naturwissenschaftlichen Fakultät
der Heinrich-Heine-Universität Düsseldorf

vorgelegt von

Julia Baronsky
aus Bonn

Düsseldorf, Mai 2009

aus dem Institut für Pharmazeutische Technologie und Biopharmazie
der Heinrich-Heine Universität Düsseldorf

Gedruckt mit der Genehmigung der
Mathematisch-Naturwissenschaftlichen Fakultät der
Heinrich-Heine-Universität Düsseldorf

Referent: Prof. Dr. Nora Anne Urbanetz
Koreferent: Prof. Dr. Peter Kleinebudde

Tag der mündlichen Prüfung: 02.07.2009

Summary

A substance may exist in several solid forms that differ with regard to the three-dimensional structure and / or the number and type of components present. Solid forms may have different physical and chemical properties. Examples of crystalline solid forms are modifications and solvates. In case of modifications (mod.), the crystal lattices are built by molecules of the substance only while in case of solvates, the lattices additionally contain solvent molecules. If the solvent is water, the solvates will be named hydrates. As active pharmaceutical ingredients (APIs) and excipients present in a drug product may also exist in different solid forms which may have a considerable impact on efficacy, performance and safety of the drug product, it is necessary to control the solid forms of APIs and excipients. For this, the forms have to be known and characterised. One method to characterise solid forms is perfusion calorimetry in which the sample is subjected to a certain relative vapour pressure of solvent while measuring thermal activity. It allows the study of the interaction between solid forms and solvent vapours. Up to now, the potential of perfusion calorimetry in solid form analysis has barely been used.

In this study, the solid forms of APIs were studied and the potential of perfusion calorimetry in solid form analysis was explored with the aim to contribute to the understanding of solid forms. The APIs investigated were toltrazuril for which a solid form screening was performed and emodepside whose solid forms I-IV were characterised in order to analyse the state of water in the forms. The potential of perfusion calorimetry in the characterisation of both substances was examined. In order to be able to reliably perform perfusion calorimetry, a general method to test the perfusion systems used to control the relative vapour pressure of solvent during measurement was developed. In addition, the use of perfusion calorimetry in a new application field, the characterisation of solvates that retain their crystal structures upon desolvation (formation of isomorphic desolvates), was investigated.

The solid form screening performed for toltrazuril resulted in the mod. B, C and D. Mod. D and C are both monotropically related to mod. B, while mod. D and C are enantiotropically related. Regarding emodepside, the characterisation of the solid forms I-IV revealed that form I represents a modification while the forms II-IV are hydrates forming isomorphic desolvates. A general method to test perfusion systems was successfully developed so that perfusion calorimetry could be reliably performed. In case of toltrazuril, perfusion calorimetry was helpful to determine the relative stabilities of the modifications. Regarding emodepside, perfusion calorimetry indicated the transition of the desolvates II-IV into the isomorphic hydrates II-IV. The investigation of further solvates forming isomorphic desolvates confirmed the general suitability of the method to indicate the presence of this type of solvate. The analysis of the solid forms of the APIs and the study of the potential of perfusion calorimetry successfully contributed to the understanding of solid forms, especially of solvates forming isomorphic desolvates.

Summary in German

Eine Substanz kann in mehreren festen Systemen vorkommen, die sich in ihrer dreidimensionalen Struktur und / oder der Anzahl und Art von Komponenten unterscheiden. Diese Systeme, die als feste Formen bezeichnet werden, können unterschiedliche physikalische und chemische Eigenschaften aufweisen. Beispiele für kristalline feste Formen sind Modifikationen und Solvate. Im Falle von Modifikationen (Mod.) bestehen die Kristallgitter einzig und allein aus Molekülen der betreffenden Substanz, wohingegen die Kristallgitter von Solvaten zusätzlich Lösungsmittelmoleküle enthalten. Handelt es sich bei dem Lösungsmittel um Wasser, liegen sogenannte Hydrate vor. Da auch Wirk- und Hilfsstoffe eines Arzneimittels in verschiedenen festen Formen vorkommen können, die unter Umständen eine erhebliche Auswirkung auf die Sicherheit, Wirksamkeit und Qualität des Arzneimittels haben, ist es notwendig, die festen Formen von Wirk- und Hilfsstoffen zu kontrollieren. Dafür müssen die verschiedenen festen Formen bekannt und charakterisiert sein. Eine mögliche Methode, feste Formen zu charakterisieren, ist die Perfusionskalorimetrie. Bei dieser Methode wird die Probe einem kontrollierten relativen Dampfdruck eines Lösungsmittels ausgesetzt, während gleichzeitig der Wärmefluss der Probe gemessen wird. Die Methode ermöglicht es, Wechselwirkungen zwischen festen Formen und Lösungsmitteldämpfen, z.B. die Bildung von Solvaten, zu untersuchen. Bis zum heutigen Zeitpunkt ist das Potenzial der Perfusionskalorimetrie weitgehend ungenutzt.

In dieser Arbeit wurden sowohl feste Formen von Wirkstoffen analysiert als auch die Möglichkeiten der Perfusionskalorimetrie in der Analyse von festen Formen untersucht mit dem Ziel, einen Beitrag zum Verständnis von festen Formen zu leisten. Bei den untersuchten Arzneistoffen handelt es sich um Toltrazuril, das auf die Existenz verschiedener fester Formen hin untersucht wurde, und Emodepsid, dessen feste Formen I-IV unterschiedliche Mengen an Wasser sorbieren und die analysiert wurden, um die Rolle des Wassers in den Formen näher zu bestimmen. Der Nutzen der Perfusionskalorimetrie in der Charakterisierung beider Substanzen wurde untersucht. Um Perfusionskalorimetrie verlässlich ausüben zu können, wurde eine allgemeine Methode zur Überprüfung der Perfusionssysteme, die verwendet werden, um den relativen Lösungsmitteldampfdruck während der Messung zu kontrollieren, entwickelt. Zusätzlich wurde untersucht, inwieweit die Perfusionskalorimetrie zur Charakterisierung von Solvaten, die die im Kristallgitter befindlichen Lösungsmittelmoleküle unter Beibehaltung ihrer Kristallstrukturen abgeben (Bildung von sogenannten isomorphen Desolvaten), genutzt werden kann. Aufgrund der nur minimalen Änderungen im Kristallgitter durch das Verlassen der Lösungsmittelmoleküle ist die Identifizierung dieses Solvattyps mitunter schwierig, so dass die Suche nach weiteren Methoden, die geeignet sind, diesen Solvattyp zu charakterisieren, sinnvoll ist.

Bei der Untersuchung des Arzneistoffes Toltrazuril wurden drei Mod. B, C und D gefunden. Mod. D und C zeigen beide eine monotrope Beziehung zu Mod. B, wohingegen Mod. D und C eine enantiotrope Beziehung aufweisen. Bezüglich der verschiedenen Emodepsidformen wurde herausgefunden, dass es sich bei Form I um eine Modifikation handelt, während die Formen II-IV Hydrate darstellen, die isomorphe Desolvate bilden. Eine generelle Methode zum Test von Perfusionssystemen wurde erfolgreich entwickelt, so dass Perfusionskalorimetrie verlässlich ausgeübt werden konnte. Im Falle von Toltrazuril konnte die Perfusionskalorimetrie genutzt werden, um die Umwandlung der Modifikationen ineinander zu verfolgen. In Bezug auf Emodepsid erwies sich die Perfusionskalorimetrie als geeignet, die Umwandlung der Desolvate in die isomorphen Hydrate II-IV anzuzeigen. Die Untersuchung weiterer Solvate, die isomorphe Desolvate bilden, bestätigte, dass die Methode allgemein geeignet ist, die Existenz dieses Solvattyps anzudeuten. Hierbei handelt es sich um ein neues Anwendungsgebiet für die Methode. Schlussfolgernd kann gesagt werden, dass die Analyse der festen Formen der Arzneistoffe und die Untersuchung des Nutzens der Perfusionskalorimetrie erfolgreich zum Verständnis von festen Formen beitragen, insbesondere zum Verständnis von Solvaten, die isomorphe Desolvate bilden.

Table of contents

Abbreviations

A	cross section surface of the vessel
a	thermodynamic activity
A_n	pre-exponential factor
API	active pharmaceutical ingredient
C_p	heat capacity at constant pressure
ΔG^*	activation energy of nucleation
$\Delta G_{I\text{-}II}$	difference in the Gibbs energies of polymorph I and II
$\Delta G_{S\rightarrow S,(n)Solv}$	Gibbs energy of solvate formation
$\Delta G^{\ominus}_{S\rightarrow S,(n)Solv}$	standard Gibbs energy of solvate formation
ΔH_f	enthalpy of fusion
ΔH_t	enthalpy of transition
ΔS_f	entropy of fusion
D	diffusion coefficient
d	distance
DSC	differential scanning calorimetry
EtOH	ethanol
f	degrees of freedom
f	force constant
$f = dV / dt$	volume flow rate
f_0	total flow of nitrogen passed to the perfusion ampoule
f_{dry}	volume flow rate entering the dry line
f_{in}	total volume flow entering the reaction vessel
FT-IR spectroscopy	Fourier-transform infrared spectroscopy
FT-NIR spectroscopy	Fourier-transform near-infrared spectroscopy
FT-Raman spectroscopy	Fourier-transform Raman spectroscopy
f_{wet}	volume flow rate entering the wet line
f_{wet*}	volume flow rate of the wet line after having passed the solvent reservoirs filled with solvent
G	Gibbs energy
H	enthalpy
hkl	Miller indices
HT screening	high-throughput screening
IMC	isothermal microcalorimetry
J	nucleation rate
K	equilibrium constant
k	Boltzmann`s constant
m	mass
MeOH	methanol
MIR spectroscopy	mid-infrared spectroscopy
mod.	modification

mp	melting point
n	sample size
n	amount of substance
n_0	amount of substance of nitrogen
n_{Solv}	amount of substance of solvent
n_x	amount of substance of a gas x
p	pressure
p_{Solv}	partial vapour pressure of solvent
$p_{Solv,in}$	partial pressure of solvent inside the reaction vessel
$p_{Solv,sat}$	saturation vapour pressure of solvent
p_{tot}	total pressure
p_x	partial vapour pressure of a gas x
q	heat
R	gas constant
R^2	coefficient of determination
r_c	critical radius of the cluster
RH	relative humidity
RT	room temperature
RVP	relative vapour pressure
RVP_{in}	relative vapour pressure of solvent inside the vessel
RVP_{MeOH}	relative vapour pressure of methanol
RVP_{mfc}	actual relative vapour pressure provided by the two mass flow controllers
RVP_{set}	relative vapour pressure set in the software
RVP_{Solv}	relative vapour pressure of solvent
RVP_{valve}	actual relative vapour pressure provided by the valve
S	unsolvated crystalline form composed of API molecules
s	standard deviation
S	entropy
s	solubility
S,(n)Solv	solvate with n solvent molecules per molecule of API
$\langle$S,(n)Solv$\rangle$	solvate with n solvent molecules per molecule of API, isomorphic with $\langle$S,($n + p$)Solv$\rangle$
$\langle$S,($n + p$)Solv$\rangle$	solvate with (n + p) solvent molecules per molecule of API, isomorphic with $\langle$S,(n)Solv$\rangle$
SE	standard error
SNV method	standard normal variate method
Solv	solvent
T	temperature
T_g	glass transition temperature
tp	transition point
U	electrical potential

V	volume
VT	variable temperature
$\bar{x}$	arithmetic mean
XRPD	X-ray powder diffraction
α	level of significance
γ	interfacial free energy between the nucleus and the supersaturated solution
δ	diffusion layer thickness
ε	proportionality constant
λ	wavelength
ν	molecular volume
ν	vibrational frequency
$\bar{\nu}$	wavenumber
τ	time constant
σ	supersaturation ratio
Θ	angle

1 Introduction

In recent years, pharmaceutical industry became aware of the importance to search for different solid forms of active pharmaceutical ingredients (APIs) and excipients early in development (Newman and Byrn, 2003). Like any other substance, APIs and excipients may exist in different solid forms such as polymorphs, solvates and amorphous forms that may differ in their physical and chemical properties. Properties affected include key properties for the performance of the drug, e.g. compression behaviour being important in processing (Burger *et al.*, 1999) and solubility being critical for bioavailability (Stegemann *et al.*, 2007). Hence, for pharmaceutical industry, the existence of different solid forms represents a risk and an opportunity at the same time. The risk is the possibility that an undesired solid form suddenly appears during processing or storage, for example, which may, in the worst case, force the company to withdraw the drug product from the market, as happened for ritonavir (Chemburkar *et al.*, 2000). In order to minimise the risk of such an undesired event, a profound screening for solid forms is necessary. The opportunity however which comes along with the existence of different solid forms is the possibility to choose the solid form that has the most favourable properties, e.g. with regard to the manufacturing process or bioavailability.

The growing interest in solid form analysis requires a variety of characterisation methods. New techniques have been developed, e.g. terahertz spectroscopy, to expand the range of existing tools (Zeitler *et al.*, 2007). However, equally important to the development of new methods is to make full use of the potential of established techniques, e.g. calorimetric methods. One of the calorimetric methods is perfusion calorimetry which is used to characterise the interaction between solids and solvent vapours. It has been used to characterise amorphous material, for example (Danforth and David, 2006). However, its potential in other application fields, e.g. the characterisation of solvates, has been barely used. Hence, one aim of this study is to investigate the potential of perfusion calorimetry in solid form analysis. In order to reliably perform perfusion calorimetry, it is important that the perfusion system controlling the atmosphere over the sample works accurately. To verify its accurate performance, a general testing method was developed. Additionally, perfusion calorimetry was used to investigate two APIs found in veterinary drug products, emodepside and toltrazuril. They exist in different solid forms that were thoroughly characterised within this study. For toltrazuril, a solid form screening was carried out. Perfusion experiments were performed with special focus on the study of a certain solvate type, namely solvates that form isomorphic desolvates upon desolvation. The characterisation of this type of solvates may be a challenging task and therefore, further methods suitable to characterise this type are required. The overall aim of this study is to contribute to the understanding of solid forms.

2 Theory

2.1 Solid forms

2.1.1 Introducing remarks

The term “solid forms” has been frequently used in the solid state analysis of active pharmaceutical ingredients (APIs). It is used as general term in reference to the different types of solid systems in which an API molecule might exist, such as polymorphs, solvates, salts or amorphous systems (Chawla *et al.*, 2003; He *et al.*, 2000; Hilfiker *et al.*, 2006a; Stephenson *et al.*, 2001). However, the use of the term is not consistent and a generally accepted definition is missing. In this thesis, “solid forms” will be used as umbrella term for solid materials of the API that differ in their Gibbs energies at given conditions (temperature (T), pressure (p) and the amount of substance of each component (n_1,…,n_i)). The different Gibbs energies may result in different physical and chemical properties of the solid forms. Solid forms may be subdivided into two main classes: crystalline solids and amorphous solids.

2.1.2 Crystalline solids

The crystalline state is characterised by the regular arrangement of building blocks which may be atoms, molecules and groups of atoms, molecules or ions (Atkins and de Paula, 2006; Byrn *et al.*, 1999a). The three-dimensional expanded array of building blocks is known as the crystal lattice (Atkins and de Paula, 2006). The structural unit from which the crystal lattice is generated by translational repetition is termed the unit cell (Massa, 2002). Depending on whether the crystal lattice is composed of one component (API molecules) or several components (API plus one or more other components), crystalline solids may be classified into one- and multi-component systems (Rodriguez-Spong *et al.*, 2004). Various types of multi-component systems have been described such as solvates, co-crystals and salts (Khankari and Grant, 1995; Shan and Zaworotko, 2008; Stahl and Sutter, 2006). The lack of precise and generally accepted definitions of these terms and the existence of multi-component systems that are difficult to assign have made a concise classification difficult (Desiraju, 2003; Dunitz, 2003; Griesser, 2006; Vishweshwar *et al.*, 2006). This chapter will deal with solvates being the type of multi-component systems relevant for this work. Another important type of crystalline solids that has also been subject to discussions regarding its definition are polymorphs (Threlfall, 1995). Since part of this thesis is the investigation of polymorphs, they will be discussed in this chapter also.

2.1.2.1 Polymorphs

2.1.2.1.1 Definition

In 1965, McCrone defined a polymorph as “a solid crystalline phase of a given compound resulting from the possibility of at least two crystalline arrangements of the molecules of that compound in the solid state” (McCrone, 1965). According to this definition, polymorphs of an API are one-component systems being composed of only API molecules. In recent publications, a broader definition for polymorphs has been used: two polymorphs are crystalline solids of the same chemical composition which differ in their unit cells (Brittain, 2007; Hilfiker *et al.*, 2006a). The definition implies that polymorphs may also represent multi-component systems. In this thesis, the broader definition of polymorphs will be used. Polymorphs that are one-component systems will be referred to as modifications of the API.

2.1.2.1.2 Thermodynamics

At given T, p, the Gibbs energy of a polymorph, G, is expressed as:

$$G = H - TS \tag{1}$$

where H is the enthalpy and S is the entropy (Bernstein *et al.*, 1999). At absolute zero (T = 0 K), the entropy of a perfect crystal is zero according to the third law of thermodynamics (Grant, 1999). The term TS vanishes and G becomes equal to H. With rising temperature, the enthalpy H and the entropy S of the polymorph increase. As the term TS rises more quickly than H, the Gibbs energy G decreases with increasing temperature. The slope of G plotted against T is:

$$\left(\frac{\mathrm{d}G}{\mathrm{d}T}\right)_p = -S \tag{2}$$

The slope of the enthalpy function versus T equals the heat capacity of the polymorph at constant pressure, C_p:

$$\left(\frac{\mathrm{d}H}{\mathrm{d}T}\right)_p = C_p \tag{3}$$

In case of two polymorphs I and II with different Gibbs energies G_I and G_II at specified conditions (T, p), the polymorph having the lower Gibbs energy represents the more stable form (Bernstein *et al.*, 1999). Whether the stability order of the polymorphs changes with temperature depends on their thermodynamic relationship being either monotropic or enantiotropic. Both types of thermodynamic relationship

may be illustrated using energy-temperature diagrams (Fig. 1) (Burger and Ramberger, 1979a; Grunenberg *et al.*, 1996; Lohani and Grant, 2006).

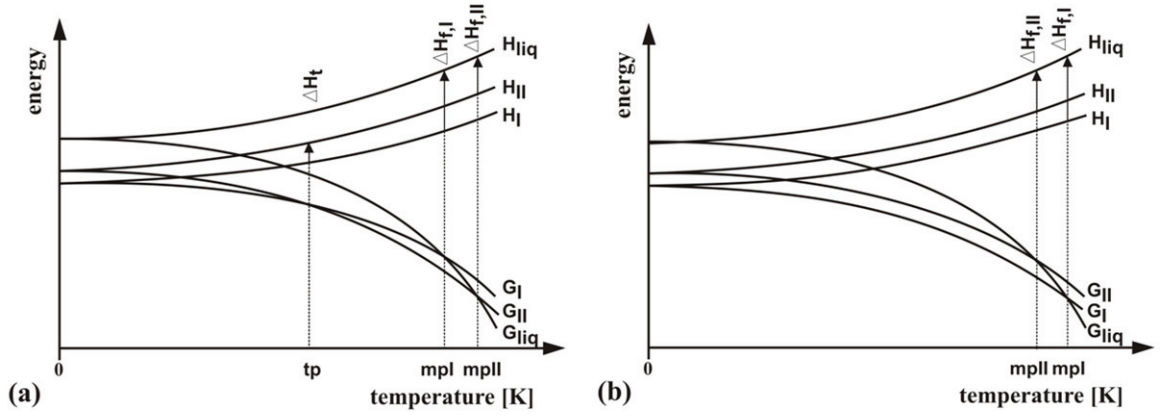

Fig. 1. Energy-temperature diagrams for an enantiotropic (a) and a monotropic (b) system; *G* is the Gibbs energy, *H* is the enthalpy, ΔH is the change in enthalpy, mp is the melting point, tp is the transition point and the subscripts I, II and liq refer to polymorph I, polymorph II and to the liquid phase (adapted from (Grunenberg *et al.*, 1996)).

In an energy-temperature diagram, the enthalpies and the Gibbs energies of both polymorphs I and II and of the liquid phase are plotted versus temperature (pressure is constant). Let polymorph I have the lower Gibbs energy at absolute zero ($G_I < G_{II}$). The *G*-isobars of the two polymorphs intersect the *G*-curve of the liquid phase at the melting points of the forms (mp_I and mp_{II}). At the melting point of a polymorph, the Gibbs energy of the polymorph equals the Gibbs energy of the liquid phase, i.e. both phases are in equilibrium with each other. In an enantiotropic system (Fig. 1a), there is a transition point (tp) below the melting point of the lower-melting form. At this transition temperature, the *G*-isobars of the two polymorphs intersect meaning that both forms are in equilibrium with each other having equal Gibbs energies. The difference in the enthalpies of the two polymorphs at tp is the heat of transition, ΔH_t. Below tp, polymorph I exhibits a lower Gibbs energy being the more stable form ($G_I < G_{II}$). Spontaneous phase transformation of polymorph II into polymorph I may take place below tp. Above tp, polymorph II is more stable having the lower Gibbs energy ($G_{II} < G_I$). As a consequence, form I may undergo spontaneous transformation into polymorph II above tp. In a monotropic relationship (Fig. 1b), there is no transition point between absolute zero and the melting point of the lower melting polymorph. Hence, the polymorph more stable at absolute zero, polymorph I, is the more stable form at all temperatures below mp_I. Polymorph II as the metastable form that has the higher Gibbs energy may undergo spontaneous transformation into form I.

Burger and Ramberger deduced that the polymorph being less stable at absolute zero (polymorph II) always has the higher heat capacity at $T > 0$ K (Burger and Ramberger, 1979a). Hence, as the heat capacity represents the slope of *H* plotted versus *T*, the enthalpy of polymorph II rises more quickly than the enthalpy of

polymorph I. Since polymorph II also has the higher zero-point enthalpy, it follows that polymorph II has the higher enthalpy at all temperatures below mp_I and that the enthalpy curves of the polymorphs diverge with rising temperature (Fig. 1). Consequently, in case of an enantiotropic relationship, a transition of polymorph II into I observed below tp is exothermic whereas a transformation of polymorph I into II that may occur above tp is endothermic. If the polymorphs are monotropically related, a possible transformation of polymorph II into I will be exothermic.

2.1.2.1.3 Assessment of relative stability

There are several rules used to predict whether two polymorphs display a monotropic or an enantiotropic relationship (Burger and Ramberger, 1979a; Burger and Ramberger, 1979b; Grunenberg *et al.*, 1996; Lohani and Grant, 2006; Yu, 1995). The above mentioned statements concerning the heat of observed transitions form the basis of one of the rules, the heat-of-transition rule. This rule states that if an endothermic transition is observed at a certain temperature, a transition point will be below this temperature, i.e. the relationship is enantiotropic; in case of an exothermic transition, there will be no transition point below the temperature of the observed transition meaning that the relationship is either monotropic or the thermodynamic transition point is higher. According to Burger and Ramberger, this rule gives correct results in more than 99 % of cases (Burger and Ramberger, 1979b). Other rules are the heat-of-fusion rule, the entropy-of-fusion rule, the heat capacity rule, the density rule and the infrared rule. Aside from the heat capacity rule whose use is restricted (Lohani and Grant, 2006), the rules will be described in the following.

The heat-of-fusion rule states that if the polymorph with the higher melting point has the lower heat of fusion, the polymorphs have an enantiotropic relationship, otherwise, they are monotropically related. This rule assumes that the heat of transition of two enantiotropically related polymorphs, ΔH_t, may be estimated by the difference in the heats of fusions, $\Delta H_{f,I} - \Delta H_{f,II}$. The error of the estimation is caused by the divergence of the enthalpy curves of the polymorphs with rising temperature. Therefore, there may be exceptions to this rule if the melting points differ by more than about 30 K (Grunenberg *et al.*, 1996). In these cases, the entropy-of-fusion rule is advantageous as it accounts for temperature. According to the rule, the higher melting polymorph has the lower entropy of fusion in an enantiotropic relationship. In case the polymorphs are monotropic, the higher melting form also exhibits the higher entropy of fusion. The entropy of fusion, ΔS_f, is expressed as follows:

$$\Delta S_f = \frac{\Delta H_f}{T} \tag{4}$$

The density rule assumes that at absolute zero, the polymorph with the closer packing of molecules has stronger intermolecular interactions and consequently a lower Gibbs energy. Based on this supposition, the rule states that if a polymorph

has a lower density at room temperature, it represents the less stable form at absolute zero. The rule may not be applicable for hydrogen-bonded polymorphs, because hydrogen-bonds substantially influence the zero-point Gibbs energy so that a correlation between density and stability may not be given (Burger and Ramberger, 1979a).

By contrast, the infrared rule only applies for hydrogen-bonded polymorphs. It states that if the frequency of the first absorption band in the infrared spectrum is higher for one hydrogen-bonded polymorph than for the other, the polymorph absorbing at higher frequency has the greater entropy and thus is less stable at absolute zero. However, there are exceptions to this rule that were investigated by Burger and Ramberger (Burger and Ramberger, 1979b).

If two polymorphs I and II are found to have an enantiotropic relationship, the transition temperature may be estimated by assessing the difference in the Gibbs energies of the polymorphs, $\Delta G_{\text{I-II}}$, at different temperatures (Rodriguez-Spong *et al.*, 2004). One way to obtain $\Delta G_{\text{I-II}}$ is the measurement of solubility (Bennema *et al.*, 2008). The Gibbs energy of a polymorph is proportional to the thermodynamic activity (a) of the form in solution (Grant, 1999). In case of a dilute solution, the activity is approximately proportional to the solubility (s). Hence, the difference in the Gibbs energies of the polymorphs I and II at given conditions (p, T) is described as:

$$\Delta G_{\text{I-II}} = RT\ln\left(\frac{a_{\text{I}}}{a_{\text{II}}}\right) \approx RT\ln\left(\frac{s_{\text{I}}}{s_{\text{II}}}\right) \tag{5}$$

with R being the gas constant. Irrespective of the solvent, the polymorph with the lower Gibbs energy has the lower solubility. At the transition temperature, both polymorphs display equal solubilities. In order to estimate the temperature of equal solubilities, the solubilities of the polymorphs are measured at different temperatures. The plot of log solubility versus the reciprocal of the temperature (van`t Hoff plot) permits to assess the transition temperature (Burger and Lettenbichler, 2000; He *et al.*, 2000). However, the solubility of the metastable polymorph might not be accessible due to fast solution-mediated transformation into the more stable polymorph. Solution-mediated transformation is explained by the higher solubility of the metastable polymorph which leads to the supersaturation of the solution with respect to the more stable polymorph. The latter will crystallise and as a result, the concentration in solution will drop below the solubility of the metastable polymorph. This causes further dissolution of the metastable polymorph. The process continues until the metastable polymorph has completely transformed into the more stable polymorph. Unlike in solubility measurements, solution-mediated transformation is desired in slurry conversion experiments that represent a second possibility to assess the transition temperature (He *et al.*, 2000; McCrone, 1965). In slurry conversion studies, a mixture of the polymorphs I and II is suspended in a solvent or

solvent mixture at different temperatures. At each temperature, the polymorph less stable at that temperature will transform into the more stable polymorph. The knowledge of the more stable polymorph at different temperatures allows the narrowing of the transition temperature range. The transformation into the more stable polymorph is either solution-mediated (see above) or it represents a solid-solid transition induced by the presence of solvent (2.2.2). Slurry conversion studies may not be helpful to narrow the transition temperature range in case a solid form exists that is more stable than both polymorphs at experimental conditions (e.g. a solvate) since transformation into this form may occur (He *et al.*, 2000).

2.1.2.2 Solvates

2.1.2.2.1 Introducing remarks

The incorporation of solvent molecules into the crystal lattice of an API results in a crystalline multi-component system containing at least the API (as neutral molecule or as ion plus counterion) and the solvent. There are numerous terms related to this type of multi-component systems such as solvate, co-crystal, pseudopolymorph, inclusion compound, molecular complex, solid solution and clathrate. Unfortunately, the views on how to define and to use these terms differ in literature (Almarsson and Zaworotko, 2004; Bernstein, 2005; Desiraju, 2003; Desiraju, 2004; Dunitz, 2003; Griesser, 2006). In this thesis, the term solvate is used to describe crystalline multi-component systems containing one or more solvents. A solvate is defined as a crystalline multi-component system in which a solvent (or several solvents) “is coordinated in or accommodated by the crystal structure” (Griesser, 2006). In case the solvent is water, the solid form is named hydrate. Besides solvate formation, there are other ways in which a solvent may be associated with a crystalline solid. One way is the adsorption of solvent molecules to the crystal surfaces via non-covalent interaction (Carvajal and Staniforth, 2006; Kontny and Zografi, 1995). The extent of adsorption depends, among other parameters, on the surface area available and may significantly affect surface properties. Adsorption may result in capillary condensation or deliquescence (Newman *et al.*, 2008). A further way for a solvent to associate with a crystalline solid is liquid inclusion which may occur during the crystallisation from solution. It describes the entrapment of small quantities of liquid in the growing crystal (Griesser, 2006). Additionally, solvent molecules may be absorbed into disordered defect regions caused by milling, for example (Ahlneck and Zografi, 1990; Airaksinen *et al.*, 2005; Saleki-Gerhardt *et al.*, 1994). The difference between the described ways of association and solvate formation is that in case of solvate formation, the solvent becomes part of the crystal structure. Hence, only in solvates, the solvent is present in the unit cell of the crystal lattice.

Solvates are of complex nature due to the various possibilities of incorporation of the solvent molecules into the crystal lattice. As water is omnipresent, studies have focussed on hydrates. However, the thermodynamic models and classification

schemes derived for hydrates may be translated into solvates. Hydrates (solvates) have been classified based on the environment of the water (solvent) molecules in the crystal lattice (Khankari and Grant, 1995; Morris, 1999). An alternative classification not requiring any structural information is the division into stoichiometric and non-stoichiometric solvates which will be described in the following (Griesser, 2006; Vippagunta *et al.*, 2001).

2.1.2.2.2 Stoichiometric solvates

A stoichiometric solvate is a solvate that, within the range of solvent activity its crystal structure exists in (at given p,T), has a fixed amount of solvent molecules inside the crystal lattice (Authelin, 2005; Griesser, 2006). The solvent molecules are usually ordered. However, there are also examples of molecules having some disorder (Alkhamis *et al.*, 2005). The unchanging number of solvent molecules inside the crystal lattice may be explained by two possible reasons. One possible reason is that solvent molecules are not able to enter / exit the lattice as channels or interlayer spaces of a sufficient size are absent, e.g. observed for cephradine dihydrate (Morris, 1999). In this case, the departure of the solvent molecules is destructive, i.e. the crystal structure has to be destroyed in order for the solvent molecules to be able to leave (Petit and Coquerel, 1996). The destructive desolvation process results either in amorphous material as in case of cephradine dihydrate (Morris, 1999) or in the formation of an unsolvated form with a different crystal structure (no structural filiation between the solvate and the unsolvated form). However, quite a few stoichiometric solvates have channels through which the solvent molecules might leave and enter the lattice, e.g. caffeine hydrate (Ahlqvist and Taylor, 2002). For these solvates, the reason for a fixed amount of solvent inside the crystal lattice is that the solvent molecules considerably contribute to the lattice energy, i.e. their presence is necessary to maintain the crystal structure. In case of desolvation, the departure of the solvent molecules itself may not destroy the crystal structure (cooperative departure), since the solvent molecules may leave along the channels (Byrn *et al.*, 1999b). However, without the solvent, the crystal structure is unstable and therefore becomes amorphous or turns into an unsolvated crystalline form with a different crystal structure. Due to the cooperative departure, structural filiations between solvate and the obtained unsolvated crystalline form are possible (Petit and Coquerel, 1996).

Summarising, the desolvation of a stoichiometric solvate results in the formation of either an amorphous form or an unsolvated crystalline form with a different crystal structure. The stoichiometric solvate and the form generated by desolvation (amorphous or crystalline) represent different solid forms and different phases. According to IUPAC, a phase is an entity of a material system which is uniform in chemical composition and physical state (IUPAC, 2006). This definition implies that in order for two solid forms to form a single phase, the three-dimensional structures have to be identical in order to achieve a uniform physical state. Since the

stoichiometric solvate and the form generated by desolvation differ in their structures, they represent different phases.

In the following, the thermodynamic model of stoichiometric solvates will be briefly described (Authelin, 2005; Lohani and Grant, 2006; Zhu *et al.*, 1996a). The model considers a system that is composed of the unsolvated crystalline phase (API as component), the solvate phase (API and solvent as components) and the vapour phase (solvent as component). The API and the solvent represent independent components being necessary to define this system (Authelin, 2005). The formation of the solvate with *n* solvent molecules per molecule of API may be represented by the following equilibrium (Zhu *et al.*, 1996a):

$$\mathrm{S} + n\mathrm{Solv} \Leftrightarrow \mathrm{S},(n)\mathrm{Solv} \tag{6}$$

S is the unsolvated form, Solv is the solvent and *S*,(*n*)Solv represents the solvate. Applying the law of mass action gives the equilibrium constant, $K_{\mathrm{solvate,formation}}$:

$$K_{\mathrm{solvate,formation}} = \frac{a(\mathrm{S},(n)\mathrm{Solv})}{a(\mathrm{S})a(\mathrm{Solv})^n} \tag{7}$$

The activities (*a*) of the pure solid phases (unsolvated form and solvate) are equal to 1 which simplifies Eq. (7). As the Gibbs energy of solvate formation, $\Delta G_{\mathrm{S}\rightarrow\mathrm{S},(n)\mathrm{Solv}}$, may be expressed in terms of the equilibrium constant, the following equation is derived for given *p*, *T* (Lohani and Grant, 2006):

$$\Delta G_{\mathrm{S}\rightarrow\mathrm{S},(n)\mathrm{Solv}} = \Delta G^{\ominus}_{\mathrm{S}\rightarrow\mathrm{S},(n)\mathrm{Solv}} + RT\ln(a[\mathrm{Solv}])^{-n} \tag{8}$$

where $\Delta G^{\ominus}_{\mathrm{S}\rightarrow\mathrm{S},(n)\mathrm{Solv}}$ is the standard Gibbs energy of solvate formation. Consequently, the Gibbs energy of solvate formation which represents the difference in the Gibbs energies of the unsolvated solid form and the solvate depends on the activity of the solvent (at given *p*, *T*). The activity of the solvent equals the ratio of the partial vapour pressure of the solvent (p_{Solv}) to the saturation vapour pressure of the solvent at the defined temperature ($p_{\mathrm{Solv,sat}}$) (Lohani and Grant, 2006). This ratio is called the relative vapour pressure of the solvent (RVP_{Solv}):

$$a(\mathrm{Solv}) = \frac{p_{\mathrm{Solv}}}{p_{\mathrm{Solv,sat}}} = RVP_{\mathrm{Solv}} \tag{9}$$

In case the solvent is water, the RVP_{Solv} is named relative humidity (*RH*). For a given temperature, there is only one *RVP* value at which the three phases (unsolvated form, solvate and vapour phase) are in equilibrium, i.e. $\Delta G_{\mathrm{S}\rightarrow\mathrm{S},(n)\mathrm{Solv}}$ is zero. Below this *RVP* value, the unsolvated form is more stable (lower Gibbs energy) whereas

above the *RVP* value, the solvate represents the more stable form. This results in a step-shaped vapour sorption isotherm. The schematic shape of such an isotherm is given in Fig. 2.

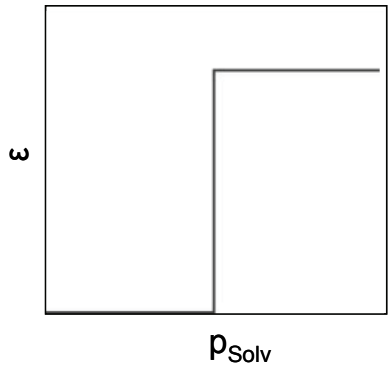

Fig. 2. Schematic shape of the sorption isotherm of a stoichiometric solvate where ε is the solvent uptake and p_{Solv} is the partial vapour pressure of solvent; modified from (Authelin, 2005).

Consequently, gravimetric vapour sorption analysis (2.3.5.1) may be used to assess the solvent activity at which both solvate and unsolvated form are in equilibrium (*p*, *T* are constant). However, this method will not be useful if the thermodynamic equilibrium is not attained due to kinetic factors. An alternative method to determine the relative stability of the solvate and the unsolvated form at different solvent activities (*p*, *T* are constant) is the conduction of slurry conversion studies using solvent mixtures to generate different activities of the solvent of interest (Zhu *et al.*, 1996a). When suspending a mixture of the solvate and the unsolvated form in a liquid with a certain solvent activity, the form metastable at the respective solvent activity will transform into the stable form via solution-mediated transformation or solid-solid transition (2.1.2.1.3). This method is based on the general rule that the stable solid form is in equilibrium with the liquid phase having the lowest solubility (Zhu *et al.*, 1996b).

2.1.2.2.3 Non-stoichiometric solvates

In contrast to a stoichiometric solvate, a non-stoichiometric solvate is a solvate that, within the range of solvent activity its crystal structure exists in (at given *p*,*T*), has a variable amount of solvent molecules inside the crystal lattice (Authelin, 2005; Griesser, 2006). Some non-stoichiometric solvates, e.g. tetracaine hydrochloride hydrate (Schmidt and Schwarz, 2006), incorporate and release solvent molecules across the whole range of solvent activity in which their crystal structures exist. For other non-stoichiometric solvates, e.g. spirapril hydrochloride monohydrate (Stephenson *et al.*, 1998), the number of solvent molecules inside the crystal lattice changes only within part of the range of solvent activity its crystal structure exists in. The crystal structure of spirapril hydrochloride hydrate exists in the range of 0 % water activity (*RH*) up to very high *RH*. The amount of water in the lattice

considerably changes in the range of 0 % to 10 % *RH*, but is more or less constant at higher *RH*.

In non-stoichiometric solvates, the solvent molecules that are incorporated into the crystal lattice without changing the three-dimensional structure are regarded as filling structural voids present in the crystal structure (Ruth *et al.*, 2003). These voids are connected to form tunnels through which the solvent molecules enter and leave the solid (Redman-Furey *et al.*, 2005; Stephenson and Diseroad, 2000). The solvent molecules incorporated are either ordered occupying fixed positions in the crystal lattice or they are disordered moving easily from one bonding position to the other (Authelin, 2005).

Often, the range of solvent activity in which the non-stoichiometric solvate incorporates and releases solvent molecules without changing its crystal structure includes zero solvent activity (0 % RVP_{Solv}). This means that at 0 % RVP_{Solv}, when all solvent molecules have left the crystal lattice, the crystal structure still maintains, i.e. the solvent molecules are not required for the crystal structure to exist (Petit and Coquerel, 1996; Stephenson *et al.*, 1998). Examples for non-stoichiometric solvates that desolvate retaining their crystal structures are spirapril hydrochloride monohydrate (Stephenson *et al.*, 1998), amlodipine besilate monohydrate (Rollinger and Burger, 2002) and thiamine hydrochloride monohydrate (Ruth *et al.*, 2003). The isostructural unsolvated form generated by desolvation is called isomorphic desolvate or desolvated solvate. It has the same space group and the same three-dimensional arrangement of the API molecules as the original solvate, however, the lattice parameters may slightly differ due to lattice contraction (see below) (Griesser, 2006). Additionally, the departure of the solvent molecules changes the local environment of molecular groups that were located next to the solvent molecules (Ruth *et al.*, 2003). Compared to the solvate in which the solvent molecules contribute to the lattice energy, the isomorphic desolvate displays a lower lattice energy and therefore represents a high-energy state (Stephenson *et al.*, 1998). It may lower its internal energy by absorbing molecules of another solvent or by lattice contraction which enhances the packing efficiency.

Other non-stoichiometric solvates have, in addition to the solvent molecules that enter and leave the lattice without changing the packing motif of the crystal, solvent molecules that are necessary for the maintainance of the three-dimensional structure. Consequently, the departure of these solvent molecules has to result in a change of the crystal structure. An example for such a non-stoichiometric solvate is cromolyn sodium hydrate (Stephenson and Diseroad, 2000). In the range of 5 % *RH* to high *RH*, the amount of solvent molecules inside the lattice changes without affecting the three-dimensional structure. However, when reducing *RH* below 5 %, the removal of the water molecules being coordinated with the sodium ions significantly disturbs the lattice resulting in the transformation into a poorly crystalline state.

Thermodynamic models were derived to describe the behaviour of non-stoichiometric solvates as a function of RVP_{Solv} at given p, T (Authelin, 2005). These models consider non-stoichiometric solvates as solid solutions in equilibrium with the vapour phase. Regarding non-stoichiometric solvates with ordered solvent molecules, two similar models have been developed which assume the non-stoichiometric solvate to be a solid solution of structural elements having n molecules of solvent per molecule of unsolvated solid (n-solvate) and structural elements having $(n+p)$ molecules of solvent per molecule of unsolvated solid (($n+p$)-solvate). One of the two models describes the equilibrium as:

$$\langle \mathrm{S},(n)\mathrm{Solv}\rangle + p\mathrm{Solv} \Leftrightarrow \langle \mathrm{S},(n+p)\mathrm{Solv}\rangle \qquad (10)$$

where $\langle \mathrm{S},(n)\mathrm{Solv}\rangle$ and $\langle \mathrm{S},(n+p)\mathrm{Solv}\rangle$ are the n-solvate and the ($n+p$)-solvate. The term “solid solution” implies that the n-solvate and the ($n+p$)-solvate are isomorphic forming a single phase. In case an isomorphic desolvate exists, it represents a specific case of the n-solvate with $n = 0$. Hence, the desolvate and the non-stoichiometric solvate are the same phase. Nevertheless, they have different Gibbs energies (as pointed out above) that lead to differences in various properties, e.g. differences in hygroscopicity and differences in chemical stability (Stephenson *et al.*, 1998). Therefore, they are regarded as different solid forms which are defined as solid systems having different Gibbs energies (see section 2.1.1). This general definition of solid forms does not include the necessity for solid forms to represent separate phases. One has to be aware that the Gibbs energy of a non-stoichiometric solvate is not constant at different solvent activities but changes due to the changing amount of solvent molecules inside the lattice. If this change in Gibbs energy was taken into account, it would follow from the definition of solid forms that at each solvent activitiy, the solvate would correspond to a different solid form. However, this would result in a huge number of solid forms which would be unfunctional causing only confusion. Therefore, the change of the Gibbs energy of a non-stoichiometric solvate as a function of solvent activity is neglected. Within the range of solvent activity the solvate exists in, i.e. within the range in which solvent molecules are present inside the lattice, the solvate is regarded as one solid form. The desolvate is regarded as a different solid form in order to differentiate between one-component and multi-component systems. Two isomorphic solvates containing different solvents are also regarded as different solid forms in order to account for the difference in the Gibbs energies of the solvates caused by the presence of different solvents and in order to differentiate between solid systems that differ in the type of components present.

In addition to non-stoichiometric solvates that contain fixed solvent molecules, there are non-stoichiometric solvates having disordered solvent molecules which were also modelled by Authelin (Authelin, 2005). The equilibrium constants derived from the

various models were used to obtain sorption isotherm equations for solvates having ordered and disordered solvent molecules, respectively. As seen in Fig. 3, non-stoichiometric solvates with well located solvent molecules display either type I or type V isotherms. By contrast, the isotherms modeled for non-stoichiometric solvates having disordered solvent molecules agree with either type III or, in case some order exists for the first solvent molecules sorbed, with type II isotherm (Fig. 4).

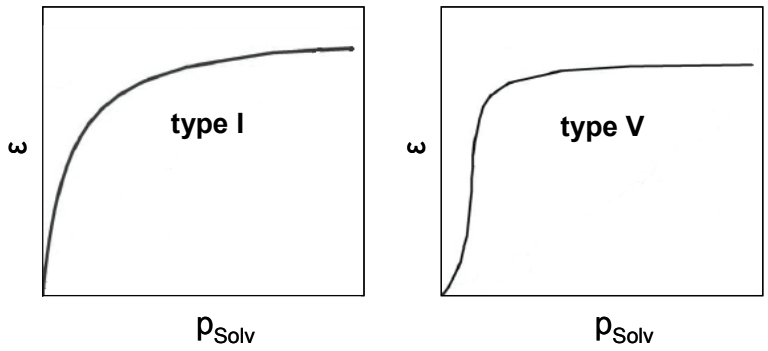

Fig. 3. Possible sorption isotherms (schematic shape) of non-stoichiometric solvates with ordered solvent molecules (ε is the solvent uptake and p_{Solv} is the partial vapour pressure of solvent), modified from (Authelin, 2005).

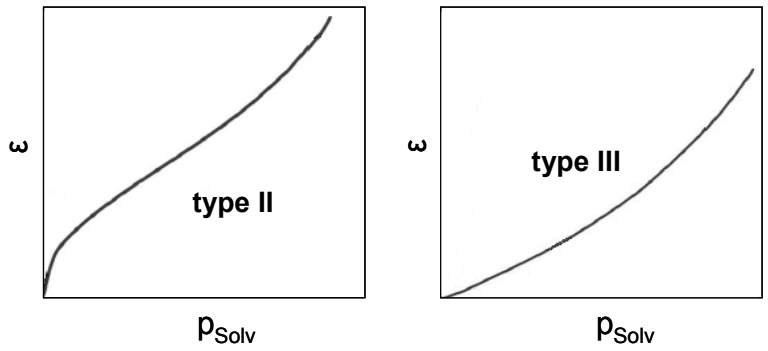

Fig. 4. Possible sorption isotherms (schematic shape) of non-stoichiometric solvates with disordered solvent molecules (ε is the solvent uptake and p_{Solv} is the partial vapour pressure of solvent), modified from (Authelin, 2005).

The shapes of the sorption isotherms of non-stoichiometric solvates (Fig. 3 and Fig. 4) differ from the shape of the isotherm characteristic for stoichiometric solvates (Fig. 2). Consequently, sorption analysis (2.3.5) is a major tool to differentiate between these types of solvate.

Although the classification into stoichiometric and non-stoichiometric solvates is useful in most cases, some substances might be difficult to assign. For example in case a channel solvate forms an intermediate isomorphic desolvate during the desolvation process before converting into an unsolvated form with a different crystal structure. If the isomorphic desolvate exists long enough to be detected, is the solvate then to be called non-stoichiometric? Despite some substances that are difficult to classify, the division into stoichiometric and non-stoichiometric solvates represents a useful concept with regard to this thesis, since the characterisation of

non-stoichiometric solvates forming isomorphic desolvates is one of the major aims of this study (see section 3).

2.1.3 Amorphous solids

Amorphous solids, also named glasses, are solids that, in contrast to crystalline forms, lack a long-range order of molecules (Yu, 2001). However, they may have local or short-range molecular order (Shah *et al.*, 2006). Compared to the crystalline state, the amorphous solid has a higher Gibbs energy meaning it is less stable (Petit and Coquerel, 2006). It may therefore spontaneously crystallise to reduce its Gibbs energy. In order to illustrate the nature of the amorphous state, a plot of the enthalpy of a substance as a function of temperature is given (Fig. 5).

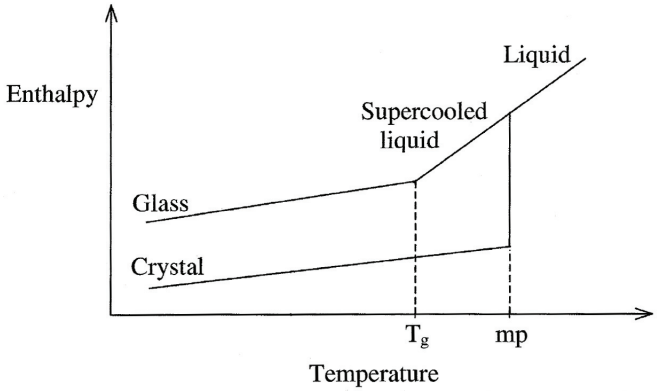

Fig. 5. Schematic plot of the enthalpy of a substance as a function of temperature to illustrate the glass transition temperature; adapted from (Petit and Coquerel, 2006).

The figure shows that when cooling the substance (liquid phase) to the melting point (mp) of the crystalline phase, crystallisation should occur being associated with a sudden decrease of enthalpy. In case the substance does not crystallise due to kinetic factors, a supercooled liquid, also termed rubbery state, is obtained. When cooling is continued, the supercooled liquid changes to the glassy state at the glass transition temperature (T_g). This transition is characterised by a decrease of the heat capacity of the material and a substantial reduction of molecular mobility. Since the slope of the line describing the enthalpy as a function of T (Fig. 5) equals the heat capacity of the substance, it decreases at T_g. The value of T_g obtained by thermal techniques depends on operating conditions such as the heating rate and the thermal history of the sample. The change in molecular mobility at T_g affects the probability of both crystallisation and chemical degradation. Thus, molecular mobility represents an important characteristic of amorphous substances.

The amorphous state being a disordered system provides free volume into which water and other solvent molecules may be absorbed. The solvent molecules act as plasticiser lowering T_g (Kontny and Zografi, 1995). The sorption of water as the most prominent plasticiser and the resulting effects on physical and chemically stability

have been studied for various amorphous substances (Ahlneck and Zografi, 1990; Airaksinen *et al.*, 2005; Kontny and Zografi, 1995).

2.1.4 Relevance for pharmaceutical industry

The solid state properties of an API affect all branches involved in the development of solid dosage forms including processing, quality control, biopharmacy and regulatory affairs (Byrn *et al.*, 1999a). Hence, the fact that different solid forms of an API exhibit different properties makes the study and control of the solid form an issue of utmost importance for pharmaceutical industry. The relevance of the topic becomes evident in the ICH Q6A Guidance on specifications. The guidance describes the possible existence of different solid forms and the necessity to set an acceptance criterion for the solid form content present in the drug substance in case the drug product safety, performance or efficacy is affected by the solid form (International Conference on Harmonisation, 1999). Numerous APIs have been shown to exist in different solid forms (Burger and Griesser, 1989; Griesser *et al.*, 2000; Henck *et al.*, 2000; Kitamura *et al.*, 1994). The various solid forms of an API may have differences in properties such as solubility, chemical stability, hygroscopicity, compression behaviour, flow properties, melting points and density (Byrn *et al.*, 1995; Byrn *et al.*, 2002; Di Martino *et al.*, 2007). Thus, as mentioned in the introduction, there is the chance to choose or even to design (crystal engineering) the solid form with the properties best suited for the drug product (Blagden *et al.*, 2007). A key property of the API in a solid dosage form is aqueous solubility, because it is, besides permeability, a critical factor for bioavailability (Stegemann *et al.*, 2007). Regarding poor soluble APIs (class 2 and 4 of the Biopharmaceutical Classification System), the enhancement of the solubility or the dissolution rate may improve bioavailability. Therefore, a form metastable at the conditions present in the gastrointestinal tract might be chosen for a drug product due to its higher solubility and dissolution rate compared to more stable forms (Blagden *et al.*, 2007; Kim *et al.*, 2008). Mebendazole represents such an example where a metastable polymorph (form C) is favoured due to its higher solubility (Gatonovic-Kustrin *et al.*, 2008). Superiority in properties important for manufacturing may also lead to the decision of formulating a metastable form (Katrincic *et al.*, 2009). However, in case a metastable form is used, it may convert into a more stable, undesirable form during the manufacturing process or during storage. Transitions during processing are well known and have been reported for caffeine (conversion of the metastable form I of caffeine into the stable form II upon grinding) and fostedil (transformation of the metastable form II of fostedil into the stable form I during compression), for example (Brittain, 2002). Factors including temperature, *RH*, solid form impurity and excipients may either impede or accelerate the transition. For example, high *RH* has been shown to promote the phase transition of famotidine form B (metastable) into form A (stable) during grinding (Cheng and Lin, 2008). However, even if a solid form stable at ambient conditions is chosen for drug development, solid form transformation

during manufacturing may be observed. The reason is that manufacturing often involves changes in temperature or composition (e.g. solvent addition) so that a solid form stable at ambient conditions may become metastable at processing conditions and conversion into a form more stable at these conditions may take place (Brittain, 2007). In addition, manufacturing steps like milling may induce the transformation into a (partly) amorphous material that may spontaneously convert into a metastable crystalline form (Brittain, 2002).

As a result, it is crucial to perform a sound solid form screening during pharmaceutical development, i.e. to investigate whether an API exists in different solid forms, and if so, to characterise these forms and to establish their relative stabilities at different conditions with the aim to ensure the stability of the selected form during processing and storage. Although a thorough study of the solid state of the API does not erase the possibility that an unknown, more stable form might appear late in development or even after the drug has been launched (Chemburkar *et al.*, 2000), it minimises the risk of such an undesirable event. In addition, a sound solid form screening may lead to an advantageous intellectual property situation (Aaltonen *et al.*, 2009). In a solid form screening, several methods to generate solid materials are usually applied in order to search for possible different solid forms of the API. The following section (2.2) gives a brief overview of various methods used to produce solid forms.

2.2 Generation of solid forms

2.2.1 Methods based on the crystallisation from solution

Crystallisation from solution occurs due to supersaturation in order to reduce the Gibbs energy of the system (Lohani and Grant, 2006). It may be described as the formation of nuclei (nucleation) that grow to crystals (crystal growth) (Bernstein *et al.*, 1999; Grant, 1999; Lohani and Grant, 2006; Rodriguez-Spong *et al.*, 2004). First, pre-nucleation molecular assemblies form (clusters). The Gibbs energy of a cluster is determined by a volume term that promotes aggregation of molecules and a surface term that favours the dissolution of the cluster. At a critical radius of the cluster (r_c), the Gibbs energy of the cluster reaches a maximum which corresponds to the activation energy of nucleation ΔG^*. The activation energy of nucleation has to be overcome in order to form nuclei having a radius $r > r_c$. Based on ΔG^*, the nucleation rate J is calculated (Lohani and Grant, 2006) by:

$$J = A_n \exp\left(\frac{-\Delta G^*}{kT}\right) = A_n \exp\left(\frac{-16\gamma^3\nu^2}{3k^3T^3(\ln\sigma)^2}\right) \quad (11)$$

where A_n is the pre-exponential factor, k is the Boltzmann`s constant, γ is the interfacial free energy between the nucleus and the supersaturated solution, ν is the molecular volume and σ is the supersaturation ratio (defined as the ratio of solute

concentration in the supersaturated solution to that in the saturated solution). Eq. (11) describes the rate of homogeneous nucleation which occurs spontaneously in solution. By contrast, nucleation at interfaces or surfaces is termed heterogeneous nucleation. The rate of heterogeneous nucleation is obtained by modifying Eq. (11) (Yu *et al.*, 2004).

For an API being able to crystallise in different solid forms, the different solid forms have different values of r_c and ΔG^* (Bernstein *et al.*, 1999; Lohani and Grant, 2006). The outcome of crystallisation, i.e. which solid form(s) crystallise(s), depends on the combination of the relative nucleation rates and the relative crystal growth rates of the solid forms.

Supersaturation being the driving force for crystallisation may be achieved by temperature change, solvent evaporation, anti-solvent addition or suspension of a solid form being metastable in the system chosen. The latter method corresponds to solution-mediated slurry conversion (2.1.2.1.3). Each crystallisation method has a variety of process variables that may affect both nucleation and crystal growth and therefore may have an effect on the outcome of crystallisation (Table 1) (Kitamura, 2002; Morissette *et al.*, 2004).

Table 1 Composition and process variables affecting the crystallisation process from solution, adapted from (Morissette *et al.*, 2004)

Composition variables	**Process variables**				
	Thermal	Anti-solvent	Evaporation	Slurry conversion	In general
Solvent / solvent combination	Rate of temperature change	Anti-solvent type	Rate of evaporation	Solvent type	Mixing rate
Degree of supersaturation	Maximum temperature	Rate of anti-solvent addition	Evaporation time	Incubation temperature	Impeller design
Additive type and concentration	Incubation temperature(s)	Temperature of anti-solvent addition	Carrier gas	Incubation time	Crystallisation vessel design
Counter-ion; acid/base ratio	Incubation time	Time of anti-solvent addition	Surface-volume ratio	Thermal cycling and gradients	
Ionic strength					
pH					

As a rule, fast crystallisation processes favour the emergence of metastable forms (including amorphous material) whereas slow crystallisation processes favour the generation of the thermodynamically stable form (Aaltonen *et al.*, 2009; McCrone, 1965). Further crystallisation methods that are not mentioned in Table 1 are freeze-drying and spray drying. They are used to produce amorphous as well as

crystalline forms (Burger *et al.*, 1999; Columbano *et al.*, 2002). In addition to the process variables, the composition of the system influences the outcome of crystallisation (Table 1). Major components as well as components being present at a very low concentration, e.g. impurities from synthesis, may have an effect on the solid form produced (Blagden *et al.*, 1998; Threlfall, 2000). Hence, additives have been used with the aim to control the outcome of crystallisation. For example, polymers have been shown to be capable of promoting the formation of the desired form (Llinas and Goodman, 2008).

2.2.2 Alternative methods

In addition to the generation of solid forms from solution, solid materials may be obtained via sublimation, via solidification of the melt and through solid-solid transformation. In case of crystallisation via sublimation, the solid material converts partially from the solid to the gaseous state upon heating followed by the crystallisation on cooler surfaces in the proximity of the heated material (Guillory, 1999). This method is applicable to thermally stable APIs and requires a certain vapour pressure. The sublimation and subsequent crystallisation of various APIs was studied by Kuhnert-Brandstätter using thermomicroscopy (Kuhnert-Brandstätter, 1971).

The generation of solid forms from the melt represents a method suitable to produce the stable form as well as metastable forms depending on the temperature program used. Rapid supercooling of the melt favours the formation of metastable materials including amorphous forms (McCrone, 1965). Examples of APIs obtained in the amorphous state by rapid supercooling are sulfapyridine and simvastatin (Ambike *et al.*, 2005; DattaChowdhury *et al.*, 2005). Crystallisation from the melt may be the sole preparation method for certain solid forms, as e.g. reported in the case of (R,S)-propoxyphylline (Griesser *et al.*, 2000).

Solid-solid transformations as a further way to yield solid forms are transitions in the solid state (Byrn *et al.*, 1999c). An example of solid-solid transformations is the phase transition of one modification into another. For various substances, the mechanisms of solid-solid transformations were studied (Dong *et al.*, 2002; Wildfong *et al.*, 2007) and models describing the mechanisms of conversions were developed. Regarding the mechanism of the transition of one modification into another, a four-step model was described (Byrn *et al.*, 1999c). In this model, the transition starts by molecular loosening in the initial crystalline form leading to the formation of an intermediate solid solution. Nucleation of the new crystalline form takes place in the intermediate state followed by the growth of this form. The first step of the transition may be facilitated by the interaction with solvent molecules present in the gaseous state (vapour-mediated transition, (Vemuri *et al.*, 2004)) or in the liquid state (solvent-mediated transition, (Byrn *et al.*, 1999c)), for example. Solid-solid conversions have been frequently observed during processing being usually regarded as an undesirable event during the manufacturing process (see section

2.1.4). However, solid-solid transition may also be used to produce the desired solid form. For example, form III of zanoterone chosen for the clinical drug product was generated by desolvating an acetonitrile solvate at 80 °C under vacuum (Rocco *et al.*, 1995).

2.2.3 Performance of a solid form screening

The previous sections reveal that there are infinitely many possibilities to generate solid materials in a solid form screening. Up to now, there are no universal guidelines on how to perform a solid form screening (Aaltonen *et al.*, 2009; Hilfiker *et al.*, 2006b). A major reason is that each substance has unique properties that require a customised solid form screening. In addition, the design of a solid form screening is complicated by the fact that processes related to the solid form formation are not yet completely understood (Davey, 2004). As there is no a priori knowledge about the conditions under which different solid forms will be obtained (provided that the API examined exists in different solid forms), it is recommended to perform a diverse solid form screening in order to enhance the probability of finding all relevant solid forms (Aaltonen *et al.*, 2009; Morissette *et al.*, 2004). The classical solid form screening is based on the manual bench-scale generation of solid forms from both the melt and the solution (Burger and Lettenbichler, 2000). The generation from the melt should be performed using different heating rates. Crystallisation from solution should include different crystallisation methods at various compositions and process conditions. In order to cover the composition and process space, a large number of experiments is required which may render a classical solid form screening a time-consuming approach (Hilfiker *et al.*, 2006b). Thus, high-throughput (HT) screening methods have been developed which are based on automation and miniaturisation (Aaltonen *et al.*, 2009; Morissette *et al.*, 2004). HT screening focuses on the generation of solid forms from solution and allows the performance of a large number of experiments in parallel while using only low amounts of API. Opposed to these advantages are some drawbacks such as the absence of other generation methods (Aaltonen *et al.*, 2009). Therefore, a solid form screening should not rely exclusively on HT methods, but should rather combine them with carefully designed complementary experiments.

As an alternative to experimental screening methods, computational methods are in development which have the aim to predict the solid forms of a substance (Price, 2004). Despite the progress made, the prediction of crystal structures remains a challenging task so that there is still a need for experiments.

2.3 Methods to characterise solid forms

2.3.1 Preface

In case the screening experiments of a solid form screening result in different solid forms of the API, the forms have to be thoroughly characterised. There are numerous methods that may be used to characterise the different solid forms of a substance. This chapter focuses on methods used in this study. The aim is not to comprehensively review each technique, but to describe basic principles and to give examples of applications in order to illustrate the usefulness of each method in solid form analysis.

2.3.2 Thermal analysis

2.3.2.1 Introductory remarks

The term thermal analysis refers to a group of methods which study one or more properties of a sample while the sample is subjected to a controlled temperature programme (Haines, 2002). In the following sections, thermal methods important for solid form analysis will be described.

2.3.2.2 Thermomicroscopy

Thermomicroscopy allows the visual inspection of crystals while they are thermally treated (Nichols, 2006). The sample is placed on a hot-stage which is then subjected to a temperature programme to observe thermally induced events such as melting or polymorphic transition. The use of polarised light represents a valuable tool in thermomicroscopy. Viewed under polarised light, anisotropic crystals show interference colours. Although the colours of crystals usually do not give information about the solid form being present, the use of polarised light e.g. facilitates the recognition of recrystallisation processes from the melt (Grunenberg, 1997). The investigation of a substance with a hot-stage microscope employing different temperature programmes may be a fast way of generating new solid forms and is therefore an important technique for solid form screening. In addition to its application as a means of producing new forms, thermomicroscopy is used to characterise and investigate the behaviour of solid forms upon thermal treatment. For example, desolvation of a solvate resulting in a solvent-free form with a different crystal structure is usually recognised by a turbidity or blackening of the originally clear crystal (Kofler, 1954). Thermomicroscopy has been combined with other solid state characterisation techniques such as Raman spectroscopy to complement and verify thermomicroscopic results (Kuhnert-Brandstätter, 1996).

2.3.2.3 Differential scanning calorimetry (DSC)

Differential scanning calorimetry measures the heat changes occurring during a thermally induced process. Differential scanning calorimeters are divided into two

categories depending on their measuring principle: heat flux or power compensation (Kuhnert-Brandstätter, 1996; Laye, 2002). In heat flux DSC, sample and reference are heated in the same furnace and the temperature difference between sample and reference is measured using thermocouples. In order to convert the measured signal (electrical potential) into the heat flow of the sample, a proportionality constant has to be experimentally determined (Burger, 1982) (see section on isothermal microcalorimetry, 2.3.5.2.1). In case of power compensation DSC, sample and reference have separate heaters and temperature sensors. When a temperature difference arises between sample and reference, the heaters are used to eliminate the difference. The differential thermal power necessary to compensate the temperature difference is the measured signal. Thus, the measured signal directly corresponds to the heat flow of the sample which is an advantage of power compensation DSC. The result of DSC is a thermogram obtained by plotting the heat flow, dq / dt, versus temperature.

The applications of DSC range from purity determination to safety studies and solid form characterisation (Laye, 2002). DSC is an inherent part of solid form screening (Giron, 1995; Giron *et al.*, 1997; Liggins *et al.*, 1997; Zhu *et al.*, 1997). Similar to thermomicroscopy, it is used to generate new forms from the melt as well as to identify and study solid forms. The advantage over thermomicroscopy lies in the provision of quantitative data (enthalpy changes, e.g. fusion enthalpy) that are important for the establishment of the thermodynamic relationship of polymorphs (Threlfall, 1995). Due to the fact that DSC measures heat changes, DSC is capable of observing different events such as glass transition, polymorphic conversion, desolvation and melting, because each process absorbs or produces heat. However, the method does not identify the process(es) responsible for the heat changes. Thus, especially in the case of complicated DSC curves, other techniques have to be used in addition. The advantages and limitations of DSC have been discussed by Giron (Giron, 1995).

2.3.2.4 Thermogravimetric analysis (TGA)

Thermogravimetric analysis measures the mass change of a substance as a function of temperature. It is therefore particularly used to study the desolvation of solvates and to detect sublimation and decomposition processes (Alkhamis *et al.*, 2005; Heal, 2002; Sheng *et al.*, 1999). If a weight loss is recorded, TGA will not reveal the nature of the substance lost. Therefore, it has been coupled to other techniques such mass spectroscopy or infrared spectroscopy in order to identify the gas evolved (Giron *et al.*, 2002; Rodriguez and Bugay, 1997).

2.3.3 Vibrational spectroscopy

Spectroscopy is defined as the study of physical systems by the electromagnetic radiation with which they interact or that they produce (IUPAC, 2006). In vibrational spectroscopy, the radiation originating from an external source interacts with the

physical system under study causing transitions between vibrational energy states. Vibrational spectroscopic methods covered in this section are mid-infrared (MIR), near-infrared (NIR) and Raman spectroscopy. In MIR and NIR spectroscopy, vibrations are excited by absorption of light in the mid-infrared region (4000 cm^{-1} to 400 cm^{-1}) and near-infrared region (12500 cm^{-1} to 4000 cm^{-1}), respectively (Siesler, 2002). MIR and NIR spectrometers use a polychromatic source from which the sample absorbs particular frequencies corresponding to the frequencies of its vibrational transitions. In MIR spectroscopy, mostly transitions from the ground state to the first excited vibrational state (fundamental vibrations) occur, whereas in NIR spectroscopy, transitions to higher excited vibrational levels (overtone vibrations) and combinations of fundamental vibrations are observed (Fig. 6).

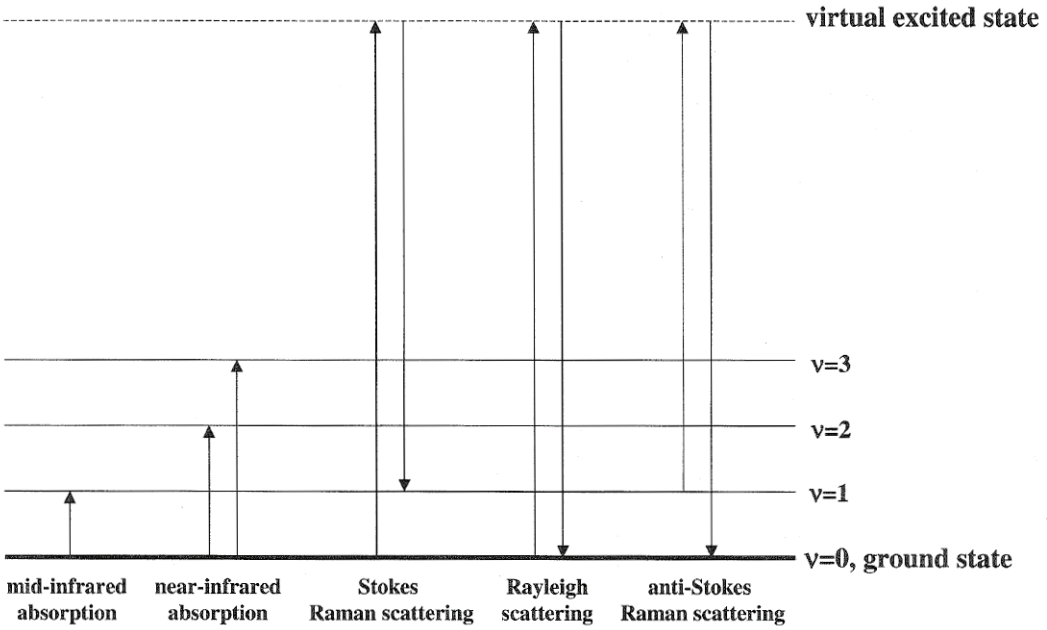

Fig. 6. Energy level diagram showing the transitions between vibrational energy states associated with infrared absorption and Raman and Rayleigh scattering; regarding near-infrared absorption, overtone vibrations are displayed; taken from (Chalmers and Dent, 2006).

Contrary to MIR and NIR spectroscopy that represent absorption techniques, Raman spectroscopy is a scattering technique (Chalmers and Dent, 2006; Schrader, 1995). In Raman spectroscopy, the sample is irradiated with monochromatic laser light. The incident photons induce the excitation of the molecules of the sample from the ground state to a virtual high energy state. Most of the molecules return to the ground state by elastic scattering (Rayleigh scattering) emitting photons that have the same frequency as the excitation radiation (Fig. 6). However, some molecules only return to the first excited vibrational state by an inelastic scattering process (Raman scattering) emitting photons of a lower frequency (Stokes line) (Fig. 6). The frequency difference to the excitation radiation corresponds to the vibrational energy absorbed in MIR spectroscopy (Siesler, 2002). Hence, the same vibrations are induced by both Raman and MIR spectroscopy, however, by different mechanisms.

Raman scattering may be also observed in molecules that are in the first excited vibrational state when being irradiated with monochromatic light. In this case, excitation is followed by the return to the ground state. Thereby photons are emitted which have a higher frequency compared to the excitation light (anti-Stokes line) (Fig. 6). As the number of molecules in the first excited vibrational state is much smaller than the number of molecules in the ground state, the Stokes lines have higher intensities compared to the anti-Stokes lines and are usually recorded to obtain the Raman spectrum.

The MIR, NIR and Raman spectrum obtained for a substance is characteristic of that substance, since its vibrational frequencies depend on molecular parameters. Based on a harmonic oscillator approximation, the vibrational frequency ν of a diatomic molecule is given by (Schrader, 1995):

$$\nu = \frac{1}{2\pi}\sqrt{f\left(\frac{1}{m_1}+\frac{1}{m_2}\right)} \tag{12}$$

where the force constant *f* is a measure of the bond strength and m_1 and m_2 are the masses of the two atoms. In vibrational spectroscopy, it is common not to measure the frequencies at which vibrational transitions take place but to measure wavenumbers. The wavenumber $\bar{\nu}$ being the reciprocal of the wavelength is proportional to the vibrational frequency. As vibrational frequencies depend on the strengths of intramolecular bonds (Eq. (12)) which are affected by intermolecular interactions, vibrational spectroscopy is sensitive to the local environment of a molecule which is different in different solid forms. Thus, vibrational spectroscopy is of great importance in solid state analysis. Major applications include the identification, characterisation and quantification of solid forms (Aaltonen *et al.*, 2007a; Burger *et al.*, 1999; Caira *et al.*, 2002; De Beer *et al.*, 2004; Stephenson *et al.*, 2001). Furthermore, vibrational spectroscopy is a valuable tool in the study of solid form transformations (Amado *et al.*, 2007; Hausman *et al.*, 2005; Kogermann *et al.*, 2007; Räsänen *et al.*, 2001; Shah *et al.*, 2006). In each of the application fields mentioned, signal processing and multivariate data analysis play an important role (Airaksinen *et al.*, 2003; Buckton *et al.*, 1999a; Heinz *et al.*, 2007; Kogermann *et al.*, 2007; Zhou *et al.*, 2003).

Due to their differences in various aspects, MIR, NIR and Raman spectroscopy each have their own benefits and limitations. MIR and Raman spectroscopy complement one another in that in MIR spectroscopy, a change of the dipole moment is required during the vibration in order for a vibrational transition to occur whereas in Raman spectroscopy, a change of the polarisability has to take place (Siesler, 2002). Hence, MIR spectroscopy focuses on polar groups while Raman spectroscopy is especially sensitive to non-polar groups. NIR spectroscopy requires, in addition to a change in the dipole moment, a large anharmonicity of the vibrating atoms. These conditions

are fulfilled by hydrogen to heteroatom bonds (X-H bonds) which therefore dominate the NIR spectrum. The sensitivity to molecules displaying X-H bonds makes NIR spectroscopy a valuable technique in the study of solid-water interactions (Cao *et al.*, 2006; Delwiche *et al.*, 1991; Lane and Buckton, 2000; Räsänen *et al.*, 2001; Vora *et al.*, 2004; Zhou *et al.*, 2003; Zhou *et al.*, 1998). Both NIR and Raman spectroscopy have several advantages such as no need for sample preparation and the suitability for non-destructive in-line measurement (Siesler, 2002; Wikström *et al.*, 2005). These benefits provide the basis for their use as process analytical technology tools (Aaltonen *et al.*, 2007b; De Beer *et al.*, 2008; Tumuluri *et al.*, 2008). Opposed to these advantages are drawbacks such as fluorescence effects in Raman spectroscopy (Bugay, 2001). By using Fourier-transform (FT) Raman spectrometers that operate with an NIR laser, this problem may be avoided. FT instruments are also common in MIR and NIR spectroscopy due to their various advantages (Kawata, 2002). Further insight into the use, benefits and limitations of the different vibrational spectroscopic techniques is provided in literature (Aaltonen *et al.*, 2008; Blanco *et al.*, 1998; Bugay, 2001).

2.3.4 X-ray diffraction

In contrast to vibrational spectroscopy that probes the short-range structure in solid materials, X-ray diffraction is sensitive to long-range order (Yu *et al.*, 1998). The long-range order of atoms in a crystal allows the crystal to act as a three-dimensional diffraction grating to light having wavelengths comparable to the interatomic distances (Brittain, 1999; Byrn *et al.*, 1999a). As the interatomic distances in a crystal are in the order of magnitude of Angströms (Å), X-rays having wavelengths of 1 Å to 10 Å are suitable for diffraction. When monochromatic X-rays impinge on a crystal, they are scattered as a result of the interaction with the electron clouds of the atoms. Depending on their path difference, the scattered X-rays may reinforce due to constructive interference resulting in the observation of diffracted radiation. The incident X-rays may be regarded as if they were reflected from a set of parallel planes passing through the crystal (Byrn *et al.*, 1999a). Constructive interference occurs when the path difference between two reflected X-ray waves differs by an integral number n of the wavelength λ. This condition is described by the Bragg equation (Massa, 2002):

$$2d \sin\Theta = n\lambda \tag{13}$$

where $2d \sin\Theta$ is the path difference with d being the distance between the planes and Θ being the angle between the incident rays and the set of planes. The direction and spacing of a family of lattice planes are defined by the Miller indices (hkl). These indices are the reciprocals, reduced to integers, of the intercepts that a plane has with the unit cell axes. Each family of lattice planes has a corresponding Bragg diffraction angle at which constructive interference occurs.

In single crystal X-ray diffraction, a crystal that ideally does not have any defects (single crystal) is usually irradiated with monochromatic X-rays. The resulting diffracted radiation is recorded as a pattern of spots (diffraction pattern) (Brittain, 1999). Each spot, also called reflection, corresponds to a set of planes being in a position to diffract. The angles at which the spots occur are used to deduce the unit cell dimensions. The relative intensities of the diffracted radiation allow the determination of the positions of the atoms within the unit cell. Hence, single crystal X-ray diffraction provides detailed structural information on crystals (Othman *et al.*, 2007; Yu *et al.*, 1998). However, the requirement of a suitable single crystal and the complexity of data analysis prevent it from being used as a routine method for solid form characterisation.

In X-ray powder diffraction (XRPD), the sample being irradiated is a powder (Allmann, 2003). In a powdered crystalline sample, crystals are differently orientated with respect to the X-ray beam. For each set of planes, there are several crystals being in the position to diffract. Hence, the intensity of the diffracted radiation corresponding to a set of planes (recorded at a certain angle of the incident beam) depends on the number of crystals being in a position to diffract. In order that the relative intensities of the diffracted radiation may be used to determine the unit cell contents, the crystals have to be randomly orientated. However, preferred orientation takes place in most of the cases. This is one of the factors that complicate the determination of the crystal structure from X-ray powder data which is therefore not frequently performed. Nevertheless, the X-ray powder pattern of a crystalline solid form, i.e. the plot of the diffracted X-ray intensity versus diffraction angle, is characteristic for the crystal structure of the form making XRPD a method of great importance in the analysis of solid forms (Davidovich *et al.*, 2001; Saleki-Gerhardt *et al.*, 1994).

2.3.5 Vapour sorption analysis

2.3.5.1 Gravimetric analysis

A common method to study the sorption of solvent vapours by a solid material is gravimetric measurement (Reutzel-Edens and Newman, 2006). This method is based on measuring the mass change of a sample exposed to different relative vapour pressures of a solvent (RVP_{Solv}) at constant temperature. The mass change corresponds to the amount of solvent sorbed. At each RVP_{Solv}, the stabilisation of the mass of the sample is awaited (attainment of steady state), thus, information about the rate at which the steady state is reached is obtained. The steady state solvent content of the sample is plotted versus RVP_{Solv} to obtain the sorption isotherm. It is important to provide sufficient time to allow the sample to reach a steady state at each RVP_{Solv} chosen. Whether, in the steady state, the sample is or is not in thermodynamic equilibrium depends on kinetic factors. The lack of equilibrium attainment either caused by an insufficient equilibration criterion or by kinetic factors

is a major reason for the observation of sorption / desorption hysteresis (Newman *et al.*, 2008; Reutzel-Edens and Newman, 2006). Another possible reason for hysteresis is that the equilibrium solvent content of the sample during sorption differs from the equilibrium solvent content during desorption. This will be the case for porous solids, for example, if capillary condensation occurs within the pores during sorption.

Due to the omnipresence of water, gravimetric water vapour sorption analysis is most relevant (Airaksinen *et al.*, 2005; Kontny and Zografi, 1995; Newman *et al.*, 2008; Umprayn and Mendes, 1987). Knowledge of the moisture sorption behaviour of both the API and the excipients is important as sorbed water vapours may have various effects, e.g. chemical stability, flow properties and compression behaviour may be affected. To appraise the impact that the sorption of solvent vapours may have on physical and chemical properties, it is crucial to know the type of solvent-solid interaction underlying the sorption process (Reutzel-Edens and Newman, 2006). The various types of solvent-solid interaction have been outlined in section 2.1.2.2.1. As different solvent-solid interactions lead to differences in the sorption isotherm, the sorption isotherm provided by gravimetric vapour sorption analysis may indicate the type of interaction present (Authelin, 2005; Newman *et al.*, 2008). The ability to provide information about solvent-solid interactions such as solvate formation makes gravimetric analysis a valuable method in the identification and characterisation of solvates (Giron *et al.*, 2002; Newman *et al.*, 2008; Schmidt and Schwarz, 2006; Wadso and Markova, 2001). However, since gravimetric vapour sorption analysis is not specific to any type of solvent-solid interaction due to the fact that each type of interaction is accompanied by an increase in mass, further methods may be necessary to determine the way the solvent is associated with the solid. Combination or hyphenation of gravimetric analysis with either vibrational spectroscopy or X-ray diffraction has been performed to enhance the understanding of solvent-solid interaction (Gift and Taylor, 2007; Giron *et al.*, 2002; Vora *et al.*, 2004).

2.3.5.2 Isothermal microcalorimetry

2.3.5.2.1 Introducing remarks

Isothermal microcalorimetry (IMC) represents another method suitable to study solvent vapour sorption, since each type of solvent-solid interaction is associated with heat changes. Because the thermal activity measured is related to the amount and energetics of solvent vapour sorption, which are both different in different solvent-solid associations, the type of solvent-solid interaction underlying the sorption process may be deduced from the calorimetric signal (Jakobsen *et al.*, 1997; Markova *et al.*, 2001; Reutzel-Edens and Newman, 2006; Sheridan *et al.*, 1995). However, due to the non-specific nature of calorimetry, a subsequent analysis of the sample is required using techniques such as vibrational spectroscopy to ensure that the calorimetric response has been interpreted correctly. In addition, the fact that the

thermal activity monitored is the sum of the heat changes of all processes occurring in the sample ampoule may further complicate interpretation (Buckton, 2000). IMC is based on heat conduction calorimetry, i.e. it uses the same measuring principle as heat flux DSC (2.3.2.3). In isothermal heat conduction calorimetry, sample and reference are kept at a constant temperature using a thermostat (heat-sink) (Gaisford, 2007). When the sample produces heat, the heat first accumulates in the sample vessel leading to a rise in the temperature of the vessel (heat accumulation). As a result, a temperature gradient between the vessel and the heat-sink is generated causing heat to flow towards the heat-sink (heat transfer). The heat is transferred across thermopiles located between sample vessel and heat-sink which generate an electrical potential, *U*, proportional to the heat transfer. The raw heat flow (power) signal of the sample, d*q* / d*t*, which corresponds to the sum of the heat accumulation and the heat transfer, is calculated from *U* using the following equation (Tian equation):

$$\frac{\mathrm{d}q}{\mathrm{d}t} = \varepsilon\left(U + \tau\frac{\mathrm{d}U}{\mathrm{d}t}\right) \tag{14}$$

where ε is the differential proportionality constant that has to be experimentally determined, it depends on the heat transfer coefficient and on the sensitivity of the thermopiles; τ is the differential time constant describing the delay in measurement response which is due to the temperature gradient that has to be created first. The equation also applies to reactions where the sample absorbs heat.
In this thesis, a Thermal Activity Monitor (TAM) heat conduction calorimeter supplied by TA Instruments, New Castle, Delaware, was used. For this instrument, there are two ways of subjecting the sample to a specific relative vapour pressure while measuring thermal activity. Both techniques will be outlined below.

2.3.5.2.2 Miniature humidity chamber

The first technique is based on a small glass tube which is placed inside the sample vessel (Angberg *et al.*, 1992). The tube is filled either with a saturated aqueous salt solution (Angberg *et al.*, 1982; Columbano *et al.*, 2002; Vemuri *et al.*, 2004) or with organic solvents or mixtures of solvents (Samra and Buckton, 2004; Yonemochi *et al.*, 1999) in order to create a certain *RVP* of water or solvent inside the sample ampoule. The “miniature humidity chamber” method has been used to assess low amounts of amorphous content in crystalline powders as well as to study the process of crystallisation of various amorphous substances (Ahmed *et al.*, 1996; Buckton *et al.*, 1995; Fiebich and Mutz, 1999; Kawakami *et al.*, 2001). It is a simple and inexpensive technique but has several disadvantages, e.g., a controlled change of *RVP* within an experiment is not possible.

2.3.5.2.3 Vapour pressure control device (perfusion calorimetry)

The alternative way of exposing the sample to a specific *RVP* of solvent (RVP_{Solv}) is the use of a perfusion system (Gaisford and Buckton, 2001). In a special perfusion ampoule, a carrier gas with a predefined RVP_{Solv} flows over the sample. The RVP_{Solv} may be altered stepwise or continuously during the experiment. The perfusion system is mainly used to control *RH*. *RH* perfusion calorimetry has a wide range of applications including the assessment of powder surface energies, the formation of hydrates, the onset of deliquescence and the study of amorphous material (Buckton *et al.*, 1999; Danforth and David, 2006; David *et al.*, 2003; Jakobsen *et al.*, 1997; Lehto and Laine, 1998; Timmermann *et al.*, 2006). Since the design of the perfusion system also allows the control of the *RVP* of organic solvents, perfusion calorimetry represents a valuable tool to study the sorption of organic solvent vapours. However up to now, this potential has barely been used (Mackin *et al.*, 2002; Markova *et al.*, 2001). A detailed description of the operating modes of the perfusion systems used in perfusion calorimetry will be given in section 2.4.

2.3.6 Special methods to identify solvates forming isomorphic desolvates

The previous sections have described a variety of methods used to characterise and identify different solid forms. This section will briefly highlight the methods suitable to identify non-stoichiometric solvates forming isomorphic desolvates, since the characterisation of this type of solvate is one of the major aims of this thesis as stated earlier. In case a solvate desolvates to a solid form with a different crystal structure or to an amorphous form, its identification is usually straightforward since the readily detected structural changes upon desolvation reveal that the solvent is coordinated in or accommodated by the crystal structure. Non-stoichiometric solvates that form isomorphic desolvates, however, might be challenging to identify due to the fact that desolvation causes only subtle changes to the crystal lattice (Reutzel-Edens and Newman, 2006; Rollinger and Burger, 2002). Additionally, since it is common for non-stoichiometric solvates to show an early and continuous loss of solvent when analysed with TGA and to have vapour sorption and desorption curves with little hysteresis (Schmidt and Schwarz, 2006; Stephenson *et al.*, 1998), the data might be misinterpreted and the solid might be regarded as single component system with solvent adsorbed to the crystal surface and / or absorbed into disordered defect regions.

Yet, there are certain methods permitting the identification of this type of solvate. Crystal structure determination is the most powerful of these methods since it reveals the contents of the unit cell (Ruth *et al.*, 2003). Other methods employed are XRPD and spectroscopic techniques (Stephenson *et al.*, 1997; Stephenson *et al.*, 1998). XRPD detects anisotropic shrinking of the crystal lattice which often takes place upon desolvation (2.1.2.2.3). This reduction in the unit cell volume leads to small shifts of peaks in the X-ray diffraction pattern towards smaller *d* spacings, shown for example

for the dehydrates of cephalexin monohydrate and erythromycin A dihydrate (Stephenson *et al.*, 1998). Though, in case the X-ray powder diffractogram does not exhibit any changes upon the removal of the solvent molecules (as the positions of the peaks do not necessarily have to shift (Stephenson *et al.*, 1998)), XRPD is not an adequate detection method. Spectroscopic techniques including vibrational spectroscopy and solid state nuclear magnetic resonance spectroscopy have been shown to be capable of identifying solvates forming isomorphic desolvates due to their sensitivity to small changes in the local chemical environment caused by the leaving of the solvent molecules (Ruth *et al.*, 2003; Stephenson *et al.*, 1997). Within the framework of this thesis, it is investigated whether perfusion calorimetry as a method used to study solvent-solid interactions might represent a further method suitable to indicate the presence of non-stoichiometric solvates forming isomorphic desolvates.

2.4 Perfusion calorimetry

2.4.1 Assembling of the vapour pressure control device

In order to control the atmosphere in the sample vessel during measurement two types of vapour pressure control device were used, both designed for the 2277 Thermal Activity Monitor (formerly Thermometric AB, Järfälla, Sweden, now TA Instruments, New Castle, Delaware). The devices each have a perfusion ampoule, but differ in the flow control system used (Fig. 7).

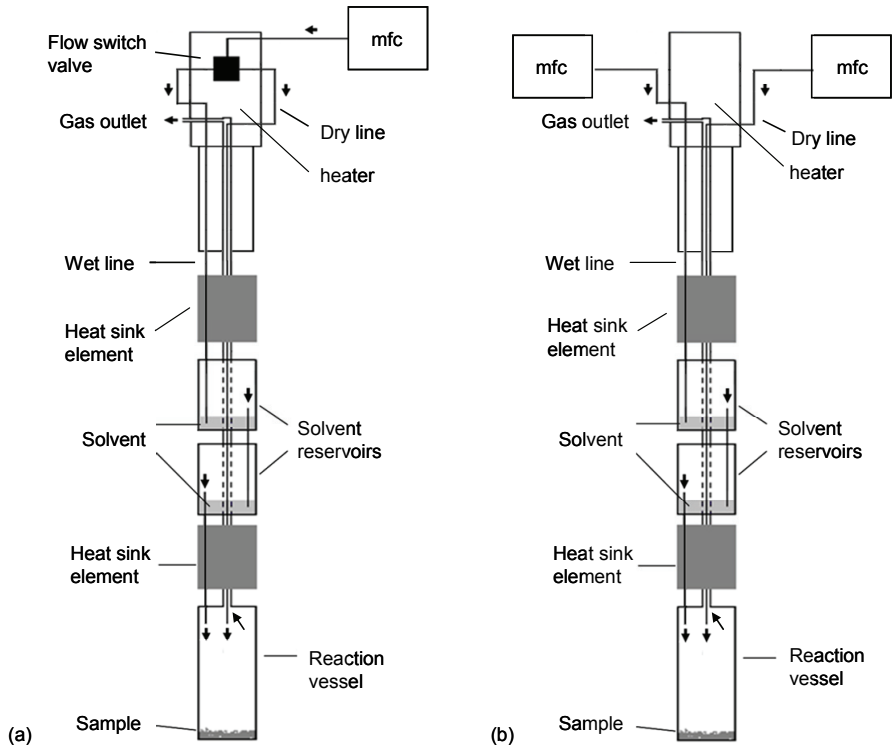

Fig. 7. Types of vapour pressure control device used: device based on a flow switch valve and a mass flow controller (mfc) (a), device operating with two mass flow controllers (b).

While the flow control system of one device is based on a flow switch valve combined with a mass flow controller, the flow in the other device is controlled with two mass flow controllers (see below). For both devices, the perfusion ampoule encompasses - from top to bottom - a heater, a heat-sink element, two solvent reservoirs, an additional heat-sink element and the reaction vessel (Fig. 7). The functions of the heater are the preheating of the incoming gas and the prevention of condensation at the gas outlet. The heat-sink elements ensure close thermal contact with the water bath. Two steel tubes, the so-called dry and wet line, are running inside the perfusion ampoule allowing the reaction vessel to be perfused with gas that exits the system again at the gas outlet. The dry line passes nitrogen directly to the reaction vessel (0 % *RVP* of solvent (RVP_{Solv})) whereas the wet line passes nitrogen through the solvent reservoirs prior to the reaction vessel in order to achieve saturation with solvent vapours (100 % RVP_{Solv}). The RVP_{Solv} inside the reaction vessel (RVP_{in}) is determined by the ratio of the volume flows of the dry line and the wet line that are controlled by the flow control system. As stated before, the flow control system of one device is based on a mass flow controller and a flow switch valve (Fig. 7a). The mass flow controller adjusts the flow of dry nitrogen being delivered to the flow switch valve. The flow switch valve sitting on top of the perfusion ampoule passes the nitrogen to either the dry line or the wet line. It represents a 3-way diverting poppet valve based on a solenoid coil system and two poppets connected with a stem. In the de-energised state of the coil, the wet line is sealed off by one of the poppets, i.e. the dry line is open (normal state of the valve). When the coil is energised, a force is applied to the second poppet that, as a result, closes the dry line. At the same time, the force is transmitted along the stem to the poppet closing the wet line and causes the poppet to open the wet line. The flow rates of the dry and wet line are determined by the ratio of the time the dry line is open to the time the wet line is open. By predefining a specific RVP_{Solv} (RVP_{set}) in the Digitam® software (TA Instruments, New Castle, Delaware) used for operating TAM, the ratio of the switching times in a switching cycle is set. Unfortunately, the performance of the valve easily deteriorates (personal communication with TA Instruments, New Castle, Delaware). A known sign of ageing is that the valve fails to fully open the wet line. The incomplete opening of the wet line leads to a back pressure of nitrogen and, as a result, the wet line flow falls below set value. When the valve closes the wet line to open the dry line, the accumulated nitrogen passes through the dry line increasing the volume flow of the dry line above set value. Hence, the use of the second type of vapour pressure control device is preferred whose flow control system relies on two mass flow controllers, one controlling the mass flow of the dry line, the second one regulating the flow that is delivered to the wet line (Fig. 7b). The flow rates of the dry and wet line set by the mass flow controllers depend on RVP_{set} and the desired total flow rate over the sample.

2.4.2 The *RVP* of solvent inside the reaction vessel (RVP_{in})

In an accurately performing vapour pressure control device, the RVP_{Solv} inside the reaction vessel, RVP_{in}, does not equal the RVP_{set} value defined in the software but is somewhat higher (except for 0 % and 100 % RVP_{set}). The RVP_{set} value sets the ratio of the volume flows being delivered to the dry and wet line. However, as the volume flow of the gas entering the wet line increases while passing through the wet line due to the uptake of solvent molecules, a slightly different ratio of the volume flows of the dry and wet line is created inside the reaction vessel. Consequently, RVP_{in} being determined by the ratio of the volume flows inside the vessel differs from RVP_{set}. The RVP_{in} at a given RVP_{set} may be calculated making the following assumptions (Thermometric AB, Sweden, 2000): first, the pressure inside the vapour pressure control device is assumed to be equal to the atmospheric pressure as the total flow rate used is small; secondly, the perfect gas law is applicable:

$$p_x V = n_x RT \tag{15}$$

p_x is the partial pressure of a gas x, n_x is the amount of substance of the gas and V is the volume. In a first step to approach the equation to calculate RVP_{in}, the total flow of nitrogen that is passed to the perfusion ampoule, f_0, is derived from the gas law. Regarding the vapour pressure control device based on the flow switch valve, f_0 corresponds to the flow passing from the mass flow controller to the flow switch valve whereas in case of the other type of device, f_0 represents the sum of the flow rates adjusted by the mass flow controllers that control the gas supply to the dry and the wet line. The equation describing f_0 is:

$$f_0 = \frac{\mathrm{d}V}{\mathrm{d}t} = \frac{RT}{p_{tot}} \frac{\mathrm{d}n_0}{\mathrm{d}t} \tag{16}$$

$\mathrm{d}V / \mathrm{d}t$ is the volume flow rate of the gas and $\mathrm{d}n_0 / \mathrm{d}t$ is the flow of nitrogen; p_{tot} is the total pressure which is equal to the atmospheric pressure. As nitrogen is the only component of the gas stream entering the perfusion ampoule, p_{tot} is at the same time the partial pressure of nitrogen, p_0. The volume flow f_0 and RVP_{set}, both defined in the software, determine the volume flow directed to the wet line, f_{wet}, and to the dry line, f_{dry}, respectively. Regarding the device based on the flow switch valve, f_{wet} and f_{dry} are set by the valve while in case of the second type of device, f_{wet} and f_{dry} are the flow rates adjusted by the two mass flow controllers used. The flow rates f_{wet} and f_{dry} are calculated as follows:

$$f_{wet} = f_0 \frac{RVP_{set}}{100\%} \tag{17}$$

$$f_{\text{dry}} = f_0\left(1-\frac{RVP_{\text{set}}}{100\%}\right) \tag{18}$$

The gas directed to the wet line enters the solvent reservoirs in which the total pressure p_{tot} corresponds no longer to the partial pressure of nitrogen. The gaseous phase now contains nitrogen as well as solvent molecules. Consequently, the total pressure p_{tot} is the sum of the partial pressure of nitrogen, p_0, and the partial pressure of the solvent used. The partial pressure of the solvent is the saturated vapour pressure of the solvent at the temperature T, $p_{\text{Solv,sat}}$:

$$p_{\text{tot}} = p_0 + p_{\text{Solv, sat}} \tag{19}$$

Because p_{tot} still equals the atmospheric pressure (no pressure build-up), p_0 has to diminish by the value of $p_{\text{Solv,sat}}$. The decline in the partial pressure of nitrogen causes the volume flow of nitrogen to increase. This rise in the volume flow may also be described with the uptake of solvent molecules into the gas stream. The gas flow leaving the second reservoir, $f_{\text{wet*}}$, is expressed as follows:

$$f_{\text{wet}*} = f_0\,\frac{RVP_{\text{set}}}{100\%}\,\frac{p_{\text{tot}}}{p_{\text{tot}}-p_{\text{Solv,sat}}} = \frac{RT}{p_{\text{tot}}-p_{\text{Solv,sat}}}\,\frac{\mathrm{d}n_0}{\mathrm{d}t}\,\frac{RVP_{\text{set}}}{100\%} \tag{20}$$

The total volume flow entering the reaction vessel, f_{in}, is the sum of f_{dry} and $f_{\text{wet*}}$

$$f_{\text{in}} = f_{\text{dry}} + f_{\text{wet}*} = f_0\left[1+\left(\frac{\text{RVP}_{\text{set}}}{100\%}\,\frac{p_{\text{Solv, sat}}}{p_{\text{tot}}-p_{\text{Solv, sat}}}\right)\right] \tag{21}$$

The partial pressure of solvent inside the reaction vessel, $p_{\text{Solv,in}}$, is:

$$p_{\text{Solv,in}} = \frac{RT}{f_{\text{in}}}\,\frac{\mathrm{d}n_{\text{Solv}}}{\mathrm{d}t} \tag{22}$$

where $\mathrm{d}n_{\text{Solv}} / \mathrm{d}t$ is the mass flow of the solvent molecules entering the reaction vessel. It is described by the following equation:

$$\frac{\mathrm{d}n_{\text{Solv}}}{\mathrm{d}t} = f_{\text{wet}*}\,\frac{p_{\text{Solv,sat}}}{RT} \tag{23}$$

Incorporating Eqs. (21) and (23) into Eq. (22) gives:

$$p_{\mathrm{Solv,in}} = p_{\mathrm{Solv,sat}} \frac{1}{\left[1 - \frac{p_{\mathrm{Solv,sat}}}{p_{\mathrm{tot}}}\left(1 - \frac{RVP_{\mathrm{set}}}{100\%}\right)\right]} \frac{RVP_{\mathrm{set}}}{100\%} \tag{24}$$

Eq. (24) describes the partial pressure of solvent as a function of RVP_{set}. In order to relate $p_{\mathrm{Solv,in}}$ to the RVP_{Solv} inside the reaction vessel, RVP_{in}, the following definition is used:

$$RVP_{\mathrm{in}} = \frac{p_{\mathrm{Solv,in}}}{p_{\mathrm{Solv,sat}}} 100\% \tag{25}$$

Combining Eqs. (24) and (25), RVP_{in} as a function of RVP_{set} is obtained:

$$RVP_{\mathrm{in}} = \frac{1}{\left[1 - \frac{p_{\mathrm{Solv,sat}}}{p_{\mathrm{tot}}}\left(1 - \frac{RVP_{\mathrm{set}}}{100\%}\right)\right]} RVP_{\mathrm{set}} \tag{26}$$

Fig. 8 illustrates Eq. (26) using methanol as example. The figure shows a plot of the RVP_{in} of methanol at 25 °C and p_{tot} = 1.01325 bar versus RVP_{set}. The dashed line in Fig. 8 is drawn to point out the bending of the curve (solid line) describing the relation between RVP_{in} and RVP_{set}. Due to the increase of the volume flow of the gas passing through the wet line, RVP_{in} is higher than RVP_{set} except for 0 % and 100 % RVP_{set}. From RVP_{set} > 0 % up to 50 %, the ratio $f_{\mathrm{wet*}} / f_{\mathrm{in}}$ increases compared to the ratio $f_{\mathrm{wet}} / (f_{\mathrm{wet}} + f_{\mathrm{dry}})$ resulting in an increase of $\mathrm{RVP_{in}}$ compared to RVP_{set}. From RVP_{set} > 50 % up to 100 %, the ratio $f_{\mathrm{wet*}} / f_{\mathrm{in}}$ again approaches the ratio $f_{\mathrm{wet}} / (f_{\mathrm{wet}} + f_{\mathrm{dry}})$ so that RVP_{in} converges towards RVP_{set}.

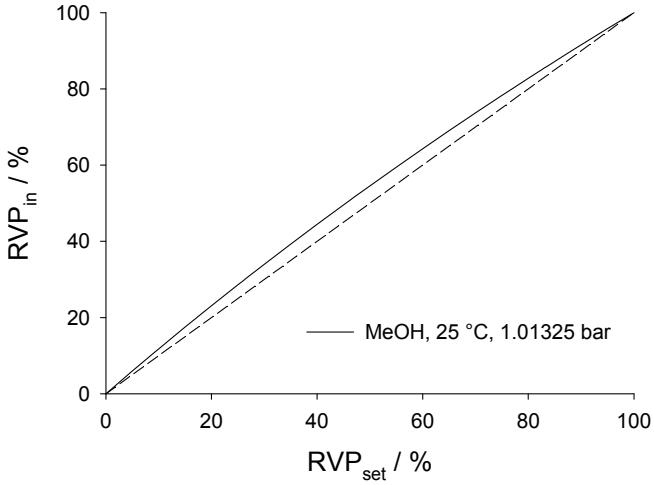

Fig. 8. RVP_{in} of methanol at 25 °C and 1.01325 bar as a function of RVP_{set} (solid curve) in case of an accurately working perfusion system; the dashed line is drawn to emphasise the bending of the curve.

Eq. (26) shows that RVP_{in} may be calculated if $p_{Solv,sat}$, p_{tot} and RVP_{set} are known. This is only valid provided that the following two conditions are met: (1) the flow control system accurately sets f_{dry} and f_{wet} so that Eqs. (17) and (18) are valid; (2) an RVP_{Solv} of 100 % is obtained in the wet line. Hence, the key factors in the generation of RVP_{in} are the performance of the flow control system and the saturation of the gas passing through the wet line.

In order to reliably perform perfusion calorimetry, it is important to verify the performance of the vapour pressure control device, i.e. to check whether the actual RVP_{in} value generated corresponds to the theoretical value calculated using Eq. (26). If the perfusion system is used to create a specific *RH*, the generation of the predefined *RH* inside the sample vessel has been checked with the help of saturated aqueous salt solutions (Buckton, 2000). Saturated salt solutions maintain a constant *RH* at a certain temperature. Placing a saturated salt solution inside the sample vessel of the *RH* perfusion ampoule, the heat flow will become zero if the *RH* of the gas flowing over the solution corresponds to the *RH* of the salt solution.

However, a method suited to ascertain the *RVP* of organic solvents has not been reported yet. Therefore, a general method applicable to any solvent is required. The development of such a method is one of the aims of this thesis.

2.5 Active pharmaceutical ingredients used

2.5.1 Emodepside

Emodepside is one example of the cyclooctadepsipeptides, a new chemical class of anthelmintics in veterinary medicine. Its molecular structure is given in Fig. 9.

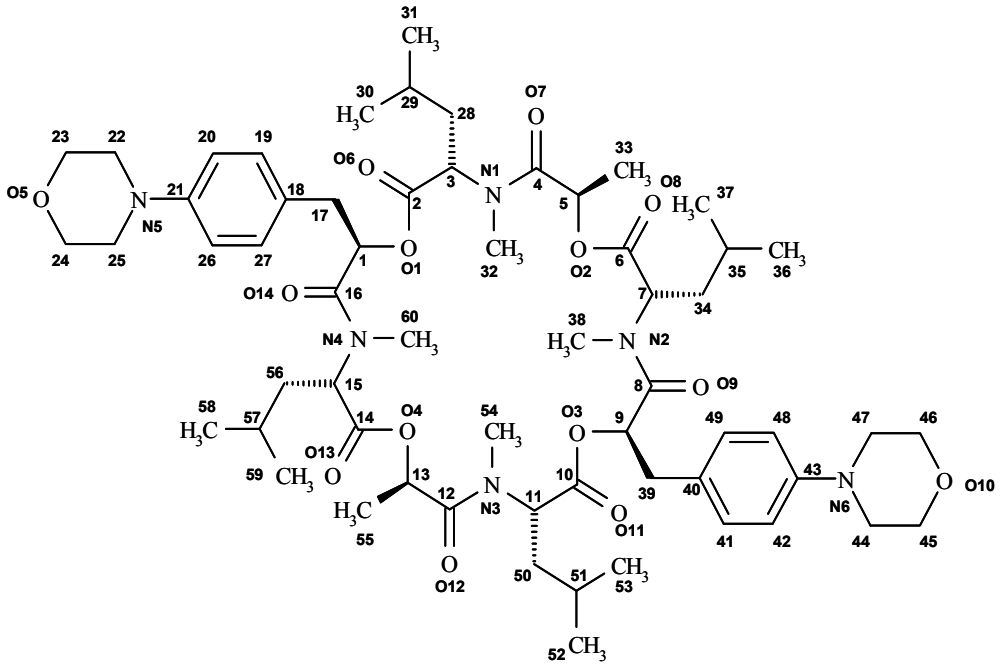

Fig. 9. Molecular structure of emodepside.

Emodepside is the first representative of this class brought to the market. In combination with Praziquantel being a well-established anthelmintic compound, it is used in a dermal spot-on formulation to deworm cats. The product, Profender Spot on® (Bayer Animal Health GmbH, Leverkusen, Germany), was introduced into the market in 2005. Emodepside is effective against a variety of nematodes in different animal species. Its mode of action is based on the stimulation of the latrophilin-like receptor which causes the release of inhibitory neuropeptides. This results in the inhibition of pharyngeal pumping and locomotion and eventually in the death of the nematodes. Emodepside (molar mass of 1119.42 $g*mol^{-1}$) represents a semi-synthetic derivative based on a fermentation product of fungal nature. A patent application describing a process for producing emodepside was published in 1993 (WO 93 / 19053). In 1997, a second patent application was published giving an alternative process suited for industrial-scale production (WO 97 / 02256). A third patent application published in 1999 (WO 99 / 24412) describes different crystalline forms of emodepside. The patent application states that the forms of emodepside produced by the methods disclosed in WO 93 / 19053 (amorphous) and WO 97 / 02256 (crystalline, prior art crystals) have disadvantages. The disadvantages named for the amorphous form are drawbacks in terms of production efficiency and handle-ability. Regarding the prior art crystals, poor filtration properties during crystallisation, poor fluidity and a high specific volume are stated to negatively affect the production efficiency and the yield of the crystals. The patent application presents three novel crystalline forms that are claimed to have enhanced production efficiency and an increased yield due to good filtration properties, good fluidity and / or a small specific volume. The novel forms and the prior art crystals are described in terms of their X-ray diffraction patterns, their differential thermal analysis curves (revealing the melting points) and their infrared spectra. The filtration properties of the different forms during crystallisation, the specific volume and the water content at ambient temperature determined in an experimental example are listed. Furthermore, methods for producing the different forms are given in the patent application. In 2002, a fourth patent application was published (WO 02 / 066048 A1). WO 02 / 066048 A1 relates to the use of the crystal form with the highest melting point for producing medicaments. In the filing, the different forms are given the numbers I to IV according to the order of their melting points (form I having the highest melting point). The patent application discloses that form I is the form with the highest bioavailability and activity and is therefore recommended to be used in formulations containing solid emodepside.

Summarising, four different crystalline forms of emodepside are known. The patent application WO 99 / 24412 discloses that the forms partly contain considerable amounts of water (Table 2).

Table 2 Water contents of the different forms of emodepside determined in an experimental example (patent application WO 99 / 24412)

	g water per 100 g emodepside	mol water per 1 mol emodepside
Form I	0.20	0.12
Form II	0.98	0.61
Form III	3.16	1.96
Form IV	2.45	1.52

Therefore, the question about how the water is associated with the different forms arises. The present characterisation of the forms given in WO 99 / 24412 does not reveal whether the forms are hydrates (two-component systems, 2.1.2.2) or whether they represent modifications (one-component systems, 2.1.2.1.1) of emodepside with water adsorbed on the crystal surface and / or absorbed into disordered defect regions. In the framework of this study, the different forms were extensively analysed in order to characterise the state of water in the different forms.

2.5.2 Toltrazuril

Toltrazuril (molar mass of 425.38 g*mol^{-1}) represents a symmetric triazinon having the following molecular structure:

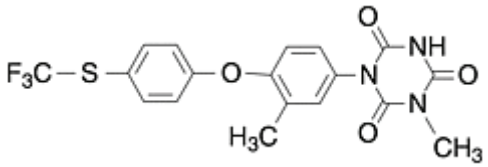

Fig. 10. Molecular structure of toltrazuril.

The substance is used as anticoccidial drug in veterinary medicine (Baycox® 2.5 % oral solution and 5 % suspension, Bayer Animal Health GmbH, Leverkusen, Germany). Coccidiosis caused by protozoan parasites of the family Eimeriidae is an infection of intestinal epithelium. Different animal species may be infected. Toltrazuril damages all intracellular development stages of Eimeria and is therefore used for both therapy and metaphylaxis in various animals.

Toltrazuril was introduced in the market in the 1980s. Two patents (DE 2413722 C3 and DE 2718799 C2) exist relating to processes for producing toltrazuril and to its uses. There are not any patents on the existence of different solid forms of toltrazuril. In order to search for possible different solid forms of toltrazuril, a solid form screening was performed by Grunenberg, Bayer HealthCare AG (personal communication). In this screening, toltrazuril was found to exist in four crystalline forms presented in Table 3 and in an amorphous form.

Table 3 Crystalline forms obtained in the screening of toltrazuril

Crystalline form	Melting point [°C]	Remarks
A	194	A thermogram was the only evidence provided for the existence of form A (an endotherm overlapping with the melting peak of form B was attributed to the melting of A)
B	192	Starting material; characterised by Raman, DSC and TGA
C	186	Produced from the melt; characterised by Raman and DSC
D	168	Crystallised from solution; characterised by Raman, DSC and TGA

The study performed was not extensive, since it was regarded as a short screening rather than an in-depth analysis. Thus, a comprehensive screening is performed within the framework of this thesis in order to search for further solid forms and to thoroughly characterise the forms already described using different methods including perfusion calorimetry.

3 Objectives of the study

The objectives of this study are to investigate the solid state behaviour of APIs and to explore the potential of perfusion calorimetry in solid form analysis with the aim to make a contribution to the understanding of solid forms. The specific aims of the study are:

- to develop a general method to verify the performance of the vapour pressure control devices used in this study to perform perfusion calorimetry
- to apply the method to test the vapour pressure control devices available in order to be able to reliably perform perfusion calorimetry
- to perform a profound solid form screening on the anticoccidial drug substance toltrazuril
- to use a variety of methods to characterise the solid forms of the anthelmintic compound emodepside, with focus on the state of the water associated with the different forms
- to investigate the value of perfusion calorimetry in the solid phase characterisation of both APIs
- to test the general applicability of perfusion calorimetry as a tool to identify solvates forming isomorphic desolvates

4 Results and discussion

4.1 Evaluation of vapour pressure control devices

4.1.1 Introducing comments

The use of perfusion calorimetry requires a suitable method to verify the performance of the vapour pressure control device employed to generate the *RVP* of solvent inside the reaction vessel (RVP_{in}). Regarding the vapour pressure control devices used in this study, such a method exists only for water (Thermometric AB,Sweden, 2003), not for organic solvents. Hence, a general approach to test the performance of the vapour pressure control devices was developed. It is based on the verification of the significant elements in the creation of RVP_{in} which are the performance of the flow control system used and the saturation of the gas passing through the wet line with solvent vapours (section 2.4.2). The flow control system, consisting of either two mass flow controllers or a flow switch valve combined with a mass flow controller, is tested using volume flow measurements whereas the saturation of the wet line is verified in a calorimetric experiment employing methanol as model solvent. The results of the measurements are used to calculate RVP_{in}.

In the following sections, the method is first applied to a flow switch valve based device for which the method was originally developed. An adapted version of the method is then used to check devices operating with two mass flow controllers. The described testing of two mass flow controller based devices includes several optimisation steps in order to obtain a method more time efficient. Subsequently, the performances of the tested devices are compared by conducting two test experiments taking into account the results from the device check. Since testing of the various devices has shown that the wet line may not be saturated with solvent vapours, the factors influencing the saturation of the wet line are studied. At last, the method is applied to devices that use water and ethanol as solvents in order to demonstrate the general applicability of the method.

4.1.2 Device operating with a flow switch valve

4.1.2.1 Check of the flow switch valve

The following sections describe the testing of a flow switch valve based device. In order to verify the accuracy of the operation of the flow switch valve which is one of the two significant elements in the creation of RVP_{in}, the volume flow rates of the wet line (f_{wet}) and the dry line (f_{dry}) being set by the valve were measured. Measurements were performed using a 10 ml soap film flow meter. The total flow rate was set to 50 $ml*h^{-1}$ (0 °C, 1.01325 bar) which was the flow rate used in this study when working with a flow switch valve based device. For different *RVP* values set in the software (RVP_{set} values), the volume leaving the wet line and the dry line, respectively, within

a period of 10 min was measured. In order that the volume leaving the wet line corresponded to f_{wet}, the solvent reservoirs had to be emptied prior to measurement. Otherwise, the volume flow leaving the wet line would have exceeded f_{wet} due to the uptake of solvent molecules in the solvent reservoirs (2.4.2). To readily detect whether the valve shows the sign of ageing described in section 2.4.1, the density of reading points was increased in the region of high RVP_{set}. The ageing phenomenon being the failure to fully open the wet line results in an increase of the dry line flow relative to the set value which is most pronounced at high RVP_{set} values. The results of the volume flow measurements are presented in Table 4.

Table 4 Volume flow rates of the wet and the dry line at 0 °C, 1.01325 bar ($\bar{x}$ ± s, n = 3) and the RVP_{valve} values calculated from the volume flow rates (RVP_{valve} ± SE) at different RVP_{set}

RVP_{set} [%]	f_{dry} [ml*h^{-1}]	f_{wet} [ml*h^{-1}]	RVP_{valve} [%]
0	52.9 ± 0.72	-	0
20	42.4 ± 0.16	10.9 ± 0.10	20.4 ± 0.06
40	32.0± 0.24	21.1 ± 0.20	39.8 ± 0.18
60	21.6 ± 0.17	31.7 ± 0.18	59.4 ± 0.12
80	11.2 ± 0.02	42.0 ± 0.21	78.9 ± 0.05
85	8.4 ± 0.02	44.7 ± 0.12	84.2 ± 0.03
90	6.1 ± 0.09	47.0 ± 0.21	88.6 ± 0.06
95	3.4 ± 0.03	49.7 ± 0.22	93.6 ± 0.01
100	-	52.2 ± 0.42	100

Throughout the measurements, the temperature ranged from 21.7 °C to 22.0 °C. Atmospheric pressure varied between 1.006 bar and 1.016 bar. Because of these fluctuations, the measured flow rates were normalised to standard conditions (0 °C and 1.01325 bar). The converted flow rates are listed in Table 4 (mean value ($\bar{x}$) ± standard deviation (s), sample size n = 3). The flow rates of the dry and wet line were used to calculate RVP_{valve} as a term providing information about the accuracy of the valve:

$$RVP_{valve} = \frac{f_{wet}}{f_{wet} + f_{dry}} 100\% \qquad (27)$$

RVP_{valve} at a specific RVP_{set} is the ratio of f_{wet} to the sum of the flow rates coming out of the wet and the dry line at RVP_{set}, multiplied by 100 %. It represents the fraction of the gas directed to the wet line. If the valve works accurately, RVP_{valve} equals RVP_{set}. Consequently, RVP_{valve} describes the actual *RVP* provided by the flow switch valve.

The RVP_{valve} values for the different RVP_{set} values tested are displayed in Table 4. For each RVP_{valve} value (except 0 % and 100 %), the standard error (SE) is given calculated according to the Gaussian error propagation. Table 4 shows that the absolute deviation of RVP_{valve} from RVP_{set} is low within the whole *RVP* range. The highest absolute deviation is at 90 % and 95 % RVP_{set} being 1.4 %. To assess whether the differences found between RVP_{valve} and set value (RVP_{set}) are statistically significant, 1-sample t-tests were performed (level of significance $\alpha = 0.05$). As RVP_{valve} does not represent the mean of a directly measured variable but is calculated using both the mean value of the wet line flow (n = 3) and the mean value of the dry line flow (n = 3), the degrees of freedom (f) used in the tests are f = 6 - 2 = 4. As a result, the differences between RVP_{valve} and RVP_{set} are statistically significant ($\alpha = 0.05$) at each RVP_{set} value tested except 40 % RVP_{set}.
With rising RVP_{set} value, RVP_{valve} decreases compared to RVP_{set}. At 20 % RVP_{set}, RVP_{valve} is 20.4 % ± 0.06 % whereas at 95 % RVP_{set}, RVP_{valve} is 93.6 % ± 0.01 %. In order to investigate this phenomenon, the ratio of the actual flow rate of the wet line, and the dry line, respectively, to the set value was calculated at the different RVP_{set} values. The set value for the wet line flow and dry line flow, respectively, at a certain RVP_{set} was obtained by multiplying the sum of the flow rates coming out of the wet and the dry line at RVP_{set} with RVP_{set} / 100 % and (1 - RVP_{set}) / 100 %, respectively. The calculated ratio ± SE (according to the Gaussian error propagation) was plotted against RVP_{set} (Fig. 11).

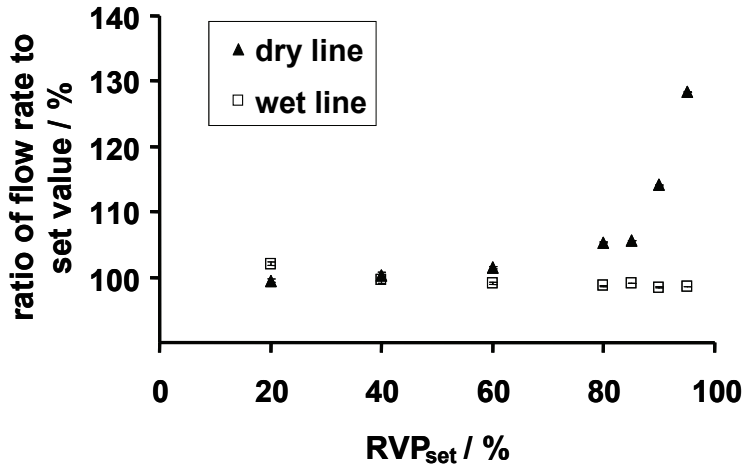

Fig. 11. Ratio of the actual flow rate of the wet line, respectively the dry line, to the set value (multiplied by 100 %), plotted against RVP_{set}; the error bars given for each ratio were calculated according to the Gaussian error propagation; they are partly hidden behind the symbols used.

Fig. 11 shows that for the wet line flow, the ratio is near 100 % at each RVP_{set} tested whereas for the dry line flow, the ratio increases at higher RVP_{set} values. To determine whether the ratios calculated significantly differ from 100 %, 1-sample t-tests were performed ($\alpha = 0.05$, f = 4). Regarding the dry line flow, the ratio

significantly (α = 0.05) exceeds 100 % at RVP_{set} ≥ 60 %. Fig. 11 reveals that the ratio considerably increases from 85 % to 95 % RVP_{set} having a value of 128.4 % ± 0.02 % at 95 % RVP_{set}. Regarding the wet line flow, the ratio significantly (α = 0.05) differs from 100 % at each RVP_{set} value tested except 40 % RVP_{set}. While the ratio is somewhat above 100 % at 20 % RVP_{set} (102.1 % ± 0.30 %), a value slightly below 100 % is found at RVP_{set} ≥ 60 % (Fig. 11). The ratios of the measured dry line flow and wet line flow, respectively, to the set value explain the finding that RVP_{valve} decreases compared to RVP_{set} with rising RVP_{set} value (Table 4).

The ratios of the actual flow rate to the nominal value found at higher RVP_{set} values indicate that the valve has aged. In case of ageing (incomplete opening of the wet line), the wet line flow is below set value whereas the dry line flow is above set value. Both effects are observed at RVP_{set} ≥ 60 %. The strong increase of the ratio in case of the dry line is explained by the fact that the set value for the dry line flow decreases with rising RVP_{set}. With decreasing set value, the impact of the additional nitrogen passing through rises. In case of an incomplete but precise opening of the wet line, the ratio of the wet flow to the nominal value of f_{wet} should have a value below 100 % at all RVP_{set}. However, Fig. 11 displays that the ratio exceeds 100 % at 20 % RVP_{set} decreasing to a value below 100 % at higher RVP_{set} values. A possible explanation might be that the valve opened the wet line longer than required. The extension of the opening time of the wet line by a certain time period (constant at different RVP_{set} values) superimposes the incomplete opening of the wet line. At 20 % RVP_{set}, the elongation of the opening time outweighs the incomplete opening of the wet line leading to a wet flow above set value and a dry flow below set value (Fig. 11). With increasing RVP_{set}, the effect of the prolongation of the opening time diminishes whereas the impact of the incomplete opening of the wet line rises.

Concluding one can say that the volume flow measurements provide information about the performance of the flow switch valve. RVP_{valve} calculated from the measured flow rates deviates from RVP_{set} at each RVP_{set} value tested except 40 % RVP_{set} indicating a change in the performance of the valve. The changed performance will affect the *RVP* of solvent generated inside the reaction vessel (RVP_{in}). Due to the fact that the absolute differences between RVP_{valve} and RVP_{set} are small, RVP_{in} will not change considerably. However, in order to know the exact value of RVP_{in}, the actual performance of the valve (represented by RVP_{valve}) has to be factored in the equation of RVP_{in} (4.1.2.3).

Given the fact that the valve tested shows signs of ageing, it is important to check the valve at regular intervals as the performance of the valve might deteriorate. Indeed, the valves tested in this study fell off in quality within a few weeks. Deterioration of the performance of the valves included an incomplete closing of the dry line which prevents the system from generating high RVP_{in} values. Hence, the majority of the experiments were performed using a device based on two mass flow controllers which is the more robust system.

4.1.2.2 Verification of the saturation of the wet line

The calorimetric experiment to check the saturation of the wet line was carried out at the same temperature at which later experiments were performed (25 °C). Methanol was chosen as model solvent as it is compatible with the materials of the perfusion unit. It is important to consider that some organic solvents may interact with the o-rings of the perfusion unit which impairs the performance of the system. Methanol was filled in each solvent reservoir of the *RH* perfusion ampoule and in the reaction vessel. A step-experiment was performed increasing RVP_{set} from 80 % up to 95 % in 5 % steps with a time delay of 2 h per step. Fig. 12 shows the resulting heat flow curve.

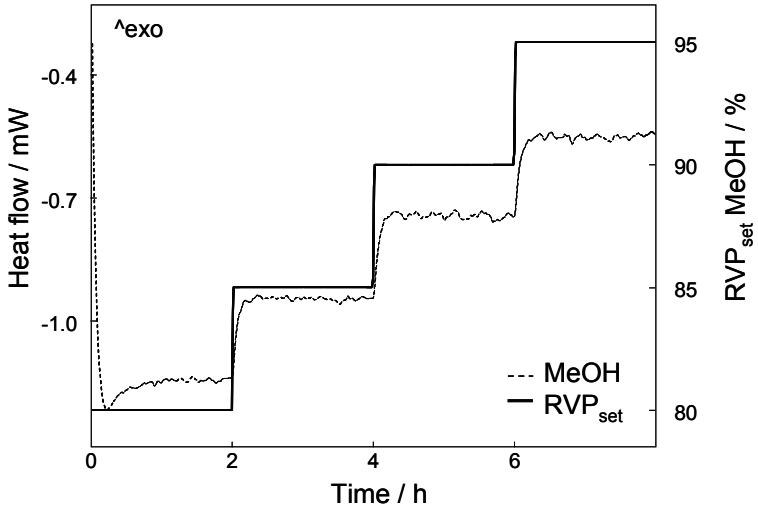

Fig. 12. Heat flow curve of methanol (0.8 ml) being exposed to increasing RVP_{set} values of methanol (25 °C).

An endothermic heat flow is observed that decreases from -1144 µW at 80 % RVP_{set} to -551 µW at 95 % RVP_{set}. The endothermic heat flow is caused by evaporation of methanol. As gaseous methanol is continuously removed by the flowing gas, saturation of the gas phase is not achieved. A constant evaporation rate is reached at each RVP_{set} resulting in steady state heat flows (Fig. 12). The steady state heat flow values are inversely proportional to RVP_{set}, since the evaporation rate increases the lower the activity of methanol in the gaseous phase. To correct for the heat changes that are associated with the perfusion of the reaction vessel, the baseline heat flow of the empty sample vessel was measured at 80 % to 95 % RVP_{set} and subtracted from the steady state heat flow values. The corrected values were plotted not against RVP_{set}, but against the corresponding RVP_{valve} values gained from the volume flow measurements (Fig. 13).

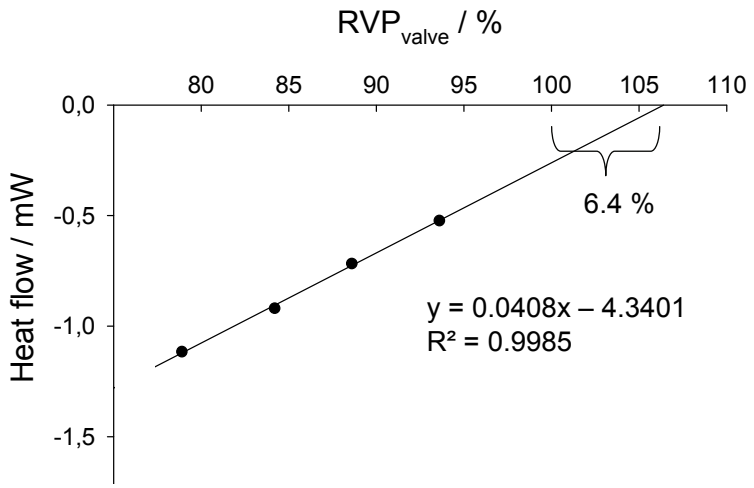

Fig. 13. Steady state heat flow values gained from the calorimetric experiment plotted against RVP_{valve}; the data were fitted to a line that intersects the x-axis above 100 % RVP_{valve}; the offset of the intersection from 100 % is given (6.4 %).

Fig. 13 shows that a linear data model is suitable to describe the relationship between heat flow and RVP_{valve}. Both variables, heat flow and RVP_{valve}, are regarded as random variables as they both were obtained from measurements and therefore contain errors. Assuming that the variables are 2-dimensional normally distributed, two regression lines are possible, one line models the heat flow as a function of RVP_{valve}, the other one describes RVP_{valve} as a function of the heat flow. The regression line presented in Fig. 13 is obtained by linear regression modelling the heat flow (regarded as dependent variable, plotted on the y-axis) as a function of RVP_{valve} (regarded as independent variable, plotted on the x-axis). The linear regression model disregards that the independent variable is, in fact, not error-free. The equation obtained by linear regression and the coefficient of determination (R^2) are given in Fig. 13. Extrapolation of the line yields the heat flow at 100 % RVP_{valve} at which only the wet line is open. In case the gas stream entering the reaction vessel via the wet line was saturated with methanol vapours, the heat flow at 100 % RVP_{valve} would be zero (intersection with the x-axis) as no evaporation of methanol would occur. Extrapolation of the fitted line however gives an endothermic heat flow of -260 µW at 100 % RVP_{valve} revealing that the *RVP* of methanol (RVP_{MeOH}) of the gas leaving the wet line is below 100 % (Fig. 13). The line intersects the x-axis at a value above 100 %, in this case at 106.4 %. The offset of the intersection (106.4 % - 100 % = 6.4 %) corresponds to the value by which the RVP_{MeOH} of the wet line deviates from 100 %. Consequently, the result of the first measurement is that the RVP_{MeOH} of the gas leaving the wet line is only 93.6 % providing an RVP_{in} of 93.6 % at 100 % RVP_{valve}. The mean value out of three experiments is 93.1 % ± 0.26 % (SE).

As described above, linear regression was used in order to obtain the RVP_{MeOH} of the wet line. When performing linear regression, the assumptions made by the model have to be checked. The assumptions of linear regression are (i) a linear relationship

between the independent and the dependent variable, (ii) normal distribution of the errors in the measurement of the dependent variable, (iii) constant variance of the errors and (iv) independence of the errors (Sachs, 2002). To test the normal distribution of the residuals, normality plots were used. For all three experiments, a line was obtained indicating normal distribution (data not shown). The other assumptions may be checked by plotting the residuals (differences between the measured heat flow value and the heat flow value predicted by the model) versus the predicted heat flow values. In case the residuals are randomly distributed around zero, the assumptions of linear relationship, constant variance and independence of errors may be regarded as fulfilled. In opposition to that, a pattern in the plot will indicate a correlation of the residuals and / or a non-linear relationship between the independent and the dependent variable while a change in the spread of the residuals will be indicative of unequal variances. For each of the three experiments, the residuals plot is given in Fig. 14.

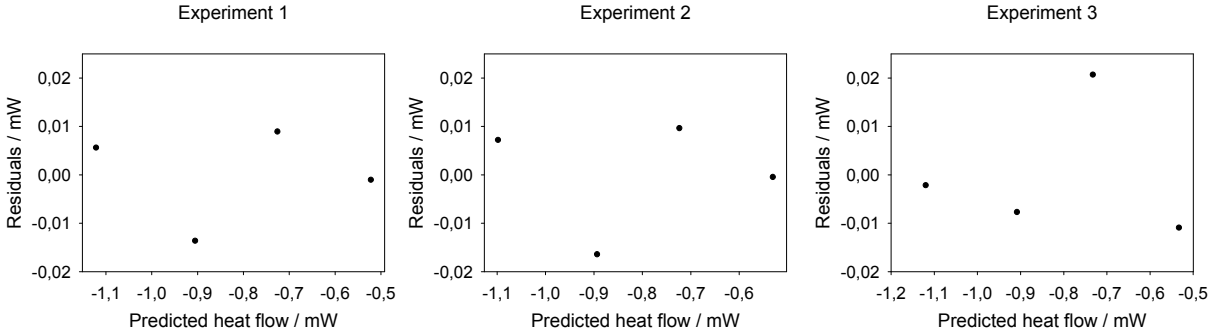

Fig. 14. Residual plots obtained for the three calorimetric experiments having the heat flow modelled as a function of RVP_{valve}.

Since neither a clear pattern nor a distinct change in the spread is recognised by visual inspection, the assumptions are found to be tenable.

As described above, the value for the RVP_{MeOH} of the wet line was determined by modelling the heat flow as a function of RVP_{valve}. It was tested whether the same value for the RVP_{MeOH} of the wet line was obtained when modelling RVP_{valve} as a function of the heat flow. In this case, the heat flow was regarded as the independent variable and linear regression was performed disregarding the errors in the heat flow values. The same mean value of the RVP_{MeOH} of the wet line (93.1 %) was obtained using this variant of data analysis. Hence, both models provide comparable results.

The presented method to obtain the RVP_{MeOH} of the wet line uses extrapolation of the fitted line. Later measurements performed with mass flow controller based devices show that this approach is correct as correlation is given up to 100 % RVP_{valve} (4.1.3.2.2).

In theory, the saturation of the wet line could have also been checked measuring the wet line flow at 100 % RVP_{set} having methanol inserted into the solvent reservoirs (measuring f_{wet^*}). However, this method will result in false values for the RVP_{MeOH} of the wet line as gaseous methanol dissolves into the soap film which leads to a

decrease in the volume flow. Consequently, the saturation of the wet line was not verified with volume flow measurements, but with the calorimetric experiment shown above.

4.1.2.3 Determination of the actual relative vapour pressure

The results of the volume flow measurements and the calorimetric experiments were used to calculate the actual RVP_{in} provided by the tested vapour pressure control device. The equation to calculate the actual RVP_{in} was obtained by adopting Eq. (26) that describes the theoretical RVP_{in} generated by an accurately working vapour pressure control device. The results of the volume flow measurements were factored by substituting RVP_{set} in Eq. (26) by RVP_{valve}, since RVP_{valve} describes the actual *RVP* set by the flow switch valve at a predefined value. The factor 0.931 was used to account for the lack of the saturation of the wet line. As a result, the following equation is obtained:

$$RVP_{in} = \frac{0.931}{\left[1 - \frac{p_{MeOH,sat}}{p_{tot}} 0.931 \left(1 - \frac{RVP_{valve}}{100\%}\right)\right]} RVP_{valve} \quad (28)$$

Eq. (28) was used to calculate the RVP_{in} of methanol at 25 °C and 1.01325 bar for different values of RVP_{set}. Table 5 compares the results for RVP_{in} using Eq. (26) (theoretical RVP_{in}) with the values obtained from Eq. (28) (actual RVP_{in}).

Table 5 Theoretical RVP_{in} of methanol versus actual RVP_{in} of methanol (± SE (according to the Gaussian error propagation)) generated in the tested device (25 °C and 1.01325 bar)

RVP_{set} [%]	Theoretical RVP_{in} [%]	Actual RVP_{in} [%]
20	23.1	21.7 ± 0.23
40	44.4	40.9 ± 0.24
60	64.3	59.0 ± 0.18
80	82.8	75.9 ± 0.09
85	87.2	80.4 ± 0.06
90	91.5	84.0 ± 0.08
95	95.8	88.0 ± 0.03
100	100.0	93.1 ± 0.26

The table shows that the actual RVP_{in} is below the theoretical RVP_{in} throughout the *RVP* range. The absolute deviation from the theoretical RVP_{in} increases with rising RVP_{set}. The highest absolute deviation is 7.8 % at 95 % RVP_{set} whereas the highest

relative deviation is found at 60 % RVP_{set} being 9.2 %. These results emphasise the need to check the performance of the vapour pressure control device assessing the actual RVP_{in} generated by the device. Knowing the actual RVP_{in} enables the user to adjust RVP_{set} in order to create the desired *RVP* inside the sample ampoule. Consequently, even though the actual RVP_{in} differs from the theoretical RVP_{in}, the user will be able to reliably perform perfusion calorimetry if the actual RVP_{in} is known. However, in case the actual RVP_{in} differs in such a way from the theoretical RVP_{in} so that the RVP_{in} value required cannot be achieved by adjusting RVP_{set}, the accuracy of the vapour pressure control device is not acceptable. Hence, the acceptable accuracy of the device depends on the RVP_{in} value which is desired, i.e. on the design of the experiment. The accuracy of the tested device is acceptable for all experiments requiring a maximum RVP_{in} of methanol equal to or less than 93.1 %. If an improved accuracy of the tested device was requested, the main focus would be to enhance the accuracy of the RVP_{MeOH} of the wet line. This requires knowledge of the factors influencing the RVP_{Solv} of the wet line. Investigations aiming at identifying the parameters in the saturation of the wet line are presented in section 4.1.4.

4.1.3 Device based on two mass flow controllers

4.1.3.1 Test of the mass flow controllers

Similar to the flow switch valve (4.1.2.1), volume flow measurements were performed in order to check the performance of the mass flow controllers. However, the design of the volume flow measurements was slightly adapted to account for the characteristics of the mass flow controllers. First, the total flow rate was changed from 50 $ml*h^{-1}$ (0 °C, 1.01325 bar) to 80 $ml*h^{-1}$ (0 °C, 1.01325 bar). Having two mass flow controllers as flow control system, the total flow rate chosen determines the minimum and maximum *RVP* values that can be set in an experiment (except 0 % and 100 % RVP_{set}). The reason is the operating range of the mass flow controllers which is 4 $ml*h^{-1}$ to 200 $ml*h^{-1}$ (0 °C, 1.01325 bar). Choosing 80 $ml*h^{-1}$ (0 °C, 1.01325 bar) as total flow rate, the minimum and maximum RVP_{set} values possible are 5 % and 95 % RVP_{set} (flow rate set by the mass flow controller of the dry line (at 95 % RVP_{set}) and the wet line (at 5 % RVP_{set}), respectively, is 4 $ml*h^{-1}$ (0 °C, 1.01325 bar)). This operating *RVP* interval was adequate for the experiments planned in this study. The second adaption was related to the selection of the reading points (i.e. the RVP_{set} values at which measurements were performed). In opposition to the higher density of reading points at high RVP_{set} used for the valve, measuring points were evenly distributed including 5 % and 95 % RVP_{set} in order to test the performance of the mass flow controllers at the lower limit of their operating range.

The mass flow controllers of two devices A and B were tested to compare the performances of two mass flow controller based devices. The results of the volume flow measurements are presented in Table 6.

Table 6 Volume flow rates of the wet and the dry line at 0 °C, 1.01325 bar ($\bar{x}$ ± s, n = 3) and the RVP_{mfc} values calculated from the volume flow rates (RVP_{mfc} ± SE) at different RVP_{set} values for the devices A and B

Device A				Device B		
RVP_{set} [%]	f_{dry} [ml*h^{-1}]	f_{wet} [ml*h^{-1}]	RVP_{mfc} [%]	f_{dry} [ml*h^{-1}]	f_{wet} [ml*h^{-1}]	RVP_{mfc} [%]
0	81.2 ± 0.40	-	0	86.2 ± 0.08	-	0
5	77.0 ± 0.18	4.3 ± 0.09	5.3 ± 0.06	81.5 ± 0.26	5.5 ± 0.10	6.3 ± 0.06
35	52.5± 0.07	29.1 ± 0.07	35.6 ± 0.04	55.7± 0.17	30.4 ± 0.14	35.3 ± 0.07
65	27.4 ± 0.14	54.0 ± 0.16	66.3 ± 0.08	29.9 ± 0.20	55.0 ± 0.20	64.8 ± 0.10
95	3.8 ± 0.30	78.9 ± 0.07	95.4 ± 0.20	3.8 ± 0.18	79.9 ± 0.20	95.5 ± 0.12
100	-	83.6 ± 0.27	100	-	84.3 ± 0.18	100

As in case of the valve, the volume flow rates determined were used to calculate the actual *RVP* provided by the two mass flow controllers, RVP_{mfc}, at a certain RVP_{set}:

$$RVP_{mfc} = \frac{f_{wet}}{f_{wet} + f_{dry}} 100\% \tag{29}$$

RVP_{mfc}, given in Table 6, corresponds to RVP_{valve} and equals RVP_{set} in case of an accurately working device. Regarding device A, RVP_{mfc} statistically significantly ($\alpha = 0.05$) differs from RVP_{set} at 5 %, 35 % and 65 % RVP_{set} whereas in the case of device B, statistically significant differences ($\alpha = 0.05$) between RVP_{mfc} and RVP_{set} are found at 5 %, 35 % and 95 % RVP_{set}. The differences observed, however, are minor differences which will cause only slight changes in RVP_{in}. Nevertheless, they have to be considered in order to accurately calculate RVP_{in}. To determine RVP_{mfc} at RVP_{set} values not tested, linear regression was used to predict the volume flow rates of the dry and wet line at a given RVP_{set}. Fig. 15 displays the regression lines obtained for device A when modelling the volume flow rates measured (single values, visible as crosses) as a function of RVP_{set}.

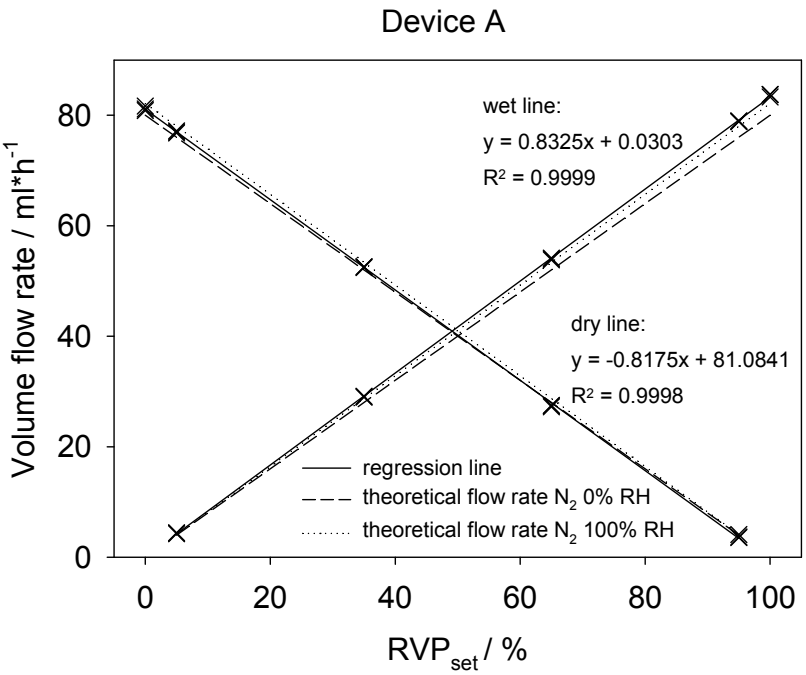

Fig. 15. Plot of the volume flow rates of the dry and the wet line versus *RVP*$_{set}$ for device A; the regression lines as well as the lines representing the theoretical flow rates of dry nitrogen and of nitrogen saturated with water vapours (explanation in the text) are given.

The figure shows that the regression lines (solid lines) well describe the data points leading to high R² values. This result indicates a linear relationship between *RVP*$_{set}$ and the volume flow rate set by the mass flow controller. The same applies for device B (Fig. 16).

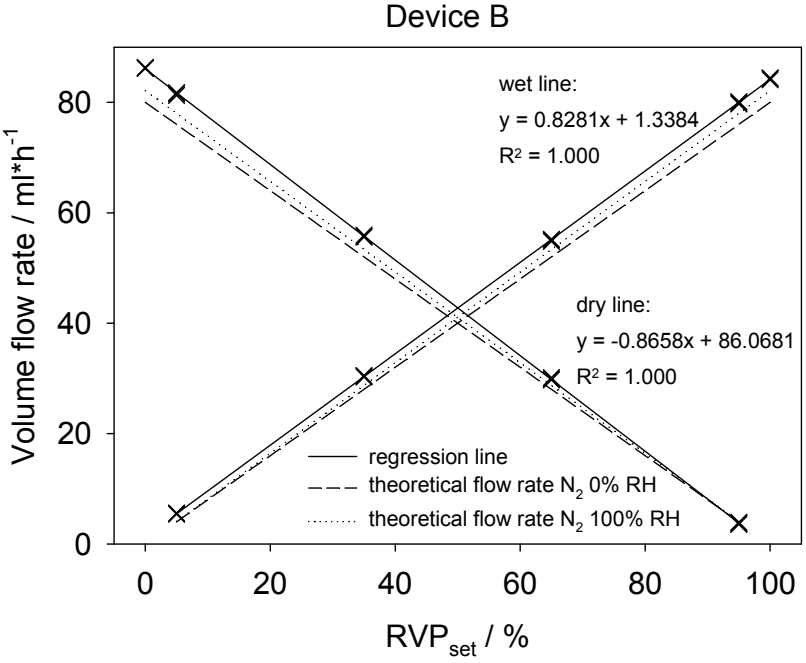

Fig. 16. Plot of the volume flow rates of the dry and the wet line versus *RVP*$_{set}$ for device B; the regression lines as well as the lines representing the theoretical flow rates of dry nitrogen and of nitrogen saturated with water vapours (explanation in the text) are given.

The 95 % confidence intervals of all regression lines are quite narrow and therefore not displayed since they would be hardly distinguishable from the regression lines. In both figures, dashed lines represent the theoretical volume flow rates which should have been set by the mass flow controllers at the different RVP_{set} values. For all mass flow controllers, the slope of the regression line is higher than the slope of the line describing the theoretical flow rate. This phenomenon was in fact expected since the volume flow rates measured do not exactly correspond to the flow rates set by the mass flow controllers, but they are slightly higher. The reason is that the flow of dry nitrogen set by the mass flow controller increases while passing through the soap film flow meter due to the uptake of water molecules. In order that the uptake of water molecules does not affect the RVP_{mfc} value determined, the relative error in measurement has to be assumed to be constant, i.e. the *RH* generated in the gas stream has to be independent of the flow rate. The same holds for the determination of RVP_{valve} (4.1.2.1). The assumption is regarded as tenable since low flow rates allow more time for the uptake of water molecules while higher flow rates favour the uptake process by dragging along the water molecules. Supposing a constant error in measurement, the measured flow rate is expected to rise more quickly than the theoretical flow rate. This expectation was fulfilled in case of all mass flow controllers which supports the validity of the assumption made.

The maximum *RH* that can be achieved in the gas stream in the soap film flow meter is 100 %. For $RH = 100$ %, the theoretical flow rates which should have been measured for both the dry and the wet line at the different RVP_{set} values are given in Fig. 15 and Fig. 16 (dotted lines). In case of accurately working mass flow controllers, the regression lines obtained for the wet and the dry line (solid lines) would be found in-between the dashed line and the dotted line and they would have the same regression coefficient (absolute value). This is not the case. For each device, the regression lines determined for the dry and the wet line differ in their regression coefficients (statistically significant ($\alpha = 0.05$), test performed according to (Sachs, 2002)) revealing slight differences in the performances of the mass flow controllers used. These differences explain the deviations of the RVP_{mfc} values from RVP_{set}. Hence, the plot of the volume flow rate versus RVP_{set} (Fig. 15 and Fig. 16) is well suited to illustrate the actual performances of the mass flow controllers. In opposition to that, the plot was not well suited to visualise the ageing phenomenon of the flow switch valve tested, therefore, a different plot was chosen to illustrate the performance of the valve (4.1.2.1).

As described in section 4.1.2.2, the use of linear regression requires the check of the assumptions of the model. To test the normal distribution of the residuals, normality plots were used. For the mass flow controllers of both devices A and B, a line was obtained indicating normal distribution (data not shown). To check for the other assumptions, the residuals were plotted versus the predicted values (Fig. 17 and Fig. 18).

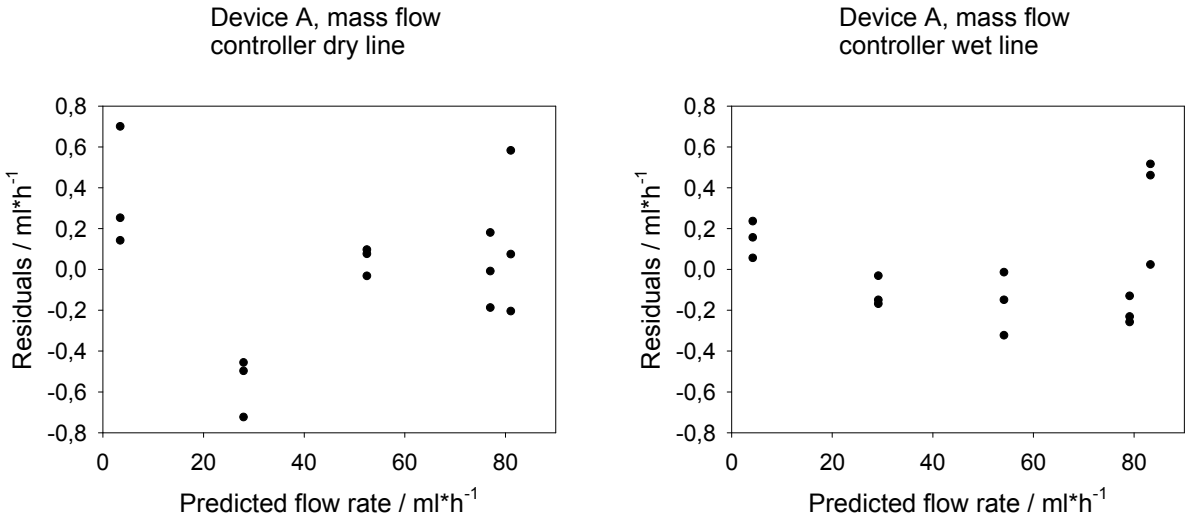

Fig. 17. Residual plots obtained for the mass flow controllers of the dry and wet line of device A having the volume flow rate modelled as a function of RVP_{set}.

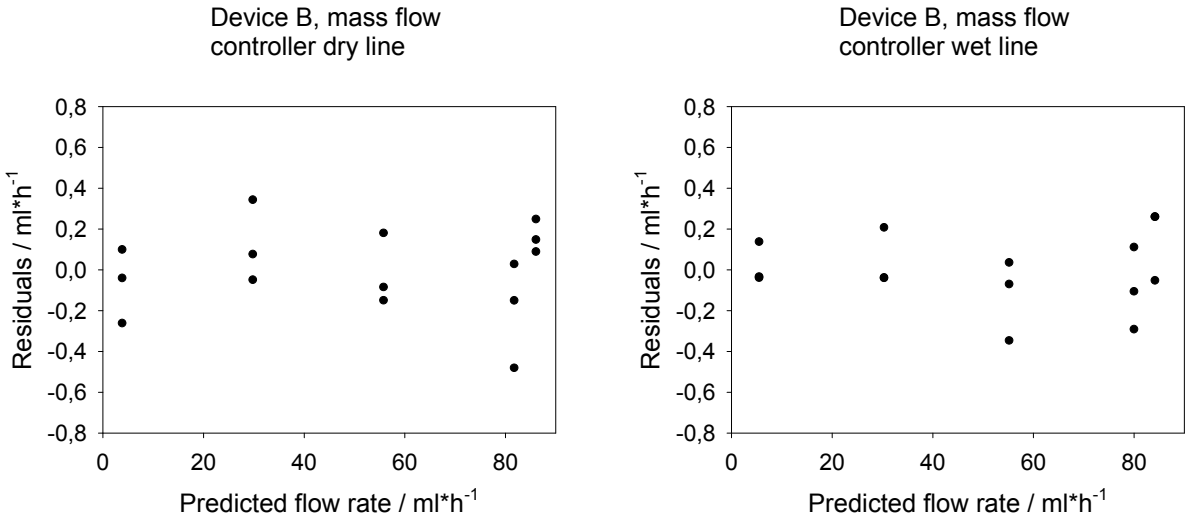

Fig. 18. Residual plots obtained for the mass flow controllers of the dry and wet line of device B having the volume flow rate modelled as a function of RVP_{set}.

Regarding device B, neither a pattern nor a decreasing or increasing spread of the residuals is visible in the plots (Fig. 18). Hence, the assumptions of linear relationship, constant variances and independence of errors are acceptable for the mass flow controllers of device B. Regarding device A, visual inspection of the plots indicates a slight pattern for the mass flow controller of the dry line and a more distinct pattern for the mass flow controller of the wet line (Fig. 17). For the mass flow controller of the dry line, all the residuals at 5 % RVP_{set} are above zero whereas all the residuals at 35 % are below zero. However, the residuals at each RVP_{set} should be randomly distributed around zero as observed for device B. Regarding the mass flow controller of the wet line, the residuals at 5 % and 100 % RVP_{set} are above zero while the residuals at 35 %, 65 % and 95 % RVP_{set} are below zero. In both cases, the pattern might be explained by a correlation of the errors caused by the way the data had been collected. For the mass flow controllers of device B, the measurements had been spread evenly throughout several days in order to include day-to-day variability.

By contrast, the majority of the measurements to test the mass flow controllers of device A had been carried out in one day. The remaining measurements had been performed at later dates. The way the data had been collected in the case of device A might have resulted in a dependency of the observed values which would explain the pattern in the residual plots (Fig. 17). The observed pattern can be neglected if the quality of prediction is acceptable. To evaluate the quality of prediction, the RVP_{mfc} was calculated at each RVP_{set} value tested using predicted flow rate values. The regression lines used to predict the dry line flow and the wet line flow at a certain RVP_{set} value were computed without using the flow rates measured at this RVP_{set} value (method of cross validation). For each device, the predicted RVP_{mfc} values are compared to the RVP_{mfc} values obtained from the measured flow rates (Table 7).

Table 7 Comparison of the RVP_{mfc} values obtained from the measured flow rates to the RVP_{mfc} values gained from the regression lines for both device A and B

	Device A		Device B	
RVP_{set} [%]	RVP_{mfc} obtained from measured flow rates [%]	RVP_{mfc} obtained using regression lines [%]	RVP_{mfc} obtained from measured flow rates [%]	RVP_{mfc} obtained using regression lines [%]
5	5.3	4.8	6.3	6.2
35	35.6	35.8	35.3	35.2
65	66.3	65.8	64.8	65.0
95	95.4	96.7	95.5	95.3

The quality of prediction is judged by the differences between the predicted and the observed RVP_{mfc} values. As expected, the quality of prediction is lower in the case of device A, i.e. larger differences between the observed and predicted RVP_{mfc} values are found compared to device B. The largest difference is 1.3 % at 95 % RVP_{set}. However, the quality of prediction for device A is nevertheless regarded as acceptable based on later experiments (4.1.3.4). Therefore, the pattern in the residuals plots for device A is neglected and the linear data model used is considered to be suitable to describe the volume flow rates set by the mass flow controllers. Since the construction of a line basically requires only two data points, further mass flow controllers were tested using a reduced number of measuring points. The reduced testing procedure encompasses the measurement of the minimum and maximum flow rate set by the mass flow controller (n = 3 at each RVP_{set} value). Considerable time saving was achieved by reducing the number of measurements.

4.1.3.2 Verification of the saturation of the wet line

4.1.3.2.1 Introducing remarks

The calorimetric experiment developed to verify the saturation of the wet line is based on the exposure of methanol to increasing RVP_{set} values of methanol (4.1.2.2). The endothermic heat flow values measured are modelled as a function of *RVP* (RVP_{valve} and RVP_{mfc}, respectively) to obtain the *RVP* at zero heat flow from which the RVP_{MeOH} of the wet line is determined. The original approach planned the experiment to be performed three times. Since the repetition of the experiment takes time, it was the aim to develop a more timesaving process by optimising the experiment. The reason for repeating the experiment had been to determine a standard error for the RVP_{MeOH} of the wet line. However, the standard error is also obtained using just one of the three experiments by modelling the *RVP* as a function of the heat flow. In this case, the *RVP* at zero heat flow which reveals the RVP_{MeOH} of the wet line is equal to the intercept of the regression line. For the intercept of the regression line, a standard error can be calculated that corresponds to the standard error of the RVP_{MeOH} of the wet line. In the original approach (modelling the heat flow as a function of *RVP*), the *RVP* at zero heat flow is equal to the intersection of the regression line with the x-axis for which a standard error cannot be calculated. Hence, repetition of the experiment was required which made the original approach more time consuming. Nevertheless, this procedure had been chosen, since the standard error of the RVP_{MeOH} of the wet line determined from one experiment was about three times higher compared to the standard error obtained from repeated measurements. However, optimising the experiment might achieve that the standard error gained from one measurement is of the same order of magnitude as the standard error determined from several measurements. In this case, the saturation of the wet line could be verified in a single measurement which would result in considerable time saving. The optimisation of the calorimetric experiment is described in the following sections. It includes the *RVP* settings, the correction of the heat flow curve using the heat flow of the empty reaction vessel and the filling level of methanol in the reaction vessel.

4.1.3.2.2 *RVP* settings and correction of heat flow curve

As described above, the standard error of the RVP_{Solv} of the wet line obtained from one measurement corresponds to the standard error of the intercept of the regression line that models the *RVP* as a function of the heat flow. Possibilities to decrease the standard error of an intercept include the increase of the size of data and the enhancement of the density of measuring points near the intercept (Sachs, 2002). Therefore, it was tested whether the extension of the calorimetric experiment using 100 % RVP_{set} as additional step was suitable to reduce the standard error of the intercept. Fig. 19 displays the heat flow curve obtained when exposing methanol (0.8 ml) to RVP_{set} values of methanol of 80 % to 100 % using device A.

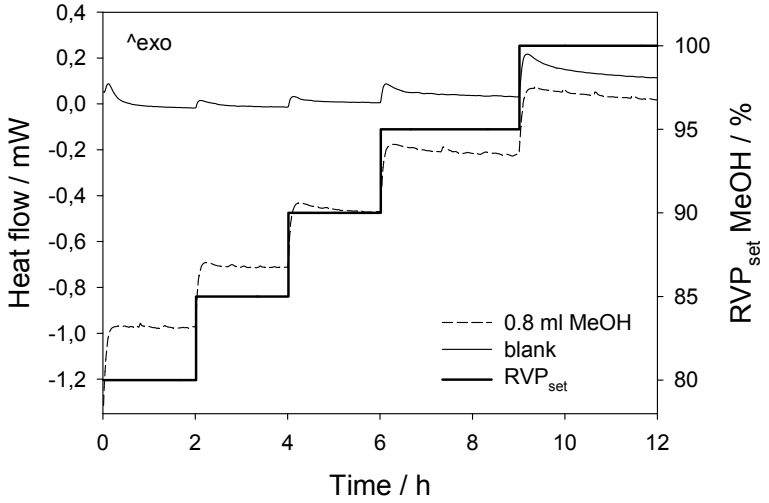

Fig. 19. Heat flow curve of 0.8 ml methanol being exposed up to 100 % *RVP*$_{set}$ of methanol and blank curve using device A (25 °C).

The figure reveals that at 95 % and 100 % *RVP*$_{set}$, the heat flow does not stabilise despite the enhanced time delay of these steps (time delay of 3 h versus 2 h for the other steps). Furthermore, it is questionable whether a stable heat flow is achieved at 90 % *RVP*$_{set}$. The experiment was repeated using an empty reaction vessel (blank experiment). The blank experiment corresponds to the heat flow that is associated with the perfusion of the reaction vessel. The heat flow of the sample experiment, however, is the sum of the heat flow related to the perfusion of the reaction vessel and the heat flow associated with the sample, in this case methanol. Fig. 19 shows that aside from the beginning of the experiment, the run of the blank curve follows the run of the sample curve. Subtracting the blank curve from the sample curve gives virtually stable heat flows at each *RVP*$_{set}$ step (Fig. 20).

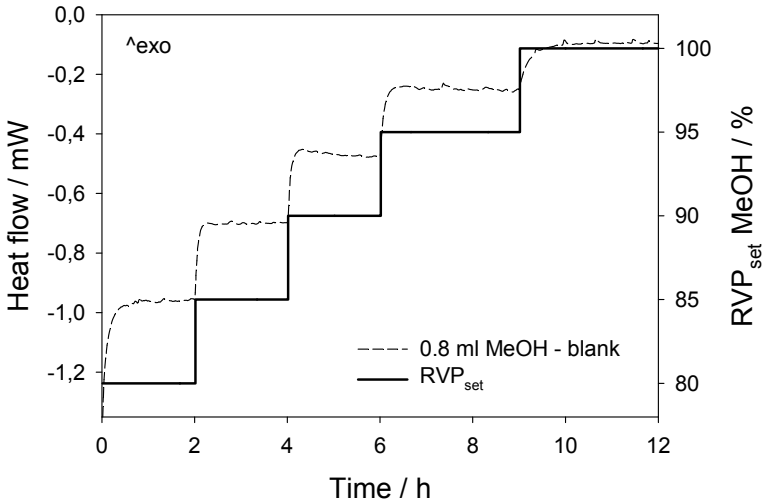

Fig. 20. Heat flow curve of 0.8 ml methanol being exposed up to 100 % *RVP*$_{set}$ of methanol using device A, blank curve subtracted (25 °C).

Hence, the heat changes associated with the perfusion of the reaction vessel cause the sample curve to decrease at 95 % and 100 % RVP_{set}. As a consequence, the subtraction of the blank curve from the sample curve is necessary to eliminate the heat changes related to perfusion. The steady state heat flows obtained after having subtracted the blank curve (Fig. 20) correspond to the constant evaporation rates of methanol reached at the different RVP_{set} steps. In order to obtain the RVP_{MeOH} of the wet line (± SE), the RVP_{mfc} values that correspond to the RVP_{set} steps used in the experiment were calculated using the regression lines obtained from volume flow measurements (4.1.3.1). The RVP_{mfc} values were modelled as a function of the steady state heat flow values (Fig. 21).

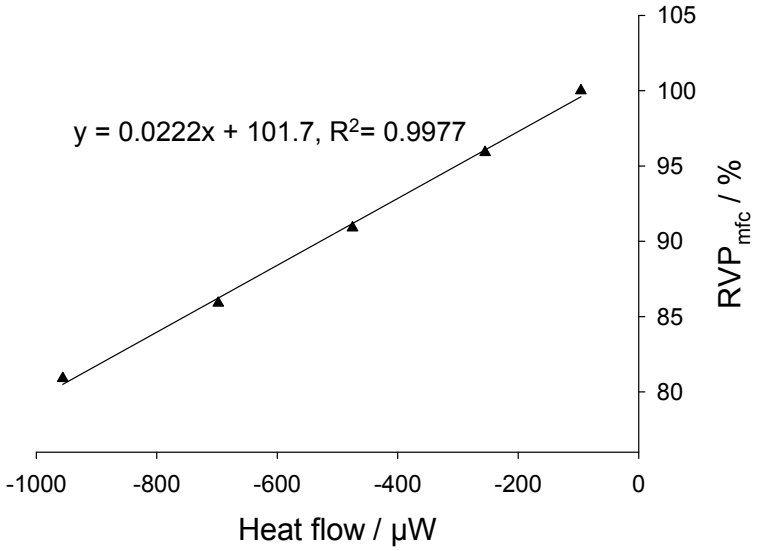

Fig. 21. Plot of RVP_{mfc} against the steady state heat flow values gained from exposing methanol up to 100 % RVP_{set} of methanol using device A; regression line is presented.

The figure shows that the regression line is well suited to describe the data points leading to a high R² value. Hence, linear regression seems to be suited to model the data up to 100 % RVP_{mfc}. The regression model will be evaluated in detail in section 4.1.3.2.4 when discussing the optimised experiment. Fig. 21 shows that the regression line intersects the RVP_{mfc}-axis (y-axis) above 100 % RVP_{mfc}. As described in section 4.1.2.2, the offset of the intersection from 100 % (in this case 1.7 %) corresponds to the value by which the RVP_{MeOH} of the wet line deviates from 100 %. Hence, the value obtained for the RVP_{MeOH} of the wet line of device A is 98.3 % ± 0.36 % (SE). This value is considerably higher than the value determined for the RVP_{MeOH} of the wet line of the flow switch valve based device which was 93.1 % ± 0.26 % (SE) (4.1.2.2).

In order to further study the heat changes associated with the perfusion of the sample vessel, a step experiment was performed increasing RVP_{set} from 0 % to 100 % in 10 % steps using an empty reaction vessel. To investigate the influence of

the solvent used on the blank curve, the experiment was repeated having first water and then ethanol inserted into the solvent reservoirs. The obtained heat flow curves are presented in Fig. 22.

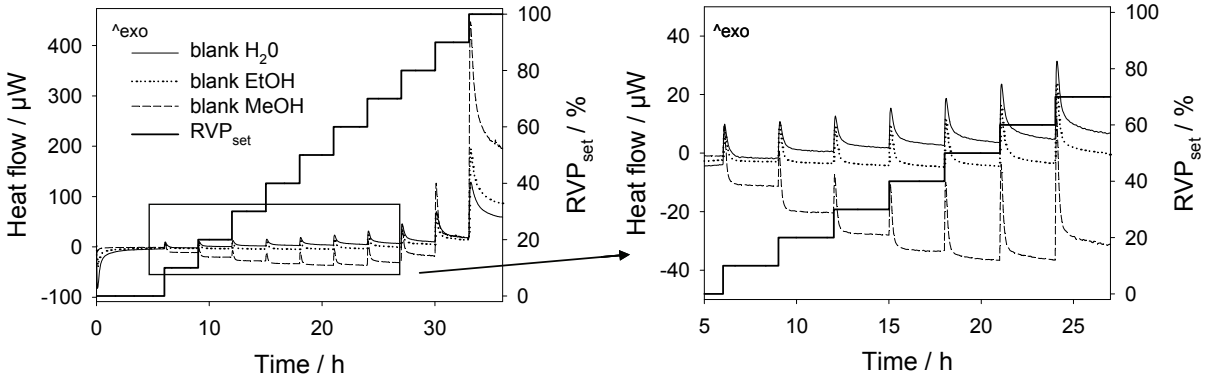

Fig. 22. Influence of the solvent on the blank curve that is obtained when increasing *RVP*$_{set}$ using device A; right: close up view (25 °C).

For all solvents used, the heat flow is virtually zero at 0 % *RVP*$_{set}$. Hence, the perfusion of the reaction vessel with dry nitrogen was not accompanied with any heat changes. At the beginning of every *RVP* step, a peak is observed for each solvent. The height of the initial peak increases with rising *RVP*$_{set}$. The curve rapidly declines to a baseline slightly exothermic (water), slightly endothermic (ethanol) or clearly endothermic (methanol) in the region of low *RVP*$_{set}$ values. Up to 50 % *RVP*$_{set}$, the endothermic effect increases for ethanol and methanol. When *RVP*$_{set}$ is further increased the endothermic effect decreases again turning into an exothermic response at high *RVP*$_{set}$ values. For water, the exothermic effect visible at low *RVP*$_{set}$ increases up to 100 % *RVP*$_{set}$. At 100 % *RVP*$_{set}$, the thermal activity is highest for methanol.

The heat changes monitored at the different *RVP*$_{set}$ values might be explained by different effects. One effect is an exothermic heat flow caused by the adsorption of solvent molecules to the inner wall of the sample vessel. Each time *RVP*$_{set}$ is increased, solvent molecules adsorb to the wall until equilibrium at the respective *RVP*$_{set}$ value is attained. In addition, there might be a second exothermic effect due to a possible slight increase of the total pressure inside the solvent reservoirs each time *RVP*$_{set}$ is increased. Inside the solvent reservoirs, the partial pressure of nitrogen theoretically diminishes by the saturation vapour pressure of the solvent used so that the total pressure remains constant (2.4.2). Practically, the increase of *RVP*$_{set}$ causes a sudden rise of the flow rate entering the solvent reservoirs. The molecules might accumulate resulting in a slight increase of the total pressure in the solvent reservoirs and in the wet line. The increase of the pressure reduces the distance between the solvent molecules. Since the solvent molecules are close to condensation due to a vapour pressure close to the saturation vapour pressure, repulsive forces dominate in the wet line. When the gas mixture containing nitrogen

and solvent molecules leaves the wet line and enters the reaction vessel, the gas expands and the pressure of the gas reduces. Due to the domination of the repulsive forces, the expansion in the reaction vessel leading to an increased distance between the solvent molecules is exothermic. Both exothermic effects described (adsorption of molecules to the inner wall of the sample vessel and a possible slight increase in the total pressure of the system) are proportional to the number of the solvent molecules leaving the wet line. Thus, the exothermic heat flow corresponding to both effects is proportional to RVP_{set} and to the saturation vapour pressure of the solvent. This is in accordance with the observation that at 100 % RVP_{set}, the exothermic heat flow is highest for methanol and lowest for water (Fig. 22).
A third effect might be an endothermic heat flow caused by the mixing of the gas coming out of the dry line (nitrogen) and the wet line (nitrogen and solvent molecules) inside the reaction vessel at RVP_{set} < 100 %. The mixing process is tantamount to a further increase of the distance of the solvent molecules. This time, attractive forces might dominate so that the process is endothermic. Whether the endothermic effect outweighs the exothermic effects depends on the solvent used. Fig. 22 indicates that for methanol and ethanol, the exothermic effects dominate first (initial peak), but then the endothermic effect prevails. In opposition to that, the exothermic effects predominate at each *RVP* step in case of water. The mixing effect rises with the number of solvent molecules leaving the wet line and with the difference between the RVP_{Solv} of the wet line and the RVP_{Solv} inside the reaction vessel. Therefore, the mixing effect is strongest at 50 % RVP_{set}. At 100 % RVP_{set}, the mixing effect is not present so that the thermal response is exothermic for all solvents. The explanations given are in accordance with the measurements performed (Fig. 22), however, there might be other reasons for the heat changes observed due to the complexity of the system.
To sum up, using 100 % RVP_{set} as additional step in the experiment results in an RVP_{MeOH} of the wet line of 98.3 % ± 0.36 % (SE) for device A. The order of magnitude of the standard error is comparable to the standard error assessed for the RVP_{MeOH} of the wet line using repeated measurements (4.1.2.2). Hence, the use of 100 % RVP_{set} as additional step is successful to reduce the standard error of the RVP_{MeOH} of the wet line obtained from a single experiment. As a next step, it was investigated whether changing the filling level of methanol in the reaction vessel affects the value determined for the RVP_{MeOH} of the wet line.

4.1.3.2.3 Filling level of solvent in the reaction vessel

In the experiments performed so far, the volume of methanol inserted into the reaction vessel was 0.8 ml. In order to investigate whether the sample volume has any influence on the heat flow observed, the experiment described in previous section (4.1.3.2.2) was repeated using the same device (device A) choosing 0.2 ml and 2.4 ml methanol as sample volumes. With the reaction vessel having a total filling volume of 4 ml, 0.2 ml represents a low filling level while 2.4 ml corresponds to

a high filling level. The filling volume of 4 ml was not fully used in order to provide enough space for perfusion. The heat flow curves obtained were compared with the heat flow curve of 0.8 ml methanol (4.1.3.2.2) (Fig. 23).

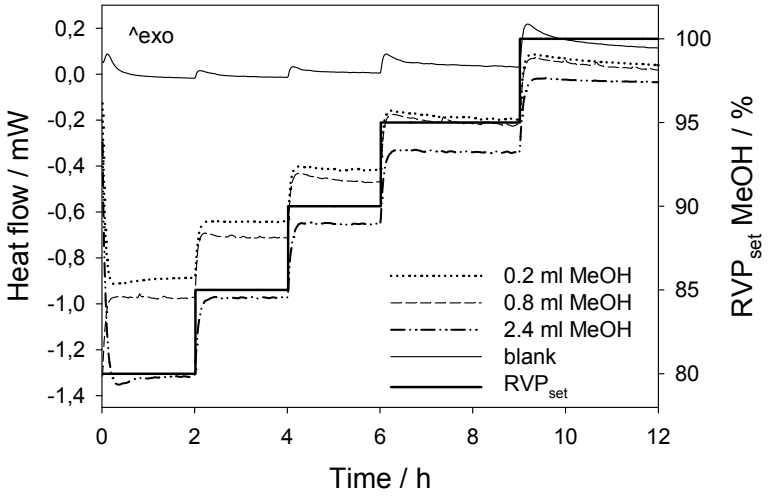

Fig. 23. Heat flow curves of 0.2 ml, 0.8 ml and 2.4 ml methanol being exposed up to 100 % *RVP*$_{set}$ of methanol and blank curve using device A (25 °C).

Fig. 23 reveals that at each *RVP*$_{set}$ step, the endothermic heat flow increases with rising sample volume. While the run of the heat flow curves of 0.2 ml and 0.8 ml methanol follow the run of the blank curve, differences are observed regarding 2.4 ml methanol. At 100 % *RVP*$_{set}$, the heat flow of 2.4 ml methanol decreases less than the heat flow of the blank. As a consequence, subtracting the blank curve from the sample curves results in an unstable heat flow at 100 % *RVP*$_{set}$ in case of 2.4 ml methanol (Fig. 24).

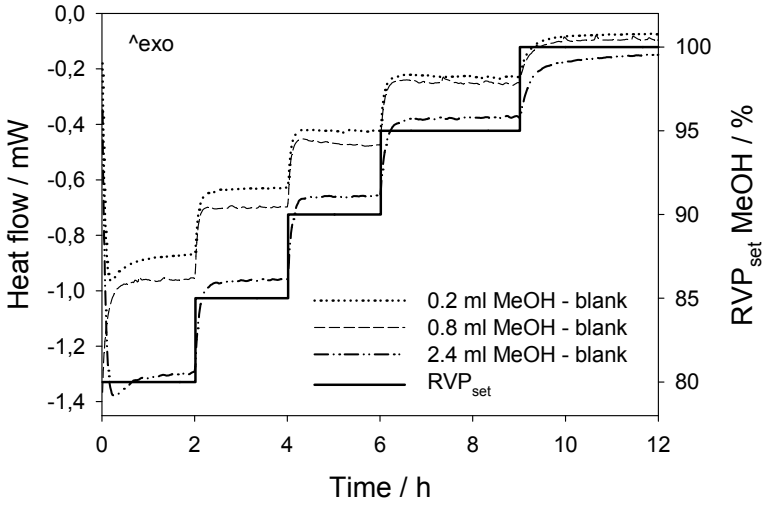

Fig. 24. Heat flow curves of 0.2 ml, 0.8 ml and 2.4 ml methanol being exposed up to 100 % *RVP*$_{set}$ of methanol using device A, blank curve subtracted (25 °C).

The finding indicates that the heat flow related to the perfusion of the empty reaction vessel differs from the heat flow associated with the perfusion of the vessel containing 2.4 ml methanol. A possible explanation might be the significantly reduced gas space available in the presence of 2.4 ml methanol.
For both 0.2 ml and 2.4 ml methanol, the steady state heat flow values obtained by subtracting the blank curve from the sample curve were used to perform linear regression modelling RVP_{mfc} as a function of the steady state heat flow values. The fact that the heat flow at 100 % RVP_{set} is unstable in case of 2.4 ml methanol was neglected using the heat flow value determined at the end of the step. The values for the RVP_{MeOH} of the wet line (± SE) obtained from the intercepts of the regression lines are 98.6 % ± 0.36 % (0.2 ml methanol) and 97.8 % ± 0.33 % (2.4 ml methanol). In comparison, an RVP_{MeOH} of the wet line of 98.3 % ± 0.36 % was determined when using 0.8 ml methanol (4.1.3.2.2). Consequently, the filling level in the reaction vessel has minor if any effect on the value determined for the RVP_{MeOH} of the wet line. The question remains why the endothermic heat flow does increase with rising sample volume at a given RVP_{set} (Fig. 23). A possible explanation is derived assuming that the evaporation of a solvent in the reaction vessel might be regarded as a process based on diffusion. A known diffusion based process is the dissolution of solids. It is supposed that the evaporation process in the reaction vessel might be described by a similar model. In this case, the Noyes-Whitney equation (Bauer *et al.*, 2002) may be used to describe the rate of evaporation:

$$\frac{dm}{dt} = \frac{AD\left(p_{Solv,sat} - p_{Solv}\right)}{\delta} \tag{30}$$

where dm / dt is the evaporation rate, A is the cross section surface of the vessel, D is the diffusion coefficient of the solvent in the gas phase, $p_{Solv,sat}$ is the saturation vapour pressure of the solvent at the surface of the solvent, p_{Solv} is the partial vapour pressure of solvent in the gas phase and δ is the diffusion layer thickness. The diffusion layer represents a rigid layer the evaporated solvent molecules have to pass to reach the bulk gas phase. In the bulk gas phase, the solvent molecules become part of the gas flow and leave the reaction vessel via the outlet tube. Thus, the partial vapour pressure of solvent in the gas phase remains constant leading to a constant value for $p_{Solv,sat} - p_{Solv}$. This holds for different filling levels of solvent inside the reaction vessel. While A is also constant at different filling levels, δ changes. With rising filling level, the surface of the solvent approaches the gas inlets of the dry and the wet line. Since the movement of the gas molecules near the gas inlets is increased, the thickness of the rigid diffusion layer is reduced. The reduction of δ leads to a higher evaporation rate which would be a possible explanation for the increase of the endothermic heat flow observed with rising filling level.
Summarising, the experiments show that the filling level of solvent in the reaction vessel does have minor if any effect on the value determined for the RVP_{MeOH} of the

wet line. However, for a high filling level, the blank curve seems to be not well suited to describe the heat changes associated with the perfusion of the ampoule. Therefore, it was decided to use the lowest sample volume (0.2 ml) to have conditions as similar as possible to the blank curve. In addition, the experiment was further optimised with regard to the first *RVP* step. Fig. 24 shows that it is not certain whether a stable heat flow is reached at 80 % RVP_{set} in case of 0.2 ml methanol. This might be due to disturbances at the beginning of the measurement in both the sample and the blank experiment. Another possible reason might be that there is not any step preceding the 80 % step so that the time required to generate the RVP_{MeOH} in the vessel is longer than the time needed at the other steps where the RVP_{MeOH} has already been controlled and just has to be changed by 5 %. Therefore, the *RVP* was first set to 75 % for one hour before shifting to 80 % to provide similar conditions for all steps.

4.1.3.2.4 Optimised calorimetric experiment

The optimised calorimetric experiment with the *RVP* settings and the sample volume derived from the experiments in sections 4.1.3.2.2 and 4.1.3.2.3 was conducted using both devices A and B. Since it was known from previous experiments that for device B, the time needed for the heat flow to stabilise at 100 % RVP_{set} was longer compared to the other steps, the 100 % step was run for 5 h. The heat flow curves obtained after the subtraction of the corresponding blank curve are given in Fig. 25.

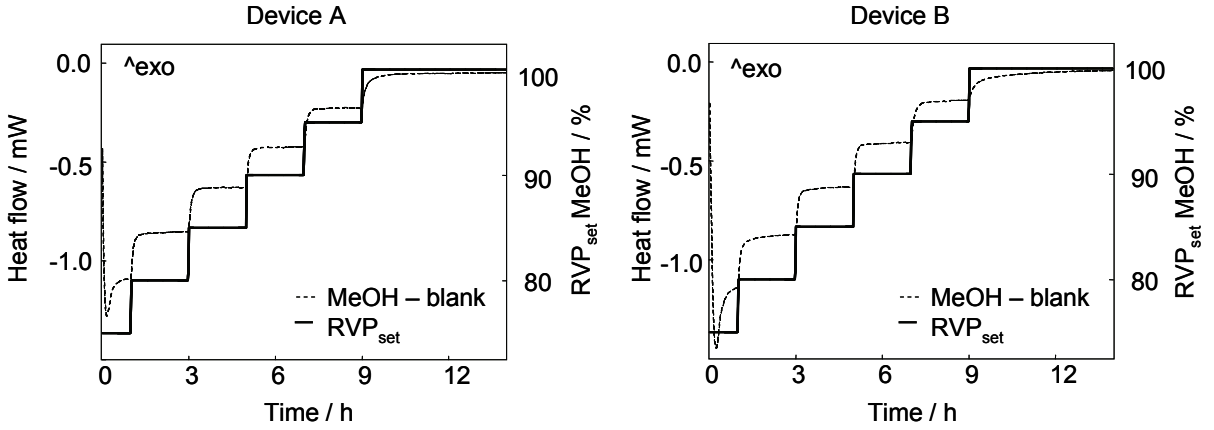

Fig. 25. Heat flow curves obtained for device A and B using 0.2 ml methanol and optimised *RVP* settings, corresponding blank curve subtracted (25 °C).

The figure shows that for device A, a stable heat flow is achieved at each step. Regarding device B, it is not sure whether the heat flow has stabilised at the end of every step or whether it is still approaching a constant value. Especially at 80 % and 100 % RVP_{set}, the heat flows seem to exhibit minor drifts. Possible reasons for this observation will be given below. For both devices, the heat flow value at the end of each step was determined neglecting the minor heat flow drifts in case of device B. The heat flow values were used for linear regression modelling RVP_{mfc} as a function of heat flow. The resulting regression lines are presented in Fig. 26.

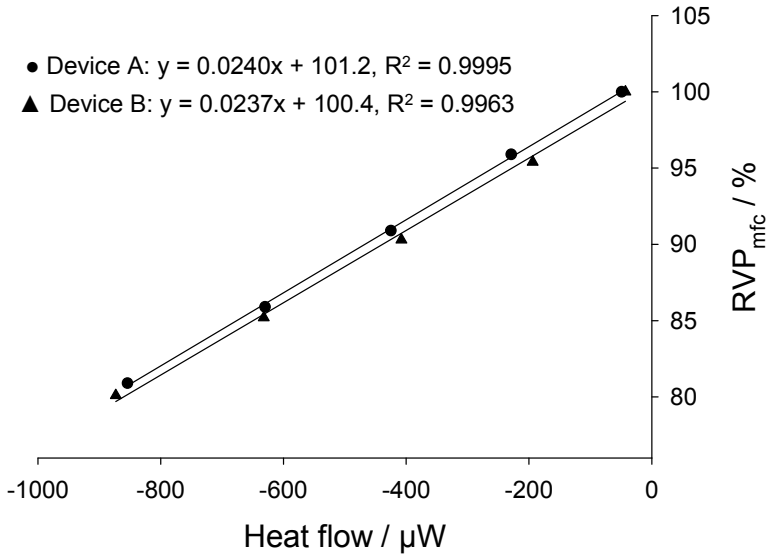

Fig. 26. Plot of RVP_{mfc} against the steady state heat flow values gained from the optimised experiment for device A and B; regression lines are presented.

The figure reveals that, also for device B, linear regression is suited to model the data up to 100 % RVP_{mfc}. Regarding device A, this conclusion was already drawn from Fig. 21 (4.1.3.2.2). The values for the RVP_{MeOH} of the wet line gained from the intercepts of the regression lines are 98.8 % ± 0.16 % (SE) and 99.6 % ± 0.44 % (SE) for device A and B. For device B, the value does not statistically significantly (α = 0.05) differ from 100 %. Consequently, the wet line is fully saturated with methanol vapours. Regarding device A, the value for the RVP_{MeOH} of the wet line is in agreement with the previously obtained values (4.1.3.2.3). It is slightly below 100 % (α = 0.05), i.e. complete saturation of the wet line is nearly achieved. To evaluate the linear regression models used, the assumptions of linear regression were checked by graphical analysis. The normality plots of the residuals (not shown) indicated a normal distribution of the residuals for both devices A and B. To check for the other assumptions, the residuals were plotted versus the predicted *RVP* values (Fig. 27).

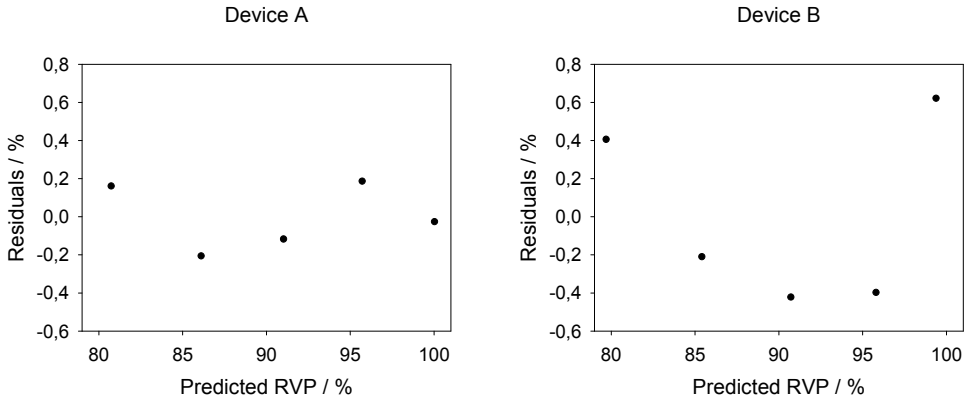

Fig. 27. Residual plots obtained for device A and B having RVP_{mfc} modelled as a function of the steady state heat flow values gained from the optimised experiment.

For device A, the residuals scatter randomly around zero showing no evidence of nonlinearity, correlation of residuals or unequal variances. By contrast, a parabolic pattern of the residuals is visible in case of device B. Such a pattern is also observed for other devices and other solvents (4.1.5). A possible explanation for the pattern is that the heat flow is regarded as the independent, error-free variable when performing linear regression. However, the heat flow values are in fact not error-free. First, the evaporation rate of the solvent present in the reaction vessel and thus, the heat flow, might still approach a constant value at the end of an *RVP* step. Secondly, the thermal activity related to the perfusion of the reaction vessel (blank curve) has to be subtracted from the sample curve. Since the sample curve and the blank curve might slightly differ in the thermal activity corresponding to the perfusion of the vessel, the heat flow values obtained after the subtraction of the blank curve might be erroneous due to the incomplete or excessive subtraction of thermal activity. Thirdly, the heat flow values determined may correlate, since the thermal activity at each step may be affected by the thermal activity of the previous step.
The first and the second source of error are detected from the heat flow curve of the sample after the blank curve has been subtracted. For both sources of error, a drift in the heat flow will be observed at the end of an *RVP* step. Indeed, minor drifts in the heat flows seem to be present for device B (Fig. 25) indicating a non-constant evaporation rate and / or differences in the thermal activity related to perfusion in comparison to the blank curve. In order to eliminate the first source of error, i.e. in order to be confident to provide enough time for the evaporation rate and thus, the heat flow, to reach a constant value, the duration of the steps should have been increased. However, using elongated steps increases the error in the heat flow values caused by the decrease of the filling level in the vessel during the experiment (due to evaporation). As known from the experiments using different filling levels in the vessel (4.1.3.2.3), the endothermic heat flow at a given RVP_{set} diminishes with decreasing filling level. Although a certain decrease of the filling level cannot be avoided during the experiment, the use of short steps minimises the resulting errors in the heat flow values. Therefore, it was decided not to elongate the steps accepting the possible small error in the heat flow values due to a non-constant evaporation rate of the solvent. The second source of error, the variations in the thermal activity related to the perfusion of the vessel, may be reduced by repeating the blank curve several times and calculating a mean blank curve that is used for subtraction. However, this procedure would negate the time saving achieved by performing just one sample experiment. In addition, it is common practice in perfusion calorimetry to just measure a single blank experiment (Danforth and David, 2006). To avoid the correlation of the heat flow values determined (third source of error), the heat flow value at each *RVP* step could be measured in a separate experiment. However, since it is common practice to perform a single experiment to monitor the thermal activity of a sample at different *RVP* steps, it was decided not to use this alternative approach. Summarising the above, several sources of error result in erroneous heat

flow values which affects the quality of linear regression and which might explain the frequently observed pattern of the residuals.
Another possible reason for the pattern of the residuals is the difference in the errors of the *RVP* values used for linear regression. From 80 % to 95 % RVP_{set}, the RVP_{mfc} values obtained from the volume flow measurements are used for linear regression. The errors of these values may be assumed to be normally distributed and to have constant variance. At 100 % RVP_{set} however, the set value (100 %) is used for linear regression. This value represents a predetermined error-free value. In order to eliminate the difference in the errors of the *RVP* values, the data pair heat flow value / 100 % RVP_{set} could be excluded from linear regression. However, the exclusion of this data pair sometimes resulted in values for the RVP_{Solv} of the wet line above 100 %. However, the RVP_{Solv} cannot exceed 100 %. Hence, the inclusion of this data pair increases the accuracy of the value determined for the RVP_{Solv} of the wet line. Consequently, the data pair was not excluded from linear regression.
Summarising one can say that linear regression is performed disregarding the errors in the heat flow values and the differences in the errors of the *RVP* values. As a result, the quality of the linear regression model is impaired (pattern in the residual plot). Nevertheless, linear regression is suitable to describe the data as revealed by Fig. 26 indicating that the quality of the model is only marginally impaired. The optimisation of the calorimetric experiment achieves to reduce the standard error of the RVP_{MeOH} of the wet line gained from a single experiment. Using the optimised experimental conditions, the standard error of the RVP_{MeOH} of the wet line ranges from 0.16 % (device A) to 0.44 % (device B). The order of magnitude of the standard is regarded as acceptable based on later experiments (4.1.3.4). Hence, a single measurement (plus blank measurement) is sufficient to verify the saturation of the wet line. Consequently, the aim of time saving was achieved.

4.1.3.3 Determination of the actual relative vapour pressure

The results from the volume flow measurements and the optimised calorimetric experiment were used to adjust Eq. (26) (equation to calculate the theoretical RVP_{in}) in order to obtain the equation that describes the actual RVP_{in} generated in device A and B respectively. For device A, the equation is:

$$RVP_{in} = \frac{0.988}{\left[1 - \frac{p_{MeOH,sat}}{p_{tot}} 0.988 \left(1 - \frac{RVP_{mfc}}{100\%}\right)\right]} RVP_{mfc} \qquad (31)$$

and for device B:

$$RVP_{\text{in}} = \frac{0.996}{\left[1 - \frac{p_{\text{MeOH,sat}}}{p_{\text{tot}}} 0.996 \left(1 - \frac{RVP_{\text{mfc}}}{100\%}\right)\right]} RVP_{\text{mfc}} \quad (32)$$

The equations were used to calculate the RVP_{in} of methanol at 25 °C and 1.01325 bar for different values of RVP_{set}. The values are presented in Table 8.

Table 8 Theoretical RVP_{in} of methanol versus actual RVP_{in} of methanol (± SE (according to the Gaussian error propagation)) generated in device A and B, respectively (25 °C and 1.01325 bar)

RVP_{set} [%]	Theoretical RVP_{in} [%]	Actual RVP_{in} Device A [%]	Actual RVP_{in} Device B [%]
5	5.9	6.0 ± 0.17	7.4 ± 0.12
10	11.8	11.9 ± 0.15	12.9 ± 0.12
15	17.5	17.7 ± 0.13	18.3 ± 0.13
20	23.1	23.3 ± 0.12	23.7 ± 0.14
40	44.4	44.7 ± 0.11	44.4 ± 0.22
60	64.3	64.4 ± 0.14	63.9 ± 0.30
80	82.8	82.6 ± 0.19	82.5 ± 0.38
85	87.2	86.9 ± 0.21	87.0 ± 0.40
90	91.5	91.2 ± 0.22	91.4 ± 0.42
95	95.8	95.4 ± 0.24	95.8 ± 0.44
100	100.0	98.8 ± 0.16	99.6 ± 0.44

The table shows that device A works accurately over nearly the whole range of *RVP*. Only at 100 % RVP_{set}, the actual RVP_{in} is a little below the theoretical value (statistically significant, α = 0.05). Device B works accurately at $RVP_{\text{set}} \geq 40$ %. Below 40 %, the actual RVP_{in} slightly exceeds the theoretical value (statistically significant, α = 0.05).

4.1.3.4 Comparison of tested vapour pressure control devices

The check of a vapour pressure control device provides the actual RVP_{in} generated by the device at a given RVP_{set} value. Knowing the actual RVP_{in} enables the user to adjust RVP_{set} to create the desired RVP_{in}. Hence, having several tested vapour pressure control devices, the same RVP_{Solv} can be created in the sample vessel of each device by adjusting RVP_{set}. Having the same RVP_{in} produced by every device, the measurement of any substance should give identical heat changes in all devices. Therefore, the performances of two tested vapour pressure control devices can be compared by choosing a suitable experiment that is carried out in both devices. The ideal test substance for the experiment would be sensitive to changes in RVP_{in} in the

entire *RVP* range. For methanol as solvent, emodepside represents a suitable test substance. As described in section 2.5.1, emodepside crystallises in the forms I-IV. Fig. 28 shows the thermal activities of the forms I and IV being first dried at 0 % RVP_{in} and then exposed to increasing RVP_{in} values of methanol.

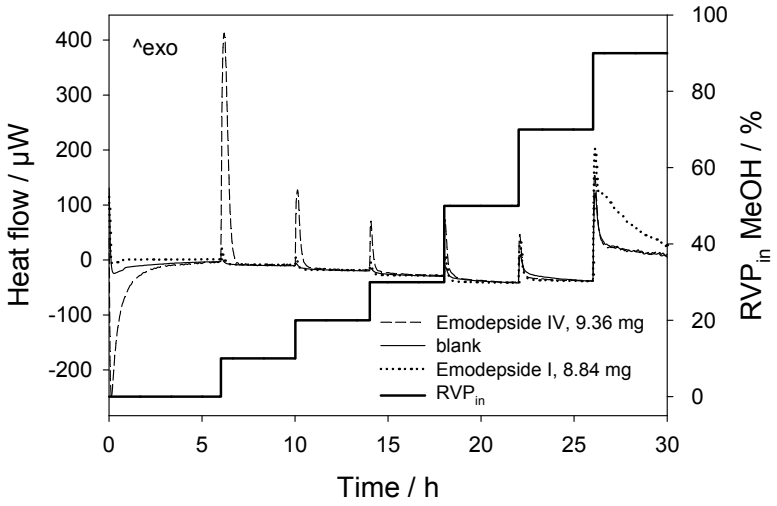

Fig. 28. Heat flow curves of emodepside form I and IV being first dried at 0 % RVP_{in} and then exposed to increasing RVP_{in} values of methanol; blank curve is also presented (25 °C).

Regarding emodepside form IV, a large amount of heat is generated in the region of low RVP_{in} values of methanol due to the formation of the isomorphic methanolate IV (section 4.4.3). By contrast, for emodepside form I, distinct heat changes are observed at 90 % RVP_{in}. The prolonged heat production corresponds to the phase transformation into methanolate IV (section 4.4.3). The use of both crystal forms of emodepside, form I and form IV, allows the comparison of tested vapour pressure control devices over the entire *RVP* range. Hence, the two crystal forms were used to compare the tested devices A and B. In case of form IV, the heat evolved at 10 %, 20 % and 30 % RVP_{in} was measured. Higher RVP_{in} values were not used since possible differences in the RVP_{in} values created by two devices would not be detected due to the low signal (sample heat flow) to noise (blank heat flow) ratio. Regarding form I, a ramp experiment (ramp rate of 4 % RVP_{set} / h) was performed to determine the critical RVP_{MeOH} of the transformation (Fig. 29).

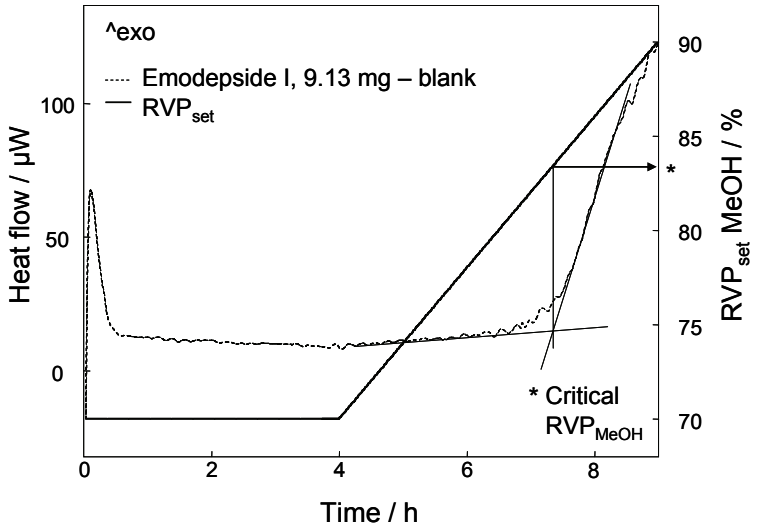

Fig. 29. Heat flow curve of emodepside form I being exposed to increasing RVP_{in} values of methanol (ramp experiment), blank curve subtracted (25 °C).

For both devices A and B, the results of the measurements are given in Table 9. For emodepside form IV, the heat values determined using device A do not differ significantly (α = 0.05) from the values gained from device B.

Table 9 Heat output for emodepside IV at 10 %, 20 % and 30 % RVP_{in} of methanol ($\bar{x}$ ± s, n = 3) and the critical RVP_{MeOH} of transformation for emodepside I ($\bar{x}$ ± s, n = 3) for device A and B

	Heat [kJ*mol^{-1}] at 10 % RVP_{in}, emodepside IV	Heat [kJ*mol^{-1}] at 20 % RVP_{in}, emodepside IV	Heat [kJ*mol^{-1}] at 30 % RVP_{in}, emodepside IV	Critical RVP_{in} [%] of transformation for emodepside I
Device A	64 ± 1.7	11.8 ± 0.46	5.3 ± 0.28	84.4± 0.24
Device B	65 ± 1.8	13.1 ± 0.95	5.0 ± 0.95	84.7 ± 0.06

The critical RVP_{MeOH} values for the transformation of emodepside I obtained from both devices do also not differ (α = 0.05). Consequently, the devices work comparably. The results indirectly show that the method used to test the devices provides accurate values for RVP_{in}.

4.1.4 Parameters influencing the saturation of the wet line

The check of the different vapour pressure control devices revealed that the saturation of the wet line with solvent vapours may not be achieved, i.e. the RVP_{Solv} of the wet line may be below 100 %. While saturation of the wet line was observed in case of device B, an RVP_{MeOH} of the wet line well below 100 % (93.1 % ± 0.26 % (SE)) was determined for the flow switch valve based device. Regarding device A, the RVP_{MeOH} of the wet line was slightly below 100 % (98.8 % ± 0.16 % (SE)). The following experiments aimed at investigating the factors influencing the RVP_{Solv} of the

wet line. Recalling the construction of the perfusion ampoule (Fig. 7), several possible parameters can be identified. These are the amount of solvent present in the solvent reservoirs, the depth of penetration of the steel tubes (through which the nitrogen stream enters the solvent reservoirs) into the solvent and the flow rate of the nitrogen passing through the solvent reservoirs. When performing the experiments to verify the saturation of the wet line, the amount of solvent inserted into the solvent reservoirs of the flow switch valve based device differed from the amount used for the devices A and B. Regarding the valve based device, 0.5 ml methanol were inserted into both solvent reservoirs prior to the start of each of the three calorimetric experiments (solvent reservoirs were emptied before they were refilled). For the devices A and B, a more rapid depletion of the solvent was expected due to the higher total flow rate used. Hence, the amount of solvent placed into the first solvent reservoir was increased to 1 ml for both devices A and B. To investigate whether the difference in the amount of solvent used for the first reservoir was the reason for the different degrees of saturation observed, the RVP_{MeOH} of the wet line of device A was determined using a minimum amount of solvent for the first reservoir (0.3 ml). The amount used for the second reservoir (0.5 ml) was not changed. After having conducted the optimised calorimetric experiment (data not shown), the first solvent reservoir was found to be nearly empty. However, RVP_{MeOH} of the wet line obtained from the experiment does not differ significantly ($\alpha = 0.05$) from the value determined when having 1 ml of methanol in the first solvent reservoir. Consequently, the different amounts of solvent used are not responsible for the differences in the RVP_{MeOH} of the wet line.

As a next step, it was examined whether the steel tubes through which the nitrogen molecules enter the reservoirs have to be immerged into the solvent in order to achieve an RVP_{MeOH} of the wet line near 100 %. For the following experiments, a third mass flow controller based device (device C) was used. The solvent reservoirs of this device had been assembled trying to maximise the depth of penetration of the steel tubes in each reservoir. The RVP_{MeOH} of the wet line was found to not differ significantly ($\alpha = 0.05$) from 100 %. To study the influence of the position of the steel tube reaching into the second reservoir, the tube was pulled up to prevent the tube from immerging into the solvent. As it was difficult to see whether the tube had actually moved, the amount of solvent placed into the second reservoir was reduced to 0.2 ml in order to ensure that the tube ended above the solvent surface (first reservoir: 0.5 ml). For the modified system, an RVP_{MeOH} of the wet line of 98.9 % ± 0.22 % (SE) was determined. This value is significantly ($\alpha = 0.05$) different from 100 % revealing that the position of the tube reaching into the second solvent reservoir has a slight effect on the RVP_{MeOH} of the wet line. Next, the device was further changed by pulling up the tube reaching into the first reservoir. This modification markedly reduced the RVP_{MeOH} of the wet line to a value of 90.2 % ± 0.38 % (SE). Consequently, the tube entering the first solvent reservoir has to immerge into the solvent in order to obtain a value near 100 % for the RVP_{MeOH} of

the wet line. The result was confirmed by the fact that after having optimised the position of the tube for the flow switch valve based device, full saturation of the wet line was observed (data not shown).

The last possible factor that may influence the saturation of the wet line is the flow rate of the gas stream passing through the solvent reservoirs. It may be assumed that a high flow rate may not provide enough time for the uptake of solvent molecules into the gas stream so that the RVP_{Solv} of the wet line may decrease. To investigate whether the RVP_{MeOH} of the wet line changes when using significantly higher flow rates, the RVP_{MeOH} of the wet line of device A was determined using a total flow rate of 160 ml*h^{-1}. The value for the RVP_{MeOH} of the wet line determined at 160 ml*h^{-1} does not significantly ($\alpha = 0.05$) differ from the value obtained at 80 ml*h^{-1}. Consequently, the flow rate does not affect the degree of saturation of the wet line up to a flow rate of 160 ml*h^{-1}.

Summarising, measurements have shown that the position of the steel tube reaching into the first solvent reservoir significantly influences the RVP_{MeOH} of the wet line. In order to have an RVP_{MeOH} near 100 %, the tube has to immerge into the solvent. In case the tube penetrates into the solvent, RVP_{MeOH} of the wet line will be independent of the amount of solvent present in the first solvent reservoir as well as the total flow rate used (tested up to 160 ml*h^{-1}). It is assumed that these results also hold for other solvents.

4.1.5 General applicability

The method developed to check a vapour pressure control device is shown to be applicable for both flow switch valve based devices and for devices working with two mass flow controllers. Both types of devices were tested using methanol as model solvent. To demonstrate that the method may also be used for other solvents, the *RVP* of the wet line was determined for both water and ethanol being solvents that are frequently used in perfusion calorimetry. The devices B and C with optimal positions for the steel tubes entering the solvent reservoirs were used for the experiments (device B for water, device C for ethanol). The amounts of solvent placed into the first and second solvent reservoir were 1 ml and 0.5 ml while 0.2 ml solvent was inserted into the reaction vessel. The resulting curves (corresponding blank curves subtracted) are displayed in Fig. 30.

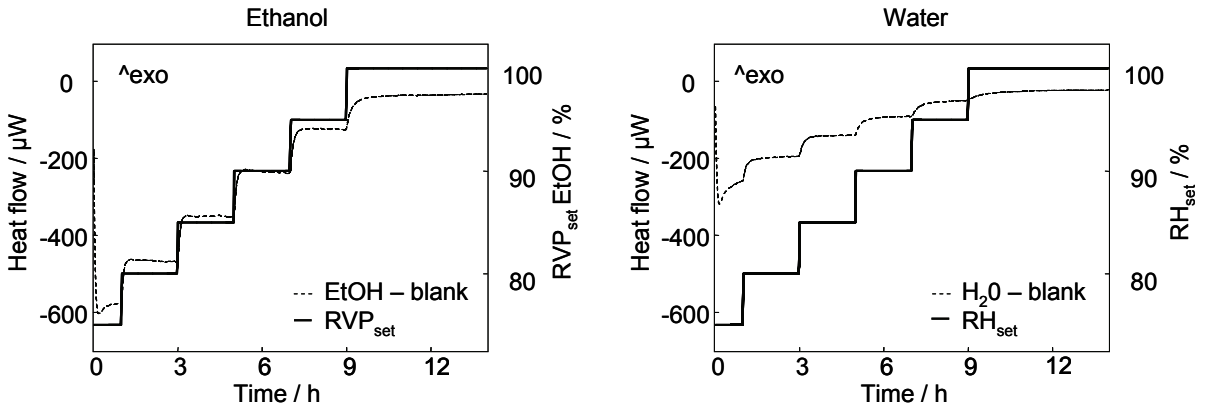

Fig. 30. Heat flow curves of 0.2 ml ethanol (left) and 0.2 ml water (right) exposed to increasing *RVP*$_{set}$ values of ethanol and water respectively using devices C and B, corresponding blank curves subtracted (25 °C).

The figure reveals that, similar to methanol, ethanol and water show endothermic heat flow curves due to the evaporation of the solvents. At each *RVP* step, steady state heat flows are obtained corresponding to constant evaporation rates. Fig. 30 shows that the steady state heat flow values for water are considerably smaller than the values for ethanol. Smaller heat flow values correspond to lower evaporation rates that are explained by the lower saturation vapour pressure of water. The constant heat flow values at each step were used for linear regression modelling *RVP*$_{mfc}$ as a function of the heat flow (Fig. 31).

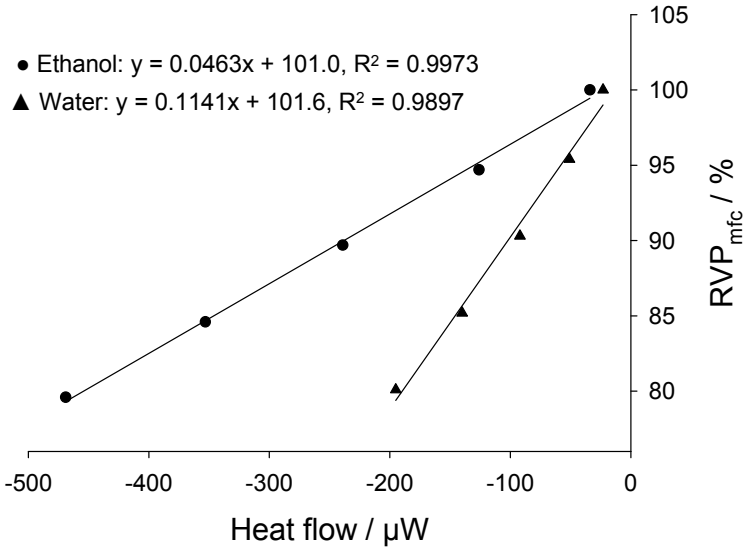

Fig. 31. Plot of *RVP*$_{mfc}$ against the steady state heat flow values gained from exposing ethanol and water respectively up to 100 % *RVP*$_{set}$ of ethanol and water respectively; regression lines are presented.

The figure shows that the regression lines obtained are suitable to describe the data for both ethanol and water. However, for water, a higher variability of the data points about the regression line is observed which results in a lower R² value. This indicates a slightly lower quality of the regression model for water. As for methanol, the

intercepts of the regression lines were used to determine the RVP_{EtOH} of the wet line for device C and the *RH* of the wet line for device B. The values obtained (± SE) are 99.0 % ± 0.40 % (ethanol) and 98.4 % ± 0.79 % (water) being not significantly (α = 0.05) different from 100 %. Consequently, the wet lines of the devices C and B are fully saturated with ethanol vapours and water vapours, respectively. The standard error of the RVP_{EtOH} of the wet line lies within the range of the standard errors obtained when using methanol (4.1.3.2.4). For water however, a higher standard error is found which is explained by the lower quality of the regression model. The differences in the quality of the models for water and ethanol are also visible in the residual plots (Fig. 32).

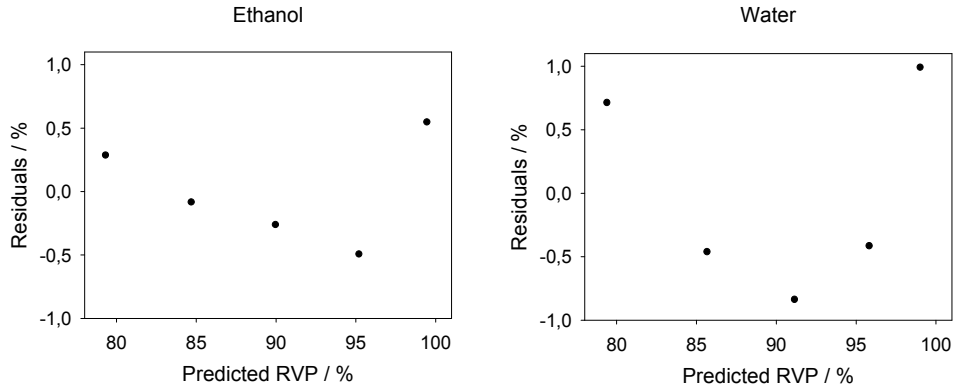

Fig. 32. Residual plots obtained for device C (ethanol) and device B (water) having RVP_{mfc} modelled as a function of the steady state heat flow values.

For water, the residuals have higher values due to the greater variability of the data about the regression line. In both residual plots, a parabolic pattern is visible. The possible reasons for the pattern have already been discussed in section 4.1.3.2.4. Additionally to the residual plots, normality plots were created to check the normal distribution of the residuals. The normality plots indicate normal distribution for both water and ethanol (data not shown).

To sum up, the calorimetric experiment developed to verify the saturation of the wet line is applicable to different solvents. Although a slightly lower quality of the regression model was obtained for water, the resulting higher standard error for the *RH* of the wet line is accepted based on later experiments (4.4.2).

4.1.6 Summary of results

A general method to verify the vapour pressure control devices used in perfusion calorimetry was developed. The method is based on the testing of the flow control system used and on the verification of the wet line of the perfusion ampoule. The volume flow measurements performed to check the flow control system are able to detect signs of ageing of a flow switch valve as well as minor differences in the performances of mass flow controllers. The calorimetric experiment used to verify the saturation of the wet line is capable of determining the RVP_{Solv} of the wet line with a

standard error less than 1 %. The method developed allows to calculcate the actual RVP_{Solv} generated by the device and thus enables the user to reliably perform perfusion calorimetry. The test of different devices has shown that it is important to check the performance of the system, especially after having re-assembled the perfusion ampoule, as the RVP_{in} may be considerably lower than expected due to mistakes made when assembling the system (e.g. wrong position of the steel tube entering the first solvent reservoir).

4.2 Solid forms of toltrazuril

4.2.1 Introductory comments

As described in section 2.5.2, a first short screening for different solid forms of toltrazuril had been performed by Grunenberg, Bayer HealthCare AG. Toltrazuril was found to exist in four crystalline forms A, B, C and D and in an amorphous form. The forms B, C and D had been identified using both Raman spectroscopy and differential scanning calorimetry (DSC). Regarding form A, a thermogram was the only evidence provided for the existence of form A (2.5.2).

Within the framework of this study, a classical solid form screening of toltrazuril was performed (2.2.3). The solid materials generated in the various experiments were identified using Fourier-transform infrared (FT-IR) spectroscopy and Fourier-transform Raman (FT-Raman) spectroscopy. Both methods are suitable to differentiate between the different solid forms found in this study (4.2.3.2). The solid forms produced in the screening are the crystalline forms B, C and D and an amorphous form. Regarding the crystalline forms, both pure forms and mixtures containing the forms B, C and / or D were obtained. A form is regarded as pure in case none of the bands of any other form is visible in the spectrum recorded (FT-IR and / or FT-Raman). The forms generated in the screening were further characterised using DSC, thermomicroscopy, X-ray powder diffraction (XRPD), density measurements, slurry conversion studies, perfusion calorimetry and annealing experiments. For some of the experiments, binary mixtures of forms were used. Unless otherwise stated, they represent 1:1 ($m*m^{-1}$) mixtures prepared using a mortar. The results obtained from the various experiments were used to determine the thermodynamic relationships between the different crystalline forms.

4.2.2 Solid forms obtained from the solid form screening

4.2.2.1 Crystallisation from solution

Acetone, acetonitrile, ethyl acetate, ethanol, methanol and toluol were selected for crystallisation experiments. The selection criteria were (1) diverse solvent properties and (2) adequate solubility of toltrazuril. Preliminary tests revealed that the solubility in the solvents chosen is > 1 $g*l^{-1}$ (0.1 % ($m*V^{-1}$)) which is regarded as sufficient to obtain a practicable yield. In addition, isobutanol was selected for crystallisation experiments since it is used in the manufacturing process of the API. API-solvent mixtures of equal concentration (2 % ($m*V^{-1}$)) were prepared. Thus, different degrees of saturation were generated in the mixtures. The solid form of toltrazuril used was form B being the solid material available. After one minute of shaking, the API was dissolved in the case of acetone and ethyl acetate indicating a higher solubility of the API in these two solvents. To achieve a certain degree of saturation, the concentration of the API was raised to 4 % ($m*V^{-1}$) in both solvents. Each API-solvent

mixture was heated to the boiling point of the solvent. At the boiling point, toltrazuril was completely dissolved within 5 min in all cases. Each hot solution was quartered to apply both slow and fast methods of crystallisation. Two portions were left at RT, one in a crystallising dish, the other one in a test tube. The third portion was filled in a test tube that was placed at 6 °C. In each case, complete evaporation of the solvent was awaited. Hence, supersaturation was achieved by evaporation and possibly cooling. Since evaporation is proportional to the surface-volume ratio and to the temperature, evaporation was fastest in case of the crystallisation dish left at RT and slowest in case of the test tube kept at 6 °C. The last portion of solution was used for anti-solvent addition. Water, cyclohexane and n-heptane were employed as anti-solvents. The precipitate obtained by anti-solvent addition was filtered off the same day and dried over night at ambient conditions. The outcome of the crystallisation experiments is presented in Table 10.

Table 10 Crystal forms of toltrazuril obtained by the crystallisation experiments using 4 % (m^*V^{-1}) API-solvent mixtures (acetone, ethyl acetate) and 2 % (m^*V^{-1}) API-solvent mixtures (acetonitrile, ethanol, isobutanol, methanol, toluol), respectively, heated to the boiling point of the corresponding solvent

	Evaporation of hot solution at RT, crystallising dish		Evaporation of hot solution at RT, test tube		Evaporation of hot solution at 6 °C, test tube		Hot solution + anti-solvent
	Inner wall	Bottom	Inner wall	Bottom	Inner wall	Bottom	
Acetone	D	B + D	B	B	B	B	B + D
Acetonitrile	B + D	B + D	B	B	B	B	B
Ethyl acetate	B + D	B + D	B	B	B	B	D
Ethanol	B + D	B	B + D	B	B	B	B + D
Isobutanol	B + D	B	B	B	B	B	B
Methanol	B + D	B + D	B	B	B	B	B + D
Toluol	D	B + D	B + D	B	B	B	D

Crystallisation experiments result in the forms B and D. Both pure forms and mixtures of B and D are found. Regarding the crystallisation approaches based on evaporation, the solid forms found at the inner wall and at the bottom of the vessel partly differ due to the increased velocity of crystallisation at the inner wall of the vessel. Table 10 shows that fast crystallisation processes (evaporation using a crystallising dish, anti-solvent addition) favour the formation of the form D whereas slower crystallisation methods (evaporation at RT and 6 °C using a test tube) result in pure form B in most of the cases. This indicates that the form D is less stable than form B at both RT and 6 °C (2.2.1).

In the experiments performed, the methods used to achieve supersaturation are evaporation and anti-solvent addition, both possibly combined with cooling. It is not

known whether cooling played a role since the solubilities of toltrazuril in the solvents at RT and at 6 °C were not determined. To investigate the outcome of crystallisation when using cooling as the method to obtain supersaturation, further experiments were carried out. In these experiments, the API was added stepwise to the boiling solvent. After each addition, dissolution of the API was awaited. When undissolved parts remained for 30 min, a small amount of solvent was added to just dissolve the API. This way, a solution near saturation was obtained. Then, the oil bath used to heat the mixture was removed and the solution being left in the round bottom flask was allowed to cool to RT. To apply a second cooling rate, another solution was prepared in the same manner as described above. This solution was cooled to RT by replacing the oil bath by an ice-water bath. In both cases, the reflux condenser sitting on top of the round bottom flask that contained the solution was sealed to avoid evaporation during the cooling process. The obtained crystals were rapidly harvested to prevent solution-mediated transformation and dried over night at ambient conditions. The results of the crystallisation experiments are given in Table 11.

Table 11 Crystal forms of toltrazuril obtained when cooling boiling solutions near saturation using different cooling rates

	Cooling of hot solution (near saturation) at RT, round bottom flask	Cooling of hot solution (near saturation) in an ice-water bath, round bottom flask
Acetone	B	B
Acetonitrile	B	B
Ethyl acetate	B	B
Ethanol	B	B
Isobutanol	B + D	D
Methanol	B	B
Toluol	D	D

Table 11 shows that similar to the previous experiments, the forms B and D are found. While pure form B is obtained in acetone, acetonitrile, ethyl acetate, ethanol and methanol, the form D crystallises in isobutanol and toluol. Except for isobutanol, slow and fast cooling result in the same form. This indicates that the solvent is the decisive factor in the crystallisation outcome. Isobutanol and toluol have considerably higher boiling points compared to the other solvents used. The boiling points are 108 °C and 111 °C, respectively. Hence, the temperature difference between the boiling point and the final temperature of cooling (RT) is larger for isobutanol and toluol. Consequently, cooling the boiling solution to RT results in a higher degree of supersaturation in these two solvents compared to the other solvents. The fact that

the form D is only observed when having a high degree of supersaturation provides further indication that the form is less stable than form B at RT (McCrone, 1965).
A solid form screening should also include crystallisation from water or from water-organic solvent mixtures in order to search for hydrates. Pure water is used in case of an adequate solubility of the API. The solubility of toltrazuril in water is pH-dependent. At an acidic, neutral or slightly alkaline pH-value, the solubility is below 1 $g*l^{-1}$ (0.1 % ($m*V^{-1}$)) (shown in preliminary tests). In a more strongly alkaline medium, the solubility considerably rises due to the deprotonation of the imide-structure (2.5.2). However, the molecule rapidly decomposes in alkaline water (opening of the triazinon ring). Hence, alkaline water was not selected for crystallisation experiments. Instead, acetone-water 1:1 ($V*V^{-1}$) was chosen. The same crystallisation experiments as described for the other solvents were conducted. However, a toltrazuril concentration of 0.5 % ($m*V^{-1}$) was used instead of 2 % ($m*V^{-1}$), since the API did not completely dissolve at the boiling point of the solvent mixture when having a concentration of 2 % ($m*V^{-1}$). In every crystallisation experiment, form B is produced.

4.2.2.2 Crystallisation from the melt

Toltrazuril form B was melted in a drying oven and cooled at room temperature (quench cooling). The amorphous form obtained was heated in a differential scanning calorimeter to induce crystallisation. The heating rates applied were 20 $°C*min^{-1}$, 5 $°C*min^{-1}$ and 1 $°C*min^{-1}$. In each case, crystallisation results in a mixture of the forms C and D (4.2.3.1.1). In addition, differential scanning calorimetry (DSC) was used to melt, cool and remelt toltrazuril (cyclic measurements). Toltrazuril form B was melted using a heating rate of 20 $°C*min^{-1}$. The melt was cooled down using both a fast cooling rate (20 $°C*min^{-1}$ down to -20 °C) and a slow cooling rate (2 $°C*min^{-1}$ down to 50 °C). The sample was then reheated with 20 $°C*min^{-1}$, 10 $°C*min^{-1}$ or 2 $°C*min^{-1}$. Crystallisation occurs during the cooling process (slow cooling rate) or in the reheating phase (fast cooling rate). However, crystallisation does not result in any new solid form, only the forms D, C and B are observed to melt. The use of another starting material (form D obtained from toluol, 4.2.2.1) does not affect the crystallisation outcome.
Additionally, crystallisation was induced at isothermal conditions (annealing). A Kofler hot bench was used to melt toltrazuril form B and to temper the molten film at different temperature ranges. The temperature ranges chosen were 165 °C to 155 °C, 135 °C to 145 °C and 115 °C to 125 °C. Within a few hours, crystallisation occurs at all temperature ranges. A mixture of the forms C and D is found in the ranges from 135 °C to 145 °C and 115 °C to 125 °C. In the range from 165 °C to 155 °C, form B is obtained. This finding is contradictory to the crystallisation outcome in the previous solid form screening (2.5.2). In the former screening, form C was obtained when tempering a molten film at this temperature range using a Kofler hot bench. Possible reasons for the different crystallisation results might be slight

differences in the temperature range and in the duration of annealing (solid-solid transformation might have occurred).

4.2.2.3 Solid-solid transformation

Pure form C is produced by solid-solid transformation of form D. Transition is induced by keeping form D at 175 °C for a few minutes in a drying oven. Furthermore, pure form C is generated by heating amorphous toltrazuril up to 178 °C at 20 °C*min^{-1} using DSC. As described in section 4.2.2.2, a mixture of the forms C and D crystallises upon heating. However, the crystals of form D transform into form C when heating is continued resulting in pure form C (4.2.3.1.1).

4.2.3 Characterisation of solid forms

4.2.3.1 Thermal analysis

4.2.3.1.1 DSC and TGA

The solid forms found in the solid form screening (the crystalline forms B, C, D and the amorphous form) were investigated using DSC. In case of form D, some batches behave differently upon heating which might be explained by differences regarding impurities or defective sites, for example. The DSC curves of the form D presented in this chapter correspond to the batch that was produced by evaporating a hot toluol solution in a crystallising dish (4.2.2.1). This batch was chosen due to the high information content of its DSC curves. Regarding the other forms, representative DSC curves are given. Fig. 33 shows the curves of the different forms obtained at 20 °C*min^{-1}.

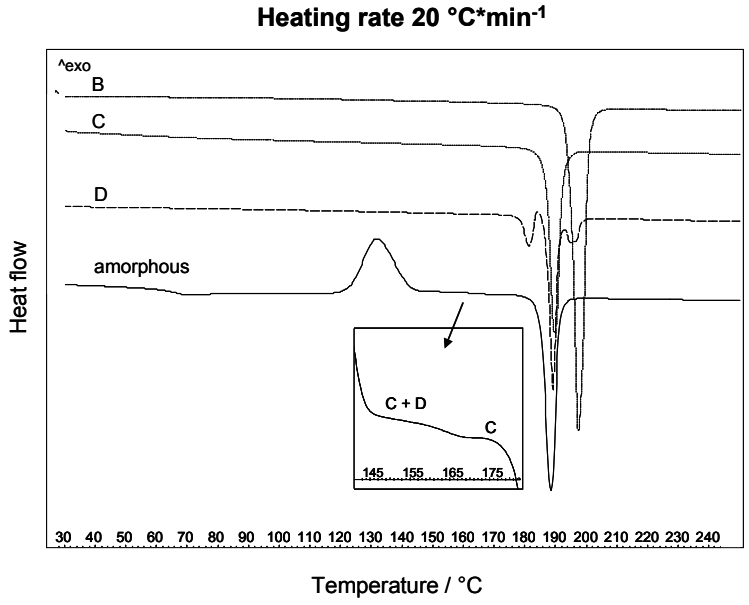

Fig. 33. DSC curves of the different solid forms of toltrazuril at a heating rate of 20 °C*min^{-1}.

For the forms B and C, a single endothermic peak is observed at 195 °C (form B) respectively 188 °C (form C) corresponding to the melting of the respective form. By contrast, form D shows an endothermic peak at 181 °C followed by a small exothermic event at 184 °C and two endothermic peaks at 188 °C and 195 °C. The first endothermic peak and the following exothermic event might correspond to the melting of the form D and the recrystallisation of the forms C and B from the melt. The subsequent endothermic peaks represent the melting of the forms C and B. The suggested recrystallisation of the forms C and B from the melt indicates that both forms do not represent solvates but modifications of toltrazuril (one-component systems, 2.1.2.1.1). To verify this assumption, thermogravimetric analysis (TGA) was performed. The TGA curves of the forms D, C and B do not show any mass loss up to 200 °C (data not shown). Hence, the three forms are modifications (mod.), i.e. they represent one-component systems of toltrazuril with different crystal structures.
When heating the amorphous form with 20 °C*min^{-1}, a glass transition is observed at 61 °C followed by a crystallisation peak at 132 °C (Fig. 33). Analysing the sample after the crystallisation peak using FT-IR spectroscopy reveals that a mixture of the mod. C and D has formed. Upon further heating, a small endothermic peak is observed at 168 °C. After this peak, pure form C is present (shown by FT-IR spectroscopy). Hence, the small endotherm corresponds to the solid-solid transformation of the existing crystals of mod. D into crystals of mod. C. The endothermic peak observed at 187 °C represents the melting of the mod. C. Fig. 34 shows the influence of a lower heating rate (5 °C*min^{-1}) on the DSC curves of the different forms.

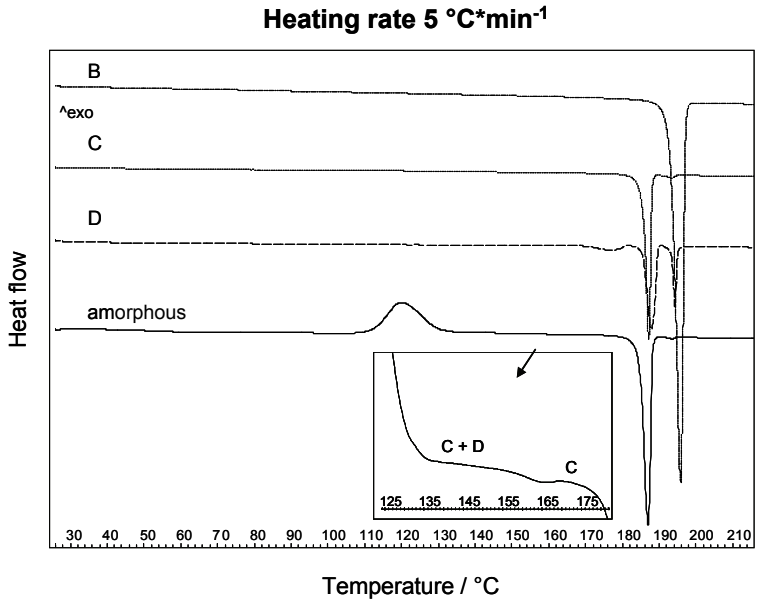

Fig. 34. DSC curves of the different solid forms of toltrazuril at a heating rate of 5 °C*min^{-1}.

The DSC curve of mod. B remains unchanged displaying the melting of the form at 195 °C. Regarding mod. C, an additional weak endotherm at 193 °C emerges

indicating the melting of a few crystals of form B that recrystallised from the melt. In case of mod. D, the onset and the shape of the first endotherm are affected by the change in the heating rate. Compared to the higher heating rate, the endotherm is broader and starts earlier. The observation indicates a solid-solid transformation of some crystals of mod. D into crystals of mod. C (and possibly mod. B) overlapping with the melting of mod. D and the recrystallisation of mod. C (and possibly mod. B) from the melt. A further change in the DSC curve is the presence of an additional small exothermic peak at 191 °C indicating that the melting of the form C overlaps with the recrystallisation of the form B from the melt. Regarding the amorphous form, crystallisation is shifted to lower temperatures with decreasing heating rate (peak at 120 °C). Crystallisation again results in a mixture of the mod. C and D (confirmed by FT-IR spectroscopy). Similar to the higher heating rate, the crystals of form D transform into form C when further heating the sample represented by the small endothermic event at 164 °C. The pure mod. C present after the endotherm (again verified by FT-IR spectroscopy) melts at 186 °C. As it was the case when heating mod. C, a small endotherm is present at 194 °C indicating the melting of a few crystals of mod. B that recrystallised from the melt. The DSC curve of form B still remains unchanged when further decreasing the heating rate to 1 °C*min^{-1} (Fig. 35).

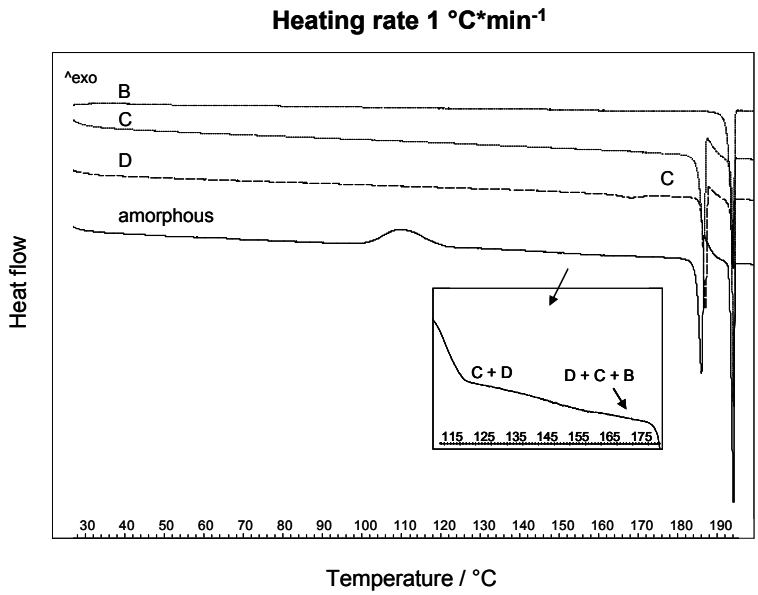

Fig. 35. DSC curves of the different solid forms of toltrazuril at a heating rate of 1 °C*min^{-1}.

Regarding mod. C, the exothermic peak at 187 °C and the clearly visible endothermic peak at 194 °C reveal that the amount of mod. B that recrystallises from the melt increases with further decrease of the heating rate. In case of mod. D, the slow heating rate results in a complete transformation into mod. C (confirmed by FT-IR analysis) represented by the small endotherm at 168 °C. The form C produced melts at 187 °C followed by the recrystallisation and melting of form B. For the amorphous form, the further decrease of the heating rate further lowers the temperature of

crystallisation (crystallisation peak at 110 °C). Similar to the higher heating rates, crystallisation leads to a mixture of the forms C and D shown by FT-IR analysis. However, in opposition to the DSC curves obtained at 5 °C*min^{-1} and 20 °C*min^{-1}, a distinct small endotherm is not observed when further heating the sample. FT-IR analysis of the sample at 170 °C reveals a mixture of the mod. C, D and B. The occurrence of mod. B indicates the continuous transformation of crystals of mod. D (and possibly mod. C) into mod. B upon heating. This continuous process is not visible in the DSC curve since it presumably disappears in the baseline. It is assumed that mod. D completely transforms into mod. B and / or mod. C before the melting point of mod. D is reached resulting in a mixture of the mod. C and B. Both forms melt at their melting points.

While mod. B is observed to melt homogeneously (i.e. no overlapping with other thermal events such as recrystallisation) at all three heating rates used, the homogeneous melting of mod. C only occurs at 20 °C*min^{-1} (Fig. 33). Therefore, the onset of melting, the enthalpy of fusion (ΔH_f) and the entropy of fusion (ΔS_f) of the two mod. were determined from the DSC curves obtained at 20 °C*min^{-1} (Table 12).

Table 12 Thermal quantities ($\bar{x}$ ± s, n = 3) of the crystalline forms of toltrazuril obtained from DSC measurements at 20 °C*min^{-1} (melting point, enthalpy of fusion, entropy of fusion) and 1 °C*min^{-1} (enthalpy of transition)

	Mod. D	Mod. C	Mod. B
Melting point [°C], DSC onset	177.7 ± 0.21	184.4 ± 0.10	193.2 ± 0.21
Enthalpy of fusion[a] [kJ*mol^{-1}]	35.5	31.7 ± 0.22	45.6 ± 0.82
Entropy of fusion[b] [J*mol^{-1}*K^{-1}]	78.9	69.4 ± 0.47	98 ± 1.8
Enthalpy of transition [kJ*mol^{-1}] into form C, DSC onset ranged from 163 °C to 167 °C	3.8 ± 0.06 (D into C)		

[a]the enthalpy of fusion of form D was estimated using the heat-of-transition rule
[b]the entropy of fusion of form D was calculated using the estimated value for the enthalpy of fusion

Compared to mod. C, mod. B has both the higher melting point and the higher enthalpy and entropy of fusion. Consequently, mod. C and B are monotropic according to the heat-of-fusion rule and the entropy-of-fusion rule (2.1.2.1.3) with mod. B being the more stable form across the entire temperature range (from absolute zero up to the melting point of form B). For mod. D, the melting point (onset) could be determined from the DSC curve at 20 °C*min^{-1} (Table 12). Its melting point is below the melting points of the mod. C and B. The heat of fusion however was not measurable due to the simultaneous recrystallisation from the melt (Fig. 33). To investigate whether the recrystallisation may be avoided by rapidly heating the sample, a heating rate of 80 °C*min^{-1} was applied (Fig. 36).

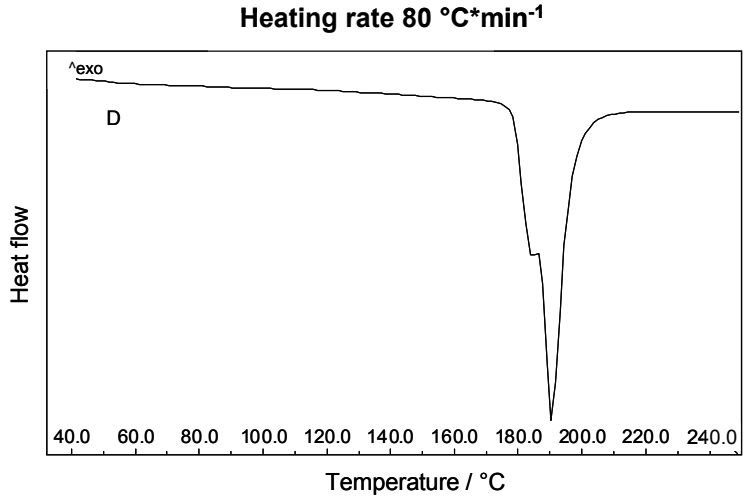

Fig. 36. DSC curve of form D of toltrazuril at a heating rate of 80 °C*min^{-1}.

At 80 °C*min^{-1}, the melting of mod. D is found to overlap with the melting of mod. C indicating a simultaneous melting / recrystallisation process despite the fast heating rate used. Other batches of mod. D were studied as well, but in none of the cases, homogeneous melting was observed. However, since the melting points of the forms D (177.7 °C ± 0.21 °C) and C (184.4 °C ± 0.10 °C) are close together and not too far apart (<30 °C) from the temperature at which the transition of mod. D into mod. C is observed (onset of transition ranges from 163 °C to 167 °C, 1 °C*min^{-1}), the enthalpy of fusion of mod. D may be estimated using the heat-of-fusion rule (Grunenberg *et al.*, 1996). The enthalpy of fusion was calculated by adding the enthalpy of transition into form C (Table 12) to the enthalpy of fusion of form C. The obtained enthalpy of fusion of mod. D was used to calculate the entropy of fusion (Table 12). Since the enthalpy curves of two modifications diverge with temperature (2.1.2.1.2), the calculated data ($\Delta H_{f,D}$ = 35.5 kJ*mol^{-1} and $\Delta S_{f,D}$ = 78.9 J*mol^{-1}*K^{-1}) represent only estimates. However, because the estimated values are well below the experimentally determined values for mod. B ($\Delta H_{f,B}$ = 45.6 kJ*mol^{-1} ± 0.82 kJ*mol^{-1} and $\Delta S_{f,B}$ = 98 J*mol^{-1}*K^{-1} ± 1.8 J*mol^{-1}*K^{-1}), it is suitable to apply the heat-of-fusion and the entropy-of-fusion rule. According to both rules, the mod. D and B have a monotropic relationship (form B more stable). Comparing the enthalpy and entropy of fusion of the mod. C and D, form D shows higher values in both cases ($\Delta H_{f,D}$ = 35.5 kJ*mol^{-1} versus $\Delta H_{f,C}$ = 31.7 kJ*mol^{-1} ± 0.22 kJ*mol^{-1} and $\Delta S_{f,D}$ = 78.9 J*mol^{-1}*K^{-1} versus $\Delta S_{f,C}$ = 69.4 J*mol^{-1}*K^{-1} ± 0.47 J*mol^{-1}*K^{-1}). While the values for the enthalpy of fusion are relatively close together, the estimated entropy of fusion of mod. D is well above the corresponding value of mod. C. Hence, it is suitable to at least apply the entropy-of-fusion rule. Since mod. D has the lower melting point but the higher entropy of fusion, the rule indicates that mod. D and C are enantiotropic. The endothermic transition observed for mod. D into mod. C is consistent with the enantiotropic relationship suggested (heat-of-transition rule, 2.1.2.1.3). According to the heat-of-transition rule, the thermodynamic transition point

for both modifications is below the temperature at which the transition is measured, i.e. it is below 163 °C (DSC onset of transition).

4.2.3.1.2 Thermomicroscopy

The batch of form D whose DSC curves are described in section 4.2.3.1.1 was further investigated using thermomicroscopy in order to verify the results obtained from the DSC measurements. The sample was heated under the microscope at 5 °C*min^{-1} (Fig. 37).

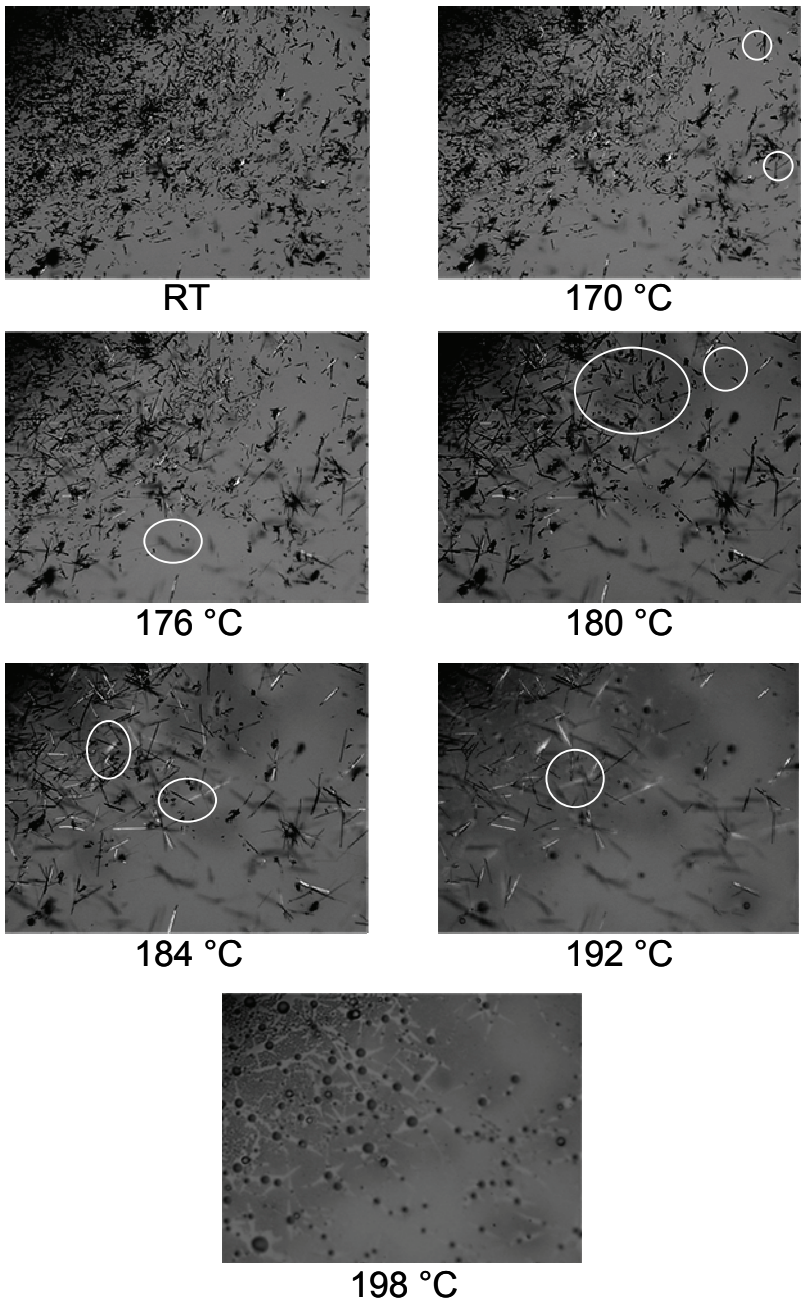

Fig. 37. Photomicrographs of mod. D of toltrazuril heated at a heating rate of 5 °C*min^{-1}; uncrossed polarisers; the diagonal of the photomicrographs is 1.1 mm.

Fig. 37 shows that the batch of mod. D consists of both very small crystals and bigger crystals shaped as needles (photomicrograph at RT). When heating the sample, the crystals of mod. D start to transform into long, needle-shaped crystals at 170 °C (highlighted in the photomicrograph). At 176 °C, quite a few newly formed crystals are present. Additionally, crystals have emerged that are out of focus (one of them is highlighted as example). These crystals are located on the coverslip showing that simultaneously to the transformation process, sublimation and subsequent recrystallisation on the coverslip occurs. At 180 °C, the remaining crystals of form D are molten. Some of the melt being visible as droplets is highlighted. Additionally, a grey shadow is faintly visible in the highlighted region. This shadow is more distinct at 184 °C. It is caused by droplets of the melt found on the coverslip. The droplets are formed by the evaporation of molecules from the melt followed by the condensation on the coverslip. Furthermore, new crystals are visible at 184 °C (some are highlighted) produced by the recrystallisation from the melt. Upon further heating, the crystals of form C formed by both solid-solid transformation and recrystallisation are observed to melt. After the melting of form C, quite a few crystals remain (photomicrograph at 192 °C). In addition, new crystals have emerged (one is highlighted) due to recrystallisation. All crystals melt in the melting range of mod. B. The photomicrograph at 198 °C shows the melt present after the melting process. To summarise, thermomicroscopic investigations show the transition into crystals of the mod. C and B, the melting of the crystals of mod. D that did not transform, the recrystallisation of both forms C and B, the melting of the crystals of mod. C, the recrystallisation of crystals of mod. B and the melting of mod. B. These findings are in accordance with the DSC curve obtained at the same heating rate (4.2.3.1.1). Additionally, the sublimation of crystals of mod. D and the evaporation of molecules from the melt are observed under the microscope. The fact that both events are clearly visible might suggest a substantial vapour pressure of mod. D and of the melt. The processes are not visible in the DSC trace, since they represent processes that continuously rise with temperature and therefore are hidden in the baseline of the DSC curve.

The batch of form D was also examined using 1 °C *min^{-1}. In the range from 160 °C to 176 °C, solid-solid transformation of the crystals of form D into long, needle-shaped crystals occurs. Fig. 38 shows a photomicrograph at the beginning of transformation (162 °C), during the transformation (166 °C) and at the end of the process (176 °C).

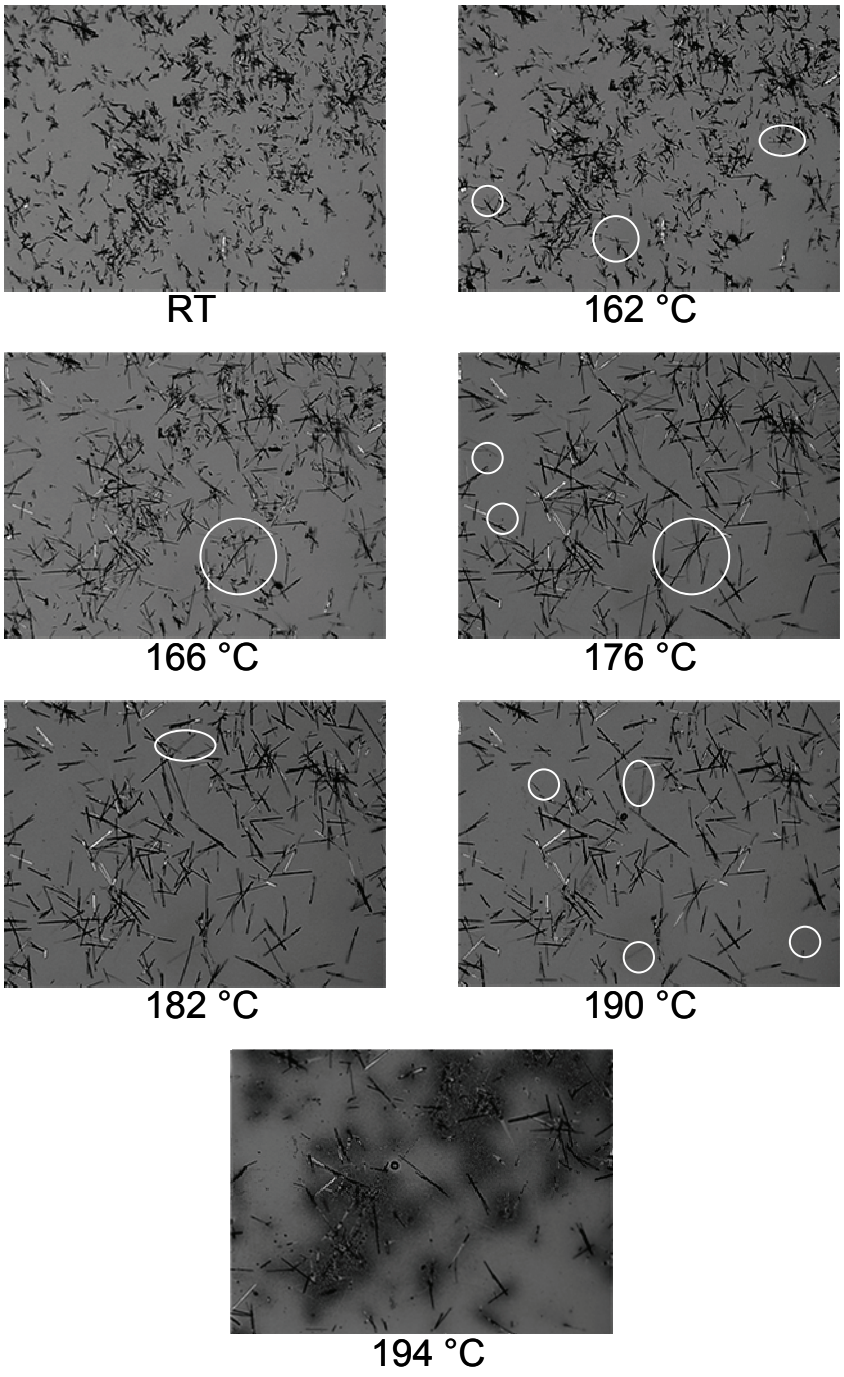

Fig. 38. Photomicrographs of mod. D of toltrazuril heated at a heating rate of 1 °C*min^{-1}; uncrossed polarisers; the diagonal of the photomicrographs is 1.1 mm.

For some crystals of mod. D, the new crystalline form seems to grow out of the existing crystals (examples are highlighted in the photomicrograph at 162 °C). The crystals of mod. D in the vicinity of the newly emerging crystals seem to vanish while at the same time the new crystals grow (one example is highlighted in the photomicrographs at 166 °C and 176 °C). The latter observation might suggest an intermediate “vaporised” state of the molecules (Byrn *et al.*, 1999c). The way how the crystals are observed to transform is in accordance with the transition viewed at 5 °C *min^{-1}. Very few crystals of form D do not transform, but melt at the beginning of

the melting range of form D (176 °C, two examples for droplets of melt are encircled). When further heating the sample, the first of the newly formed crystals vanish at 182 °C (one example is encircled) indicating the onset of melting of mod. C. At the end of the melting range of mod. C (190 °C), some crystals have disappeared (highlighted); however, quite a few crystals are still present. In addition, some new crystals have formed from the melt (one is encircled). All crystals melt in the melting range of mod. B shown in the last photomicrograph (194 °C). As already observed at 5 °C*min^{-1}, the melting is accompanied by the formation of shadows caused by the evaporation of the melt and the subsequent condensation on the coverslip. The observation that crystals melt in the melting range of mod. B reveals that mod. D transforms into crystals of both mod. C and B. In opposition to that, complete transition into mod. C is observed when heating the batch at 1 °C*min^{-1} using DSC (4.2.3.1.1). However, the different behaviour in the differential scanning calorimeter compared to the behaviour on the hot-stage microscope is not regarded as unusual, since conditions differ in both systems. While a small amount of crystals spread out on a slide is heated when performing thermomicroscopy, several milligrams of closely packed crystals are thermally treated in a differential scanning calorimeter. Hence, there might be differences such as discrepancies in the heat conduction which may lead to differences in the thermal behaviour of the sample.

4.2.3.2 Spectroscopy and X-ray diffraction

Fig. 39 displays the FT-Raman spectra of mod. B, C, D and the amorphous form. The spectrum of mod. B noticeably differs from the spectra of the other forms. On the contrary, the spectra of the mod. C and D show relatively small differences, for example in the region from 3100 cm^{-1} to 3000 cm^{-1}, 800 cm^{-1} to 700 cm^{-1} and 200 cm^{-1} to 20 cm^{-1}. In the spectrum of the amorphous form, bands are broader and reduced in number compared to the bands present in the spectra of the crystalline forms. This observation is characteristic of amorphous substances (Heinz *et al.*, 2007).

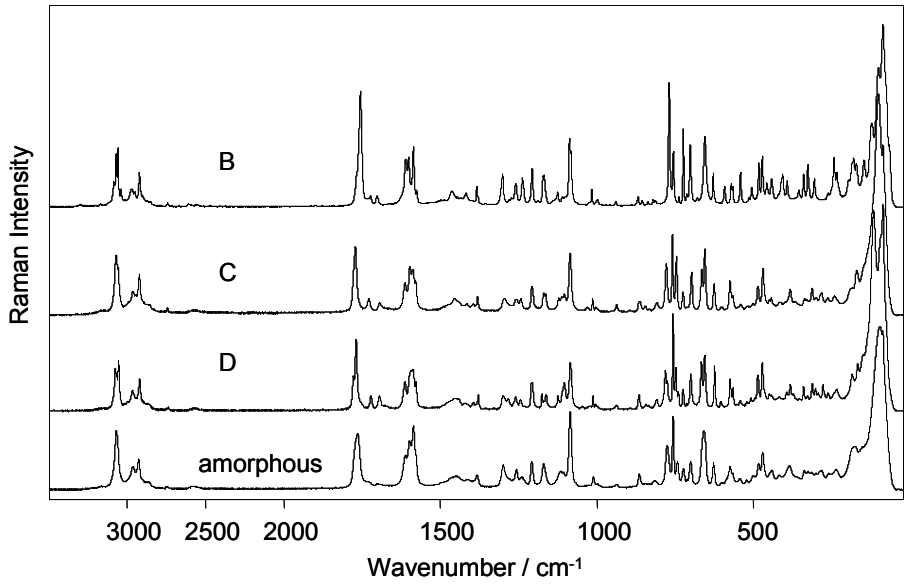

Fig. 39. FT-Raman spectra of the different solid forms of toltrazuril recorded at ambient conditions.

In accordance with FT-Raman spectroscopy, similar FT-IR spectra are found for mod. C and D while the spectrum of mod. B considerably differs (Fig. 40). Nevertheless, differences present in the spectra of mod. C and D allow for the differentiation between both forms. For example, mod. D shows a band at 1733 cm^{-1} that is absent in the spectrum of mod. C. Similar to FT-Raman spectroscopy, the bands observed in the spectrum of the amorphous form are broader compared to the spectra of the crystalline forms.

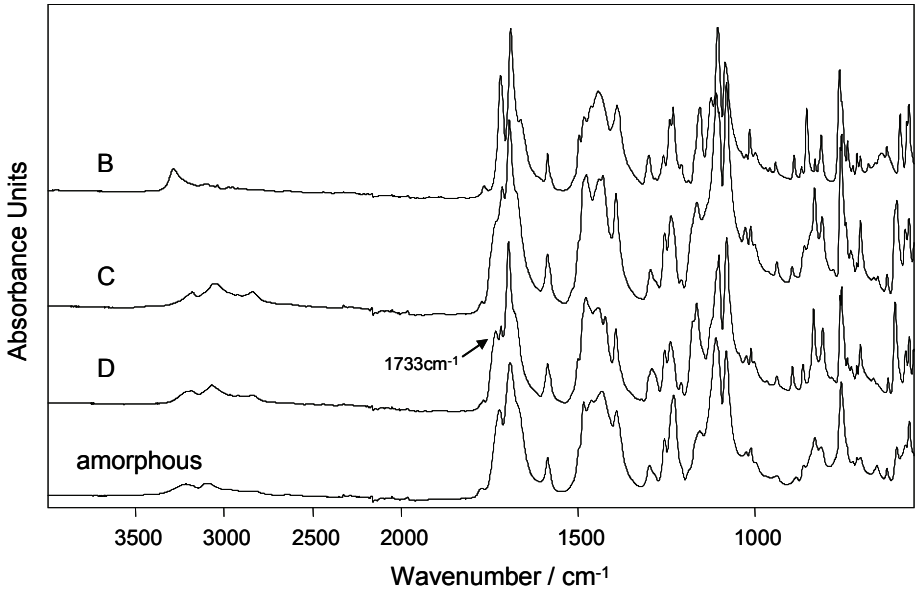

Fig. 40. FT-IR spectra of the different solid forms of toltrazuril recorded at ambient conditions.

The first absorption band present in the FT-IR spectra of the different forms is attributed to N-H stretching vibrations. The N-H stretching band of mod. B (3286 cm^{-1}) is found at a distinctly higher wavenumber than the N-H stretching bands

of the mod. C (3182 cm^{-1}) and D (3210 cm^{-1}). According to the infrared rule (2.1.2.1.3), mod. B is therefore less stable at absolute zero compared to the mod. C and D. The rule contradicts the results from thermal analysis (4.2.3.1.1). However, this finding is not unexpected, since Burger et. al (Burger and Ramberger, 1979b) found out that compounds having one or more CO-NH groups (such as toltrazuril, see molecular structure in section 2.5.2) represent exceptions to the infrared rule. Consequently, the infrared rule cannot be used in case of toltrazuril.

Summarising, both FT-Raman and FT-IR spectroscopy show differences in the spectra of all forms revealing the presence of different solid forms. To confirm that the forms B, C and D represent crystalline forms with different crystal structures, X-ray powder diffraction (XRPD) was performed. The resulting XRPD patterns are given in Fig. 41.

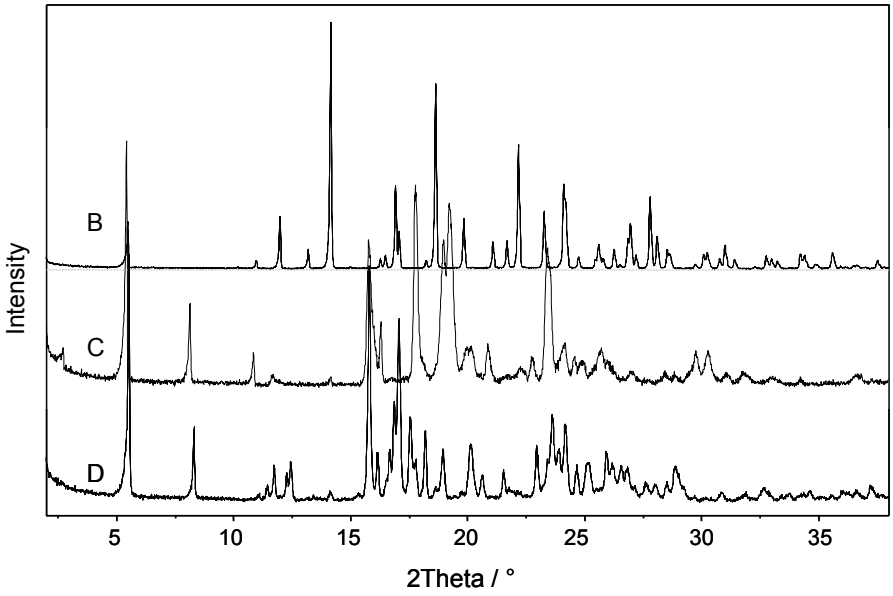

Fig. 41. XRPD patterns of the different crystalline forms of toltrazuril recorded at ambient conditions.

In accordance with FT-Raman and FT-IR spectroscopy, a characteristic XRPD pattern is found for each of the three modifications. Compared to the vibrational spectra of mod. C and D, differences are more pronounced in the diffractograms of the two forms, e.g. in the 2theta range from 15 ° to 20 °. Consequently, XRPD further demonstrates that the forms differ in their crystal structures.

4.2.3.3 Density measurements

For the mod. B, C and D, the densities determined using a helium pycnometer are 1.55 $g*cm^{-3}$, 1.46 $g*cm^{-3}$ and 1.47 $g*cm^{-3}$ (mean values out of five measurements). The measured densities have a standard error of ± 0.008 $g*cm^{-3}$ (derived from the measurement of test substances; see experimental part, section 6.2.2.6). Hence, the density of mod. B is significantly ($\alpha = 0.05$) higher than the densities of the mod. C and D. According to the density rule (2.1.2.1.3), the modification having the higher density is more stable at absolute zero. Consequently, the density rule is in

accordance with the heat-of-fusion and entropy-of-fusion rule that both suggest a monotropic relationship of the mod. D / B and C / B with B being the more stable form. The density rule cannot be applied for the mod. C and D as the densities of both forms do not differ significantly (α = 0.05).

4.2.3.4 Slurry conversion studies

According to the data obtained from DSC measurements, mod. D and C are enantiotropically related (4.2.3.1.1). In order to narrow the transition temperature range, slurry conversion studies were performed. Regarding mod. C, only a small amount of material was available. Hence, water was used for slurry experiments due to the low solubility of toltrazuril in this solvent. A 1:1 (m^*m^{-1}) mixture of the two mod. was prepared. The FT-IR and FT-Raman spectra of the mixture correspond approximately to the theoretical (computed) spectra of the mixture indicating that solid-solid transformation does not occur upon mixing. The mixture was suspended in water and kept under stirring at both RT and at 70 °C for 3 h before being analysed using FT-IR spectroscopy. Spectroscopic analysis reveals that the mixture stirred at RT has started to convert directly into mod. B whereas the mixture kept at 70 °C has already nearly completely transformed into mod. B. Due to the direct transition into mod. B, slurry conversion experiments are not suitable to narrow the transition temperature range for the D / C pair of polymorphs. However, the results verify the monotropic relationship for the mod. D / B as well as the mod. C / B. Further slurry conversion studies were performed in order to search for the thermodynamically most stable solid form in different solvents and solvent mixtures. The aim was to look for both solvates (especially hydrates) and modifications that are more stable than mod. B. A mixture of the mod. D and B was stirred in acetonitrile, isobutanol, toluol, ethanol / water (1:1 (V^*V^{-1})) and water at RT for two weeks. In all cases, pure mod. B is obtained. Although this result indicates that mod. B is the most stable form in the systems investigated, the existence of solid forms being more stable than mod. B cannot be excluded.

4.2.3.5 Annealing studies

Since slurry conversion studies were unsuccessful to narrow the transition temperature range of the enantiotropically related mod. D and C (4.2.3.4), a mixture of the two mod. was tempered at different temperatures until (partial) conversion occurred. The mixture was annealed at 65 °C, 85 °C, 100 °C and 125 °C using a drying oven. At 65 °C and 85 °C, a partial conversion of mod. C into mod. D is observed after 6 days and 3 days, respectively. At 100 °C and 125 °C, the mixture directly transforms into mod. B. The transformation of crystals of mod. C into crystals of mod. D at 65 °C and 85 °C reveals that mod. D is the more stable form up to at least 85 °C. As described in section 4.2.3.1.1, DSC measurements show a transition of mod. D into mod. C at a temperature of 163 °C or higher revealing mod. C to be more stable in the temperature range from 163 °C up to the melting point of mod. C.

Consequently, the thermodynamic transition point is between 85 °C and 163 °C. To further narrow the transition temperature range, additional annealing studies were performed at 90 °C and 95 °C. At both temperatures, the partial conversion of mod. C into mod. D. is observed after a few hours (90 °C) and 1 h (95 °C), respectively. Hence, the transition temperature is between 95 °C and 163 °C.

4.2.3.6 Perfusion calorimetry

The experimental determination of the heat of transition from DSC measurements only succeeded for the D / C pair of polymorphs (4.2.3.1.1). Therefore, it was investigated whether perfusion calorimetry is suitable to measure the enthalpies of transition for the mod. D / B ($\Delta H_{t,D\rightarrow B}$) and C / B ($\Delta H_{t,C\rightarrow B}$). Since both pairs of polymorphs are monotropic, an exothermic transition into mod. B is expected. Transformation does not occur when storing mixtures of the mod. D / B and C / B, respectively, at ambient conditions for several weeks. However, fast transition (within hours) may be observed when subjecting mod. C and D, respectively, to a high relative vapour pressure of solvent (RVP_{Solv}) using perfusion calorimetry, since the exposition to a high RVP_{Solv} has shown to facilitate polymorphic transitions (Griesser *et al.*, 2000; Urakami and Beezer, 2003; Vemuri *et al.*, 2004). Indeed, mod. C transforms completely into mod. B when being exposed to a high *RVP* of ethanol (RVP_{EtOH}) for 10 h at 25 °C. By contrast, mod. D does not transform when subjected to the same conditions. However, fast transformation into mod. B is observed when using a mixture of mod. D and B as sample. In the experiments performed, samples were first equilibrated at 0 % *RVP* (dry nitrogen) for 6 h before setting the *RVP* to 100 % (100 % RVP_{set}) for a period of 10 h. Previous testing of the vapour pressure control device in use has shown that 100 % RVP_{set} corresponds to an RVP_{EtOH} inside the reaction vessel (RVP_{in}) of 99.4 % ± 0.09 % (SE). Fig. 42 displays the heat flow curves obtained for mod. C and a 1:1 (m^*m^{-1}) mixture of D / B and the corresponding blank curve.

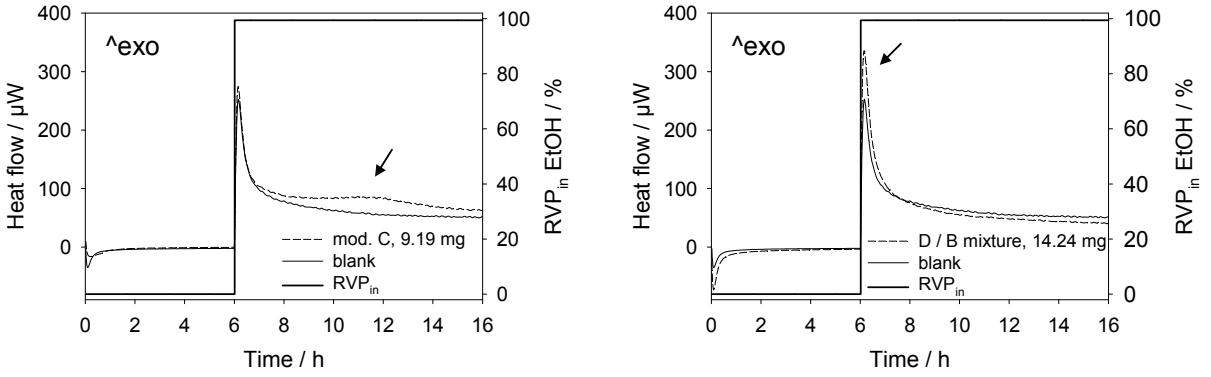

Fig. 42. Heat flow curves of mod. C (left) and a mixture of D / B (right) exposed to an RVP of ethanol of 99.4 % ± 0.09 % (SE) and blank curve (25 °C).

At 100 % RVP_{set}, mod. C first shows a small exothermic peak compared to the blank curve. After about 2 h, a broad exothermic event starts attributed to the

transformation into mod. B (marked in Fig. 42). The transition is confirmed by FT-IR and FT-Raman analysis of the sample after finishing the experiment. The small peak observed prior to the broad event may correspond to the adsorption of ethanol molecules to the crystal surface of mod. C. Contrary to mod. C, the D / B mixture shows a distinct exothermic peak compared to the blank when exposed to ethanol vapours indicating a rapid transformation of the crystals of mod. D into mod. B (peak marked in Fig. 42). FT-IR and FT-Raman analysis of the sample after the peak confirms complete conversion into mod. B. The higher transformation rate observed for mod. D in comparison to mod. C is explained by the fact that the sample represents a mixture prepared with the help of a mortar. Mixing mod. D with mod. B using a mortar ensures close contact between the crystals of both forms and increases the number of defects in the crystals thus facilitating the transformation process (Brittain, 2002). To investigate whether just the presence of mod. B is sufficient for transformation (acting as seed crystals) or whether mechanical activation is necessary, mod. D was exposed to ethanol vapours having a few crystals of mod. B (ratio of mod. D to mod. B was about 10 to 1) added into the sample vessel. The resulting sample curve only shows a small exothermic peak compared to the blank and FT-IR analysis of the sample after the measurement reveals that mod. D is still present. Consequently, mechanical activation is required for complete transformation. Mechanically treated samples show an exothermic heat flow within the first hours after treatment due to the dissipation of the energy introduced (Ziegenbalg, 2005). In order to prevent the heat flow from interfering with the measurement, the D / B mixture was stored for several days before recording.

To determine the heats of transition, $\Delta H_{t,D\rightarrow B}$ and $\Delta H_{t,C\rightarrow B}$, the areas under the curves were calculated after having subtracted the blank curve (regarding mod. C, the initial small peak was not used for integration). The values obtained for $\Delta H_{t,C\rightarrow B}$ and $\Delta H_{t,D\rightarrow B}$ are -13 kJ*mol^{-1} ± 1.1 kJ*mol^{-1} ($\bar{x}$ ± s, n = 3) and -9.0 kJ*mol^{-1} ± 0.79 kJ*mol^{-1} ($\bar{x}$ ± s, n = 3). They are in good agreement with the enthalpies of transition estimated from the DSC results ($\Delta H_{t,C\rightarrow B}$ = -13.9 kJ*mol^{-1}, $\Delta H_{t,D\rightarrow B}$ = -10.1 kJ*mol^{-1}). The estimated values were obtained by subtracting the enthalpy of fusion of mod. C and D, respectively, from the enthalpy of fusion of mod. B (Grunenberg *et al.*, 1996).

The approach used to determine the heats of transition assumes that the heat output measured is due only to the transition of mod. C and D, respectively, into mod. B. For the D / B mixture, however, it might be possible that the thermal activity associated with transition overlays with heat changes related to the adsorption of ethanol molecules to the crystal surfaces of both forms. Hence, the actual enthalpy of transition might be slightly lower than the value obtained. It also has to be taken into consideration that some crystals of mod. D might already have transformed into mod. B during the mixing process due to the energy introduced. In this case, the actual heat of transition for mod. D will be slightly higher than the value determined.

Compared to the enthalpies measured by DSC (4.2.3.1.1), the heats of transition obtained from perfusion calorimetry have higher coefficients of variation (about 9 %).

The reason is the substantial heat flow of the blank (Fig. 42) leading to a low signal (sample curve) to noise (blank curve) ratio. In order to illustrate that a major part of the thermal activity of the sample curve is caused by the perfusion of the vessel, i.e. corresponds to noise, the raw sample curves and the blank curve are presented in Fig. 42 instead of the sample curves obtained after the subtraction of the blank. The signal-to-noise ratio may be increased by using a high weight of sample. In the measurements, an amount of sample that just covers the bottom of the vessel was used (the weight of sample ranged from 11 mg to 15 mg) in order to have a maximum surface-to-volume ratio for the sample. In case of using a higher weight of sample, the sample would have formed a layer resulting in a lower surface-to-volume ratio. The reason to choose a high surface-to-volume ratio is to have a high transformation rate since the ethanol molecules are assumed to interact with toltrazuril molecules present at the crystal surfaces of the mod. C and D, respectively. The interaction leads to a loosening of intermolecular bonds in the crystals which facilitates the transformation into mod. B (2.2.2). Consequently, the transformation rate might be lower if using a higher weight of sample, since the ethanol molecules have to diffuse into the layer formed by the sample in order to interact with the surfaces of the crystals present in the layer. In case of a lower transformation rate, the signal-to-noise ratio would not improve considerably due to the broadening of the thermal event associated with transformation. Another possibility to increase the signal-to-noise ratio is to reduce the blank heat flow by using another solvent, e.g. water (4.1.3.2.2). However, transformation does not occur when exposing mod. C to high *RH* for 10 h using perfusion calorimetry (data not shown).
Summarising, perfusion calorimetry using ethanol as solvent enables the experimental determination of the enthalpies of transition for the mod. C / B and D / B, $\Delta H_{t,C\rightarrow B}$ and $\Delta H_{t,D\rightarrow B}$. The fact that mod. C, in contrast to mod. D, does not need any sample preparation in order to transform within a few hours is in agreement with the results from annealing studies (4.2.3.5) that suggest mod. D to be more stable at the operating temperature (25 °C). Regarding mod. D, a rapid transformation into mod. B is achieved when exposing a D / B mixture prepared in a mortar to ethanol vapours. The values determined for the enthalpies of transition are consistent with the values estimated from the results of DSC measurements. The relatively high coefficients of variation obtained for the heats of transition allow for method optimisation.

4.2.4 Summary of results

Summarising, the polymorph screening resulted in the three known modifications of toltrazuril named B, C and D. The fourth modification described in the previous polymorph screening (mod. A; section 2.5.2) was not obtained. However, as its existence was based solely on DSC measurements, it is questionable whether mod. A really exists. In addition to the crystalline forms, an amorphous form of toltrazuril was produced. The different solid forms of toltrazuril were thoroughly characterised

and the thermodynamic relationships between the mod. D, C and B were established. The relative thermodynamic relationships between the different modifications are summarised in a semi-schematic energy-temperature diagram (Fig. 43).

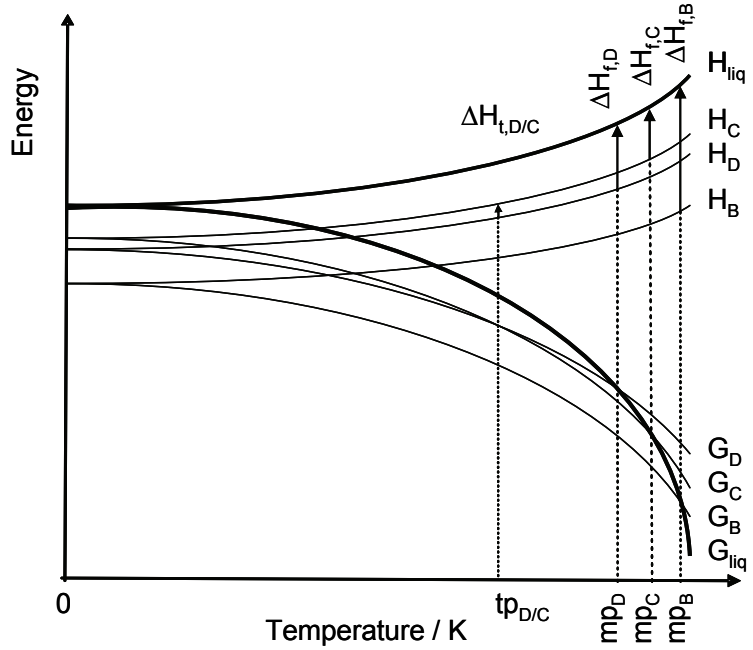

Fig. 43. Semi-schematic energy-temperature diagram of the three mod. D, C and B and the melt (liq) of toltrazuril; *H* enthalpy, *G* Gibbs energy, ΔH_f heat of fusion, ΔH_t heat of transition, tp transition point between D and C, mp melting point.

In the diagram, mod. B has the lowest Gibbs energy from absolute zero up to the melting point of mod. B, i.e. it is more stable than the mod. D and C across the entire temperature range. This conclusion is drawn from thermal analysis and density measurements. Thermal analysis data show the mod. D / B and C / B to be monotropically related with mod. B being the more stable form in both cases (heat-of-fusion rule, entropy-of-fusion rule). The higher density of mod. B compared to the densities of mod. C and D indicates mod. B to be more stable at absolute zero (density rule) which is in agreement with the monotropic relationships found. In addition, the transformation of both mod. C and D into mod. B observed in slurry conversion studies and in perfusion experiments confirms that D / B and C / B are monotropic. Regarding the C / D pair of polymorphs, thermal analysis reveals an enantiotropic relationship (entropy-of-fusion rule, heat-of-transition rule). Hence, the Gibbs curves of both forms intersect at the thermodynamic transition point (Fig. 43). Below the thermodynamic transition temperature, mod. D has the lower Gibbs energy being the more stable form whereas above the transition point, mod. C is more stable. While slurry conversion studies are not helpful to narrow the transition temperature range due to direct conversion into mod. B, annealing studies reveal mod. D to be the more stable form up to at least 95 °C. Combining this result with the findings from thermal analysis, the transition temperature has to be between 95 °C

and 163 °C. It was not possible to further narrow the temperature range as direct transition into mod. B occurs when annealing a D / C mixture at a temperature above 95 °C.

Using DSC and perfusion calorimetry, the transition enthalpies for the different pairs of modifications could be determined experimentally. For the mod. D / C, the heat of transition of mod. D into mod. C is 3.8 $kJ*mol^{-1}$ ± 0.06 $kJ*mol^{-1}$ (s, n = 3) (recorded with DSC at 163 °C). Regarding the mod. D / B and C / B, the enthalpies of transitions into mod. B could not be measured with DSC, however, it was possible to obtain the values at RT using perfusion calorimetry. The enthalpies of transition are -9.0 $kJ*mol^{-1}$ ± 0.79 $kJ*mol^{-1}$ ($\bar{x}$ ± s, n = 3) and -13 $kJ*mol^{-1}$ ± 1.1 $kJ*mol^{-1}$ ($\bar{x}$ ± s, n = 3) for D / B and C / B. The relatively small enthalpy of transition for the mod. D / C compared to the enthalpies of transition for D / B and C / B suggest similarities in the crystal structures of the mod. D and C. This assumption is in accordance with the fact that both forms show similar FT-Raman and FT-IR spectra.

4.3 Solid forms of emodepside

4.3.1 Preface

As outlined in section 2.5.1, the API emodepside exists in different solid forms. Four crystalline forms and an amorphous form have been described in the various patent applications. The patent application WO 99 / 24412 reveals that the crystalline forms noticeably differ in their water contents. In order to investigate the state of water in the different crystalline forms, thermal analysis, FT-IR, FT-Raman and FT-NIR spectroscopy, XRPD, vapour sorption measurements and single crystal structure analysis were performed.

4.3.2 Preparation of the solid forms

Regarding emodepside form I and II, batches of industrial production were used for investigations. The batch of form I was prepared by adding a hot (45 °C – 55 °C) ethyl acetate solution to hot (65 °C - 75 °C) diisopropyl ether whereas the batch of form II was formed by adding diisopropyl ether dropwise to a hot (65 °C) ethanol solution. For form II, a batch produced in laboratory scale was additionally used for studies. It was obtained by filtering off a boiling ethanol 96 % (V^*V^{-1}) solution (near saturation) into a crystallising dish at RT.
Form III crystallises from acetone as well as from isopropanol. The batches presented in this study were prepared by slurry phase conversion. For that purpose, form II of emodepside was suspended in either isopropanol (batch A) or acetone (batch B) at RT and stirred over night. Batch A was filtered off the next day whereas batch B was left undisturbed for 12 days before harvesting the crystals.
Form IV crystallises from methanol at various conditions. The batches A and B were used for investigations. Batch A was formed when stirring a suspension of form II of emodepside in methanol at RT over night. Batch B was prepared by cooling a hot (55 °C) filtered methanol solution (near saturation) at RT. Amorphous emodepside was produced by quench cooling the melt of form IV generated in a drying oven.
Regarding the preparation of the forms II and IV, the same procedure as used in the crystallisation of toltrazuril (4.2.2.1) was applied to obtain a solution near saturation. The crystals of the forms II to IV produced in laboratory scale were dried in vacuo at 45 °C over night. All forms of emodepside were stored at ambient conditions (45 % *RH* ± 15 % *RH*) unless otherwise stated until further required.

4.3.3 Characterisation of the solid forms

4.3.3.1 Thermal analysis

4.3.3.1.1 DSC and TGA

The different crystalline forms of emodepside were analysed with DSC applying a heating rate of 10 °C*min^{-1}. The resulting DSC traces are given in Fig. 44.

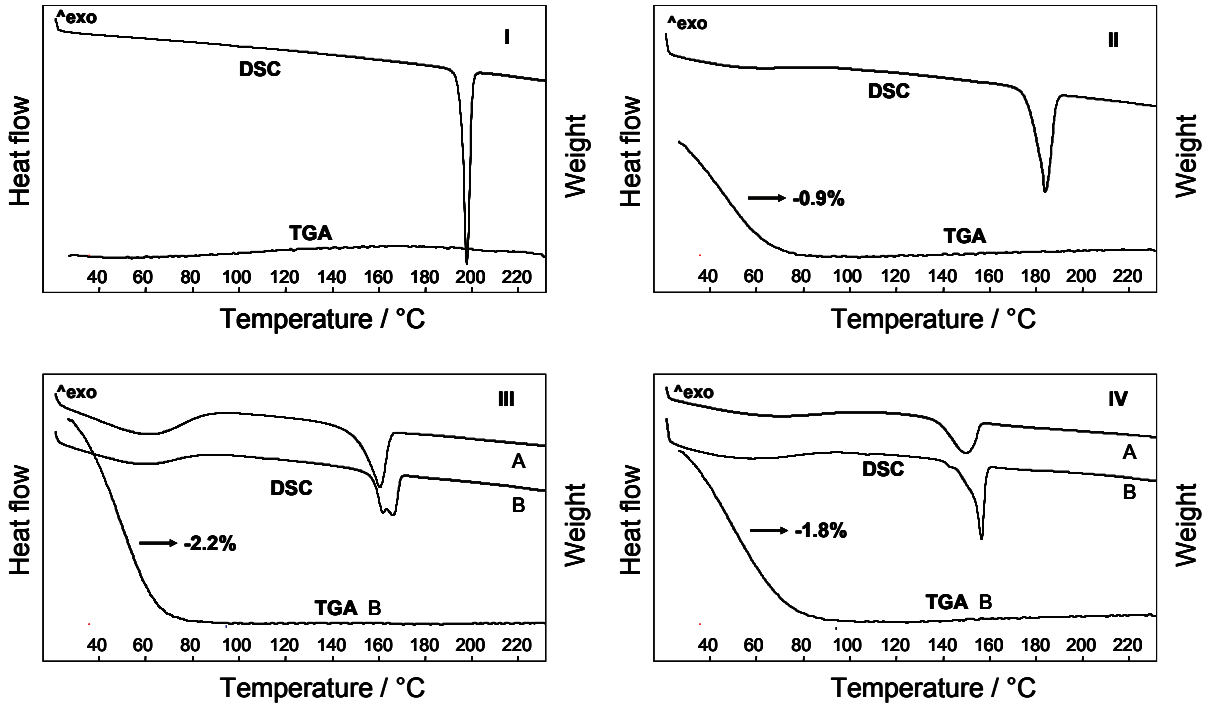

Fig. 44. DSC and TGA curves of the forms I-IV of emodepside at a heating rate of 10 °C*min^{-1}; IIIA and IIIB as well as IVA and IVB represent different batches obtained from different crystallisation procedures.

The DSC curve of form I shows a single endothermic peak corresponding to the melting of the sample. TGA reveals that the form does not exhibit any mass loss. Consequently, form I represents a modification of emodepside. Contrary to mod. I, the forms II-IV show two endothermic events. The first is observed below 100 °C having a broad shape. The endotherm is accompanied by a weight loss as revealed by TGA (Fig. 44). Evolved gas analysis using FT-IR spectroscopy (data not presented) reveals that the weight loss is due to the evaporation of water. The second endotherm represents the melting of the water-free forms II-IV.

Regarding the forms III and IV, the batches A and B differ in the shape and position of the melting peak (Fig. 44). There are also differences in the microscopical appearances of the batches (Fig. 47). The batches IIIA and IVA display agglomerates of small crystals whereas the batches IIIB and IVB represent mixtures of small crystals and crystals that are considerably bigger than the crystals present in IIIA and IVA. These big crystals are shaped like needles (IVB) and blades (IIIB), respectively. Contrarily to the differences in the DSC curves and in the microscopical appearances of the crystals, the different batches of form III (IV) display identical FT-IR spectra, FT-Raman spectra, FT-NIR spectra, powder diffractograms and TGA curves confirming that they represent the same crystal form at RT. Thermomicroscopic investigations and variable temperature FT-IR (VT FT-IR) spectroscopic analysis (data not shown) rule out the possibility that the non-uniform shape of the second endotherm of IIIB and IVB (Fig. 44) might be due to several events taking place (e.g. melting – crystallisation - melting) (data not shown). Additionally, high performance liquid chromatography reveals that the substance does not degrade during melting.

The differences in the melting behaviour might be explained by the differences in the crystal size and by the shapes of the crystals present in IIIB and IVB. Small crystals that agglomerate show better heat conduction thus melting at lower temperature than big needles or blades which have lower bulk densities and show only punctual contact. Therefore, the batches IIIB and IVB having both small crystals and big needles or blades exhibit a non-uniform melting peak. The explanation given represents a kinetic effect that should be eliminated when applying a lower heating rate. However, differences in the melting behaviour are still visible when reducing the heating rate to 1 °C*min^{-1} (data not shown). The reason for that might be that the heating rate chosen is still too high. But the result might also indicate that there is another reason for the variations in the DSC curves. Another possible explanation for the melting differences might be a higher amorphous content present in the batches IIIA and IVA in consequence of their production process. The batches IIIA and IVA were obtained by slurry phase conversion (4.3.2) which was observed as a sudden process that favours the formation of amorphous parts. Batch IIIB was also produced by slurry phase conversion however, the batch was left undisturbed for several days in its mother liquor allowing for the crystallisation of amorphous defect regions. The fact that the batches IIIA and IVA exhibit lower melting enthalpies compared to the batches IIIB and IVB (Table 13, differences significant, $\alpha = 0.05$) supports the assumption. The melting points and the enthalpies of fusion of mod. I and of the water-free forms II, III and IV are displayed in Table 13.

Table 13 Thermal quantities ($\bar{x}$ ± s, n = 3) of form I and of the water-free forms II, III and IV of emodepside obtained from DSC measurements at 10 °C*min^{-1}

	Form I	Form II	Form IIIA	Form IIIB	Form IVA	Form IVB
Melting point [°C], DSC onset	194.4 ± 0.2	178.1 ± 0.6	152.7 ± 0.9	153 ± 1.8	138.5 ± 0.1	152.5 ± 0.1
Enthalpy of fusion[a] [kJ*mol^{-1}]	65.6 ± 0.6	49.9 ± 0.7	40 ± 1.2	43.8 ± 0.4	35.6 ± 0.4	39.3 ± 0.5
Entropy of fusion[a] [J*mol^{-1}*K^{-1}]	140 ± 1.3	110 ± 1.5	94 ± 3.1	102.8 ± 0.9	87 ± 1.1	92 ± 1.1

[a] The weight of the samples of the forms II-IV used to calculate the enthalpy respectively the entropy of fusion was corrected to account for the mass loss occurring during the heating due to the evaporation of water; the amount of water sorbed by the respective form at 45 % *RH* (data taken from vapour sorption analysis) was substracted from the weight of the sample.

To confirm that the variations in the melting behaviour of the batches IIIA (IVA) and IIIB (IVB) are caused by differences in the amorphous content, ground samples of the batches IIIB and IVB (ground for 5 min using a mortar) were heated at 10 °C*min^{-1} using DSC. Grinding of the sample is expected to enhance amorphous content. The

DSC curves of the ground samples were compared with the thermograms of the untreated samples (Fig. 45).

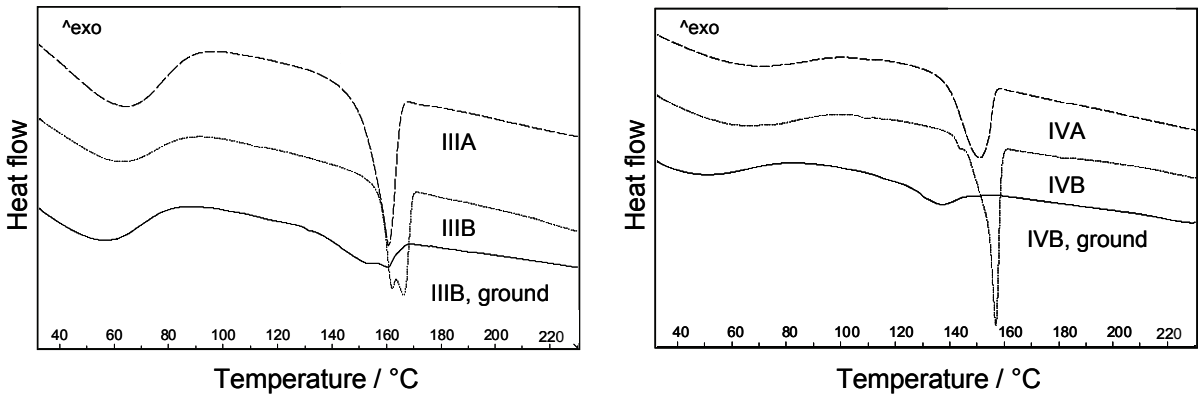

Fig. 45. Influence of grinding on the DSC traces of the batches IIIB and IVB.

The grinding of the batches IIIB and IVB lowers the melting temperature and affects the shape of the melting endotherm. The enthalpy of fusion is remarkably reduced to about 24 kJ*mol^{-1} for both batches indicating that grinding results in a considerable increase of the amorphous content. The FT-Raman spectra of the ground samples also suggest a decrease in crystallinity. Consequently, the results confirm that the differences observed in the melting behaviour of the batches IIIA (IVA) and IIIB (IVB) are due to differences in the amorphous content.

In addition to the crystalline forms of emodepside, amorphous emodepside obtained by quench cooling of the melt was investigated. Both its DSC and TGA curve are presented in Fig. 46.

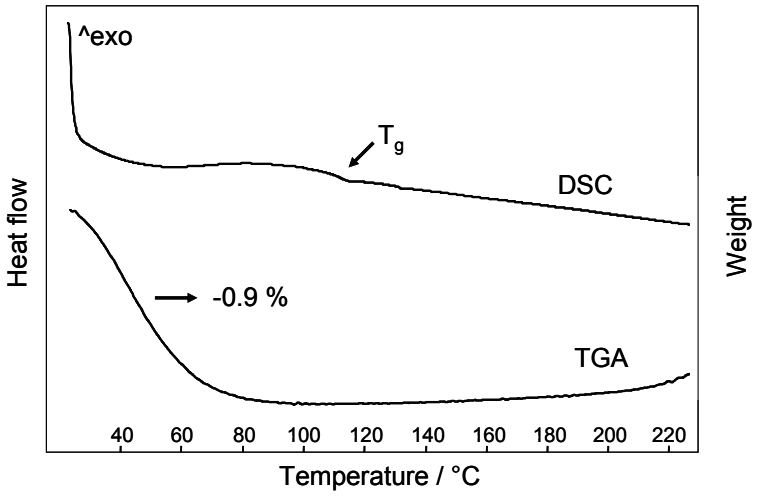

Fig. 46. DSC and TGA curves of amorphous emodepside at a heating rate of of 10 °C*min^{-1}.

Similar to the forms II-IV, amorphous emodepside shows a broad endotherm below 100 °C associated with a mass loss. The endothermic event is attributed to the evaporation of water sorbed by the amorphous form. The glass transition

temperature is found at 111 °C. Unlike the amorphous form of toltrazuril (4.2.3.1.1), crystallisation does not occur upon further heating.

To sum up, the DSC and TGA reveal that form I represents a modification of emodepside. Contrary to form I, the forms II-IV of emodepside are associated with considerable amounts of water that are readily lost upon heating. As seen in Fig. 44, the amounts of water lost by the forms II-IV are 0.9 %, 2.2 % and 1.8 %. As comparison, a monohydrate would contain 1.6 % water. The presence of considerable amounts of water suggests that the forms might represent non-stoichiometric hydrates. However, TGA and DSC are not suited to elucidate whether the forms are hydrates or modifications having water adsorbed to their crystal surfaces and / or absorbed into disordered defect regions. DSC reveals that the batches IIIA / IIIB and IVA / IVB differ in their melting behaviour. The differences are explained by a higher amorphous content present in the batches IIIA and IVA.

4.3.3.1.2 Thermomicroscopy

Thermomicroscopy was performed in order to investigate whether the loss of water causes any visible changes in the crystals of the forms II-IV. Each crystalline form of emodepside shows birefringence when examined in plane polarised light at RT (Fig. 47).

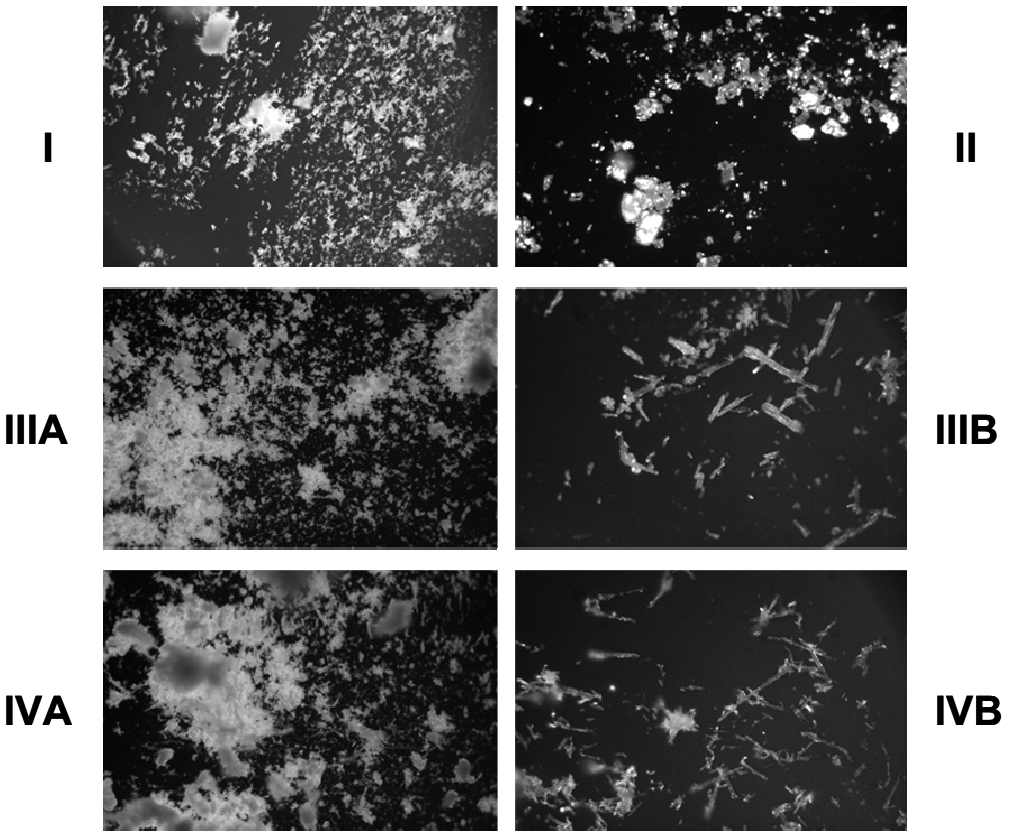

Fig. 47. Photomicrographs of the forms I-IV of emodepside viewed with plane polarised light; form III and IV: the batches A and B are presented; the diagonal of the photomicrographs is 1.2 mm.

Regarding the forms III and IV, both the batches A and B are presented. The forms were heated up to 120 °C to investigate whether the loss of water induces any visible changes in the crystals of the forms II-IV. During the heating, crystals of II and IVB are observed to “jump” which may be an indication for dehydration (Kofler, 1954). Although the jumping of the crystals might indicate that the examined crystals are hydrates, the missing of this phenomenon does not rule out the possibility that a hydrate is present. This is valid for the batch IVA as well as for form III. At 120 °C, the interference colours of the different forms are unchanged (data not presented) indicating that the three-dimensional packing of the crystals of the forms II-IV is not affected by the loss of the water molecules. Consequently, the forms II-IV are either modifications or hydrates forming isomorphic dehydrates.

4.3.3.2 Spectroscopy and powder X-ray diffraction

4.3.3.2.1 Ambient conditions

To further characterise the different solid forms of emodepside, spectroscopic analysis and XRPD at ambient conditions were performed. The FT-Raman spectra of the crystalline forms and the amorphous form are given in Fig. 48.

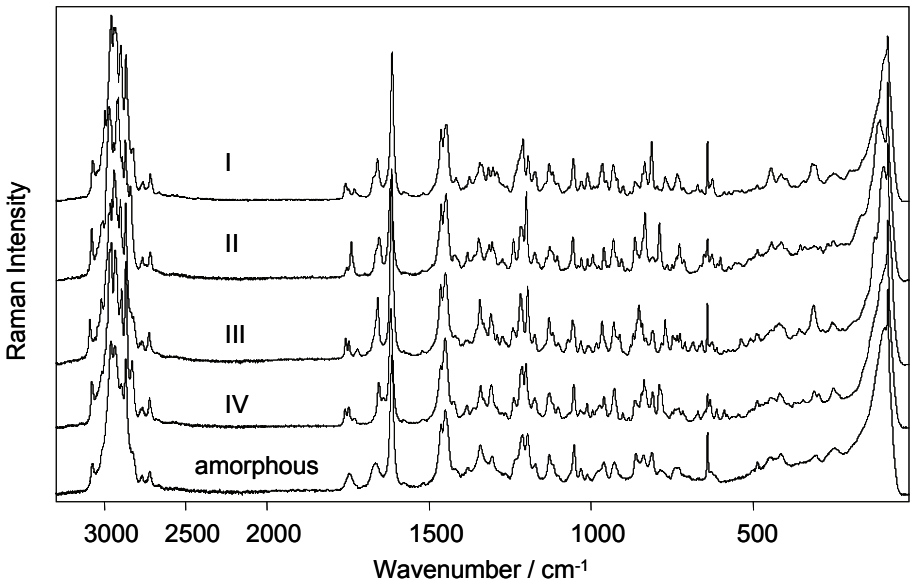

Fig. 48. FT-Raman spectra of the different solid forms of emodepside recorded at ambient conditions.

The spectra show significant differences over the entire range of the spectra. Fig. 48 reveals that the bands present in the spectrum of the amorphous form are broader compared to the bands of the crystalline forms which is in agreement with the disorder of the molecules of the amorphous form. Differences between the solid forms are also found in the FT-IR spectra (Fig. 49), although they are less striking.

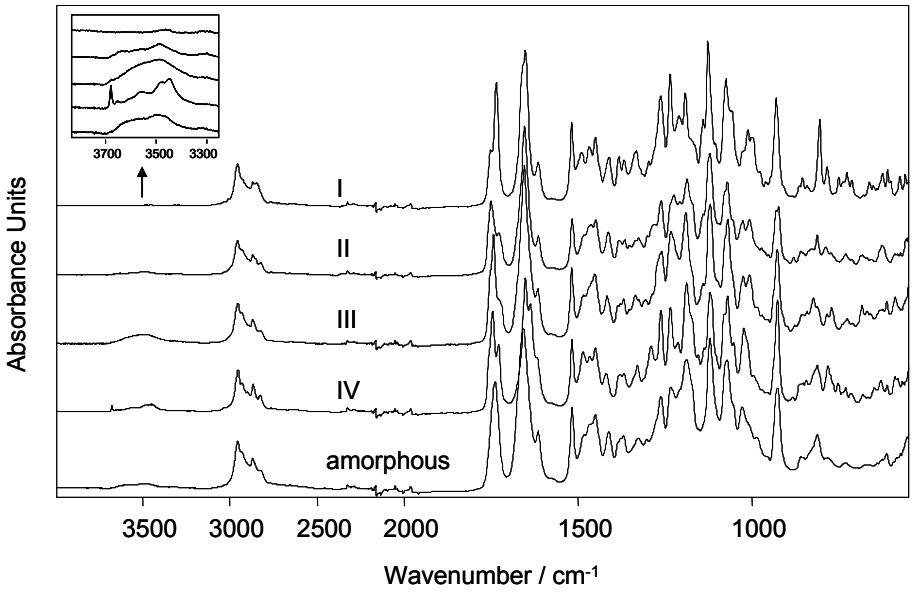

Fig. 49. FT-IR spectra of the different solid forms of emodepside recorded at ambient conditions.

Regarding the FT-IR spectra of the forms II-IV and the amorphous form, absorption bands of the associated water molecules are visible (OH stretching bands of water in the region of 3700 cm^{-1} to 3400 cm^{-1}). Form III exhibits a single broad OH stretching band centred at approximately 3484 cm^{-1}, whereas the forms II and IV have several overlapping OH stretching bands. The spectrum of form IV further shows a sharp OH stretching band at 3679 cm^{-1}. A broad OH stretching band as visible in the spectrum of form III indicates the presence of water molecules with differing energetic environment (Morris, 1999). These water molecules can be either adsorbed to the crystal surface (Morris, 1999) or disordered inside the crystal lattice (Redman-Furey *et al.*, 2005). In contrast to broad OH stretches, a sharp OH stretching band as seen in the spectrum of form IV is indicative of constrained water molecules present in the crystal lattice (Redman-Furey *et al.*, 2005). Consequently, FT-IR spectroscopy provides indication that form IV is a hydrate.

To further characterise the crystalline forms of emodepside, FT-NIR spectra and X-ray powder diffractograms were recorded (Fig. 50 and Fig. 51). The FT-NIR spectra (Fig. 50) of the forms display differences revealing that FT-NIR spectroscopy is also suitable to distinguish between the crystalline forms of emodepside. The intense absorption in the region between 1850 nm and 2000 nm present in the spectra of the forms II-IV is due to the combination of bending and anti-symmetric stretching modes ($\nu_2 + \nu_3$) of water (Maeda *et al.*, 1995). Hence, the water associated with the forms II-IV is visible in both the FT-IR and FT-NIR spectra. Fig. 51 shows that each form exhibits a unique diffraction pattern when analysed with XRPD.

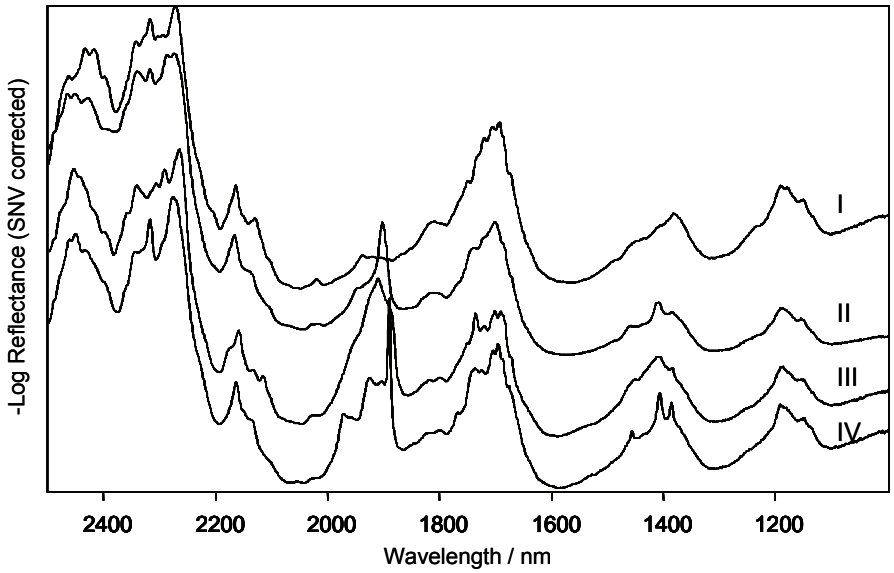

Fig. 50. FT-NIR spectra (standard normal variate (SNV) corrected) of the different crystalline forms of emodepside recorded at ambient conditions.

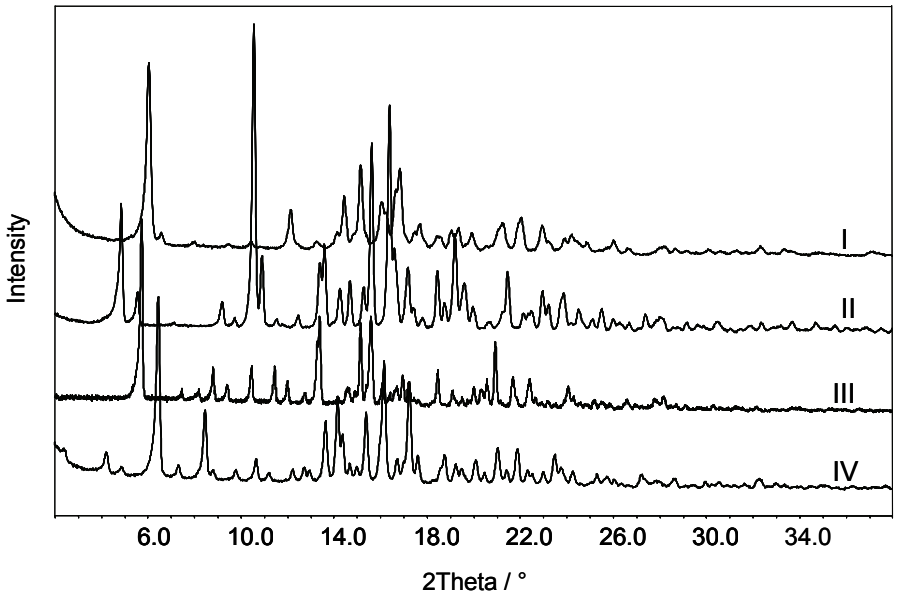

Fig. 51. X-ray powder diffractograms of the different crystalline forms of emodepside recorded at ambient conditions.

To summarise, each of the spectroscopic methods used is suitable to differentiate between the different crystalline forms of emodepside. The differences present in the spectra reflect the variations in the three-dimensional packing of the four forms. XRPD further demonstrates the existence of four different crystalline forms. In the FT-IR and FT-NIR spectra of the forms II-IV, bands representing the water associated with the forms are visible. The presence of a sharp OH stretching band of water in case of form IV provides indication that form IV is a hydrate.

4.3.3.2.2 Variable conditions

4.3.3.2.2.1 Variable temperature X-ray powder diffraction (VT XRPD)

The measurements performed so far reveal that the crystalline forms II-IV are either modifications of emodepside having water adsorbed to the crystal surface and / or absorbed into disordered defect regions or they are hydrates forming isomorphic dehydrates. Although thermomicroscopic investigations (jumping of crystals of form II and IV) and FT-IR analysis at ambient conditions (sharp OH stretching band of water in the spectrum of form IV) provide indication that at least the forms II and IV represent hydrates, these measurements do not prove that the forms are hydrates. Therefore, XRPD at variable conditions was performed being one of the methods capable of identifying solvates forming isomorphic desolvates (2.3.6). First, attempts were made to obtain the powder diffractogram of the water-free form IV by drying the form in a glove box under a dry nitrogen atmosphere for several days. Sample preparation was done in the glove box in order to avoid re-exposition to ambient humidity before measurement. In case form IV is a hydrate forming an isomorphic dehydrate, a shift of reflections towards higher 2theta values will be expected in the pattern of the water-free form IV due to lattice contraction. However, the pattern obtained is identical to the pattern recorded at ambient conditions (data not shown). Since it is difficult to verify that the atmosphere in the glove box corresponds to 0 % *RH*, it is not sure whether the water-free form was actually obtained in the glove box. Hence, VT XRPD was performed in order to generate the water-free form in situ by heating. Form IV was heated in 10 °C steps up to 120 °C. At each step, a diffractogram was recorded. Fig. 52 shows the diffraction pattern of the water-free form IV at 120 °C compared to the pattern obtained at RT.

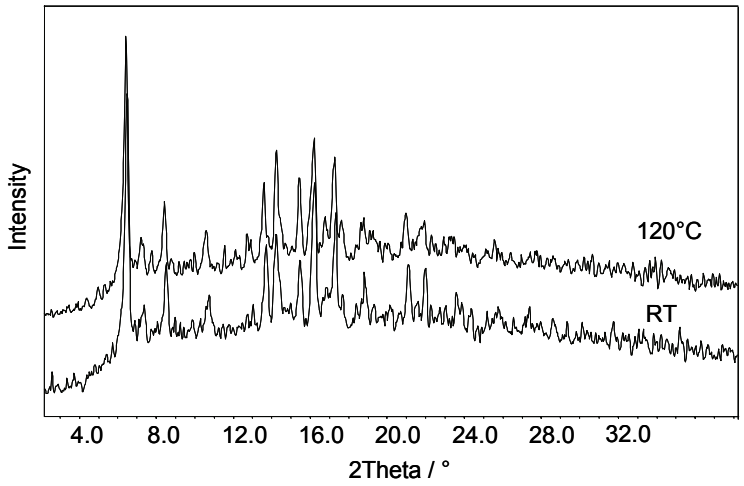

Fig. 52. XRPD pattern of emodepside form IV at RT and 120 °C.

Both diffractograms exhibit a low signal-to-noise ratio caused by the experimental setup used. At 120 °C, none of the clearly visible peaks is shifted toward higher diffraction angle values. Fig. 52 reveals that most of these diffraction peaks are rather

shifted toward lower 2theta values, i.e. higher d spacings. This might be explained by thermal lattice expansion. It is not possible to determine whether the small peaks of the pattern display shifts due to the low signal-to-noise ratio. The pattern at 120 °C is in consistence with the diffractogram of the sample dried in the glove box confirming that lattice contraction does not occur upon the leaving of water. This does not rule out the possibility that form IV is a hydrate, since lattice relaxation does not necessarily have to take place (Stephenson *et al.*, 1998). However, in case dehydration does not induce any shrinkage of the unit cell volume, VT XRPD is not suited to detect whether hydrates or modifications are present. Consequently, VT XRPD does not represent a suitable tool to prove that form IV is a hydrate. The other forms, II and III, were not measured since the aim was to find a method capable of identifying all three forms.

4.3.3.2.2.2 FT-Raman spectroscopy after storage at different *RH*

To study whether changing the *RH* does have any effect on the FT-Raman spectra of the crystalline forms II-IV which would reveal that the forms are hydrates, samples of each form including mod. I were stored at 0 % *RH* and 85 % *RH* for 7 days (using exsiccators) prior to measurement. It was not straightforward to obtain the spectra of the forms II-IV stored at 0 % *RH* due to the fast reuptake of water molecules that occurs when the samples are re-exposed to ambient humidity. To minimise the time the conditioned samples were set out ambient humidity before measurement, the samples were equilibrated in the sample holders used for measurements (glass vials). The glass vials were sealed immediately after they had been taken out of the exsiccators and were then used for measurement. This way, it was possible to record the spectra of the water-free samples. The resulting spectra were compared to the spectra obtained at ambient conditions (Fig. 53).

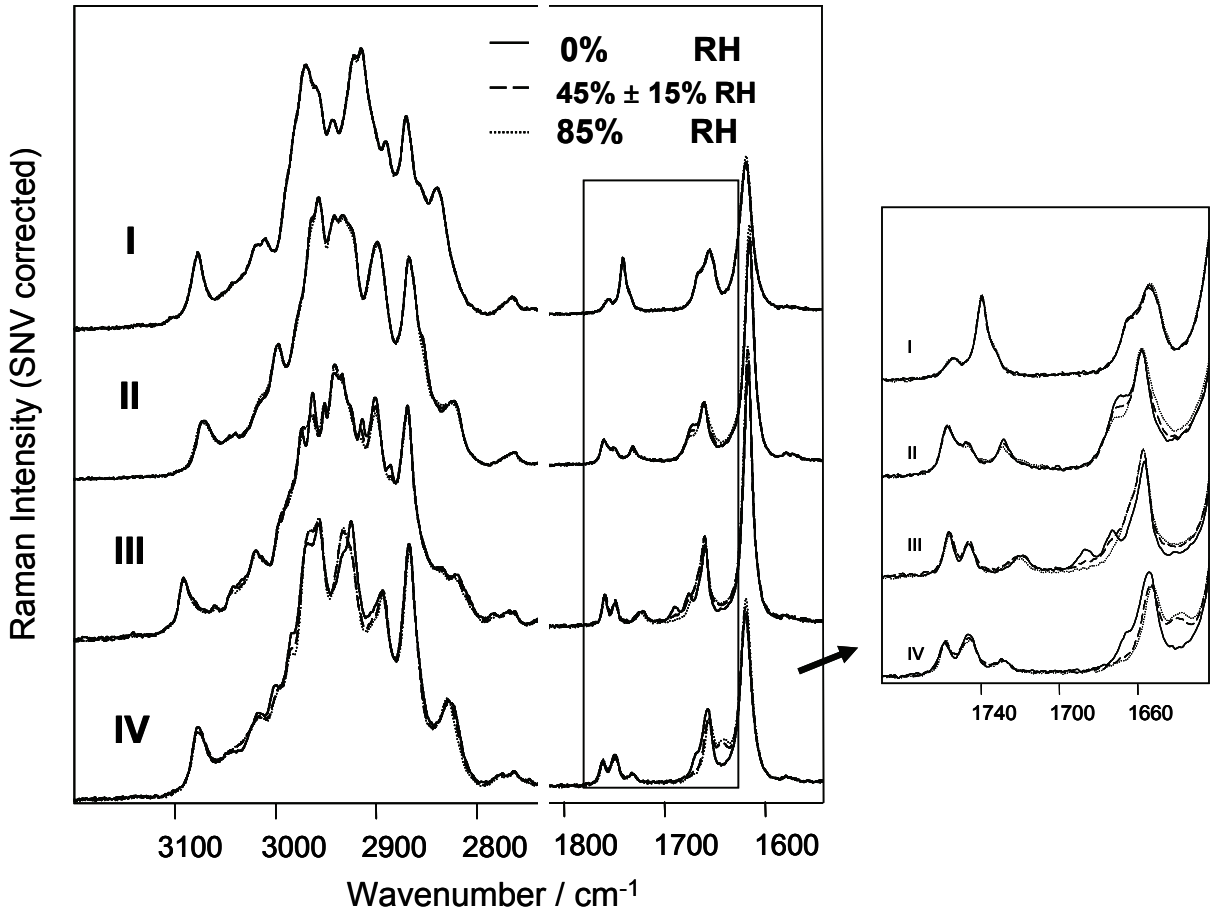

Fig. 53. FT-Raman spectra (the C-H and C=O stretching regions) of the forms I-IV of emodepside at different *RH*; the spectra are normalised using SNV.

Varying the *RH* causes small but reproducible changes in the FT-Raman spectra of the forms II-IV, especially in the C-H stretching region (3000 cm^{-1} to 2850 cm^{-1}) and in the C=O stretching region (1690 cm^{-1} to 1630 cm^{-1}). Form I has identical Raman patterns at the different *RH*. Regarding the forms III and IV, changes are pronounced when rising *RH* from 0 % to ambient humidity (45 % ± 15 % *RH*). Both forms show shifts in intensity and position of bands in the C-H stretching region. In the C=O stretching region of form IV, the band visible as shoulder of the band at 1654 cm^{-1} at 0 % *RH* is absent at ambient humidity, in addition the intensity of the band at 1654 cm^{-1} has decreased. In exchange, a band at 1639 cm^{-1} emerges at 45 % *RH*. In the C=O stretching region of form III, the two bands present at 0 % *RH* at 1687 cm^{-1} and 1673 cm^{-1} are shifted underneath the C=O vibration band at 1657 cm^{-1} at 45 % *RH* causing a broadening and an increase in the intensity of this band. Consequently, both forms exhibit a shift of C=O stretches towards lower wavenumbers when raising *RH* from 0 % to ambient humidity. When the *RH* is changed from ambient humidity to 85 %, the spectra of both forms show only minor if any changes at all in the C-H stretching region. In the carbonyl stretching region, a further shift towards lower wavenumbers is observed however being less striking compared to the changes occurring when raising the *RH* from 0 % to 45 %. In contrast to the forms III and IV, variation of *RH* causes only little if any alterations in the C-H stretching region of

form II. In the C=O stretching region, the intensity of the band at 1669 cm^{-1} diminishes with rising *RH* whereas the band at 1657 cm^{-1} broadens towards lower wavenumbers. Consequently, form II also displays shifts of C=O vibrations towards higher wavelengths.
The changes observed in the FT-Raman spectra of the forms II-IV with varying *RH* are caused by the absence (0 % *RH*) respectively the presence (45 % and 85 % *RH*) of water. As Raman spectra are sensitive to changes in the local environment inside the crystal lattice (Gift and Taylor, 2007), the measurements reveal that water molecules are increasingly incorporated into the crystal lattice with rising *RH*. Consequently, the forms II-IV represent non-stoichiometric hydrates. The spectra recorded at 0 % *RH* reflect the spectra of the isomorphic dehydrates II-IV (in the following, the general expression desolvates will be used). With rising *RH*, water molecules increasingly enter the lattice and interact with carbonyl groups via hydrogen bonding which leads to the observed shift of C=O stretches towards lower wavenumbers. Regarding the forms III and IV, the water molecules also affect C-H vibrations which is either due to direct interaction via van-der-Waals interaction or due to slight reorientations of the C-H groups caused by the presence of water molecules.
The described changes in the C=O stretching region fall into the C=O stretching region of amide groups. However, Raman measurements do not reveal which of the amide groups of emodepside interact with water molecules in the different forms as the presence of four amide groups in emodepside (Fig. 9) makes assignment of bands difficult. Additionally, it is difficult to determine whether the C=O stretching bands belonging to the four ester groups of emodepside (present between 1760 cm^{-1} and 1720 cm^{-1}) are also affected by the water molecules due to the low absolute intensity of the bands.
Summarising, FT-Raman analysis at different *RH* is suitable to prove that the forms II-IV represent non-stoichiometric hydrates forming isomorphic desolvates.

4.3.3.2.2.3 Variable temperature (VT) FT-IR spectroscopy

It was examined whether FT-IR spectroscopy is also able to distinguish between the non-stoichiometric hydrates II-IV and the corresponding isomorphic desolvates. Contrary to FT-Raman spectroscopy, it was not possible to obtain the FT-IR spectra of the forms II-IV stored at 0 % *RH* (isomorphic desolvates II-IV) due to the fast reuptake of water molecules observed at ambient conditions. Therefore, the isomorphic desolvates were generated in situ using VT FT-IR spectroscopy. The sample was heated up to 120 °C to induce dehydration. After several minutes at 120 °C, the sample was allowed to cool off to RT before recording the spectrum. During the cooling phase, the anvil of the ATR sampling system used was pressed on the sample in order to prevent the water molecules from diffusing back into the crystal lattice. In addition to the forms II-IV, form I was measured acting as reference

substance. The spectra of the forms I-IV obtained after heating were compared to the spectra of the forms recorded at ambient conditions before heating (Fig. 54).

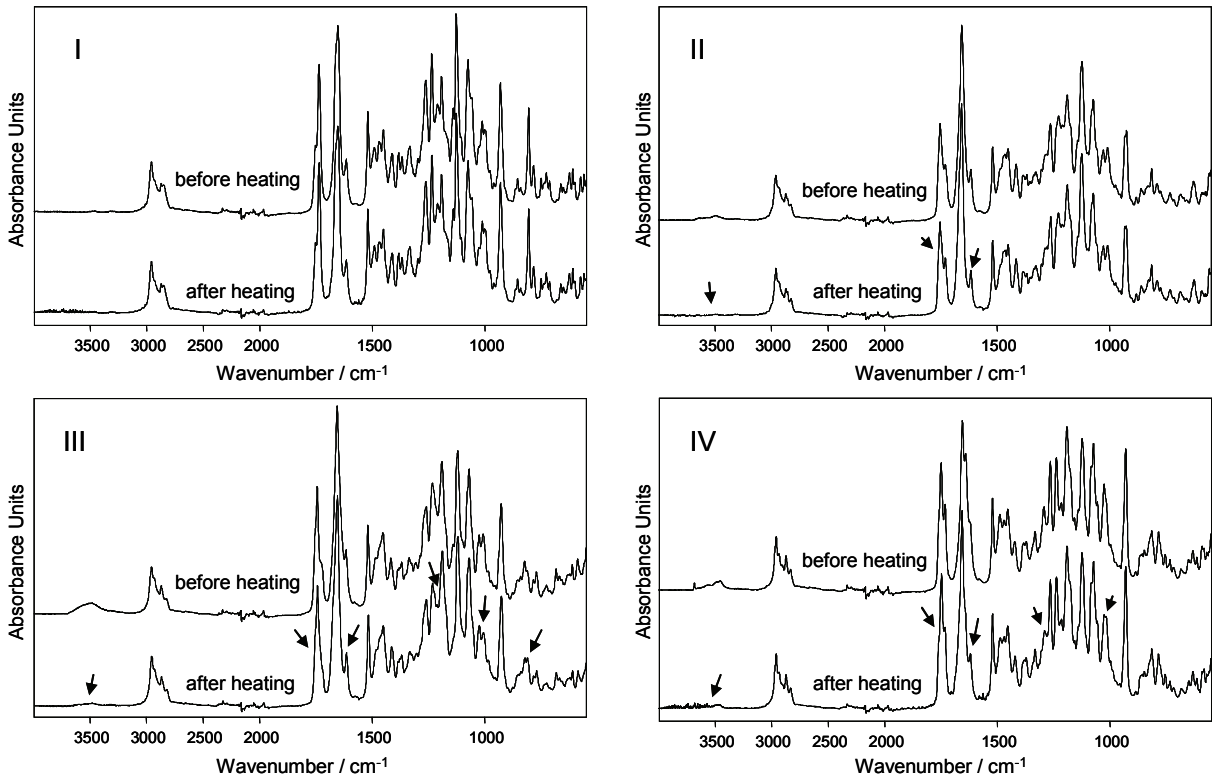

Fig. 54. FT-IR spectra (normalised using SNV) of the forms I-IV of emodepside before and after heating; differences between the spectra are marked.

As expected, identical spectra are found for form I. In opposition to that, the spectra of the hydrates II-IV obtained after heating, i.e. the spectra of the isomorphic desolvates II-IV, show small differences in comparison to the spectra of the hydrates II-IV (spectra before heating). Due to the absence of water, the spectra of the desolvates miss the OH stretching bands present in the spectra of the hydrates (in the range of 3700 cm^{-1} to 3400 cm^{-1}). In case of desolvate IV, many spikes are visible in the OH stretching region corresponding to water in the gas phase. The spectra of the hydrates and desolvates further differ in the C=O stretching region (see below). Besides the differences in the OH and C=O stretching region, the spectrum of desolvate II corresponds to the spectrum of hydrate II. By contrast, the desolvates III and IV further differ from the corresponding hydrates in the region of 1300 cm^{-1} to 900 cm^{-1}. This observation suggests that the changes in the local environment inside the crystal lattice caused by dehydration are greater for the desolvates III and IV than for desolvate II. The finding is in agreement with FT-Raman analysis (4.3.3.2.2.2). To better visualise the differences of the spectra in the C=O stretching region, a close-up view is shown in Fig. 55.

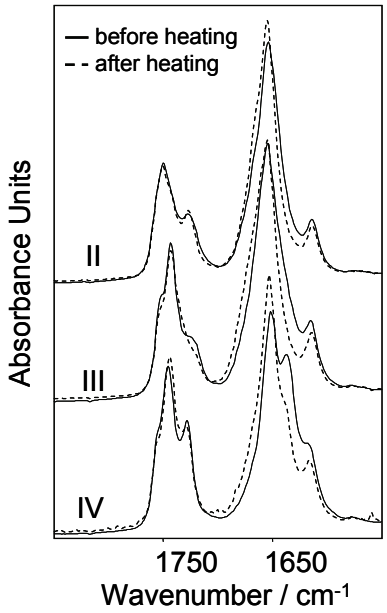

Fig. 55. C=O stretching region of the FT-IR spectra of the forms II-IV of emodepside before and after heating (close-up view).

The figure shows that the hydrates II-IV have strong, broad absorption bands at around 1650 cm^{-1} corresponding to C=O stretches of amide groups. Regarding hydrate IV, a second band maximum is visible at 1637 cm^{-1} also related to C=O vibrations of amide groups. The positions of the bands are in agreement with the positions of the C=O bands of amide groups present in the FT-Raman spectra of the hydrates at ambient conditions (4.3.3.2.2.2). The C=O stretching bands of the hydrates II-IV overlap with weak absorption bands at around 1615 cm^{-1} attributed to aromatic C=C stretches. The desolvates II-IV differ from the corresponding hydrates in the shape and intensity of the overlapping C=O and C=C bands. The differences indicate that C=O stretches of amide groups are shifted towards higher wavenumbers in the spectra of the desolvates. Contrary to the variations in the C=O stretching region of amide groups, minor if any differences are observed in the C=O stretching region of ester groups (1760 cm^{-1} to 1720 cm^{-1}). These findings indicate that the water molecules present in the hydrates II-IV are hydrogen bonded to amide groups only. The results are consistent with FT-Raman analysis (4.3.3.2.2.2).
Concluding one can say that VT FT-IR spectroscopy represents a further method suitable to reveal that the forms II-IV of emodepside are hydrates forming isomorphic desolvates.

4.3.3.2.2.4 FT-NIR spectroscopy after storage at different *RH*

From both FT-Raman analysis and VT FT-IR spectroscopy it is known that the water molecules present in the hydrates II-IV interact with amide groups of emodepside. To further study the bonding status of the water molecules incorporated into the crystal lattices with rising *RH*, samples of each form of emodepside including mod. I were

stored at different *RH* before being measured using FT-NIR spectroscopy. The obtained spectra are presented in Fig. 56.

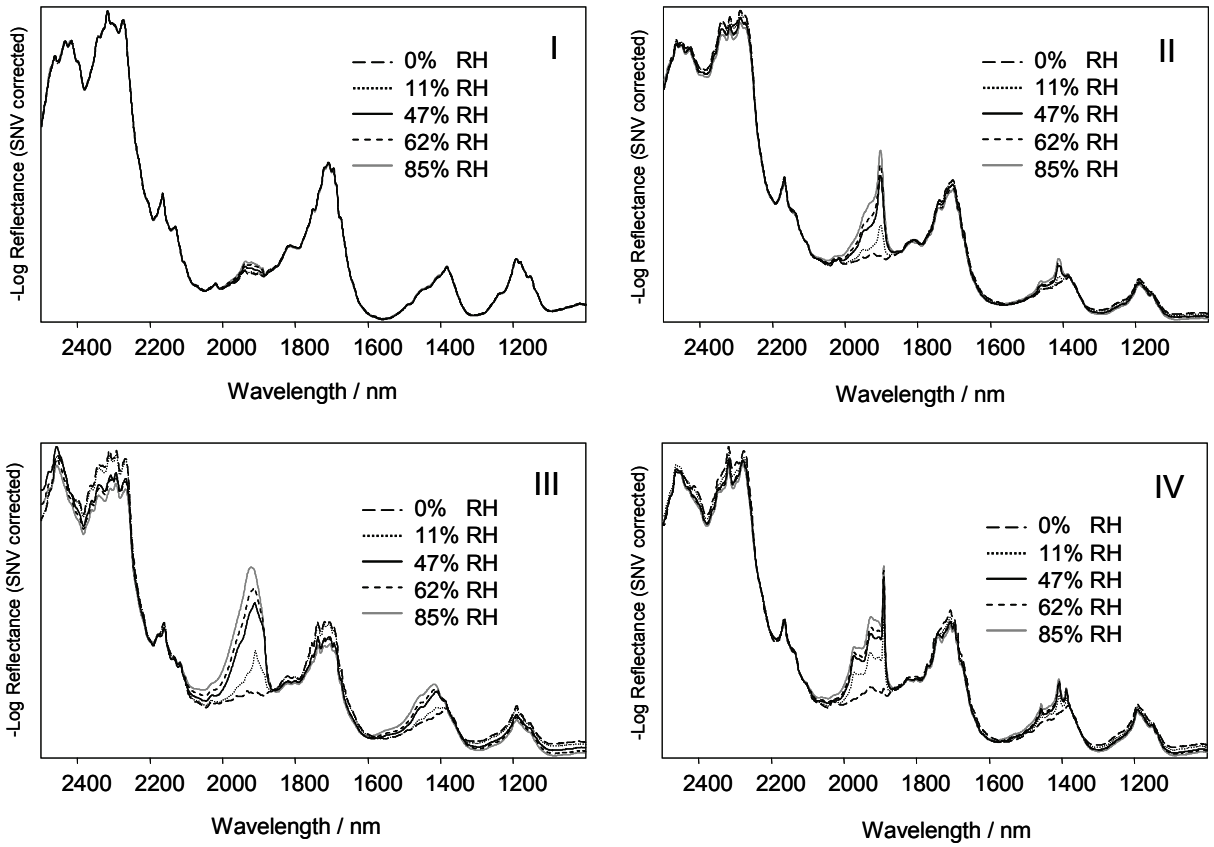

Fig. 56. FT-NIR spectra (treated with SNV) of mod. I and hydrates II-IV of emodepside stored at different *RH*.

At 0% *RH* the FT-NIR spectra of the isomorphic desolvates II-IV are recorded. With rising *RH*, absorption increases in the spectra of the hydrates II-IV around 1420 nm due to the combination of symmetric and anti-symmetric stretching modes of water ($\nu_1 + \nu_3$, overtone band) as well as around 1920 nm due to the combination of $\nu_2 + \nu_3$ (OH combination band). In the spectrum of mod. I which sorbs minor quantities of water with rising *RH*, spectral variations are only visible around 1920 nm because of the increased molar absorptivity of water in this wavelength region.

The spectra of the hydrates II-IV stored at different *RH* show several overlapping bands in both the overtone region and the OH combination region. This suggests the presence of differently bound water molecules inside the crystal lattices (different “types of water”), as the wavelengths at which water absorbs change with alterations in the strength of hydrogen bonding (Blanco *et al.*, 1998; Higgins *et al.*, 2003; Maeda *et al.*, 1995). To study the different types of water, the second derivative of the spectral data in the OH combination region was used (Räsänen *et al.*, 2001; Vora *et al.*, 2004). The second derivative has the benefit of enhancing the visual resolution, but it causes the loss of the original shape of the spectra (Heise and Winzen, 2002). In the second derivative spectra, the band maxima of the original spectra appear as

band minima of negative bands. Fig. 57 shows the second derivative spectra of the mod. I and the hydrates II-IV stored at different *RH*.

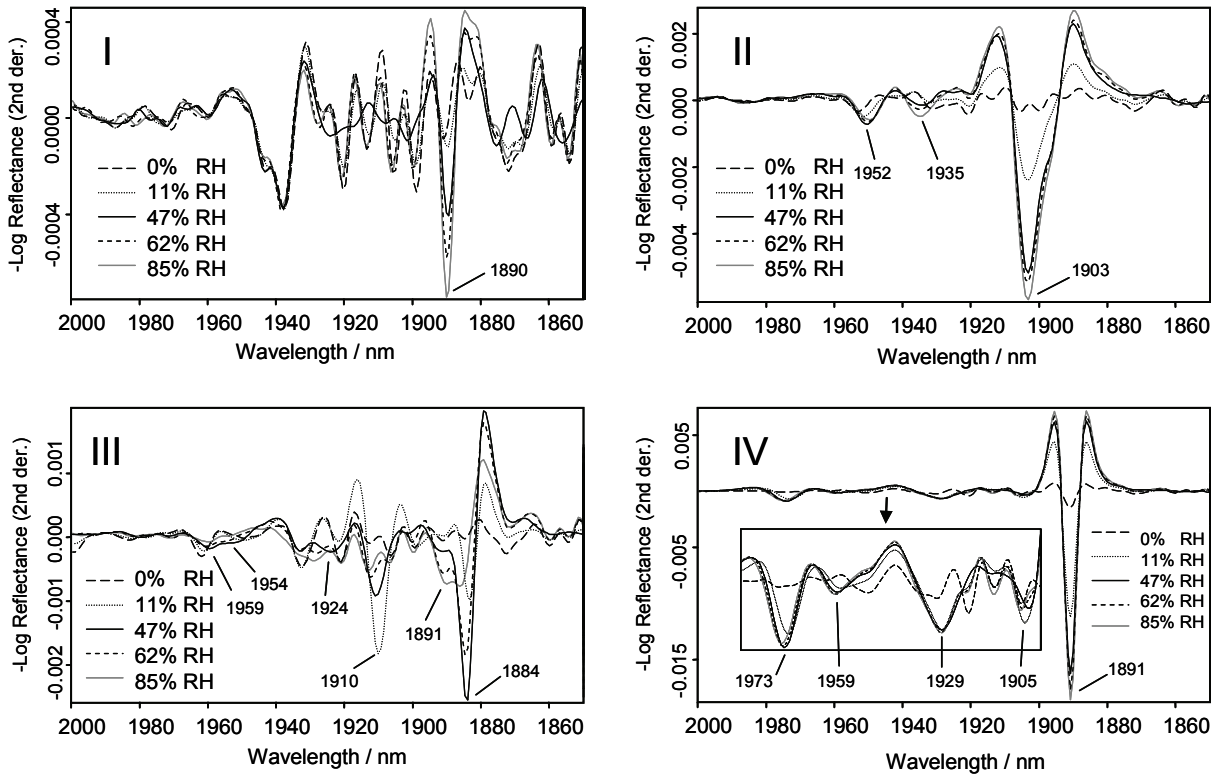

Fig. 57. FT-NIR spectra (second derivative) of mod. I and hydrates II-IV of emodepside in the range of 2000 nm to 1850 nm obtained at different *RH*.

In the second derivate spectra of the hydrates II-IV (spectra above 0 % *RH*), several negative bands are present. These negative bands correspond to the OH combination bands in the original spectra. Each negative band represents a certain type of water molecules. The greater the wavelength the band minimum is located at, the stronger is the hydrogen bonding of the water molecules represented by this band (Fornés and Chaussidon, 1978). At 11 % *RH*, hydrate II shows two negative bands (at 1903 nm and 1952 nm). The intensities of these bands increase up to 47 % *RH* (band around 1952 nm) and 85 % *RH* (band at 1903 nm), respectively. This indicates that the amount of the water molecules belonging to the water types reflected by these two bands increases inside the crystal lattice up to the mentioned *RH*. At 47 % *RH*, a third type of energetically equivalent water molecules arises (negative band at 1935 nm) and the amount of this species of water molecules increases up to high *RH*.

Hydrate III also shows two types of water at 11 % *RH* (1884 nm and 1910 nm) (Fig. 57). With rising *RH* however, the intensities of the negative bands at 1884 nm and 1910 nm decrease indicating a diminution of the amount of these types of water molecules. In exchange, stronger hydrogen bonded water molecules appear at 47 % *RH* (negative bands at 1891 nm, 1924 nm, 1954 nm and 1959 nm). The amount of the water molecules reflected by the bands at 1891 nm and around 1924 nm

increases up to 85 % *RH*. The observed changes in band positions and intensities with rising *RH* might be explained by an increase in the hydrogen bonding of the water molecules by their interaction with the water molecules that additionally enter the crystal lattice.

Regarding hydrate IV, the sharp band at 1891 nm in the raw spectrum produces a sharp and intense negative band in the second derivate spectrum (Fig. 57) which eclipses the intensity changes in the region of 1900 nm to 2000 nm. Therefore, this region is zoomed to be able to identify all the bands present. Fig. 57 reveals 5 types of water incorporated into the crystal lattice at 11 % *RH* (negative bands at 1891 nm, 1905 nm, 1929 nm, 1959 nm and 1973 nm). While the intensity of the band at 1929 nm does not change with rising *RH*, the bands at 1959 nm and 1973 nm increase up to 47 % *RH*, whereas only the band at 1891 nm rises up to high *RH*. The band at 1905 nm decreases in intensity with rising *RH*. The changes of the intensities of the bands suggest that the majority of the water molecules are incorporated at low *RH*.

In contrast to the hydrates II-IV, mod. I shows a single negative band at 1890 nm that increases slightly in intensity with raising *RH*. The wavelength the band minimum is located at and the low absolute intensity of the band are consistent with water being loosely bound to the crystal surface. To summarise, FT-NIR spectroscopy is a well suited tool to gain information on the bonding status of the water molecules incorporated into the crystal lattices of the hydrates II-IV with rising *RH*.

4.3.3.3 Water vapour sorption isotherms

The sorption and desorption curves of the various forms of emodepside are presented in Fig. 58. As expected, mod. I sorbs only minor quantities of water (0.2 mol of water per mole of anhydrous emodepside from 0 % *RH* to 95 % *RH*) which were not detectable with thermal or spectroscopic analysis. The hydrates II-IV differ in the amount of water being incorporated into the crystal lattice. Hydrate III takes up by far the highest amount of water (4.9 mol of water per mole of emodepside from 0 % *RH* to 95 % *RH* corresponding to 7.9 g water per 100 g anhydrous emodepside, i.e. 7.9 % water). On the other hand, the hydrates II and IV take up 1.8 mol of water (2.8 %) and 2.5 mol of water (4.1 %), respectively.

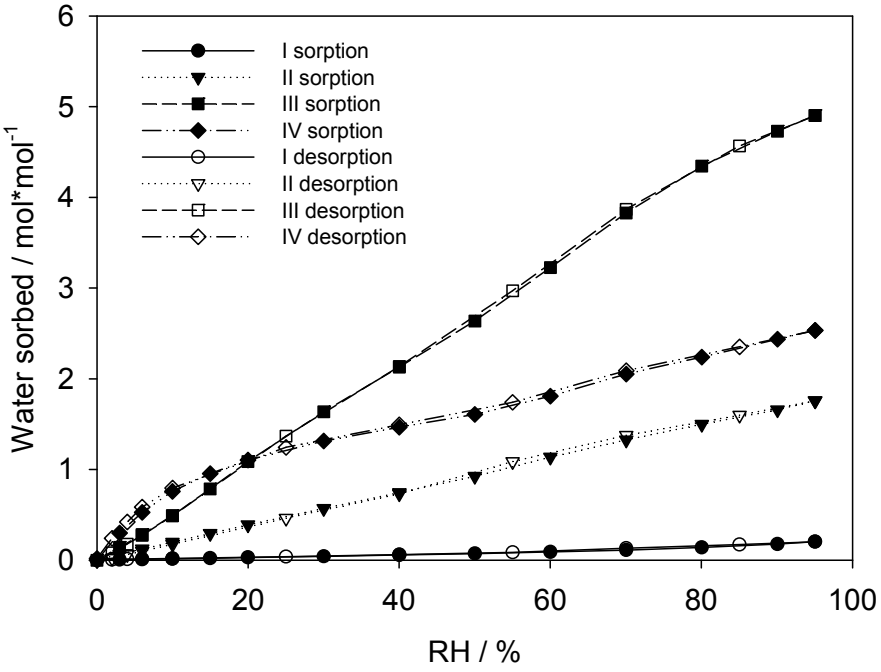

Fig. 58. Water vapour sorption isotherms of mod. I and hydrates II-IV of emodepside at 22 °C.

A common feature of the isotherms of the hydrates II-IV is that the desorption curve virtually superimposes the sorption curve (Fig. 58). Such behaviour is characteristic for non-stoichiometric hydrates (Stephenson *et al.*, 1998). Concerning the shapes of the curves, the isotherm of hydrate IV differs from the others in the region of low *RH*. The slope of the sorption curve of hydrate IV being steep from 0 % *RH* to 6 % *RH* flattens between 6 % *RH* and 20 % *RH*. According to Authelin (Authelin, 2005) who has linked the degree of order of the water molecules in non-stoichiometric hydrates to the shape of the sorption isotherm, such a change of the slope of the isotherm in the region of low *RH* indicates the presence of localised water molecules (type I isotherm) or of water molecules with at least some degree of order (type II isotherm). Consequently, the isotherm of form IV provides indication on how the water molecules are bound at low *RH*. In contrast, the shape of the isotherm of the forms II and III (virtually a straight line) does not well agree with any of the isotherm types described by Authelin. Thus, it does not give any information on the degree of order of the water molecules in the hydrates II and III.

4.3.3.4 Crystal structure analysis of form IV

For hydrate IV, single crystal structure analysis was performed to verify the results from previous measurements. Single crystals of hydrate IV were obtained by cooling a boiling methanol solution of emodepside (2 % (m^*V^{-1})) at RT in either a round bottom flask or in a test tube. The crystal data of a single crystal of hydrate IV stored at ambient humidity are given in Table 14.

Table 14 Crystal data for emodepside hydrate IV

	Emodepside form IV
Empirical formula	C60 H90 N6 O15.73
Formula weight	1146.98
Temperature [K]	100
Crystal size [mm^3]	0.60 x 0.04 x 0.04
Crystal system	Trigonal
Space group	P3
a [Å], α [°]	41.1838(3), 90
b [Å], β [°]	41.1838(3), 90
c [Å], γ [°]	6.48470(10), 120
Volume [$Å^3$]	9525.18(18)
Z	6
Density (calculated) [$g*m^{-3}$]	1200
Goodness-of-fit on F_2	1089
Final R indices [I>2sigma(I)]	R1 = 0.0403, wR2 = 0.0974
R indices (all data)	R1 = 0.0430, wR2 = 0.0990

Form IV crystallises as twin (twinning by merohedry). Fig. 59 shows that hydrate IV has two emodepside molecules and four well defined positions for water in the asymmetric unit.

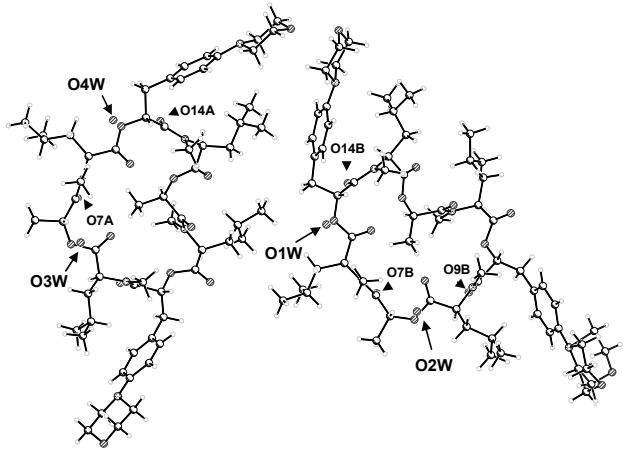

Fig. 59. Asymmetric unit of hydrate IV of emodepside found at ambient conditions; labelled: the oxygen atoms representing the four water molecules O1W, O2W, O3W and O4W and the adjacent oxygen atoms of the two emodepside molecules (O-O distance < 3 Å).

The sites of the water molecules O1W and O2W are fully occupied whereas the positions of the water molecules O3W and O4W are occupied to approximately 75 % and 70 %, respectively. This gives a ratio of 1.7 mol water to 1 mol emodepside which is found in hydrate IV at 54 % *RH* (see vapour sorption analysis, 4.3.3.3). O1W, O3W and O4W are each located in the vicinity of the oxygen atom of an amide group with an O-O distance < 3 Å which suggests the formation of hydrogen bonds (Fig. 59). O1W and O4W have similar O-O distances (O1W-O14B: 2.874 Å, O4W-O14A: 2.859 Å) whereas O3W displays a larger O-O distance (O3W-O7A: 2.994 Å) suggesting that O3W is comparatively weakly hydrogen bonded. In the environment of O2W, the oxygen atoms of two amide groups display O2W-O distances < 3 Å (O2W-O7B: 2.959 Å, O2W-O9B: 2.982 Å) which indicates that O2W has two relatively weak hydrogen bonds.
As hydrate IV dehydrates forming an isomorphic desolvate, the water molecules have to be able to enter and leave the crystal lattice without disrupting the crystal structure. The unit cell (Fig. 60) shows that the water molecules are isolated being located in different structural voids.

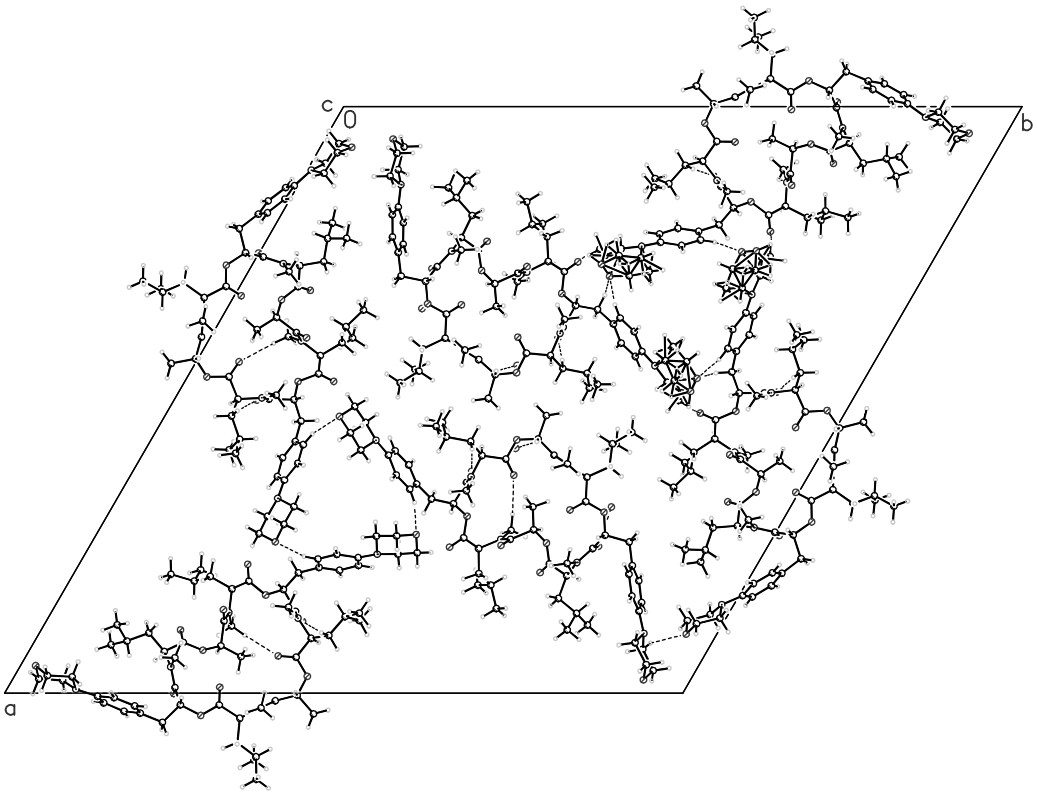

Fig. 60. Unit cell of hydrate IV of emodepside at ambient conditions viewed down the c axis.

These voids do not form a straight channel through which the water molecules could easily escape. Therefore, it is difficult to predict how the water molecules leave the crystal. Attempts were made to obtain the single crystal structure of the isomorphic desolvate by drying the single crystal in situ on the machine using a warm dry nitrogen stream. The dry crystal differs from the hydrate by significantly decreased

diffraction properties and by the presence of additional reflections. The short a-axis is not affected by the leaving of the water molecules; however, additional reflections appear between the reflexions of the two long axes. Partially, the reflections touch each other being not isolated. It is concluded that the merohedral twin breaks into something less symmetric giving at least two fragments of crystals. It was not possible to solve the crystal structure of the dry crystal.
Summarising, crystal structure determination reveals form IV to be a hydrate with four well defined water positions. The results are consistent with the conclusions drawn from FT-Raman and FT-IR analysis at variable conditions as well as from vapour sorption analysis. Both FT-Raman measurements at different *RH* and VT FT-IR spectroscopy show that form IV is a hydrate with water molecules hydrogen bonded to C=O groups of amid functions. The shape of the sorption isotherm of hydrate IV (the change of the slope of the isotherm in the region of low *RH*) indicates the presence of localised water molecules in the crystal lattice at low *RH*. Regarding FT-NIR analysis, the spectra of hydrate IV at varying *RH* reveal differently bound water molecules to be present inside the crystal lattice. Having four different water positions in the asymmetric unit, four different bands might be expected in the OH combination region at ambient humidity. However, five bands are visible in the spectra at 47 % and 62 % *RH* (4.3.3.2.2.4). A possible explanation might be that one of the singly hydrogen bonded water molecules O1W, O3W or O4W exists in two different energetic states due to two possible orientations of the non hydrogen bonded hydrogen atom.

4.3.3.5 Thermodynamic relationships

For pharmaceutical development, it is important to know the thermodynamic relationships between the different forms of emodepside. It is not possible to use the rules described in section 2.1.2.1.3 to determine the thermodynamic relationships between mod. I and the hydrates II-IV, because they apply only to polymorphs. However, the rules may be used to assess the thermodynamic relationships for mod. I and the isomorphic desolvates II-IV since the desolvates are one-component systems regarded as modifications of emodepside. According to both the heat-of-fusion rule and the entropy-of-fusion rule, the desolvates II-IV are all monotropic to mod. I with mod. I being the thermodynamically most stable modification across the entire temperature range. This is in accordance with the fact that the desolvates represent high energy states due to the absence of the stabilising solvent molecules (2.1.2.2.3). To experimentally determine the relative stabilities of mod. I and the hydrates II-IV in water at RT, they were suspended in water (pH 4) under stirring for 10 days. However, the experiments were not helpful to assess the relative stabilities since slurry phase conversion did not take place and differences in the solubilites of the forms could not be detected due to the low solubility of emodepside in water.

4.3.4 Summary of results

The thorough examination of the different solid forms of emodepside reveals that form I represents a modification whereas the forms II-IV are non-stoichiometric hydrates forming isomorphic desolvates. Whereas FT-Raman and FT-IR analysis at variable conditions are suitable to identify the forms II-IV as hydrates, FT-NIR analysis of the hydrates stored at different *RH* provides information on the bonding status of the water molecules incorporated with rising *RH* showing that each hydrate has differently bound water molecules. Vapour sorption analysis indicates the presence of ordered water molecules in hydrate IV. Regarding hydrate IV, results are verified by crystal structure analysis performed at ambient conditions. Although the crystal structure of hydrate III is not known, the results of the various measurements indicate the presence of large channels in the crystal structure. This conclusion was drawn because of the following results: (1) hydrate III incorporates the highest amount of water molecules; (2) dehydration is not accompanied by a jumping of the crystals indicating that the water molecules can very easily leave the crystal structure; (3) the strength of the bonding of the water molecules incorporated into the crystal lattice rises with increasing *RH* suggesting the interaction with the water molecules that additionally enter the lattice; (4) the water molecules do not only affect vibrations of C=O groups, but they also have an effect on vibrations of C-H groups.

4.4 Potential of perfusion calorimetry

4.4.1 Introducing comments

The following experiments aimed at evaluating the potential of perfusion calorimetry in the characterisation of non-stoichiometric solvates forming isomorphic desolvates. The experiments were performed using mass flow controller based devices that had been tested according to the method described in 4.1. Experimental temperature was 25 °C and the total flow rate used was 80 ml*h^{-1} (set value). First, the different non-stoichiometric hydrates of emodepside were investigated. They were exposed to 0 % *RH* in the reaction vessel of the perfusion system in order to obtain the isomorphic desolvates. The *RH* was then increased stepwise up to 90 % *RH* monitoring the thermal activity associated with the uptake of water molecules. The sorption isotherms obtained from the calorimetric data were compared to the isotherms gained from gravimetric analysis. Furthermore, the thermal activity of the isomorphic desolvates exposed to stepwise increasing RVP_{MeOH} values was recorded. After finishing the perfusion experiments, FT-Raman spectroscopy was used to determine whether methanol molecules had been incorporated into the crystal lattices, i.e. whether isomorphic methanolates had formed. The results of FT-Raman spectroscopy were compared to the heat output of the samples. To investigate the general potential of perfusion calorimetry in indicating whether solvent molecules are incorporated into the crystal lattice of a substance without any changing of the three-dimensional structure, further substances were examined.

4.4.2 Emodepside hydrates

To monitor the thermal activity of the different hydrates of emodepside in dependence of *RH*, samples of each form were first exposed to 0 % *RH* for 6 h. The *RH* inside the vessel was then increased to 10 %, 20 %, 30 %, 50 %, 70 % and 90 %. Each *RH* step was held for 4 h. The reason to use more steps at low *RH* was to investigate the strong uptake of water of desolvate IV taking place at low *RH* (4.3.3.3). Mod. I was also measured to investigate whether perfusion calorimetry is able to differentiate between the adsorption of water to the crystal surface (mod. I) and desolvate-isomorphic hydrate formation (hydrates II-IV). The weight of sample used for mod. I was about 9 mg. Having this amount of sample, the sample just covers the bottom of the reaction vessel. Although a higher weight of sample would be preferable in terms of the signal-to-noise ratio, it would lead to a layer formed by the sample. As the diffusion of the water molecules through the layer might be a limiting factor in the attainment of equilibrium, the amount of sample that just covers the bottom of the vessel was used. Regarding the hydrates II-IV, the amounts of water sorbed as a function of *RH* are considerably higher in comparison to mod. I (4.3.3.3). Hence, it has to be considered that (especially at low *RH*) the amount of water molecules supplied by the wet line may limit the equilibration of the samples. In

order to prevent the amount of water entering the vessel to be a limiting factor, lower sample weights were used for the hydrates II-IV compared to mod. I. For hydrate II, a sample weight of about 7 mg was used. Regarding the hydrates III and IV that sorb more water at low *RH* than hydrate II (4.3.3.3), the sample weight was further reduced to about 3 mg to 4 mg. The heat flow curves of the samples and the blank are given in Fig. 61.

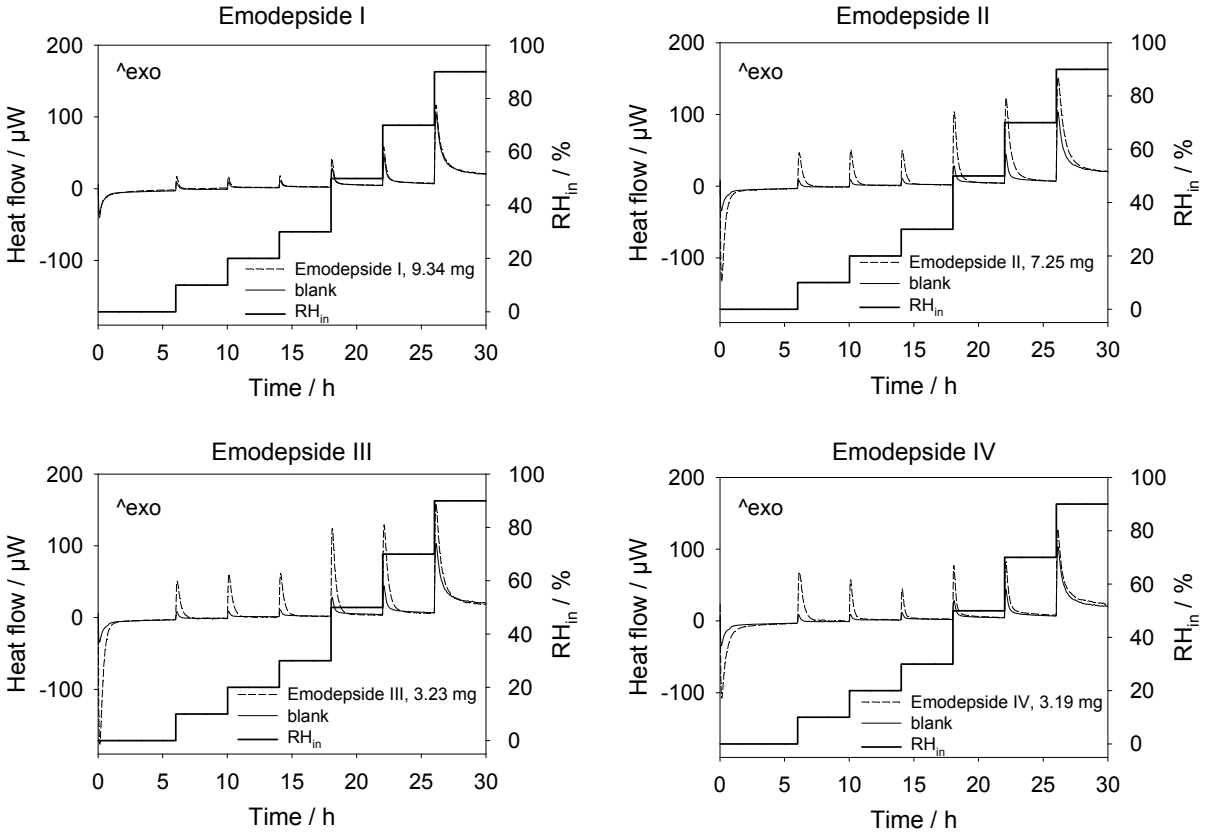

Fig. 61. Heat flow curves of mod. I and hydrates II-IV of emodepside being first dried at 0 % *RH* for 6 h and then exposed to increasing *RH* (25 °C).

At the beginning of the experiment, the non-stoichiometric hydrates II-IV show considerable endothermic heat flows corresponding to dehydration. After 1 h to 2 h, the heat flow curves have returned to the baseline (blank curve) revealing the end of the dehydration process. When increasing the *RH* to 10 %, the isomorphic desolvates II-IV obtained by dehydration show distinct exothermic peaks compared to the blank curve caused by the incorporation of water molecules into the crystal lattices. By contrast, mod. I of emodepside exhibits a minor exothermic peak compared to the blank (hardly visible) corresponding to the adsorption of water molecules to the crystal surface.

The heat flow curves of the isomorphic desolvates reach the blank curve after about 1 h indicating the attainment of equilibrium. Gravimetric analysis of the water sorption occurring when increasing *RH* from 0 % to 10 % reveals that the uptake of water molecules is practically finished after 20 min (desolvate II), 30 min (desolvate III) and 40 min (desolvate IV), respectively (data not shown). The longer equilibration times

observed in the calorimetric experiments may be due to thermal activity associated with slight accommodations of molecular groups inside the lattices induced by the incorporation of water molecules. It might also be possible that, despite the reduced sample weights used, the delivery of water molecules by the wet line is still the rate limiting step. Under the experimental conditions used (total flow rate, *T*, weight of sample), the amounts of water sorbed by the desolvates at 10 % *RH* are supplied after about 10 min. Possibilities to investigate whether the water supply limits the equilibration process are to further reduce sample weights or to increase the total flow rate in order to increase the amount of water being delivered by the wet line. If the process was limited by the amount of water entering the vessel, shorter equilibration times would be observed in both cases nevertheless, the heat flow curves would still be peak-shaped. However, the main interest is not to determine the exact equilibration times but to obtain the shape of the curves which provides indication about the kinetics of the process observed. Furthermore, both the reduction of the weight of sample and the increase of the total flow rate would result in a lower signal-to-noise ratio. Therefore, the experimental setup was not changed.
The peak shape of the curves, i.e. the rapid increase and decrease of the heat flow of the desolvates II-IV observed at 10 % *RH*, reflects the fast uptake of water molecules and the resulting short equilibration time which are typical for desolvates forming isomorphic solvates (Stephenson *et al.*, 1998). The rapidness of hydration is due to several factors, one of them being the low activation energy of the process caused by the fact that structural changes are not required (Stephenson *et al.*, 1998).
The thermal activity of the different samples at higher *RH* values is similar to the activity observed 10 % *RH*. The distinct peaks of the non-stoichiometric hydrates II-IV at higher *RH* values correspond to the incorporation of further water molecules into the crystal lattices while the small exothermic peaks of mod. I (again hardly visible) are due to the further adsorption of water molecules to the crystal surface. In case of hydrate IV, the sample curve fails to return to the blank curve at 90 % *RH* which is due to slight differences between sample and blank curve regarding the heat changes associated with the perfusion of the vessel.
In order to obtain the heats of sorption at the individual *RH* steps for the different samples measured, the blank curve was subtracted from each sample curve and the areas under the peaks were calculated. For every crystalline form of emodepside, the experiment was repeated twice so that the heats of sorption determined at the different *RH* steps represent mean values out of three measurements. The cumulative heat of sorption of each form was assessed by adding the heats of sorption at the different *RH* steps. Fig. 62 shows the cumulative heat of sorption and the corresponding amount of water being sorbed (obtained from gravimetric sorption analysis, 4.3.3.3) as a function of *RH*. Both quantities are expressed per mole emodepside.

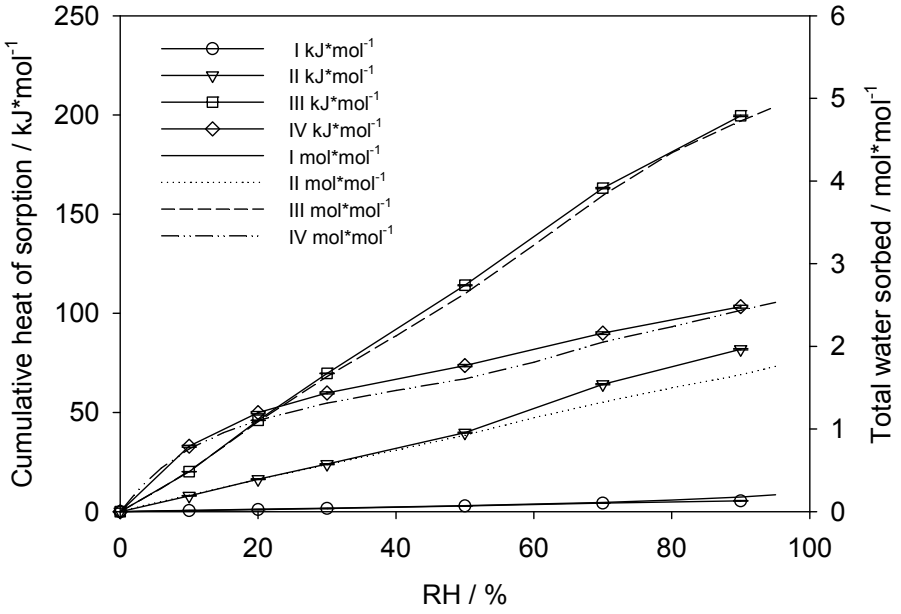

Fig. 62. Comparison of the calorimetric sorption isotherms of emodepside I-IV (obtained at 25 °C) versus the corresponding gravimetric sorption isotherms recorded at 22 °C; the error bars given for the cumulative heats of sorption were calculated according to the Gaussian error propagation.

For each crystalline form, the shape of the isotherm obtained from calorimetric data is similar to the shape of the isotherm determined from gravimetric studies which shows that the heat of sorption is proportional to the amount of water being sorbed. Slight differences found between the calorimetric and the gravimetric isotherm for the hydrates II-IV may be explained by the fact that the heat of sorption is not only a function of the number of water molecules taken up by the solid, but it is also dependent on the strength of water bonding (Sheridan *et al.*, 1995). The heat of sorption further depends on the enthalpy changes associated with the accommodations induced by the incorporation of the water molecules which include the changes in the local environment inside the lattice and possible adaptations of the entire lattice (lattice expansion, not for hydrate IV (4.3.3.2.2.1)).

Summarising, perfusion calorimetry is suitable to discriminate between mod. I of emodepside and the non-stoichiometric hydrates II-IV. The isomorphic desolvates II-IV formed at 0 % *RH* as well as the hydrates present at higher *RH* are characterised by substantial exothermic peaks that occur when increasing *RH*. The notable heat changes observed suggest the incorporation of water molecules into the crystal lattices. The peak shape of the heat flow curves indicates the retention of the crystal structures during the uptake of the water molecules. In addition, perfusion calorimetry is able to distinguish between the different hydrates providing isotherms that are in agreement with the isotherms obtained from gravimetric analysis.

4.4.3 Emodepside methanolates

In the following perfusion experiments, the thermal activity of the different crystalline forms of emodepside exposed to methanol vapours was examined. For that, samples of mod. I and hydrates II-IV were first dried in situ using dry nitrogen before being subjected to stepwise increasing RVP_{MeOH} values. The same experimental setup was used as described in section 4.4.2. Only in case of form II, the *RVP* steps were run for 6 h instead of 4 h in order to ensure the attainment of equilibrium at each step. Due to the notably higher saturation vapour pressure of methanol at 25 °C compared to water, it is not likely that the amount of methanol molecules limits the attainment of equilibrium at each *RVP* step. Hence, the weight of sample was about 9 mg for all forms being regarded as the optimal weight of sample (bottom of the reaction vessel just covered, 4.4.2). The resulting heat flow curves are displayed in Fig. 63.

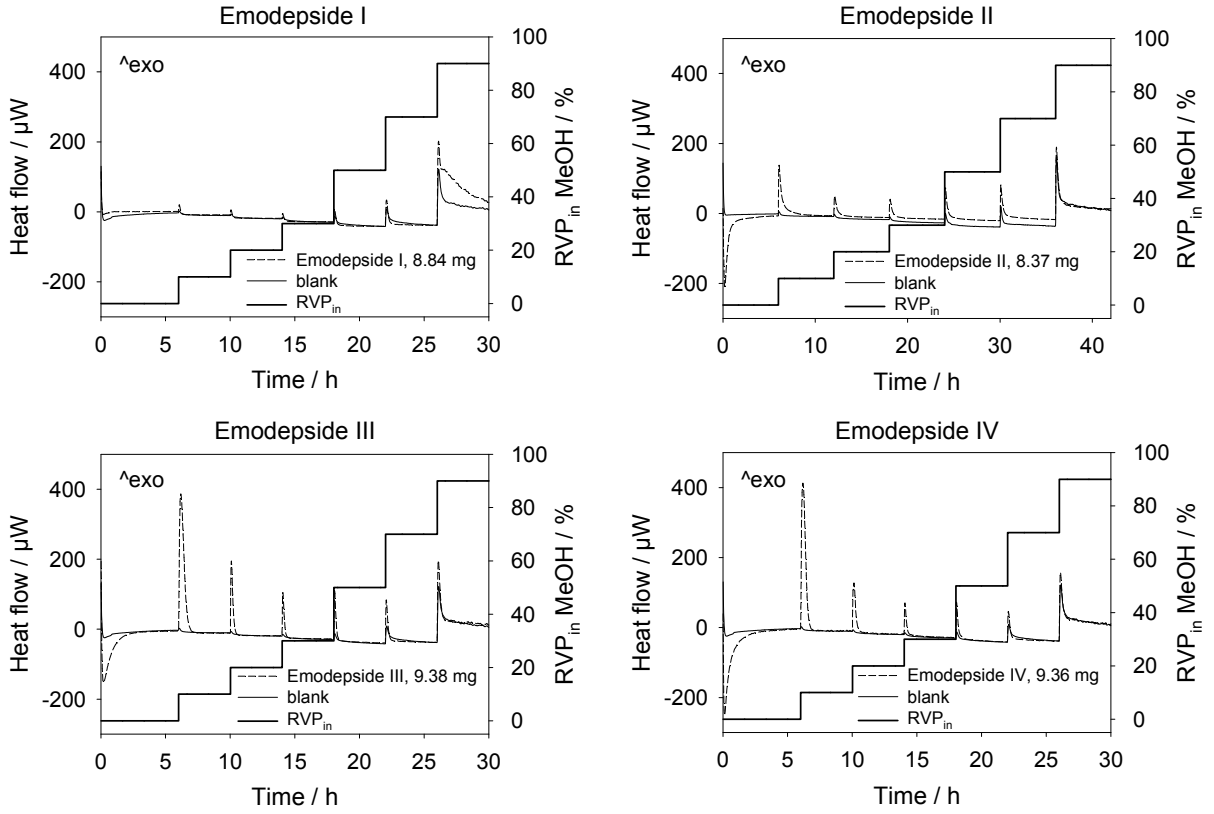

Fig. 63. Heat flow curves of mod. I and hydrates II-IV of emodepside being first dried at 0 % *RVP* for 6 h and then exposed to increasing RVP_{in} values of methanol (25 °C).

The desolvates II-IV formed during the initial drying period exhibit substantial exothermic peaks when exposed to 10 % RVP_{MeOH}. The distinct heat changes and the shape of the curves (peak-shaped) suggest that the desolvates incorporate methanol molecules without changing their three-dimensional structures. While the heat flow curves of the desolvates III and IV are nearly identical, the curve of desolvate II somewhat differs. Compared to the desolvates III and IV, a lower maximum heat flow value is observed for the desolvate II. Additionally, the heat flow decreases less rapidly so that the time required for the curve to return to the baseline

is longer than the time needed in case of the desolvates III and IV. The longer equilibration time found for desolvate II might be related to slight accommodations of the crystal lattice induced by the incorporation of the methanol molecules. At higher RVP_{MeOH} values, the sample curves show also exothermic peaks in comparison to the blank. However, the heat changes occurring at higher RVP_{MeOH} are considerably smaller compared to the first RVP_{MeOH} step which indicates a smaller number of methanol molecules entering the crystal lattices. In case of emodepside II, the baselines of the sample curve and the blank curve are offset at higher RVP_{MeOH} which is again due to differences in the heat changes associated with the perfusion of the ampoule.

To verify the incorporation of methanol molecules into the crystal lattices of the desolvates II-IV, the samples were analysed by FT-Raman and FT-IR spectroscopy after having finished the measurements. The obtained spectra were compared to the spectra of the desolvates and to the spectra of the non-stoichiometric hydrates recorded at ambient conditions. Both the FT-Raman and FT-IR spectra of the samples exposed to methanol vapours slightly differ from the spectra of the desolvates and hydrates revealing that methanol molecules entered the crystal lattices of the desolvates II-IV without changing the crystal structures. Consequently, isomorphic methanolates have formed named methanolate II, III and IV. Fig. 64 presents the Raman spectra of the methanolates in comparison to the spectra of the desolvates and hydrates. The C-H and the C=O stretching region are presented since changes are most distinct in these regions.

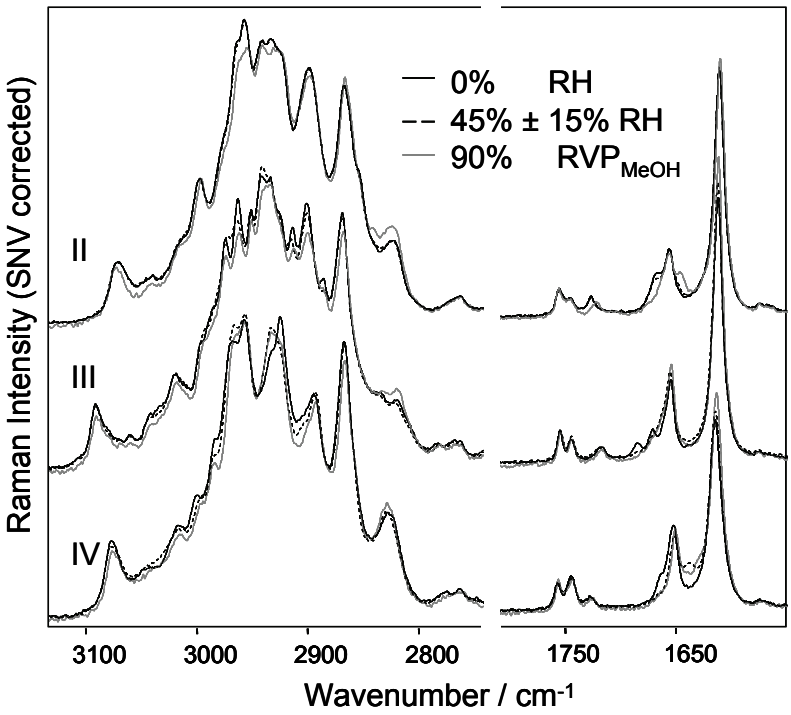

Fig. 64. FT-Raman spectra of the desolvates II-IV exposed to methanol vapours (90 % RVP_{MeOH}) compared to the spectra of the desolvates II-IV (0 % *RH*) and the hydrates II-IV (45 % ± 15 % *RH*).

The spectrum of methanolate II differs from the spectra of desolvate II and hydrate II in the relative intensities of the bands present in the C-H stretching region. Differences are also found in the C=O stretching region. The band present at 1729 cm^{-1} in the spectra of hydrate II and desolvate II is shifted to 1724 cm^{-1} in the spectrum of methanolate II. Additionally, the band at 1669 cm^{-1} visible in the spectra of desolvate II and hydrate II is absent in the spectrum of methanolate II. In exchange, a band at lower wavenumber (1649 cm^{-1}) has emerged. Regarding the spectrum of methanolate III, the intensities of bands present in the C-H stretching region are changed in comparison to the spectra of desolvate III and hydrate III. In addition, the band maximum at 2941 cm^{-1} found in the spectra of desolvate III and hydrate III is absent in the spectrum of methanolate III. In the C=O stretching region, the spectrum of methanolate III more or less corresponds to the spectrum of hydrate III. In case of methanolate IV, the C-H stretching region is similar to the C-H stretching region of hydrate IV, however, slight differences in the intensities of bands are present. In the C=O stretching region, the interaction of methanol molecules with C=O groups of the lattice causes the shoulder of the band at 1654 cm^{-1} present in the spectrum of the desolvate to shift to 1633 cm^{-1} in the spectrum of methanolate IV.
The described differences between the spectra of the methanolates and the spectra of the corresponding hydrates and desolvates represent the changes in the local environment of the C-H and C=O groups caused by the presence of methanol molecules. Similar to the water molecules present in the hydrates, methanol molecules interact with C=O groups of the lattices leading to a shift of C=O stretches towards lower wavenumbers (in comparison to the C=O stretches present in spectra of the corresponding desolvates). Regarding methanolate II and IV, C=O vibrations are further shifted than the C=O vibrations in the spectra of the hydrates II and IV indicating hydrogen bonding to be stronger in the methanolates. For the spectrum of methanolate II, the differences to the spectrum of desolvate II are more pronounced than the differences between the spectra of hydrate II and desolvate II which suggests that the incorporation of the methanol molecules induces more changes in the local environment inside the crystal lattice than the uptake of water molecules. This suggestion is in agreement with the elongated equilibration time found for methanolate II (Fig. 63).
Regarding mod. I of emodepside, the sample curve is similar to the blank curve up to 70 % RVP_{MeOH} (Fig. 63). Only minor exothermic peaks (hardly visible) are measured compared to the blank suggesting the adsorption of methanol molecules to the crystal surface. At 90 % RVP_{MeOH}, a sharp initial peak occurs followed by a prolonged exothermic event. Analysing the sample after the measurement using FT-Raman and FT-IR spectroscopy reveals that mod. I has transformed into methanolate IV. To further study the transformation, a ramp experiment was performed to determine the critical RVP_{MeOH} of transition. The ramp experiment is presented in section 4.1.3.4 as one of two experiments conducted to compare the performances of tested vapour pressure control devices used for perfusion experiments. The critical RVP_{MeOH} for the

transformation found using device A and a ramp rate of 4 % RVP_{MeOH} / h is 84.4 % ± 0.24 % ($\bar{x}$ ± s, n = 3).

For the methanolates II-IV, the heats of sorption were determined at each *RVP* step measured (mean values out of three measurements) in order to calculate the cumulative heat of sorption as a function of RVP_{MeOH} (calorimetric sorption isotherms). Regarding mod. I, the sorption isotherm was determined from the curve presented in Fig. 63 neglecting the fact that equilibrium is not attained at the end of the 90 % RVP_{MeOH} step. The inaccuracy of the isotherm at 90 % RVP_{MeOH} is accepted, since the isotherm is only used to reveal the differences between its shape and the shape of the isotherms of the methanolates (Fig. 65).

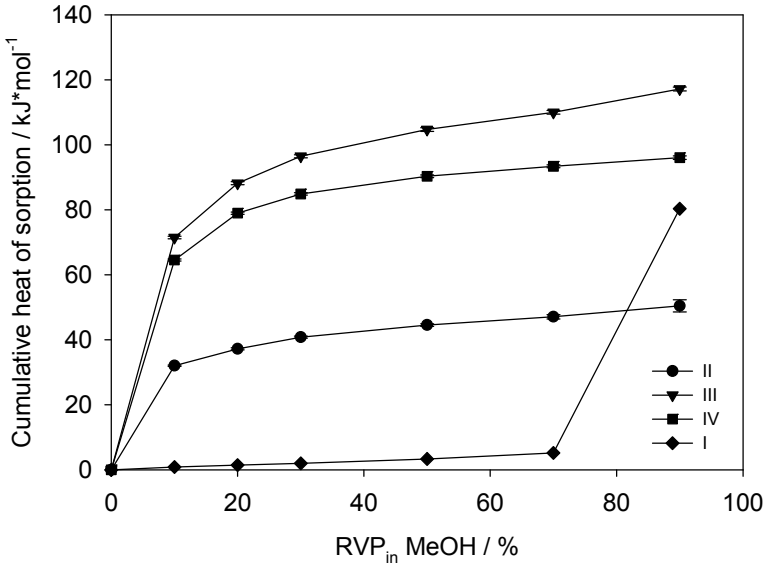

Fig. 65. Calorimetric sorption isotherms of emodepside I-IV using methanol as solvent (25 °C); for emodepside II-IV, the error bars for the cumulative heats of sorption are given (calculated according to the Gaussian error propagation); they are mostly hidden behind the symbols used.

Fig. 65 shows that the isotherm of mod. I considerably differs from the isotherms of the non-stoichiometric methanolates forming isomorphic desolvates. The latter show a steep increase at low RVP_{MeOH} due to the incorporation of methanol molecules into the crystal lattices whereas the isotherm of mod. I increases only slightly up to 70 % RVP_{MeOH} which corresponds to the adsorption of methanol molecules to the crystal surface. The steep increase of the isotherm of mod. I from 70 % to 90 % RVP_{MeOH} represents the phase transformation into methanolate IV. Regarding the isotherms of the methanolates II-IV, a flattening of the slope is observed at higher RVP_{MeOH}. Since the heat of sorption is proportional to the amount of molecules sorbed (4.4.2), the flattening of the slope indicates that the number of methanol molecules entering the lattices decreases with rising RVP_{MeOH}, i.e. most of the structural voids inside the lattices being available for methanol molecules are filled at low RVP_{MeOH}. Fig. 65

reveals that in comparison to the methanolates II and IV, methanolate III exhibits the highest heat output as a function of RVP_{MeOH} which provides indication that the lattice of methanolate III incorporates the highest amount of methanol molecules. This suggestion is in agreement with the presence of large channels assumed for the crystal structure of emodepside III (4.3.4).

Concluding it can be said that perfusion calorimetry has been able to indicate the transformation of the desolvates II-IV into both the hydrates II-IV (4.4.2) and the methanolates II-IV, i.e. it has been able to indicate solvate formation that is characterised by the retention of the crystal structure of the desolvate (desolvate-isomorphic solvate formation). The incorporation of solvent molecules into the lattice without structural rearrangement is deduced from both the calorimetric isotherm and the kinetic of sorption (peak-shaped heat flow curve). Although the adsorption of water molecules (4.4.2) as well as methanol molecules to the crystal surface of mod. I exhibits similar sorption kinetics, the heat changes associated are distinctly smaller leading to different calorimetric isotherms. The transformation of mod. I into methanolate IV which represents solvate formation that is accompanied by changes in the crystal structure differs from the transformation of the desolvates II-IV into the hydrates II-IV and methanolates II-IV, respectively, by the kinetic of the process. Compared to the rapid increase and decrease of the heat flow observed for the desolvate-isomorphic solvate formation, the heat flow associated with the transition of mod. I into methanolate IV changes less rapidly resulting in an elongated equilibration time. The elongated equilibration time is caused by the structural changes that are not required in case of the desolvate-isomorphic solvate formation.

4.4.4 Other substances

To study the general ability of perfusion calorimetry to indicate desolvate-isomorphic solvate formation, additional substances were measured. The substances chosen are erythromycin A dihydrate, spirapril hydrochloride monohydrate and sulfaguanidine. Erythromycin A dihydrate and spirapril hydrochloride monohydrate are further examples of non-stoichiometric hydrates forming isomorphic desolvates (Stephenson *et al.*, 1998). Both hydrates were dehydrated in situ in the sample vessel of the perfusion unit and then exposed to increasing *RH* and RVP_{MeOH}, respectively. The experimental setup corresponded to that used for the emodepside samples (4.4.2 and 4.4.3) except for the initial drying period that was set to 10 h instead of 6 h to ensure complete dehydration of erythromycin A dihydrate. Similar to the hydrates II-IV of emodepside, the weights of sample used were below the amounts needed to cover the bottom of the vessel to prevent the amount of solvent delivered by the wet line to limit the equilibration process. The third substance, sulfaguanidine, exists as both anhydrate and monohydrate which have different crystal structures (Gift and Taylor, 2007). The transformation of the anhydrate into the monohydrate taking place at higher *RH* was used as further example to test the ability of perfusion

calorimetry to differentiate between solvate formation that is accompanied by structural rearrangement and desolvate-isomorphic solvate formation. For that, the sulfaguanidine anhydrate was obtained by heating the monohydrate in a drying oven at 110 °C over night (Gift and Taylor, 2007). The anhydrate was then exposed to increasing *RH* using the same experimental setup as described in section 4.4.2. The heat flow curves of the test substances subjected to increasing *RH* are given in Fig. 66.

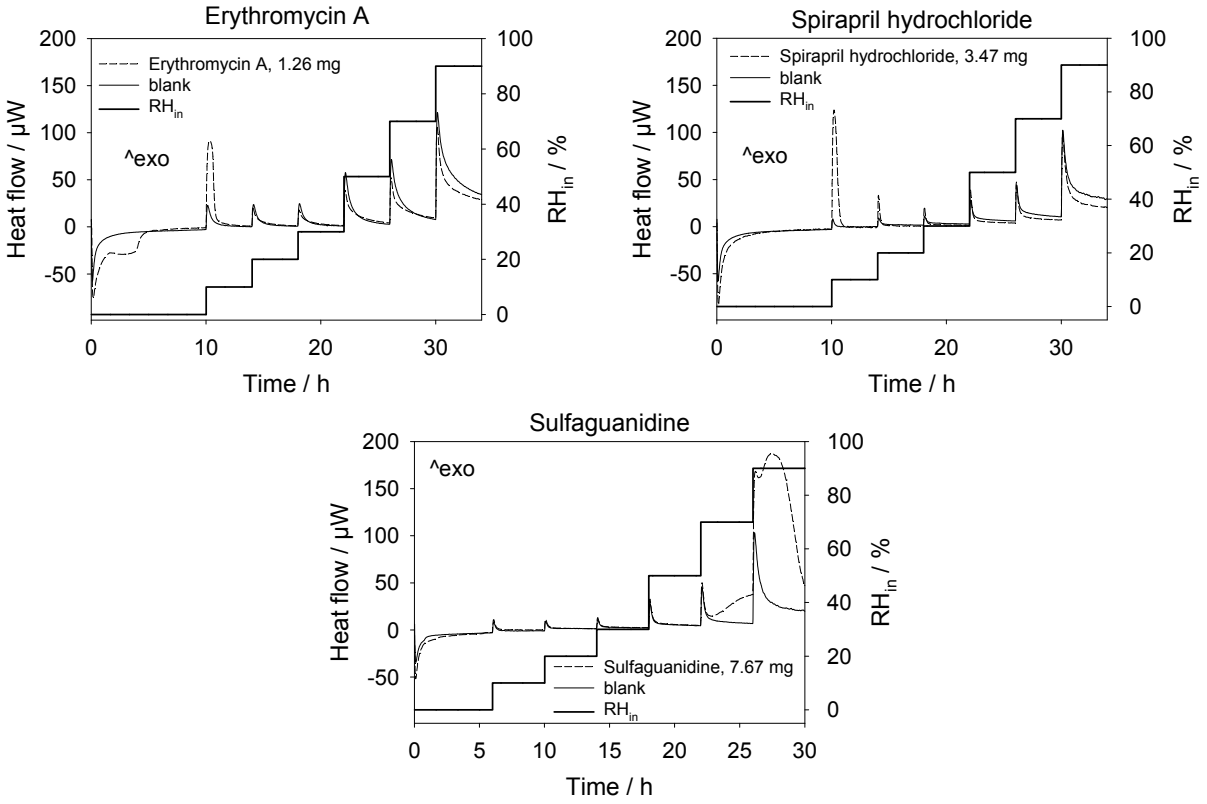

Fig. 66. Heat flow curves of erythromycin A dihydrate, spirapril hydrochloride monohydrate and sulfaguanidine anhydrate being first exposed to 0 % *RH* and then exposed to increasing *RH* (25 °C).

At 0 % *RH*, both erythromycin A dihydrate and spirapril hydrochloride monohydrate show distinct endothermic heat flows corresponding to dehydration. For erythromycin A dihydrate, the dehydration process takes longer. This might be explained the fact that the hydrogen bonding of the water molecules is stronger in case of erythromycin A dihydrate (Stephenson *et al.*, 1998) which might hinder the dehydration process. Similar to the desolvates II-IV of emodepside, the desolvates of erythromycin A dihydrate and spirapril hydrochloride monohydrate exhibit substantial exothermic peaks when increasing *RH* to 10 % due to the incorporation of water molecules into the solvent-free lattices. After about 1 h to 1.5 h, the samples have equilibrated at 10 % *RH*. Similar to the desolvates II-IV of emodepside, the calorimetric equilibration times are longer than the gravimetric equilibration times reported in literature (Stephenson *et al.*, 1997; Stephenson *et al.*, 1998). Possible explanations are given in section 4.4.2. At higher *RH*, the sample curves more or less correspond to the

blank curves. For both spirapril hydrochloride and erythromycin A, the heat flow curve is observed to fall below the blank curve at higher *RH* which is due to slight differences between sample and blank curve regarding the heat changes associated with the perfusion of the vessel. Erythromycin A was recorded a few months later than spirapril hydrochloride. Around the same time, the blank curve was repeated to have a realtime blank. It is presented together with the sample curve of erythromycin A (Fig. 66). The thermal activity of the repeated blank curve is higher compared to the thermal activity of the first blank (presented together with the sample curve of spirapril hydrochloride). One possible reason is that the surface of the inner wall of the reaction vessel may have changed (e.g. due to scratches) which is expected to influence the blank heat flow since one of the effects that are attributed to the blank heat flow is the adsorption of solvent molecules to the inner wall of the vessel (4.1.3.2.2). The calorimetric data were used to determine the cumulative heats of sorption as a function of *RH* (calorimetric isotherms) for both erythromycin A and spirapril hydrochloride (Fig. 67).

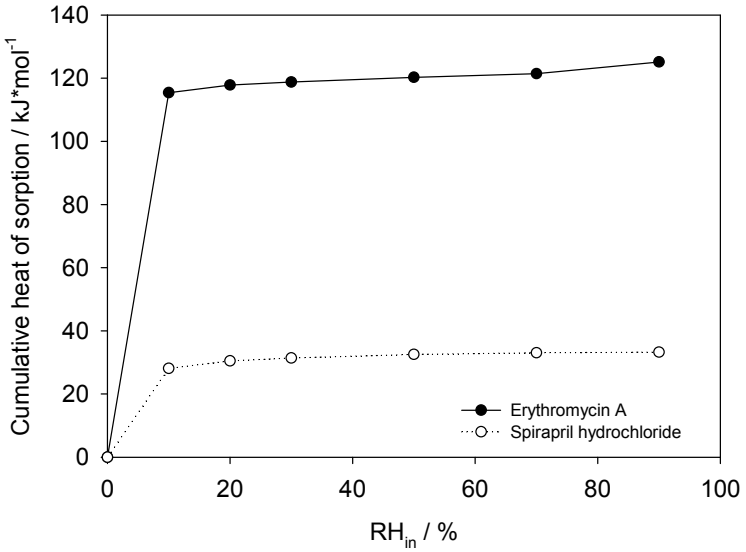

Fig. 67. Calorimetric sorption isotherms of erythromycin A and spirapril hydrochloride using water as solvent (25 °C).

The isotherms of both substances show a steep increase at low *RH* suggesting the presence of desolvates forming isomorphic solvates (Authelin, 2005). The shape of the isotherms agrees well with the shape of the corresponding gravimetric isotherms reported in literature (Stephenson *et al.*, 1998). However, what differs from the gravimetric results is the relative position of the calorimetric isotherms. The cumulative heat of sorption of erythromycin A is about 5 times the cumulative heat of sorption of spirapril hydrochloride (Fig. 67). In opposition to that, the total amount of water sorbed by erythromycin A (mol*mol^{-1}) is twice the amount incorporated by spirapril hydrochloride (Stephenson *et al.*, 1998). The higher heat of sorption (heat of hydration) found for erythromycin A indicates a stronger increase in lattice energy

induced by the presence of the water molecules relative to the increase in the lattice energy of spirapril hydrochloride.

In contrast to the desolvates of erythromycin A dihydrate and spirapril hydrochloride monohydrate, sulfaguanidine anhydrate shows minor if any thermal activity up to 50 % *RH* (Fig. 66). At 70 % *RH*, the heat flow starts to slowly increase after about 1 h suggesting the start of the hydrate formation. At 90 % *RH*, the slope of the heat flow curve becomes steeper indicating an increase in the rate of the transition into the hydrate. The heat flow reaches a maximum after about 2 h before it starts to return to the baseline. FT-Raman analysis of the sample after the experiment confirms the transformation into sulfaguanidine monohydrate. The *RH* step at which hydration starts and the observed dependence of the rate of transition on *RH* are consistent with literature (Gift and Taylor, 2007). Similar to the transition of emodepside mod. I into methanolate IV, the heat flow corresponding to the formation of sulfaguanidine monohydrate changes less rapidly compared to the heat flow that describes desolvate-isomorphic solvate formation. Hence, perfusion calorimetry has also been suitable to distinguish sulfaguanidine hydrate formation from desolvate-isomorphic solvate formation.

The exposure of the desolvates of erythromycin A and spirapril hydrochloride to increasing RVP_{MeOH} results in the following heat flow curves (Fig. 68).

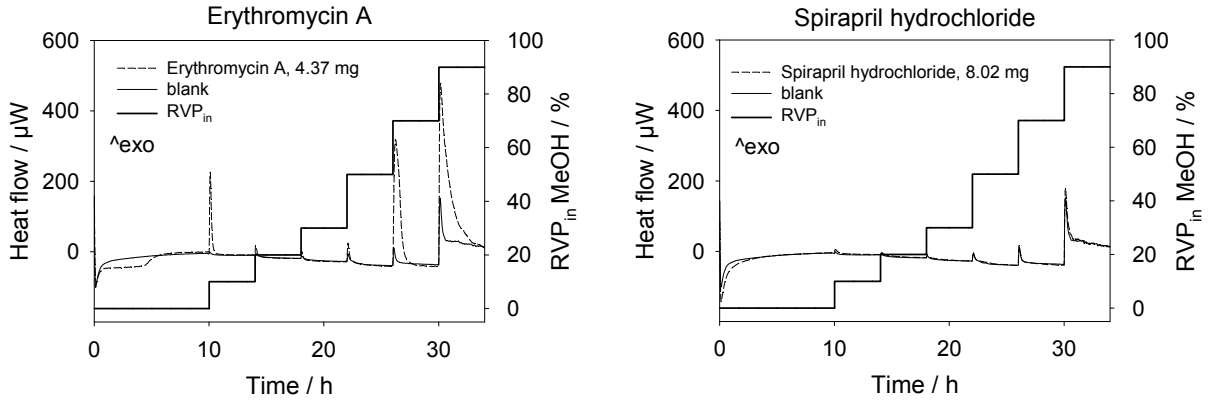

Fig. 68. Heat flow curves of erythromycin A dihydrate and spirapril hydrochloride monohydrate being first exposed to 0 % *RVP* and then exposed to increasing RVP_{in} of methanol (25 °C).

Throughout the RVP_{MeOH} range, the heat flow curve of the desolvate of spirapril hydrochloride corresponds to the blank curve. This finding suggests that the formation of an isomorphic methanolate does not occur since the structural voids present in the lattice of the desolvate are not sufficient in size to accommodate methanol molecules. After finishing the measurement, the sample was analysed using FT-Raman and FT-IR spectroscopy. The transfer of the sample into the sample holder (FT-Raman spectroscopy) respectively the ATR unit (FT-IR spectroscopy) required the sample to be shortly exposed to ambient conditions prior to measurement. The exposure time was sufficient for the desolvate to re-hydrate so that for both FT-Raman and FT-IR spectroscopy, the spectrum of the monohydrate is

obtained (data not shown). Regarding the desolvate of erythromycin A, a substantial exothermic peak is observed at 10 % RVP_{MeOH} indicating methanolate formation. When the RVP_{MeOH} is further increased, remarkable enthalpy changes are recorded at 70 % and 90 % RVP_{MeOH}. Visual examination of the sample after the measurement reveals that the sample has changed into a saturated methanol solution (deliquescence). To confirm that methanol molecules enter the lattice at 10 % RVP_{MeOH}, the experiment was repeated and stopped at the end of the 10 % step in order to examine the sample using FT-Raman and FT-IR spectroscopy. The FT-Raman spectrum of the sample more or less corresponds to the spectrum of the desolvate of erythromycin A (data not shown). The desolvate had been obtained by storing erythromycin A dihydrate over P_20_5 for 4 days. There might be slight differences between both spectra, however, due to a low signal-to-noise ratio, it is not possible to decide whether differences are significant. In opposition to that, the FT-IR spectrum of the sample shows slight but significant differences in comparison to the spectra of the desolvate and the dihydrate (Fig. 69).

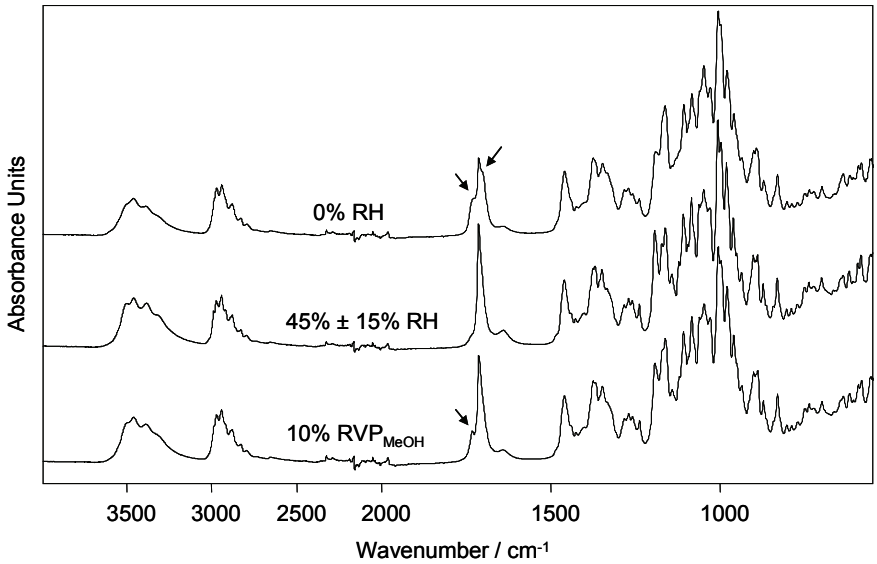

Fig. 69. FT-IR spectra of the desolvate of erythromycin A exposed to 10 % RVP_{MeOH} compared to the spectra of the desolvate (0 % *RH*) and the hydrate of erythromycin A (45 % ± 15 % *RH*).

For example, differences are readily visible in the C=O stretching region. While all solid forms have a band at 1713 cm^{-1}, the sample obtained from the perfusion experiment additionally exhibits an absorption maximum at 1732 cm^{-1} whereas in case of the desolvate, two further bands overlap with the band at 1713 cm^{-1} visible as shoulders. The differences in the spectra confirm the desolvate-isomorphic methanolate formation suggested from perfusion calorimetry.

4.4.5 Summary of results

The investigation of several non-stoichiometric solvates forming isomorphic desolvates has shown that perfusion calorimetry is a valuable tool to indicate desolvate-isomorphic solvate formation. Isomorphic solvate formation is deduced

from both the calorimetric isotherm (thermodynamics) and the shape of the heat flow curve (kinetics). It is characterised by a substantial exothermic event at low *RVP*. This thermal activity results in a notable increase of the calorimetric isotherm in the region of low *RVP*. The heat flow curve associated with solvate formation is peak-shaped reflecting the rapid uptake of solvent molecules which is typical for desolvate-isomorphic solvate formation. Since the presence of a desolvate / isomorphic solvate system is, among other things, deduced from the shape of the heat flow curve, it has to be taken into consideration that the amount of solvent supplied by the wet line may limit the attainment of equilibrium and thus may affect the shape of the curve. Possibilities to prevent the amount of solvent delivered to limit equilibration are to use small weight of samples and to increase the total flow rate used. Contrary to the rapid increase and decrease of the heat flow observed for the desolvate-isomorphic solvate formation, the heat flow associated with solvate formation that is accompanied by structural rearrangement changes less rapidly resulting in an elongated equilibration time. The elongated equilibration time is caused by the structural changes that are not required in case of the desolvate-isomorphic solvate formation. However, it has to be taken into consideration that the energy barriers to structural rearrangement may be (partly) overcome by milling the sample, for example (generation of defective sites that facilitate solid-solid transition). In this case, a peak-shaped heat flow curve may be obtained. Consequently, the history of the sample has to be known. Although perfusion calorimetry, due to its unspecific nature, is not able to prove the existence of desolvate-isomorphic solvate formation, it is suitable to provide indication within a short period of time.

5 Conclusions

A general method to test the vapour pressure control devices used in perfusion calorimetry to control the atmosphere over the sample was successfully developed. The method allows the user to determine the relative vapour pressure (*RVP*) of solvent generated inside the sample vessel. The knowledge of the actual *RVP* inside the vessel enables the user, if necessary, to adjust experimental settings in order to expose the sample to the desired *RVP*. The method is suitable to test devices based on a flow switch valve as well as devices operating with two mass flow controllers. Furthermore, it is applicable to different solvents. Consequently, the method developed enables the user to reliably perform perfusion calorimetry.

The solid form screening of toltrazuril was successful in producing different solid forms resulting in three modifications and an amorphous form. The characterisation of the modifications permitted the determination of their thermodynamic relationships. Regarding emodepside, the use of a variety of methods succeeded in the characterisation of the state of water in the forms I-IV revealing that the forms II-IV are hydrates forming isomorphic desolvates.

Perfusion calorimetry turned out to be a valuable tool in the characterisation of both APIs. Regarding toltrazuril, the method enabled to measure the heats of transition of modifications. Although the use of isothermal microcalorimetry to monitor the transformation of one modification into another in the presence of solvent vapours has been described in literature, only the “miniature humidity chamber” method has been used so far (Vemuri *et al.*, 2004). In case of emodepside, the study of the hydrates II-IV using water vapours as well as methanol vapours showed that perfusion calorimetry is a valuable tool to investigate desolvate-isomorphic solvate formation. The measurement of further solvates forming isomorphic desolvates confirmed the general suitability of the method to indicate the presence of this type of solvate. The use of perfusion calorimetry in the characterisation of solvates forming isomorphic desolvates represents a new application field of perfusion calorimetry. In comparison to other methods used to identify this type of solvate, perfusion calorimetry has the advantage of being a fast tool to provide indication whether desolvate-isomorphic solvate formation takes place, for any solvent that is of interest. Furthermore, the non-destructive nature of perfusion calorimetry allows for the subsequent analysis of the sample with FT-Raman or FT-IR analysis making it possible to verify the indication provided by perfusion calorimetry.

Summarising, this study successfully revealed the use of perfusion calorimetry in solid form analysis. The study of the solid forms of toltrazuril and emodepside and the thorough investigation of the potential of perfusion calorimetry significantly contribute to a better understanding of solid forms, in particular to the investigation of solvates forming isomorphic desolvates.

6 Experimental part

6.1 Materials

6.1.1 Raw materials

Substance	Manufacturer / supplier	Batch
acetone, p.a.	Merck, Darmstadt, Germany	several
acetonitrile Lichrosolv®, gradient grade	Merck, Darmstadt, Germany	several
ammonium nitrate, p.a.	Merck, Darmstadt, Germany	several
emodepside form I	KVP, Kiel, Germany	KP00JFS
emodepside form II	Fujisawa Pharmaceutical, Osaka, Japan	K7001B
erythromycin A dihydrate, analytical standard	Riedel de Haen, Seelze, Germany	3050X
ethanol, p.a.	Merck, Darmstadt, Germany	several
ethylacetate, p.a.	Merck, Darmstadt, Germany	several
isobutanol, p.a.	Merck, Darmstadt, Germany	several
isopropanol, p.a.	Merck, Darmstadt, Germany	several
lithium chloride, p.a.	Merck, Darmstadt, Germany	several
methanol, p.a.	Merck, Darmstadt, Germany	several
Milli-Q® water	in-house production using a Milli-Q® Gradient System	several
phosphorous pentoxide Sicapent®	Merck, Darmstadt, Germany	ZC750243539
potassium chloride, p.a.	Merck, Darmstadt, Germany	K38145536
potassium thiocyanate, p.a.	Merck, Darmstadt, Germany	several
spirapril hydrochloride monohydrate, CRS	European Directorate for the Quality of Medicines & HealthCare	1
sulfaguanidine monohydrate, analytical standard	Fluka, Buchs, Switzerland	8016X
toltrazuril mod. B	KVP, Kiel, Germany	KP00J8601, KP04H0401
toluol, p.a.	Merck, Darmstadt, Germany	several

6.1.2 Solid form preparation

The preparation of the solid forms of toltrazuril and emodepside, respectively, investigated in this study is described in the chapter results and discussion (4.2.2 and 4.3.2, respectively). The preparation of sulfaguanidine anhydrate was performed as described in literature (Gift and Taylor, 2007).

6.2 Methods

6.2.1 Solid form screening

The performance of the solid form screening of toltrazuril is described in 4.2.2. The Kofler hot bench used for crystallising the melt was manufactured by Wagner & Munz, München, Germany.

6.2.2 Solid form characterisation

6.2.2.1 Thermal analysis

6.2.2.1.1 Thermomicroscopy

Microscopic investigations were performed using a Thermovar polarising light microscope (Leica Biosystems Nussloch GmbH, Wetzlar, Germany) and an Axioskop 40 (Carl Zeis MicroImaging GmbH, Göttingen, Germany), both equipped with a hot-stage. Samples were placed between two coverslips for investigations.

6.2.2.1.2 DSC

DSC curves were recorded using a DSC 822e calorimeter as well as a DSC 823e calorimeter (both Mettler Toledo GmbH, Giessen, Germany). About 3 mg to 7 mg of the sample was weighed into an aluminium pan and sealed with a perforated lid. The sample was heated using nitrogen purge (50 ml*min^{-1}). An empty pan was taken as reference. Before starting a series of measurements, the calorimeter was calibrated at 10 °C*min^{-1} using indium. The calibration at 10 °C*min^{-1} was sufficient for the calorimeter to be also calibrated at the other heating rates applied (verified with the help of test measurements).

6.2.2.1.3 TGA

To monitor the mass change of the sample, a TG system (Mettler Toledo GmbH, Giessen, Germany) equipped with a TGA850 thermobalance was used. The samples were heated with 10 °C*min^{-1} in an open aluminium pan while nitrogen was passed along the open pan (50 ml*min^{-1}) as well as along the balance (10 ml*min^{-1}). Prior to a series of measurements, the temperature was calibrated using indium and aluminium.

6.2.2.1.4 Evolved gas analysis

Evolved gas analysis was performed using a Bruker Vector 22 spectrometer (Bruker Optik GmbH, Ettlingen, Germany) with a modified sampling system. The sampling system consisted of a furnace combined with a gas cell. The furnace was used to heat the sample and the gases evolved were analysed in the gas cell by transmission spectroscopy. About 400 mg of the sample was heated up to 200 °C applying a heating rate of 3 °C*min^{-1}. The sample was kept at 200 °C for 23 min. Spectra of the gases evolved were recorded from 4000 cm^{-1} to 550 cm^{-1} at a resolution of 4 cm^{-1} (5 scans).

6.2.2.2 Spectroscopy

6.2.2.2.1 FT-Raman spectroscopy

Raman spectra were acquired with a Bruker RFS 100S spectrometer (Bruker Optik GmbH, Ettlingen, Germany) using a Nd:YAG laser (1064 nm) as excitation source and a high sensitivity Ge-detector (cooled with liquid nitrogen). The spectra were recorded from 3500 cm^{-1} to 20 cm^{-1} at a resolution of 1 cm^{-1} (128 scans) using a laser output of 750 mW.

6.2.2.2.2 FT-IR spectroscopy and VT FT-IR spectroscopy

Infrared analysis was carried out with a FT-IR Bruker Tensor 37 spectrometer (Bruker Optik GmbH, Ettlingen, Germany) using a Heated Diamond Top-plate as sampling system (attenuated total reflection method). Spectra were recorded over the range of 4000 cm^{-1} to 550 cm^{-1} at a resolution of 2 cm^{-1} (64 scans). Variable temperature measurements were performed using the heaters embedded in the Top-plate. In the experiments described in section 4.3.3.2.2.3, the samples were heated to 120 °C applying a heating rate of 20 °C*min^{-1}. The samples were kept at 120 °C for 10 min before being allowed to cool down to RT. During the heating phase, the anvil was not pressed on the samples in order to allow for water evaporation. During the cooling phase however, the anvil was pressed on the samples to prevent the reuptake of water. In the experiments performed to investigate the differences in the melting behaviour of the batches A and B of form III (IV) of emodepside (4.3.3.1.1), samples were first heated up to 130 °C at a heating rate of 20 °C*min^{-1}. The anvil was not pressed on the samples during the heating phase. At 130 °C, spectra of the samples were taken. Then, the samples were further heated in 5 °C steps up to 175 °C (batches of form IV) and 180 °C (batches of form III), respectively, using a heating rate of 10 °C*min^{-1}. At each step, spectra were recorded.

6.2.2.2.3 FT-NIR spectroscopy

NIR spectra were recorded on a Bruker IFS 28N spectrometer (Bruker Optik GmbH, Ettlingen, Germany) equipped with a fibre optic probe. The scanned wavelength range was 1000 nm to 2500 nm at a resolution of 8 cm^{-1} (15 scans).

6.2.2.2.4 Sample preparation

To obtain spectra at ambient conditions, samples were measured without any preparation. To acquire spectra at different *RH*, samples were stored at 22 °C in exsiccators containing either phosphorous pentoxide (0 % *RH*) or a saturated aqueous solution of lithium chloride (11 % *RH*), potassium thiocyanate (47 % *RH*), ammonium nitrate (62 % *RH*) or potassium chloride (85 % *RH*). After a storage period of 7 days, spectra were recorded. In case of FT-Raman spectroscopy, samples were equilibrated directly in the sample holders (glass vials) that were sealed immediately after being taken out of the exsiccators in order to minimise the time the conditioned samples were exposed to ambient humidity before recording started.

6.2.2.2.5 Data treatment

Data treatment included the standard normal variate (SNV) method and second derivative treatment. SNV was used to correct multiplicative effects. In case of FT-IR and FT-NIR spectroscopy, the entire measuring range was used for SNV. Regarding the FT-Raman spectra of emodepside samples, SNV was performed over the range of 3200 cm^{-1} to 570 cm^{-1}. The region below 570 cm^{-1} was excluded from normalisation because of the presence of spectral features (baseline drift and a single, very intense and sharp band at around 84 cm^{-1}) that would impair the result of SNV normalisation if included into the spectral data range being treated with SNV. Second derivative treatment was used to enhance the visual resolution of FT-NIR spectra. The second derivative spectra were obtained using the Savitzky-Golay method (9 smoothing points).

6.2.2.3 X-ray diffraction

6.2.2.3.1 X-ray powder diffraction (XRPD)

Samples were analysed with either a STOE STADI-P transmission diffractometer (STOE & Cie GmbH, Darmstadt, Germany) or a PANalytical X`Pert Pro transmission diffractometer (PANalytical, Almelo, Netherlands) using $CuK\alpha_1$ radiation, a voltage of 45 kV (STOE) and 40 kV (PANalytical), respectively, and a current of 35 mA (STOE) and 40 mA (PANalytical), respectively. The STOE STADI-P transmission diffractometer was equipped with a linear Position Sensitive Detector. Data were collected over the range of 2 ° to 38 ° (2theta) at a scan rate of 310 s per step and a step size of 0.01 °. The PANalytical X`Pert Pro transmission diffractometer used a

PixCel detector having a resolution of 0.001 °. Samples were scanned from 2 ° to 38 ° (2theta).

6.2.2.3.2 VT XRPD

Measurements were performed on a STOE STADI-P fixed stage diffractometer (STOE & Cie GmbH, Darmstadt, Germany) equipped with a furnace using $CuK\alpha_1$ radiation, a voltage of 45 kV and a current of 35 mA. The sample placed in an open capillary was heated in 10 °C steps up to 120 °C at a heating rate of 5 °C*min^{-1}. At each step, a diffractogram was recorded after a holding time of 10 min. An Imaging Plate Detector was used. Data were collected from 1.89 ° to 104.88 ° (2theta). Each measurement took 720 s.

6.2.2.3.3 Single crystal structure analysis

Crystal structure determination was carried out using a Xcalibur diffractometer (Oxford diffraction Ltd, Abingdon, United Kingdom) equipped with CuK radiation (λ = 1.54178 Å), a Cryojet low temperature device (T = 100 K) and a CCD area detector (model Ruby). Crystal structure solution was achieved using direct methods as implemented in SHELXTL (Sheldrick, 2008). Least-squares refinement on F2 using all measured intensities was carried out using SHELXTL.

6.2.2.4 Sorption analysis

6.2.2.4.1 Gravimetric sorption analysis

Sorption / desorption isotherms were recorded using an in-house temperature and humidity controlled moisture balance at 22 °C. After the insertion of the samples, the system was evacuated and the samples were dried for 140 h. The desired *RH* was then set by allowing the influx of the appropriate amount of water vapour. The *RH* was increased from 0 % *RH* to 90 % *RH* in 10 % steps using 3 % *RH*, 6 % *RH*, 15 % *RH* and 95 % *RH* as additional steps (sorption isotherm). To obtain the desorption isotherm, the *RH* was decreased to 85 % *RH* first and then lowered from 85 % *RH* to 10 % *RH* in 15 % steps. Finally, the *RH* was reduced to 6 % *RH*, 4 % *RH*, 2 % *RH* and 0 % *RH*. The absolute value of the rate of change in mass had to be ≤ 2 ppm*h^{-1} before the *RH* was changed to the next step.

6.2.2.4.2 Perfusion calorimetry

Experiments were performed using a 2277 Thermal Activity Monitor (formerly Thermometric AB, Järfälla, Sweden, now TA Instruments, New Castle, Delaware). To expose the sample to a controlled RVP_{Solv} during measurement, both vapour pressure control devices based on a flow switch valve and vapour pressure control devices working with two mass flow controllers were used. Control devices of the first type consist of the 2250-010 4 ml *RH* Perfusion Ampoule (TA Instruments, New Castle, Delaware) a mass flow controller (Bronkhorst High-Tech, AK Ruurlo,

Netherlands), a flow switch valve (TA Instruments, New Castle, Delaware) and the 2281 Flow Switch Module (TA Instruments, New Castle, Delaware). The mass flow controller based devices are composed of the 2250-010 4 ml *RH* Perfusion Ampoule, two mass flow controllers (Bronkhorst High-Tech, AK Ruurlo, Netherlands) and the 3811 Flow Control Module (TA Instruments, New Castle, Delaware). The operating modes of the devices are described in section 2.4.1. All experiments were carried out at 25 °C. The experimental conditions slightly differed depending on the type of control device used. When working with a flow switch valve based device, the total flow rate was set to 50 ml*h^{-1} (0 °C, 1.01325 bar) and the amount of solvent placed into each of the two solvent reservoirs of the perfusion ampoule was 0.5 ml. The switching cycle time of the valve was set to 10 s. For experiments conducted with mass flow controller based devices, the total flow rate was set to 80 ml*h^{-1} or 160 ml*h^{-1} (0 °C, 1.01325 bar). The amount of solvent placed into the first and second solvent reservoir of the perfusion ampoule was 1 ml and 0.5 ml, respectively. Irrespective of the type of device used, the heater of the perfusion ampoule was set to 45 °C.

In case an API was measured, it was accurately weighed and transferred into the reaction vessel. The weight of sample ranged between 1 mg and 15 mg. For experiments conducted to determine the RVP_{Solv} of the wet line, the solvent (0.2 ml to 2.4 ml) was directly inserted into the reaction vessel. The loaded reaction vessel was connected to the perfusion ampoule which was then equilibrated in the different equilibration positions for 20 min before starting the measurement. The sorption experiments described in section 4.4 were carried out using tested control devices. The results from the testing procedure were used to adapt *RVP* settings in order to create the desired RVP_{in} values.

Experiments were performed having an empty, closed stainless steel ampoule in the reference position. Before starting a series of measurements, the calorimeter was calibrated using a static calibration. The calibration heat flow generated by the internal calibration heater resistors was 1000 µW. Only for the measurements performed to verify the saturation of the wet line with methanol vapours, a calibration heat flow of 3000 µW was used. The calibration was performed having the perfusion ampoule inside the measuring position and the reference ampoule inside the reference position. During calibration, the solvent reservoirs and the reaction vessel of the perfusion ampoule were empty and the gas flow was turned off.

After each experiment, the amount of solvent left in the solvent reservoirs was checked. If there was the risk that the reservoirs might drain during the following experiment, the reservoirs were refilled prior to measurement.

6.2.2.5 Volume flow measurements

Measurements were performed using a 10 ml soap film flow meter (Agilent Technologies, Santa Clara, California) wetted with a soap solution. In order to carry out the volume flow measurements, the *RH* perfusion ampoule was placed outside

the microcalorimeter. The solvent reservoirs were emptied and the heater was turned off. The reaction vessel was removed giving the possibility of connecting either the dry line or the wet line to the soap film flow meter. For each *RVP* tested, a new calorimetric experiment was started in the Digitam® software of the TAM 2277. When testing a flow switch valve, the RVP_{set} values checked were 0 %, 20 %, 40 %, 60 %, 80 %, 85 %, 90 %, 95 % and 100 %. In order to verify the performance of mass flow controllers, the volume flow rates were first tested at 0 %, 5 %, 35 %, 65 %, 95 % and 100 % RVP_{set}. After having established that the performance of the mass flow controllers may be described by a linear model (4.1.3.1), a reduced number of measuring points was used for the testing of further mass flow controllers (0 %, 5 %, 95 % and 100 %). At each *RVP* tested, the volume leaving the wet and the dry line respectively within a certain time period was measured. The time period depended on the total flow rate used. It was chosen so that the minimum volume to be read was 0.5 ml. Each measurement was repeated twice. At the beginning of each measurement, ambient temperature and pressure were recorded.

6.2.2.6 Density measurements

The true density of a sample was measured at 25 °C using a helium pycnometer. The instrument used was a NPY1 Micropycnometer (Quantachrome Instruments, Boynton Beach, Florida). Regarding the solid forms C and D of toltrazuril, the measuring cell was only half-full due to the limited amount of substance available. Before starting a series of measurements, a system suitability test was performed by measuring the densities of two test substances (glycine and DL-leucine).

6.2.2.7 Annealing studies

A few milligrams of a 1:1 ($m*m^{-1}$) mixture of the forms D and C of toltrazuril (preparation: 4.2.1) placed in a crystallising dish were annealed in a drying oven until (partial) transformation was detected by FT-IR analysis. Annealing studies were performed at 65 °C, 85 °C, 90 °C, 95 °C, 100 °C and 125 °C.

6.2.2.8 Slurry conversion studies

Slurry conversion studies at RT were conducted in 20 ml conical flasks sealed with glass stoppers. Studies at 70 °C were performed in an oil bath using a 20 ml round bottom flask and a reflux condenser. Suspensions were stirred for 3 h and 2 weeks, respectively, depending on the aim of the experiment (4.2.3.4). The preparation of the mixtures of the toltrazuril modifications used for experiments is given in section 4.2.1. After the designated stirring time, suspensions were filtered off, air dried and analysed using FT-IR spectroscopy.

6.2.2.9 High pressure liquid chromatography

Measurements were performed using an Agilent HP 1100 system (Agilent Technologies, Santa Clara, California) equipped with a stainless steal column

(diameter 4.6 mm, length 15 cm) packed with Waters Symmetry C18, 5 µm (Waters Corporation, Milford, Massachusetts). The column temperature was 35 °C, the flow 1.0 ml*min^{-1} and the detection wavelength was 254 nm (ultraviolet detector). The emodepside samples were dissolved in acetonitrile. Water and acetonitrile were used as eluents. The gradient was increased from 50 % acetonitrile up to 100 % in 30 min. The gradient was then kept at 100 % for 5 min before changing it back to 50 %. It was held at 50 % for 10 min before ending the gradient. The retention time of emodepside was about 18 min.

7 Acknowledgements

This study was a co-operation between the Institute of Pharmaceutics and Biopharmaceutics, Heinrich-Heine-University Düsseldorf, Germany, and Bayer Animal Health GmbH, Research & Development, Analytics, Leverkusen, Germany. I would like to thank all the people who supported me during my work.

I am most grateful to my supervisors, Prof. Nora Anne Urbanetz and Dr. Michael Träubel. I thank them for their guidance, their support, for all the fruitful discussions and the great time we spent together.

Prof. Dr. Peter Kleinebudde is thanked very much for reviewing this thesis.

I also thank the all the people working at the department Research & Development, Analytics for the good reception to the team, for their helpfulness and technical assistance. Special thanks go to Dr. Sabine Giesa for being my supervisor in the last weeks of my studies and to Dr. Martina Preu (current head of department) and Dr. Sabine Bongaerts (previous head of department) for funding my research.

Furthermore, I am very grateful to Dr. Britta Olenik from Bayer Crop Science for allowing me to use the facilities in her laboratory. I sincerely thank her and her team for their support and affection.

I would also like to express my gratitude to Dr. Alfons Grunenberg from Bayer Schering Pharma for interesting discussions, valuable comments and for the possibility to use the facilities in his laboratory. The members of his team, especially Birgit Keil, are thanked for showing me how to use the equipment and for their helpfulness.

I thank the whole research group at the Institute of Pharmaceutics and Biopharmaceutics for interesting discussions in the seminar series.

My colleagues at Bayer Animal Health, Petra Lange, Claudia Selbach, Alexander Müller, Birgitta Pausch, Sabine Kölling and Niclas Förster are thanked for encouragement, useful discussions and friendship throughout my time at Bayer.

Dr. Hans-Christoph Weiß from Currenta GmbH is thanked for the conduction of the single crystal structure analysis.

Finally, I would like to deeply thank my family and Markus for their love and support.

8 References

Aaltonen, J., Strachan, C.J., Pollanen, K., Yliruusi, J. and Rantanen, J., Hyphenated spectroscopy as a polymorph screening tool, J. Pharm. Biomed. Anal. 44 (2007a) 477-483.

Aaltonen, J., Kogermann, K., Strachan, C.J. and Rantanen, J., In-line monitoring of solid-state transitions during fluidisation, Chem. Eng. Sci. 62 (2007b) 408-415.

Aaltonen, J., Gordon, K.C., Strachan, C.J. and Rades, T., Perspectives in the use of spectroscopy to characterise pharmaceutical solids, Int. J. Pharm. 364 (2008) 159-169.

Aaltonen, J., Alles, M., Mirza, S., Koradia, V., Gordon, K.C. and Rantanen, J., Solid form screening - A review, Eur. J. Pharm. Biopharm. 71 (2009) 23-37.

Ahlneck, C. and Zografi, G., The molecular basis of moisture effects on the physical and chemical stability of drugs in the solid state, Int. J. Pharm. 62 (1990) 87-95.

Ahlqvist, M.U.A. and Taylor, L.S., Water dynamics in channel hydrates investigated using H/D exchange, Int. J. Pharm. 241 (2002) 253-261.

Ahmed, H., Buckton, G. and Rawlins, D.A., The use of isothermal microcalorimetry in the study of small degrees of amorphous content of a hydrophobic powder, Int. J. Pharm. 130 (1996) 195-201.

Airaksinen, S., Luukkonen, P., Jorgensen, A.C., Karjalainen, M., Rantanen, J. and liruusi, J., Effects of Excipients on Hydrate Formation in Wet Masses Containing Theophylline, J. Pharm. Sci. 92 (2003) 516-528.

Airaksinen, S., Karjalainen, M., Shevchenko, A., Westermarck, S., Leppänen, E., Rantanen, J. and Yliruusi, J., Role of Water in the Physical Stability of Solid Dosage Formulations, J. Pharm. Sci. 94 (2005) 2147-2165.

Alkhamis, K.A., Salem, M.S. and Obaidat, R.M., Comparison between Dehydration and Desolvation Kinetics of Fluconazole Monohydrate and Fluconazole Ethylacetate Solvate using Three Different Models, J. Pharm. Sci. 95 (2005) 859-870.

Allmann, R., Röntgenpulverdiffraktometrie, Springer-Verlag, Berlin, Germany, 2003, pp. 51-86.

Almarsson, Ö. and Zaworotko, M.J., Crystal engineering of the composition of pharmaceutical phases. Do pharmaceutical co-crystals represent a new path to improved medicines?, Chem. Commun. (2004) 1889-1896.

Amado, A.M., Nolasco, M.M. and Ribeiro-Clar, P.J.A., Probing pseudopolymorphic transitions in pharmaceutical solids using Raman spectroscopy: Hydration and dehydration of theophylline, J. Pharm. Sci. 96 (2007) 1366-1379.

Ambike, A.A., Mahadik, K.R. and Paradkar, A., Physico-Chemical Characterization and Stability Study of Glassy Simvastatin, Drug Dev. Ind. Pharm. 31 (2005) 895-899.

Angberg, M., Nystrom, C. and Castensson, S., Evaluation of heat-conduction microcalorimetry in pharmaceutical stability studies. VI. Continuous monitoring of the interaction of water vapour with powders and powder mixtures at various relative humidities, Int. J. Pharm. 83 (1982) 11-23.

Angberg, M., Nystrom, C. and Castensson, S., Evaluation of heat-conduction microcalorimetry in pharmaceutical stability studies. V. A new approach for continuous measurements in abundant water vapour, Int. J. Pharm. 81 (1992) 153-167.

Atkins, P.W. and de Paula, J., Physikalische Chemie, WILEY-VCH Verlag GmbH & Co. KGaA, Weinheim, Germany, 2006, pp. 773-824.

Authelin, J.-R., Thermodynamics of non-stoichiometric pharmaceutical hydrates, Int. J. Pharm. 303 (2005) 37-53.

Bauer, K.H., Frömming, K.-H. and Führer, C., Lehrbuch der Pharmazeutischen Technologie, Wissenschaftliche Verlagsgesellschaft mbH, Stuttgart, Germany, 2002, pp. 59-60.

Bennema, P., van Eupen, J., van der Wolf, B.M.A., Los, J.H. and Meekes, H., Solubility of molecular crystals: Polymorphism in the light of solubility theory, Int. J. Pharm. 351 (2008) 74-91.

Bernstein, J., Davey, R.J. and Henck, J.-O., Concomitant Polymorphs, Angew. Chem. Int. Ed. 38 (1999) 3440-3461.

Bernstein, J., ...And Another Comment on Pseudopolymorphism, Cryst. Growth Des. 5 (2005) 1661-1662.

Blagden, N., Davey, R.J., Rowe, R. and Roberts, R., Disappearing polymorphs and the role of reaction by-products: the case of sulphathiazole, Int. J. Pharm. 172 (1998) 169-177.

Blagden, N., de Matas, M., Gavan, P.T. and York, P., Crystal engineering of active pharmaceutical ingredients to improve solubility and dissolution rates, Adv. Drug Deliv. Rev. 59 (2007) 617-630.

Blanco, M., Coello, J., Iturriaga, H., Maspoch, S. and de la Pezuela, C., Near-infrared spectroscopy in the pharmaceutical industry, Analyst 123 (1998) 135R-150R.

Brittain, H.G., Methods for the Characterization of Polymorphs, in: Brittain, H.G. (Ed.), Polymorphism in Pharmaceutical Solids, Marcel Dekker Inc., New York, 1999, pp. 227-278.

Brittain, H.G., Effects of Mechanical Processing on Phase Composition, J. Pharm. Sci. 91 (2002) 1573-1580.

Brittain, H.G., Polymorphism and Solvatomorphism 2005, J. Pharm. Sci. 96 (2007) 705-728.

Buckton, G., Darcy, P., Greenleaf, D. and Holbrook, P., The use of isothermal microcalorimetry in the study of changes in crystallinity of spray-dried salbutamol sulphate, Int. J. Pharm. 116 (1995) 113-118.

Buckton, G., Yonemochi, E., Yoon, W.L. and Moffat, A., Water sorption and near IR spectroscopy to study the differences between microcrystalline cellulose and silicified microcrystalline cellulose before and after wet granulation, Int. J. Pharm. 181 (1999a) 41-47.

Buckton, G., Dove, J.W. and Davies, P., Isothermal microcalorimetry and inverse phase gas chromatography to study small changes in powder surface properties, Int. J. Pharm. 193 (1999b) 13-19.

Buckton, G., Isothermal microcalorimetry water sorption experiments: calibration issues, Thermochim. Acta 347 (2000) 63-71.

Bugay, D.E., Characterization of the solid-state: spectroscopic techniques, Adv. Drug Deliv. Rev. 48 (2001) 43-65.

Burger, A. and Ramberger, R., On the Polymorphism of Pharmaceuticals and Other Molecular Crystals. I. Theory of Thermodynamic Rules, Mikrochim. Acta 2 (1979a) 259-271.

Burger, A. and Ramberger, R., On the Polymorphism of Pharmaceuticals and Other Molecular Crystals. II. Applicability of Thermodynamic Rules, Mikrochim. Acta 2 (1979b) 273-316.

Burger, A., DTA und DSC: Grundlagen, Methodik und Anwendung, Pharmazie in unserer Zeit 6 (1982) 177-189.

Burger, A. and Griesser, U.J., Charakterisierung und Identifizierung von 11 Kristallformen von Succinylsulfathiazol, Sci. Pharm. 57 (1989) 293-305.

Burger, A., Henck, J.-O., Hetz, S., Rollinger, J.M., Weissnicht, A.A. and Stöttner, H., Energy/Temperature Diagram and Compression Behavior of the Polymorphs of D-Mannitol, J. Pharm. Sci. 89 (1999) 457-468.

Burger, A. and Lettenbichler, A., Polymorphism and preformulation studies of lifibrol, Eur. J. Pharm. Biopharm. 49 (2000) 65-72.

Byrn, S., Pfeiffer, R., Ganey, M., Hoiberg, C. and Poochikian, G., Pharmaceutical Solids: A Strategic Approach to Regulatory Considerations, Pharm. Res. 12 (1995) 945-954.

Byrn, S.R., Pfeiffer, R.R. and Stowell, J.G., Solid-state chemistry of drugs, SSCI, Inc., West Lafayette, Indiana, 1999a, pp. 3-44.

Byrn, S.R., Pfeiffer, R.R. and Stowell, J.G., Solid-state chemistry of drugs, SSCI, Inc., West Lafayette, Indiana, 1999b, pp. 279-284.

Byrn, S.R., Pfeiffer, R.R. and Stowell, J.G., Solid-state chemistry of drugs, SSCI, Inc., West Lafayette, Indiana, 1999c, pp. 259-278.

Byrn, S.R., Pfeiffer, R.R. and Stowell, J.G., Polymorphs, Regulations, Crystallisation, and Solid-State Chemistry, Am. Pharm. Rev. 5 (2002) 92-99.

Caira, M.R., Bettinetti, G. and Sorrenti, M., Structural Relationships, Thermal Properties, and Physicochemical Characterization of Anhydrous and Solvated Crystalline Forms of Tetroxoprim, J. Pharm. Sci. 91 (2002) 467-481.

Cao, W., Mao, C., Chen, W., Lin, H., Krishnan, S. and Cauchon, N., Differentiation and Quantitative Determination of Surface and Hydrate Water in Lyophilized Mannitol Using NIR Spectroscopy, J. Pharm. Sci. 95 (2006) 2077-2086.

Carvajal, M.T. and Staniforth, J.N., Interactions of water with the surfaces of crystal polymorphs, Int. J. Pharm. 307 (2006) 216-224.

Chalmers, J.M. and Dent, G., Vibrational Spectroscopic Methods in Pharmaceutical Solid-state Characterization, in: Hilfiker, R. (Ed.), Polymorphism in the Pharmaceutical Industry, WILEY-VCH Verlag GmbH & Co. KGaA, Weinheim, Germany, 2006, pp. 95-138.

Chawla, G., Gupta, P., Thilagavathi, R., Chakraborti, A.K. and Bansal, A.K., Characterization of solid-state forms of celecoxib, Eur. J. Pharm. Sci. 20 (2003) 305-317.

Chemburkar, S.R., Bauer, J., Deming, K., Spiwek, H., Patel, K., Morris, J., Henry, R., Spanton, S., Dziki, W., Porter, W., Quick, J., Bauer, P., Donaubauer, J., Narayanan, B.A., Soldani, M., Riley, D. and McFarland, K., Dealing with the impact of Ritonavir polymorphs on the late stages of bulk drug process development, Org. Process Res. Dev. 4 (2000) 413-417.

Cheng, W.T. and Lin, S.Y., Famotidine polymorphic transformation in the grinding process significantly depends on environmental humidity or water content, Int. J. Pharm. 357 (2008) 164-168.

Columbano, A., Buckton, G. and Wikeley, P., A study of the crystallisation of amorphous salbutamol sulphate using water vapour sorption and near infrared spectroscopy, Int. J. Pharm. 237 (2002) 171-178.

Danforth, P.M. and David, L., Rapid Assessment of the Structural Relaxation Behavior of Amorphous Pharmaceutical Solids: Effect of Residual Water on Molecular Mobility, Pharm. Res. 23 (2006) 2291-2305.

DattaChowdhury, B., Alexander, K.S., Riga, A.T. and Chatterjee, K., Evaluation of Crystallization Kinetics of Amorphous Sulfapyridine by DSC, Am. Pharm. Rev. 8 (2005) 60-68.

Davey, R.J., Crystallization: how come you look so good?, Nature 428 (2004) 374-375.

David, L., Aziz, B. and Danforth, P.M., Microcalorimetric Measurement of the Interactions Between Water Vapor and Amorphous Pharmaceutical Solids, Pharm. Res. 20 (2003) 308-318.

Davidovich, M., Mueller, R., Raghavan, K., Ranadive, S., Vitez, I., Sarsfield, B., DiMarco, J., Gougoutas, J. and Newman, A., The Role of Powder X-ray Diffraction as a Powerful Tool in Characterization of Various Hydrates of a Drug Substance, American Pharmaceutical Review 4 (2001) 53-60.

De Beer, T.R.M., Vergote, G.J., Baeyens, W.R.G., Remon, J.P., Vervaet, C. and Verpoort, F., Development and validation of a direct, non-destructive quantitative method for medroxyprogesterone acetate in a pharmaceutical suspension using FT-Raman spectroscopy, Eur. J. Pharm. Sci. 23 (2004) 355-362.

De Beer, T.R.M., Bodson, C., Dejaegher, B., Walczak, B., Vercruysse, P., Burggraeve, A., Lemos, A., Delattre, L., Heyden, Y.V., Remon, J.P., Vervaet, C. and Baeyens, W.R.G., Raman spectroscopy as a process analytical technology (PAT) tool for the in-line monitoring and understanding of a powder blending process, J. Pharm. Biomed. Anal. 48 (2008) 772-779.

Delwiche, S.R., Pitt, R.E. and Norris, K.H., Examination of Starch-Water and Cellulose-Water Interactions With Near Infrared (NIR) Diffuse Reflectance Spectroscopy., starch/stärke 43 (1991) 415-422.

Desiraju, G.R., Crystal and co-crystal, Cryst. Eng. Commun. 5 (2003) 466-467.

Desiraju, G.R., Counterpoint: What`s in a Name?, Cryst. Growth Des. 4 (2004) 1089-1090.

Di Martino, P., Censi, R., Barthélémy, C., Gobetto, R., Joiris, E., Masic, A., Odou, P. and Martelli, S., Characterization and compaction behaviour of nimesulide crystal forms, Int. J. Pharm. 342 (2007) 137-144.

Dong, Z., Salsbury, J.S., Zhou, D., Munson, E.J., Schroeder, S.A., Prakash, I., Vyazovkin, S., Wight, C.A. and Grant, D.J.W., Dehydration Kinetics of Neotame Monohydrate, J. Pharm. Sci. 91 (2002) 1423-1431.

Dunitz, J.D., Crystal and co-crystal: a second opinion, Cryst. Eng. Commun. 5 (2003) 506-506.

Fiebich, K. and Mutz, M., Evaluation of Calorimetric and Gravimetric Methods to Quantify the Amorphous Content of Desferal, J. Therm. Anal. Calorim. 57 (1999) 75-85.

Fornés, V. and Chaussidon, J., An interpretation of the evolution with temperature of the $\nu_2 + \nu_3$ combination band in water, J. Chem. Phys. 68 (1978) 4667-4671.

Gaisford, S. and Buckton, G., Potential applications of microcalorimetry for the study of physical processes in pharmaceuticals, Thermochim. Acta 380 (2001) 185-198.

Gaisford, S., Pharmaceutical isothermal calorimetry, Informa Healthcare Inc., New York, 2007, pp. 13-32.

Gatonovic-Kustrin, S., Glass, B.D., Mangan, M. and Smithson, J., Analysing the crystal purity of mebendazole raw material and its stability in a suspension formulation, Int. J. Pharm. 361 (2008) 245-250.

Gift, A.D. and Taylor, L.S., Hyphenation of Raman spectroscopy with gravimetric analysis to interrogate water-solid interactions in pharmaceutical systems, J. Pharm. Biomed. Anal. 43 (2007) 14-23.

Giron, D., Thermal analysis and calorimetric methods in the characterisation of polymorphs and solvates, Thermochim. Acta 248 (1995) 1-59.

Giron, D., Draghi, M., Goldbronn, C., Pfeffer, S. and Piechon, P., Study of the polymorphic behaviour of some local anesthetic drugs, J. Therm. Anal. 49 (1997) 913-927.

Giron, D., Goldbronn, Ch., Mutz, M., Pfeffer, S., Piechon, Ph. and Schwab, Ph., Solid State Characterizations of Pharmaceutical Hydrates, J. Therm. Anal. Calorim. 68 (2002) 453-465.

Grant, D.J.W., Theory and Origin of Polymorphism, in: Brittain, H.G. (Ed.), Polymorphism in Pharmaceutical Solids, Marcel Dekker, Inc., New York, 1999, pp. 1-33.

Griesser, U.J., Auer, M.E. and Burger, A., Micro-thermal analysis, FTIR- and Raman-microscopy of (R,S)-proxyphylline crystal forms, Microchem. J. 65 (2000) 283-292.

Griesser, U.J., The Importance of Solvates, in: Hilfiker, R. (Ed.), Polymorphism in the Pharmaceutical Industry, VILEY-VCH Verlag GmbH & Co. KGaA, Weinheim, Germany, 2006, pp. 211-233.

Grunenberg, A., Henck, J.-O. and Siesler, H.W., Theoretical derivation and practical application of energy/temperature diagrams as an instrument in preformulation studies of polymorphic drug substances, Int. J. Pharm. 129 (1996) 147-158.

Grunenberg, A., Polymorphie und Thermische Analyse pharmazeutischer Wirkstoffe, Pharmazie in unserer Zeit 26 (1997) 224-231.

Guillory, J.K., Generation of Polymorphs, Hydrates, Solvates, and Amorphous Solids, in: Brittain, H.G. (Ed.), Polymorphism in Pharmaceutical Solids, Marcel Dekker, Inc., New York, 1999, pp. 183-226.

Haines, P.J., Introduction, in: Haines, P.J. (Ed.), Principles of thermal analysis and calorimetry, Royal Society of Chemistry, Cambridge, UK, 2002, pp. 1-9.

Hausman, D.S., Cambron, R.T. and Sakr, A., Application of on-line Raman spectroscopy for characterizing relationships between drug hydration state and tablet physical stability, Int. J. Pharm. 299 (2005) 19-33.

He, X., Griesser, U.J., Stowell, J.G., Borchardt, T.B. and Byrn, S., Conformational Color Polymorphism and Control of Crystallization of 5-Methyl-2-[(4-methyl-2-nitrophenyl)amino]-3-thiophenecarbonitrile, J. Pharm. Sci. 90 (2000) 371-388.

Heal, G.R., Thermogravimetry and Derivative Thermogravimetry, in: Haines, P.J. (Ed.), Principles of Thermal Analysis and Calorimetry, Royal Society of Chemistry, Cambridge, UK, 2002, pp. 10-54.

Heinz, A., Savolainen, M., Rades, T. and Strachan, C.J., Quantifying ternary mixtures of different solid-state forms of indomethacin by Raman and near-infrared spectroscopy, Eur. J. Pharm. Sci. 32 (2007) 182-192.

Heise, H.M. and Winzen, R., Chemometrics in near-infrared spectroscopy, in: Siesler, H.W., Ozaki, Y., Kawata, S. and Heise, H.M. (Eds.), Near-Infrared Spectroscopy. Principles, Instruments, Applications, WILEY-VCH Verlag GmbH & Co.KGaA, Weinheim, Germany, 2002, pp. 147-149.

Henck, J.-O., Finner, E. and Burger, A., Polymorphism of Tedisamil Dihydrochloride, J. Pharm. Sci. 89 (2000) 1151-1159.

Higgins, J.P., Arrivo, S.M. and Reed, R.A., Approach to the determination of hydrate form conversions of drug compounds and solid dosage forms by near-infrared spectroscopy, J. Pharm. Sci. 92 (2003) 2303-2316.

Hilfiker, R., Blatter, F. and von Raumer, M., Relevance of Solid-state Properties for Pharmaceutical Products, in: Hilfiker, R. (Ed.), Polymorphism in the Pharmaceutical Industry, VILEY-VCH Verlag GmbH & Co. KGaA, Weinheim, Germany, 2006a, pp. 1-19.

Hilfiker, R., De Paul, S.M. and Szelagiewicz, M., Approaches to Polymorphism Screening, in: Hilfiker, R. (Ed.), Polymorphism in the Pharmaceutical Industry, WILEY-VCH Verlag GmbH & Co.KGaA, Weinheim, Germany, 2006b, pp. 287-308.

International Conference on Harmonisation, ICH Harmonised Tripartite Guideline Q6A, Test procedures and acceptance criteria for new drug substances and new drug products: chemical substances, http://www.ich.org/cache/compo/276-254-1.html (1999).

IUPAC, Compendium of Chemical Terminology, 2nd ed. (the "Gold Book"), XML on-line corrected version: http://goldbook.iupac.org (2006) created by Nic, M., Jirat, J. and Kosata, B.

Jakobsen, D.F., Frokjaer, S., Larsen, C., Niemann, H. and Buur, A., Application of isothermal microcalorimetry in preformulation. I. Hygroscopicity of drug substances, Int. J. Pharm. 156 (1997) 67-77.

Katrincic, L.M., Sun, Y.T., Carlton, R.A., Diederich, A.M., Mueller, R.L. and Vogt, F.G., Characterization, selection, and development of an orally dosed drug polymorph from an enantiotropically related system, Int. J. Pharm. 366 (2009) 1-13.

Kawakami, K., Numa, T. and Ida, Y., Assessment of Amorphous Content by Microcalorimetry, J. Pharm. Sci. 91 (2001) 417-423.

Kawata, S., Instrumentation for Near-Infrared Spectroscopy, in: Siesler, H.W., Ozaki, Y., Kawata, S. and Heise, H.M. (Eds.), Near-Infrared Spectroscopy. Principles, Instruments, Applications., WILEY-VCH Verlag GmbH & Co.KGaA, Weinheim, Germany, 2002, pp. 43-74.

Khankari, R.K. and Grant, D.J.W., Pharmaceutical hydrates, Thermochim. Acta 248 (1995) 61-79.

Kim, M.S., Jin, S.J., Kim, J.S., Park, H.J., Song, H.S., Neubert, R.H.H. and Hwang, S.J., Preparation, characterization and in vivo evaluation of amorphous atorvastatin calcium nanoparticles using supercritical antisolvent (SAS) process, Eur. J. Pharm. Biopharm. 69 (2008) 454-465.

Kitamura, M., Controlling factor of polymorphism in crystallization process, J. Cryst. Growth 237-239 (2002) 2205-2214.

Kitamura, S., Chang, L.-C. and Guillory, J.K., Polymorphism of mefloquine hydrochloride, Int. J. Pharm. 101 (1994) 127-144.

Kofler, A., Thermomikro-Methoden zur Kennzeichnung organischer Stoffe und Stoffgemische, Verlag Chemie, Weinheim, Germany, 1954, pp. 28-32.

Kogermann, K., Aaltonen, J., Strachan, C.J., Pollanen, K., Veski, P., Heinamaki, J., Yliruusi, J. and Rantanen, J., Qualitative in situ analysis of multiple solid-state forms using spectroscopy and partial least squares discriminant modeling, J. Pharm. Sci. 96 (2007) 1802-1820.

Kontny, M.J. and Zografi, G., Sorption of Water by Solids, in: Brittain, H.G. (Ed.), Physical Characterization of Pharmaceutical Solids, Marcel Dekker AG, Basel, Switzerland, 1995, pp. 387-418.

Kuhnert-Brandstätter, M., Thermomicroscopy in the Analysis of Pharmaceuticals, Pergamon Press, Oxford, UK, 1971, pp. 385-406.

Kuhnert-Brandstätter, M., Thermische Analyse in der Pharmazie, Pharmazie 51 (1996) 443-457.

Lane, R.A. and Buckton, G., The novel combination of dynamic vapour sorption gravimetric analysis and near infra-red spectroscopy as a hypenated technique, Int. J. Pharm. 207 (2000) 49-56.

Laye, P.G., Differential Thermal Analysis and Differential Scanning Calorimetry, in: Haines, P.J. (Ed.), Principles of Thermal Analysis and Calorimetry, Royal Society of Chemistry, Cambridge, UK, 2002, pp. 55-93.

Lehto, V.-P. and Laine, E., Assessment of physical stability of different forms of cefadroxil at high humidities, Int. J. Pharm. 163 (1998) 49-62.

Liggins, R.T., Hunter, W.L. and Burt, H.M., Solid-State Characterization of Paclitaxel, J. Pharm. Sci. 86 (1997) 1458-1463.

Llinas, A. and Goodman, J.M., Polymorph control: past, present and future, Drug Discov. Today 13 (2008) 198-210.

Lohani, S. and Grant, D.J.W., Thermodynamics of Polymorphs, in: Hilfiker, R. (Ed.), Polymorphism in the Pharmaceutical Industry, WILEY-VCH Verlag GmbH & Co. KGaA, Weinheim, Germany, 2006, pp. 21-42.

Mackin, L., Zanon, R., Park, J.M., Foster, K., Opalenik, H. and Demonte, M., Quantification of low levels (<10%) of amorphous content in micronised active batches using dynamic vapour sorption and isothermal microcalorimetry, Int. J. Pharm. 231 (2002) 227-236.

Maeda, H., Ozaki, Y., Tanaka, M., Hayashi, N. and Kojima, T., Near infrared spectroscopy and chemometrics studies of temperature-dependent spectral variations of water: relationship between spectral changes and hydrogen bonds, J. Near Infrared Spectrosc. 3 (1995) 191-201.

Markova, N., Sparr, E. and Wadso, L., On application of an isothermal sorption microcalorimeter, Thermochim. Acta 374 (2001) 93-104.

Massa, W., Kristallstrukturbestimmung, Teubner Verlag, München, Germany, 2002, pp. 8-9.

McCrone, W.C., Polymorphism, in: Fox, D., Labes, M.M. and Weissberger, A. (Eds.), Physics and chemistry of the organic solid state, Interscience Publishers, New York, 1965, pp. 725-767.

Morissette, S.L., Almarsson, Í., Peterson, M.L., Remenar, J.F., Read, M.J., Lemmo, A.V., Ellis, S., Cima, M.J. and Gardner, C.R., High-throughput crystallization: polymorphs, salts, co-crystals and solvates of pharmaceutical solids, Adv. Drug Deliv. Rev. 56 (2004) 275-300.

Morris, K.R., Structural Aspects of Hydrates and Solvates, in: Brittain, H.G. (Ed.), Polymorphism in Pharmaceutical Solids, Marcel Dekker AG, Basel, Switzerland, 1999, pp. 125-181.

Newman, A.W. and Byrn, S.R., Solid-state analysis of the active pharmaceutical ingredient in drug products, Drug Discov. Today 8 (2003) 898-905.

Newman, A.W., Reutzel-Edens, S.M. and Zografi, G., Characterization of the "Hygroscopic" Properties of Active Pharmaceutical Ingredients, J. Pharm. Sci. 97 (2008) 1047-1059.

Nichols, G., Light Microscopy, in: Hilfiker, R. (Ed.), Polymorphism in the Pharmaceutical Industry, WILEY-VCH Verlag GmbH & Co.KGaA, Weinheim, Germany, 2006, pp. 167-210.

Othman, A., Evans, J.S.O., Evans, I.R., Harris, R.K. and Hodgkinson, P., Structural study of polymorphs and solvates of finasteride, J. Pharm. Sci. 96 (2007) 1380-1397.

Petit, S. and Coquerel, G., Mechanism of Several Solid-Solid Transformations between Dihydrated and Anhydrous Copper(II) 8 Hydroxyquinolinates. Proposition for a Unified Model for the Dehydration of Molecular Crystals, Chem. Mater. 8 (1996) 2247-2258.

Petit, S. and Coquerel, G., The amorphous state, in: Hilfiker, R. (Ed.), Polymorphism in the Pharmaceutical Industry, WILEY-VCH Verlag GmbH & Co.KGaA, Weinheim, Germany, 2006, pp. 259-285.

Price, S.L., The computational prediction of pharmaceutical crystal structures and polymorphism, Adv. Drug Deliv. Rev. 56 (2004) 301-319.

Räsänen, E., Rantanen, J., Jorgensen, A.C., Karjalainen, M., Paakkari, T. and Yliruusi, J., Novel Indentification of Pseudopolymorphic Changes of Theophylline During Wet Granulation Using Near Infrared Spectroscopy, J. Pharm. Sci. 90 (2001) 389-396.

Redman-Furey, N., Dicks, M., Bigalow-Kern, A., Cambron, R.T., Lubey, G., Lester, C. and Vaughn, D., Structural and analytical characterization of three hydrates and an anhydrate form of risedronate, J. Pharm. Sci. 94 (2005) 893-911.

Reutzel-Edens, S.M. and Newman, A.W., Physical Characterization of Hygroscopicity in Pharmaceutical Solids, in: Hilfiker, R. (Ed.), Polymorphism in the Pharmaceutical Industry, WILEY-VCH Verlag GmbH & Co. KGaA, Weinheim, Germany, 2006, pp. 235-258.

Rocco, W.L., Morphet, C. and Laughlin, S.M., Solid-state characterization of zanoterone, Int. J. Pharm. 122 (1995) 17-25.

Rodriguez, C. and Bugay, D.E., Characterization of Pharmaceutical Solvates by Combined Thermogravimetric and Infrared Analysis, J. Pharm. Sci. 86 (1997) 263-266.

Rodriguez-Spong, B., Price, C.P., Jayasankar, A., Matzger, A.J. and Rodriguez-Hornedo, N., General principles of pharmaceutical solid polymorphism: A supramolecular perspective, Adv. Drug Deliv. Rev. 56 (2004) 241-274.

Rollinger, J.M. and Burger, A., Physico-chemical characterization of hydrated and anhydrous crystal forms of amlodipine besylate, J. Therm. Anal. Calorim. 68 (2002) 361-372.

Ruth, L.T., Griesser, U.J., Morris, K.R., Byrn, S.R. and Stowell, J.G., X-ray Diffraction and Solid-State NMR Investigation of the Single-Crystal to Single-Crystal Dehydration of Thiamine Hydrochloride Monohydrate, Cryst. Growth Des. 3 (2003) 997-1004.

Sachs, L., Angewandte Statistik, Springer-Verlag, Berlin, Germany, 2002, pp. 490-561.

Saleki-Gerhardt, A., Ahlneck, C. and Zografi, G., Assessment of disorder in crystalline solids, Int. J. Pharm. 101 (1994) 237-247.

Samra, R.M. and Buckton, G., The crystallisation of a model hydrophobic drug (terfenadine) following exposure to humidity and organic vapours, Int. J. Pharm. 284 (2004) 53-60.

Schmidt, A.C. and Schwarz, I., Solid-state characterization of non-stoichiometric hydrates of ester-type local anaesthetics. Part XI. Crystal polymorphism of local anaesthetic drugs, Int. J. Pharm. 320 (2006) 4-13.

Schrader, B., General survey of vibrational spectroscopy, in: Schrader, B. (Ed.), Infrared and Raman Spectroscopy. Methods and Applications, VCH VerlagsgesellschaftmbH, Weinheim, Germany, 1995, pp. 7-62.

Shah, B., Kakumanu, V.K. and Bansal, A.K., Analytical techniques for quantification of amorphous/crystalline phases in pharmaceutical solids, J. Pharm. Sci. 95 (2006) 1641-1665.

Shan, N. and Zaworotko, M.J., The role of cocrystals in pharmaceutical science, Drug Discov. Today 13 (2008) 440-446.

Sheldrick, G.M., A short history of SHELX, Acta Cryst. A64 (2008) 112-122.

Sheng, J., Venkatesh, G.M., Duddu, S.P. and Grant, D.J.W., Dehydration Behavior of Eprosartan Mesylate Dihydrate, J. Pharm. Sci. 88 (1999) 1021-1029.

Sheridan, P.L., Graham, B. and David E.Storey, Development of a Flow Microcalorimetry Method for the Assessment of Surface Properties of Powders, Pharm. Res. 12 (1995) 1025-1030.

Siesler, H.W., Introduction, in: Siesler, H.W., Ozaki, Y., Kawata, S. and Heise, H.M. (Eds.), Near-Infrared Spectroscopy. Principles, Instruments, Applications., WILEY-VCH Verlag GmbH & Co.KGaA, Weinheim, Germany, 2002, pp. 1-10.

Stahl, P.H. and Sutter, B., Salt Selection, in: Hilfiker, R. (Ed.), Polymorphism in the Pharmaceutical Industry, WILEY-VCH Verlag GmbH & Co.KGaA, Weinheim, Germany, 2006, pp. 309-332.

Stegemann, S., Leveiller, F., Franchi, D., de Jong, H. and Lindén, H., When poor solubility becomes an issue: From early stage to proof of concept, Eur. J. Pharm. Sci. 31 (2007) 249-261.

Stephenson, G.A. and Diseroad, B.A., Structural relationship and desolvation behavior of cromolyn, cefazolin and fenoprofen sodium hydrates, Int. J. Pharm. 198 (2000) 167-177.

Stephenson, G.A., Forbes, R.A. and Reutzel-Edens, S.M., Characterization of the solid state: quantitative issues, Adv. Drug Deliv. Rev. 48 (2001) 67-90.

Stephenson, G.A., Stowell, J.G., Toma, P.H., Pfeiffer, R.R. and Byrn, S.R., Solid-state Investigations of Erythromycin A Dihydrate: Structure, NMR Spectroscopy, and Hygroscopicity, J. Pharm. Sci. 86 (1997) 1239-1244.

Stephenson, G.A., Groleau, E.G., Kleemann, R.L., Xu, W. and Rigsbee, D.R., Formation of Isomorphic Desolvates: Creating a Molecular Vacuum, J. Pharm. Sci. 87 (1998) 536-542.

Thermometric AB, Sweden, Use of the RH Perfusion System at elevated temperatures, Experimental & Technical Note EN 013 a (2000).

Thermometric AB, Sweden, How to control the humidity in the RH perfusion ampoule, Experimental & Technical Note EN 013 d (2003).

Threlfall, T.L., Analysis of Organic Polymorphs, Analyst 120 (1995) 2435-2460.

Threlfall, T., Crystallisation of Polymorphs: Thermodynamic Insight into the Role of Solvent, Org. Process Res. Dev. 4 (2000) 384-390.

Timmermann, I.L., Steckel, H. and Trunk, M., Assessing the re-crystallization behaviour of amorphous lactose using the RH-perfusion cell, Eur. J. Pharm. Biopharm. 64 (2006) 107-114.

Tumuluri, V.S., Kemper, M.S., Lewis, I.R., Prodduturi, S., Majumdar, S., Avery, B.A. and Repka, M.A., Off-line and on-line measurements of drug-loaded hot-melt extruded films using Raman spectroscopy, Int. J. Pharm. 357 (2008) 77-84.

Umprayn, K. and Mendes, R.W., Hygroscopicity and moisture adsorption kinetics of pharmaceutical solids: a review, Drug Dev. Ind. Pharm. 13 (1987) 653-693.

Urakami, K. and Beezer, A.E., A kinetic and thermodynamic study of seratrodast polymorphic transition by isothermal microcalorimetry, Int. J. Pharm. 257 (2003) 265-271.

Vemuri, M.N., Chrzan, Z. and Cavatur, R., Use of isothermal microcalorimetry in pharmaceutical preformulation studies. Part I. Monitoring crystalline phase transitions, J. Therm. Anal. Calorim. 78 (2004) 47-54.

Vippagunta, S.R., Brittain, H.G. and Grant, D.J.W., Crystalline Solids, Adv. Drug Deliv. Rev. 48 (2001) 3-26.

Vishweshwar, P., McMahon, J.A., Bis, J.A. and Zaworotko, M.J., Pharmaceutical Co-Crystals, J. Pharm. Sci. 95 (2006) 499-516.

Vora, K.L., Buckton, G. and Clapham, D., The use of dynamic vapour sorption and near infra-red spectroscopy (DVS-NIR) to study the crystal transitions of theophylline and the report of a new solid-state transition, Eur. J. Pharm. Sci. 22 (2004) 97-105.

Wadso, L. and Markova, N., Comparison of three methods to find the vapor activity of a hydration step, Eur. J. Pharm. Biopharm. 51 (2001) 77-81.

Wikström, H., Marsac, P.J. and Taylor, L.S., In-Line Monitoring of Hydrate Formation during Wet Granulation Using Raman Spectroscopy, J. Pharm. Sci. 94 (2005) 209-219.

Wildfong, P.L.D., Morris, K.R., Anderson, C.A. and Short, S.M., Demonstration of a shear-based solid-state phase transformation in a small molecular organic system: Chlorpropamide, J. Pharm. Sci. 96 (2007) 1100-1113.

Yonemochi, E., Inoue, Y., Buckton, G., Moffat, A., Oguchi, T. and Yamamoto, K., Differences in Crystallization Behavior Between Quenched and Ground Amorphous Ursodeoxycholic Acid, Pharm. Res. 16 (1999) 835-840.

Yu, L.X., Lionberger, R.A., Raw, A.S., D'Costa, R., Wu, H. and Hussain, A.S., Applications of process analytical technology to crystallization processes, Adv. Drug Deliv. Rev. 56 (2004) 349-369.

Yu, L., Inferring Thermodynamic Stability Relationship of Polymorphs from Melting Data, J. Pharm. Sci. 84 (1995) 966-974.

Yu, L., Reutzel, S.M. and Stephenson, G.A., Physical characterization of polymorphic drugs: an integrated characterization strategy, Pharm. Sci. Technol. To. 1 (1998) 118-127.

Yu, L., Amorphous pharmaceutical solids: preparation, characterization and stabilization, Adv. Drug Deliv. Rev. 48 (2001) 27-42.

Zeitler, J.A., Kogermann, K., Rantanen, J., Rades, T., Taday, P.F., Pepper, M., Aaltonen, J. and Strachan, C.J., Drug hydrate systems and dehydration processes studied by terahertz pulsed spectroscopy, Int. J. Pharm. 334 (2007) 78-84.

Zhou, G.X., Ge, Z., Dorwart, J., Izzo, B., Kukura, J., Bicker, G. and Wyvratt, J., Determination and Differentiation of Surface and Bound Water in Drug Substances by Near Infrared Spectroscopy, J. Pharm. Sci. 92 (2003) 1058-1065.

Zhou, X., Hines, P. and Borer, M.W., Moisture determination in hygroscopic drug substances by near infrared spectroscopy, J. Pharm. Biomed. Anal. 17 (1998) 219-225.

Zhu, H., Yuen, C. and Grant, D.J.W., Influence of water activity in organic solvent + water mixtures on the nature of the crystallizing drug phase. 1. Theophylline, Int. J. Pharm. 135 (1996a) 151-160.

Zhu, H., Khankari, R.K., Padden, B.E., Munson, E.J., Gleason, W.B. and Grant, D.J.W., Physicochemical Characterization of Nedocromil Bivalent Metal Salt Hydrates. 1. Nedocromil Magnesium, J. Pharm. Sci. 85 (1996b) 1026-1034.

Zhu, H., Padden, B.E., Munson, E.J. and Grant, D.J.W., Physicochemical Characterization of Nedocromil Bivalent Metal Salt Hydrates. 2. Nedocromil Zinc, J. Pharm. Sci. 86 (1997) 418-429.

Ziegenbalg, O., Einsatzmöglichkeiten der Mikrokalorimetrie bei der Formulierungsentwicklung in der Veterinaerpharmazie, Dissertation Rheinische Friedrich-Wilhelms-Universität Bonn, Germany (2005).